REPORT DOCUMENTATION PAGE

Form Approved
OMB No. 0704-0188

PLEASE DO NOT RETURN YOUR FORM TO THE ABOVE ORGANIZATION.

1. REPORT DATE *(DD-MM-YYYY)*	2. REPORT TYPE	3. DATES COVERED *(From - To)*
31-03-2011	FINAL REPORT	01-04-2008 to 30-11-2010

4. TITLE AND SUBTITLE
NUMERICAL SIMULATION OF TRANSITION IN HYPERSONIC BOUNDARY LAYERS

5a. CONTRACT NUMBER
FA9550-08-1-0211

5b. GRANT NUMBER

5c. PROGRAM ELEMENT NUMBER

6. AUTHOR(S)
Dr. Hermann F. Fasel

5d. PROJECT NUMBER

5e. TASK NUMBER

5f. WORK UNIT NUMBER

7. PERFORMING ORGANIZATION NAME(S) AND ADDRESS(ES)
Department of Aerospace and Mechanical Engineering,
1130 N. Mountain, P.O. Box 210119,
Tucson, Arizona, 85721

8. PERFORMING ORGANIZATION REPORT NUMBER

9. SPONSORING/MONITORING AGENCY NAME(S) AND ADDRESS(ES)
Air Force Office of Scientific Research,
4015 Wilson Blvd., Room 713,
Arlington, VA 22203

10. SPONSOR/MONITOR'S ACRONYM(S)
AFOSR/RSA

11. SPONSOR/MONITOR'S REPORT NUMBER(S)
AFRL-OSR-VA-TR-2012-0255

12. DISTRIBUTION/AVAILABILITY STATEMENT
A - Approved For Public Release; Distribution is Unlimited.

13. SUPPLEMENTARY NOTES

14. ABSTRACT

The laminar-turbulent transition process in supersonic and hypersonic boundary layers was investigated using spatial and temporal Direct Numerical Simulations (DNS). Our previous research indicated that oblique breakdown might be a highly relevant nonlinear mechanism for supersonic boundary layers. However, a nonlinear mechanism would only be relevant for the transition process if this mechanism can lead to fully developed turbulence. Hence, to address this question, the late nonlinear transition regime of a supersonic flat-plate boundary layer at Mach 3 was studied using spatial DNS. These simulations demonstrated that a fully turbulent flow can develop via oblique breakdown. We also investigated the nonlinear disturbance development in a hypersonic boundary layer on a sharp circular cone at Mach 8 using spatial and temporal DNS. It was confirmed in these simulations that fundamental resonance and oblique breakdown are the viable paths to transition in hypersonic boundary layers.

15. SUBJECT TERMS

16. SECURITY CLASSIFICATION OF:			17. LIMITATION OF ABSTRACT	18. NUMBER OF PAGES	19a. NAME OF RESPONSIBLE PERSON
a. REPORT	b. ABSTRACT	c. THIS PAGE			Dr. Hermann F. Fasel
U	U	U	UU	280	19b. TELEPHONE NUMBER *(Include area code)* 5204810819

Reset

Final Report

AFOSR Grant No. FA9550-08-1-0211

Numerical Simulation of Transition in Hypersonic Boundary Layers

by

Hermann F. Fasel

Department of Aerospace and Mechanical Engineering

The university of Arizona

Tucson, AZ 85721

Contributors:

Andreas Gross

Clayton Koevary

Andreas Laible

Christian Mayer

Jayahar Sivasubramanian

Submitted to

Dr. John D. Schmisseur, Program Manager

The Air Force Office of Scientific Research

F e b r u a r y 2 0 1 1

Table of Contents

Table of Contents—*Continued*

Table of Contents—*Continued*

Table of Contents—*Continued*

List of Figures

List of Figures—*Continued*

List of Figures—*Continued*

List of Figures—*Continued*

List of Figures—*Continued*

List of Figures—*Continued*

List of Figures—*Continued*

List of Figures—*Continued*

List of Figures—*Continued*

List of Figures—*Continued*

List of Figures—*Continued*

List of Figures—*Continued*

List of Figures—*Continued*

List of Figures—*Continued*

List of Figures—*Continued*

List of Figures—*Continued*

List of Figures—*Continued*

List of Figures—*Continued*

List of Figures—*Continued*

List of Figures—*Continued*

List of Figures—*Continued*

List of Figures—*Continued*

List of Tables

List of Symbols

Abbrevations

2D, 3D	Two-/three-dimensional
DNS	Direct Numerical Simulation
EXP	Experiments
FFT	Fast Fourier Transformation
IC	Initial Condition
LST	Linear Stability Theory
NSCC	Navier–Stokes Compressible in C
PSE	Parabolic Stability Equations
TDNS	Temporal Direct Numerical Simulation
TPS	Thermal Protection System

Greek

α	Complex streamwise wavenumber
α_i	Streamwise amplification rate
α_r, β	Streamwise, spanwise/azimuthal wavenumber
γ	Ratio of specific heats
δ	Boundary layer thickness
δ_c	Boundary layer thickness from Reynolds-averaged streamw. velocity
δ_1	Displacement thickness
Δt	Stepsize in time
Δx, Δy, Δz	Grid spacing in streamw., spanw. and spanw./azimuthal direction
η	Factor that determines grid size close to the wall
θ	Phase
θ_c	Cone half angle
Θ	Momentum thickness
κ	Von Kármán constant

List of Symbols—*Continued*

λ_x, λ_z	Streamwise and spanwise/azimuthal wave length
μ	Dynamic viscosity
ν	Kinematic viscosity
ρ	Density
σ	Faktor to determine degree of upwinding
τ_{ij}	Stress tensor
ψ	Wave angle
ω	Angular frequency
ω_x, ω_z	Streamwise, spanw./azimuthal vorticity

Roman

a	Speed of sound
A	Disturbance amplitude
c_f	Skin-friction coefficient
$c_{f,i}$	Incompressible reference skin-friction coefficient
c_p, c_v	Specific heats at constant pressure and volume, respectively
c_{ph}	Phase speed in propagation direction
e	Disturbance voltage from hot-wire measurements
E	Mean voltage from hot-wire measurements
$\boldsymbol{E_c}$, $\boldsymbol{F_c}$, $\boldsymbol{G_c}$	Convective flux vectors
$\boldsymbol{E_d}$, $\boldsymbol{F_d}$, $\boldsymbol{G_d}$	Dissipative flux vectors
E_t	Total energy
$E_{\alpha\alpha}$	One-dimensional energy spectrum for quantity α
f	Frequency
F	Normalized frequency
F_c	Skin-friction transformation function
F_x	Reynolds number transformation function

List of Symbols—*Continued*

$\boldsymbol{H}$	Source term
H_{12}	Shape factor
i_e	Internal energy
k	Thermal conductivity/Fourier mode
$\vec{k}$	Wave vector
k_c	Azimuthal modenumber
K	Number of spectral modes for the spanw./azimuthal direction
L	Arbitrary reference length
L_e	Viscous length scale used for linear stability theory
M	Mach number
M'	Fluctuation Mach number
M_t	Turbulent Mach number
n_x, n_y, n_z	Grid points in streamw., wall-normal, spanw./azimuthal direction
N	Normalized amplitude
p	Pressure
Pr	Prandtl number
$\boldsymbol{q}$	Heat-flux vector
Q	Q-criterion (Vortex identification)
r	Radius of the conical coordinate system
r_{nose}	Cone nose radius
r_{turb}	Turbulent recovery factor
R	Specific gas constant for air
Re	Reynolds number
Re_x	Local Reynolds number
$Re_{x,i}$	Incompressible reference local Reynolds number
R_x	Square root of local Reynolds number

List of Symbols—*Continued*

Re_θ	Reynolds number based on momentum thickness
t	Time
t_1	Pulse duration for the generation of a wave packet
t_{sim}	Duration of a simulation
T	Temperature/Disturbance period
$T_{forcing}$	Forcing period
u, v, w	Streamwise, wall-normal and spanwise velocity component
U, V	Streamwise, wall-normal mean velocity
$\boldsymbol{U}$	Vector of conservative variables
U_c	Van Driest transformed streamwise velocity
v_p	Streamw. velocity distribution over the disturbance hole/slot
x, y, φ/z	Streamwise, wall-normal and azimuthal/spanwise direction
x_1, x_2	Start and end position of disturbance hole/slot in streamw. direction
x_0, x_L	Position of inflow and outflow
y_c	Wall-normal position of critical layer
y_H	Domain height
y_0	Wall-normal position where $c_{ph,x} = 1 - 1/\tilde{M}_e$
z_W	Domain width

Subscripts

ad	Adiabatic
aw	Adiabatic wall value
e	Boundary layer edge conditions
$[h, k]$	[Integer multiples of frequency, spanw./azimuthal wavenumber]
∞	Approach-flow conditions
max	Maximum
ref	Reference

List of Symbols—*Continued*

sec	Secondary
w	Wall value

Superscripts

c	Asymmetric (**c**osine mode)
s	Symmetric (**s**ine mode)
$-$	Reynolds-averaged flow quantity
$'$	Disturbance quantity/fluctuation about Reynolds average
$''$	Fluctuation about Favre average
$+$	In near-wall units
$*$	Dimensional value
$\sim$	Variable in Fourier space/Rotated coordinate system

Abstract

With funding from AFOSR Grant No. FA9550-08-1-0211 the laminar–turbulent transition process in supersonic and hypersonic boundary layers was investigated using spatial and temporal Direct Numerical Simulations (DNS).

Our previous research indicated that oblique breakdown might be a highly relevant nonlinear mechanism for supersonic boundary layers. However, a nonlinear mechanism would only be relevant for the transition process if this mechanism can lead to fully developed turbulence. Hence, to address this question, the late nonlinear transition regime of a supersonic flat-plate boundary layer at Mach 3 was studied using spatial direct numerical simulations. A set of highly resolved DNS of the entire transition path from the linear regime to the turbulence stage was conducted. These simulations demonstrated that a fully turbulent flow can develop via oblique breakdown.

We also investigated the nonlinear disturbance development in a hypersonic boundary layer on a sharp circular cone at Mach 8 using spatial direct numerical simulations. The two main goals were to determine which nonlinear mechanisms are dominant in a broad band, "natural" disturbance environment and then to perform controlled transition simulations of these mechanisms. Towards this end, the flow conditions from the experiments by Stetson *et al.* (1983*b*) are used. Wave packet simulations were performed to understand the nonlinear interactions in a "natural" disturbance environment. These simulations showed that the strongest nonlinear growth occurred for oblique waves near the most amplified axisymmetric wave frequency, suggesting fundamental resonance mechanism. Additionally, a nonlinear growth of low frequency waves was observed, which were shown to be most likely caused by resonance triads.

Spatial simulations with controlled disturbance input showed that fundamental resonance will initiate the transition process for the given flow conditions. The nonlinear regime of transition could be simulated up to the late stages, however, a fully turbulent state could not be reached due to the overwhelming needs for computa-

tional resources. For comparison, controlled simulations of oblique breakdown were also performed. Results showed that the onset of transition is more benign for oblique breakdown than for fundamental breakdown. However, definite conclusions could not be drawn regarding which of the two mechanisms would be more relevant in a natural disturbance environment. Nevertheless, our simulations clearly demonstrate that both of these mechanisms are likely to be relevent for hypersonic boundary layers.

In addition, temporal direct numerical simulations (TDNS) were performed to compliment our investigations using spatial direct numerical simulations. Three different transition mechanisms, namely oblique breakdown, symmetric subharmonic resonance and fundamental resonance were investigated using TDNS. Although subharmonic resonance mechanisms were also detected for these flow conditions, this mechanism is unlikely to lead to complete breakdown to turbulence. In contrast, it was confirmed in these TDNS that fundamental resonance and oblique breakdown are indeed viable paths to transition in hypersonic boundary layers.

1. Introduction

1.1 Research Motivation

Laminar–turbulent transition in hypersonic boundary layers is a major unresolved topic in Fluid Dynamics. Although significant progress has been made in recent years, crucial aspects of the transition physics are still in the dark. For the future High–Speed Civil Transport (HSCT) (Parikh & Nagel, 1990), as well as for numerous defense–related applications such as high–speed missiles (Hingst, 1990; Korejwo & Holden, 1992), high–speed reconnaissance aircraft (Scott, 1996), the Theater Missile Defense (TMD) interceptors (Johnson *et al.*, 1997), and the Hyper–X program (Berry *et al.*, 2001; Borg *et al.*, 2008), considerable progress toward the understanding of high–speed boundary layer transition is required in order to develop reliable transition prediction methods that can be used for the design and safe operation of such advanced flight vehicles. The crucial need for reliable transition prediction methods for high–speed applications is due to the fact that transition to turbulence in supersonic/hypersonic boundary layers is associated with considerable increases in heat transfer. The increased heat loads (caused by transition) on the structure of the flight vehicles represent the main difficulties in designing and operating high–speed vehicles. Appropriate measures to guard against the heat transfer due to aero–thermal loads are expensive and/or result in significant weight penalties. Good estimates of the transition location are of vital importance because only then can the aero–thermal loads and surface temperatures be adequately predicted. In addition to surface heating, transition to turbulence also has a significant effect on the aerodynamic performance of high–speed flight vehicles, as the skin friction for turbulent boundary layers is considerably higher than for the laminar boundary layer.

The understanding of transition for low–speed (incompressible) boundary layers is far ahead of that for high–speed (compressible) boundary layers, although many

crucial aspects are also still not understood even for the low–speed case. There are several important reasons for the significant gap in understanding of high–speed transition relative to low–speed transition. Of course, historically, high–speed flight, in particular hypersonic flight, has not been considered until recently and therefore the need to understand and predict transition did not exist earlier. However, there are two other main reasons why it is more difficult to obtain knowledge for high–speed boundary layer transition than for the low–speed case: i) Quality experiments for high–speed transition are considerably more difficult to carry out than for incompressible transition and require high–speed testing facilities that are expensive to construct and expensive to operate. ii) The physics of high–speed boundary layer transition are much more complex than for low–speeds.

From linear stability theory (Mack, 1969), it is known that multiple instability modes exist for high–speed boundary layer flows, in contrast to only one mode (Tollmien–Schlichting, TS) for the incompressible case. The so-called first mode in supersonic boundary layers is equivalent to the TS–mode in incompressible boundary layers. However, in contrast to incompressible boundary layers, where, according to Squires theorem, two–dimensional waves are generally more amplified than three–dimensional waves, for supersonic boundary layers three–dimensional (oblique) waves are more amplified than two–dimensional ones. Thus, experiments and theory always have to address the more complex problem of three–dimensional wave propagation. In addition to the first mode, which is viscous, higher modes exist for supersonic boundary layers that result from an inviscid instability mechanism. According to Linear Stability Theory (LST), the most unstable higher modes are two–dimensional unlike oblique first modes. Also from linear stability theory, it is known that the first mode is dominant (higher amplification rates) for low supersonic Mach numbers while for Mach numbers above 4 the second mode is dominant (most amplified). In addition, for typical supersonic/hypersonic flight vehicle configurations, the three-dimensional nature of the boundary layers that develop, for example, on swept wings

and/or lifting bodies, can give rise to so-called cross–flow instabilities and, as a consequence, cross–flow vortices that can be stationary or traveling. Due to the difficulties in carrying out experiments (and "controlled" experiments, in particular) and due to the existence of multiple instability modes, the role and importance of the various instability modes in a realistic transition process are not understood at all. Of course, when amplitudes of the various instability modes reach high enough levels, nonlinear interactions of these modes can occur. As a consequence, the transition process in high–speed boundary layers is highly non–unique, which means that slight changes in the environment or vehicle geometry may significantly alter the transition process.

An additional difficulty arises from the fact that for high–speed boundary layers the transition processes in free flight may be very different from those in the laboratory. As shown by Eissler & Bestek (1996), the difference between conditions for free flight ("hot," atmospheric conditions) and the laboratory ("cold" conditions) has a considerable effect on the stability behavior and, as a consequence, on the transition processes. This is best summarized by a quote from Stetson (1990), a pioneer in experimental high–speed transition research: "... one should not expect a transition Reynolds number obtained in any wind tunnel, conventional or quiet, to be directly relatable to flight." Furthermore, there are still crucial unresolved issues in the understanding of hypersonic transition (e.g. roughness, nose radius, approach flow conditions, etc.) that hamper the progress needed for the development of hypersonic flight vehicles.

These facts clearly indicate the critical need of investigating high–speed boundary layer transition. The numerical simulation codes can be tested and validated by detailed comparison with laboratory experiments. Thereafter, they can be applied with confidence to predict the effects of various conditions on the transition processes and the resulting aerodynamic and aero–thermodynamic behavior. Thus, simulations can provide the crucial understanding and information necessary for design and safe operation of high–speed vehicles.

1.2 Related Previous Research on High–Speed Boundary Layer Transition

1.2.1 Theoretical Investigations

There is a large number of scientific publications available on transition research, with the majority of them focusing on low–speed transition. More recent investigations of transition, both high– and low–speed, were presented at the IUTAM Symposium on Laminar Turbulent Transition (Fasel & Saric, 1999; Govindarajan, 2004; Schlatter & Henningson, 2009). Some of the most important aspects of high–speed transition are discussed below.

Presently, the main body of knowledge on high–speed transition is still based on Linear Stability Theory (LST) by Mack (1969, 1975, 1984, 2000). According to the findings by Mack, the linear stability behavior of compressible (supersonic/hypersonic) boundary layers differs from the incompressible case in several significant aspects:

1. More than one instability mode exists for $M > 2.2$: the first mode and the second and higher (multiple) modes.
2. The first–mode disturbances are viscous (vortical) and are similar to the Tollmien-Schlichting (TS) modes of incompressible boundary layers. First-mode disturbances dominate (largest amplification rates) at low supersonic Mach numbers. However, in contrast to the incompressible case, the most amplified first-mode disturbances are three–dimensional (oblique) and not two–dimensional.
3. The second and higher modes are inviscid (acoustic) and dominate at Mach numbers higher than about 4, where the most unstable second–modes are always two–dimensional (in contrast to the first mode).
4. In addition to the inviscid (acoustic) higher modes, Mack identified additional viscous modes ("viscous multiple solutions) which, to date, have not been identified in experiments. However, they were also found in the Direct Numerical

Simulations of Eissler & Bestek (1996).

5. First–mode disturbances can be attenuated (as for the incompressible case in air) by wall cooling, wall suction, and favorable pressure gradients (Malik, 1989).

6. The second and higher inviscid modes can be stabilized by favorable pressure gradients, suction and porous coating; however, they are destabilized by wall cooling.

For a linear stability analysis, the effects of the growing boundary layer on the disturbance growth are typically neglected ("parallel theory"). However, nonparallel effects can be included by using the Parabolized Stability Equations (PSE) approach (Bertolotti, 1991; Bertolotti *et al.*, 1992; Chang & Malik, 1993; Pruett & Chang, 1993; Herbert, 1994). Depending on various parameters (Mach number, Reynolds number, frequency, etc.), nonparallel effects can significantly influence the disturbance growth rates. LST and linear PSE are only applicable for the first (linear) stage of the transition process where disturbance amplitudes are small and nonlinear interactions are negligible. Nonlinear PSE, on the other hand, is applicable to the nonlinear stages of transition (Bertolotti *et al.*, 1992; Herbert, 1994), although the computational effort increases tremendously when the development becomes strongly nonlinear as in the later stages of transition. Also, analogous to incompressible boundary layer transition, several attempts have been made to apply secondary instability theory to model the initial three–dimensional nonlinear development (see, for example, Masad & Nayfeh (1990); El-Hady (1991, 1992); Ng & Erlebacher (1992). However, whether or not any of these secondary instability mechanisms are relevant for supersonic transition is still an open question because it is very difficult to unequivocally identify them in experiments.

Theoretical work by Seddougui & Bassom (1997) who investigated the linear stability behavior of flow over cones following the triple–deck–formulation revealed the importance of the shock location relative to the cone radius. However, they only

considered viscous modes and conceded that inviscid instabilities might alter their findings. Seddougui & Bassom (1997) revealed that with increasing radius, i.e. moving in downstream direction, first–mode waves are more amplified than higher–mode waves – a phenomenon already observed by Stetson *et al.* (1983*a*) in their experiments. Additionally, Seddougui & Bassom (1997) stated that with the shock moving away from the cone surface, amplification rates generally drop and axisymmetric waves become more unstable than oblique waves.

Tumin (2007) investigated the three–dimensional spatially growing perturbations in a compressible boundary layer within the scope of the linearized Navier–Stokes equations. He solved the Cauchy problem under the assumption of a finite growth rate of the disturbances and demonstrated that the solution could be presented as an expansion into a biorthogonal eigenfunction system. This result can be applied to decompose flow fields obtained by numerical simulations when pressure, temperature, and all the velocity components, together with some of their derivatives, are available (Gaydos & Tumin, 2004). Using this technique, Tumin *et al.* (2007, 2010) compared the filtered amplitudes of the two discrete normal modes (the slow mode S and the fast mode F) and the fast acoustic spectrum with the solution of a linear receptivity problem obtained by direct numerical simulation. This example illustrates how the multimode decomposition technique may serve as a powerful tool for gaining insight into results obtained by numerical simulations.

1.2.2 Experimental Investigations

Conducting transition experiments in high–speed flows is extremely difficult and very expensive. Therefore, relatively few successful experimental efforts have been reported in the open literature. Most experiments have focused on the linear regime and the early stages of the transition process. Some examples are the experiments by Laufer & Vrebalovich (1960); Kendall (1975); Stetson *et al.* (1983*a*,*b*); Stetson (1988); Kosi-

nov *et al.* (1990); Stetson & Kimmel (1992*a*); Schneider *et al.* (1996); Horvath (2002); Schneider (2007), and Casper *et al.* (2009). An overview of the experimental efforts on conical geometries up to 2001 is given by Schneider (2001*b*). The experiments essentially verified some important parts of linear theory. However, quantitative differences often occur that may be explained by the fact that in the experiments the transition process was "natural," i.e., it was initiated by the environmental disturbances, and not by "controlled" disturbance input (analogous to a vibrating ribbon as in incompressible transition experiments). Also, quantitative differences between experimental measurements and LST may be caused by the nonparallel effects of the growing boundary layer being neglected in the linear stability analysis ("parallel theory").

All experimental efforts have suffered, more or less, from difficulties in controlling the disturbance environment such as sound radiated from turbulent boundary layers on the tunnel walls (Schneider, 2001*a*, 2008). Nevertheless, these "natural" transition experiments could identify first and second instability modes (Kendall, 1975; Stetson *et al.*, 1983*a*). However, for example for Mach 8, considerable discrepancies arose between planar boundary layers and boundary layers on axisymmetric cones when "blow down" facilities were used. For axisymmetric cones, high-frequency second modes were dominant, while for the planar boundary layer only low–frequency first-mode disturbances were observed (Stetson & Kimmel, 1992*b*). In contrast, in an experiment using a Ludwieg tube for a sharp–nosed cone at Mach 5, no dominant second-mode disturbances could be detected (Wendt, 1993).

With the more recent experiments for a flat plate and axisymmetric cones at Mach number 3.5 in the NASA-Langley "Quiet Tunnel," a number of discrepancies between LST and other experiments were resolved (Chen *et al.*, 1989; Cavalieri, 1995; Corke *et al.*, 2002). Indications of nonlinear developments in the transition process were observed by Stetson *et al.* (1983*a*) for a cone at Mach 8. Most of the experimental efforts suffered from the deficiency that no "controlled" disturbances could be

introduced to allow for detailed quantitative comparisons with linear theory and, in particular, to allow for systematic investigations of the nonlinear stages of transition. Because of the lack of experimental evidence concerning the process in the later stages of transition, it is still completely unclear which instability modes and which nonlinear mechanisms are responsible for the final breakdown to turbulence in high–speed boundary layers. However, the controlled experiments for a Mach 2 boundary layer by Kosinov *et al.* (1994), using a harmonic point source for the disturbance excitation, have indicated, that secondary instability mechanisms were present. In fact, Kosinov & Tumin (1996) speculated that it was a subharmonic resonance of "oblique" fundamental disturbances which was later confirmed by our simulations (Mayer & Fasel, 2008).

Laddon & Schneider (1998) analyzed the stability behavior of controlled disturbances (introduced via a glow discharge) in a flow over a circular cone at small angles of attack at $M = 4$. They measured a phase speed of 0.9 times the free–stream velocity and observed large rms–amplitude values in the outer part of the boundary layer - both indications that a second–mode instability is present. They speculated that although amplitude growth was significant, the disturbance amplitude of the glow discharge was too small in order to cause transition. Kimmel *et al.* (1999) investigated the three–dimensional boundary–layer flow over a cone with elliptical cross–section (ratio 2 : 1) at Mach 8. Their measurements revealed that inflection–point profiles are present close to the centerline where the boundary layer is also significantly thicker than away from the centerline. With the laminar state of the flow already very complex, they could only speculate that transition at the centerline is caused by the inflection point while close to the shoulder of the cone transition is induced by cross–flow instabilities. The instability of the inflectional boundary layer appeared to be stronger than the instability of the cross flow so that transition occurred first at the centerline and farther downstream at the shoulder of the cone. Continuing work of Poggie *et al.* (2000) revealed second–mode disturbance waves close to the centerline

of the elliptical cone. It remained unclear if cross–flow disturbances or first–mode waves are present at the shoulder of the cone. According to Poggie *et al.* (2000), an indication towards the presence of cross–flow instabilities is that the measured wave length was rather short and because the group velocity vector of leading–edge disturbances did not deviate more than 1 degree from the edge velocity vector, they hypothesized that oblique leading edge disturbances do not play an important role in the stability behavior at the shoulder of the cone. Although the amplitudes under investigation were too high for a receptivity study, Schmisseur *et al.* (2002) saw a response to thermal disturbances generated by a laser placed in the free stream close to the shoulder of his 4:1 elliptic cone at $M = 4$.

More recently, Maslov and coworkers (see Shiplyuk *et al.* (2003), Bountin *et al.* (2008)) reported "controlled" experiments for a sharp–nosed cone at $M = 5.95$ using a glow–discharge actuator to generate harmonic point source disturbances. They investigated several nonlinear interactions and identified a "classical" subharmonic resonance (with a two–dimensional second mode wave as the primary disturbance) as a possible breakdown mechanism, possibly involving a three–dimensional first mode as the subharmonic. However, in order to confirm this conjecture, a very high spatial and temporal resolution of the measurements would be required which, of course, is difficult experimentally. In fact, Shiplyuk *et al.* (2003) state in their paper, that "numerical calculations would be helpful to clarify the scenarios of nonlinear interactions that are identified in the present work."

In a panel discussion at the 45th AIAA science meeting in Reno (2007), researchers from industry, government labs, and academia, recognized that the current incomplete understanding of roughness–induced transition in supersonic and hypersonic boundary layer flows is a major bottleneck for the development of supersonic and hypersonic flight vehicles. In the past, numerous experimental investigations of different flow configurations have been performed to gain insight into the physical effects of roughness on the transition process. A detailed survey of these experimental studies

was recently compiled by Schneider (2007). The purpose of these studies is to establish a correlation between roughness parameters and transition onset. Reda (2002) or Berry & Horvarth (2007), for example, propose power–law relationships between the location of transition onset (e.g. Reynolds number based momentum thickness) and shape of the roughness (e.g. roughness height over momentum thickness). Most of these correlations are, however, only valid for a certain flow configuration and for roughness heights smaller than the boundary layer thickness.

1.2.3 Numerical Investigations

Due to the difficulties in experimental investigations of high–speed boundary layer transition and due to the limitations of linear stability theory, so–called Direct Numerical Simulations (DNS) represent a promising tool for high–speed transition research. In DNS, the complete Navier-Stokes equations are solved directly by proper numerical methods without making restrictive assumptions with regard to the base flow and the form and amplitude of the disturbance waves. Therefore, DNS is particularly well suited for investigations of the nonlinear development that is characteristic of the later stages of high–speed boundary–layer transition. Two fundamentally different models are used for DNS: the "temporal" and the "spatial" model. The so–called "temporal model" is based on the assumption that the base flow does not change in the downstream direction (thus excluding nonparallel effects). Also, assuming spatial (downstream) periodicity of the disturbances, the disturbance development (growth or decay) is then in the time-direction. The temporal model is analogous to the temporal approach in LST with the frequency being complex and the spatial wave number real. Due to the underlying assumptions, the temporal model can only provide qualitative results. On the other hand, since a relatively short integration domain can be used in the downstream direction (typically one or two wave lengths of the fundamental wave) temporal simulations are relatively inexpensive and can be

efficiently utilized for parameter studies.

In contrast, in the "spatial model" no assumptions are made with regard to the base flow (thus nonparallel effects are included). The disturbance development (growth or decay) is in the downstream direction as in physical laboratory or free–flight conditions. Thus, the spatial model allows realistic simulations of high–speed transition and direct comparison with wind–tunnel or free–flight experiments. However, simulations based on the spatial model are typically much more costly than for the temporal model because a much larger downstream integration domain is required (many wave lengths of the fundamental disturbance wave). This is particularly true for simulations of high–speed boundary layer transition, where the growth rates of the disturbance waves are often much smaller than for the incompressible case and where the growth rates of certain modes decrease with increasing Mach number. Moreover the transition zone length can be of the same order of magnitude as the length of the preceding laminar boundary layer. Thus, relatively large (in the downstream direction) integration domains are required to allow small disturbances to grow to the large amplitudes that characterize the nonlinear stages of the transition process and that finally lead to the breakdown to turbulence. As a consequence, spatial simulations of high–speed transition are computationally very challenging. Detailed discussions of the DNS methodology for investigations of boundary layer transition, in particular discussions of the temporal and spatial approach are given by Fasel & Konzelmann (1990), Kleiser & Zang (1991), and Reed (1993).

Probably the first transition simulation for supersonic boundary layers, although restricted to two–dimensional yet spatially evolving disturbances, was by Bayliss *et al.* (1985), who employed an approach analogous to that by Fasel (1976) for incompressible boundary layers. The first three–dimensional temporal DNS for flat–plate high–speed boundary–layer transition was performed by Erlebacher & Hussaini (1990). Here, only the linear and early nonlinear stages were explored. Other temporal simulations were performed by Normand & Lesieur (1992); Pruett & Zang (1992); Di-

navahi & Pruett (1993); Adams & Kleiser (1993). From such temporal simulations, Normand & Lesieur (1992) found that, for their case of a flat–plate boundary layer with $M = 5$, transition occurred via a subharmonic secondary instability for the second mode. This finding was consistent with results from simulations by Adams & Kleiser (1993); Pruett & Zang (1992); Dinavahi & Pruett (1993) for a boundary layer at Mach 4.5 on a hollow cylinder (the axisymmetric analog of a flat–plate boundary layer). However, the main weakness of these "temporal" simulations is the fact that they do not take the boundary–layer growth into account. In fact, experiments by Stetson & Kimmel (1993) and PSE calculations by Chang *et al.* (1991) indicate that subharmonic resonance may not be the preferred route to transition in realistic, growing boundary layers (which include nonparallel effects).

Realistic simulations of transition scenarios including the effects of the growing boundary layer require the use of the spatial simulation model. The first three–dimensional spatial simulations of transition in supersonic boundary layers were reported by Thumm (1991) for a Mach number of 1.6. In fact, from these and follow–up simulations (Fasel *et al.*, 1993), it was discovered that a new "Oblique Breakdown" mechanism produces much larger growth rates than either subharmonic or fundamental resonance and requires much lower disturbance amplitudes. Therefore, we believe that the "Oblique Breakdown" is a likely candidate for a viable path to transition for supersonic boundary layers. Using PSE calculations, Chang & Malik (1993) confirmed the validity of this oblique breakdown for a flat–plate boundary layer at $M = 1.6$. Recently the highly resolved DNS of Mayer *et al.* (2008, 2009*b*) finally demonstrated that oblique breakdown can indeed lead to a fully turbulent boundary layer for a flat plate at Mach 3. Based on our DNS code (see Fasel *et al.* (1993)), Bestek & Eissler (1996) performed simulations for Mach 4.8 and investigated various nonlinear mechanisms including the "oblique breakdown" mechanism. Bestek & Eissler (1996) also confirmed, for the first time, the existence of an additional "higher viscous" mode, which Mack (1969) had predicted using LST analysis. Pruett & Chang (1993)

carried out spatial DNS for a flat–plate boundary layer at Mach 4.5 and provided a detailed comparison with PSE results. Later, an improved version of the code (Pruett *et al.*, 1995) was applied to a simulation of transition on axisymmetric sharp cones at Mach 8 (Mach 6.8 after the shock, see Pruett & Chang (1995)). This simulation was combined with PSE calculations such that the linear and moderately nonlinear stages were computed by PSE while the strongly nonlinear and breakdown stages of transition were computed by spatial DNS. This approach was motivated by the experience that linear and moderately nonlinear wave propagations can be computed more efficiently with PSE while the strongly nonlinear and breakdown stages (requiring many spanwise Fourier modes) are computed more efficiently and more accurately with DNS. In this simulation, a second–mode–breakdown resonance was also investigated. The so–called rope–like structures obtained from numerical flow visualizations of the simulation data for this breakdown process are similar to those observed in high–speed transitional boundary layers on cones (see Pruett & Chang (1995). More recently, Zhong and coworkers (see Zhong (2001)) investigated the leading edge receptivity of high–speed boundary layers using DNS. They also explored the effects of the magnetic fields on the second–mode instabilities for a weakly ionized boundary layer at $M = 4.5$ (Cheng *et al.*, 2003).

Fezer & Kloker (2004) also investigated the same cone geometry used in the experiments by Stetson *et al.* (1983*a*) but with atmospheric conditions (hot approach flow) and a radiation–cooled wall. They claimed that a fundamental resonance (K–type) with accompanying hot streaks along the wall initiated transition in their case. The high temperature streaks along the wall resulted from streamwise vortex structures which developed during this breakdown.

The physical mechanisms responsible for roughness–induced transition are still not well understood. Reshotko & Tumin (2004) investigated the role of transient growth in roughness–induced transition, where the non–modal growth of steady longitudinal structures initiates an early breakdown to turbulence, and confirmed the correlation

by Reda (2002). Reshotko and Tumins model, however, is based on the linearized Navier-Stokes equations and cannot explain the nonlinear effects introduced by large roughness heights. The latter case can more easily be investigated using DNS. Preliminary DNS of the linear regime of roughness–induced transition were conducted by Balakumar (2003), and Zhong (2007).

Discrete roughness elements can be simulated in numerical simulations using either body–fitted grids or Immersed Boundary Techniques (IBT). Complex body–fitted grids require a generalized coordinate transformation which is CPU time intensive. For a limited number of discrete roughness elements IBT promises to be more computationally efficient. One differentiates between methods that preserve the order of accuracy of the underlying discretization by allowing for jump conditions in the solution (e.g. Linnick & Fasel (2005)) and methods that do not alter the discretization near the surface. The latter approach is less complicated and allows for an easier implementation into existing codes. Examples are Peskin & McQueen (1989); Goldstein *et al.* (1993); Fadlun *et al.* (2000); von Terzi *et al.* (2001).

Zhong (2005) and Husmeier & Fasel (2007) analyzed three different nose radii under Stetson's experimental conditions (c.f. Stetson *et al.* (1983*b*)). They observed a shift to lower dominant frequencies with increasing bluntness due to a thickening of the boundary layer. However, Zhong (2005) and Husmeier (2008) were unable to find conclusive evidence for the transition reversal as reported by Stetson & Kimmel (1992*b*). In Zhongs simulations the critical Reynolds number increased monotonically with increasing nose radius, whereas in the experiments of Stetson & Kimmel (1992*b*) the initial increase in critical Reynolds number was followed by a decrease. As a result, there was an optimal nose radius regarding the transition delay in these experiments. More recently, Lei & Zhong (2009, 2010) performed stability investigations of the Mach 5.5 blunt cone experiments of Stetson & Rushton (1967), however, they also did not observe transition reversal in their simulations.

Relatively few attempts have been made to employ Large–Eddy Simulation (LES)

for transitional supersonic boundary layers (see, for example, Normand & Lesieur (1992); Zang *et al.* (1992). The few simulations reported in the literature have to be viewed as being of an exploratory nature with regard to the applicability of LES for boundary layer transition. Nevertheless, these attempts demonstrated that LES could be employed advantageously for supersonic transition simulations. The main issues in applying LES for high-speed transition are the use of proper subgrid-scale (sgs) models that are physically consistent throughout the entire transition process. Of course, LES would be a highly valuable tool for investigating the late stages of transition. As mentioned previously, spatial DNS for supersonic boundary layer transition is very expensive due to the large computational domains that are required in the downstream direction. In addition, for DNS that include the final stages of transition (the actual breakdown to turbulence), an extremely fine grid is required which, as a consequence, places high demands with regard to computer memory and computation times. LES on the other hand requires considerably less resolution and, as a consequence, the amount of computer memory and computation times is reduced accordingly.

2. Governing Equations

The flow considered here is governed by the unsteady, three-dimensional, compressible Navier–Stokes equations, consisting of the equations for the conservation of mass, momentum and energy. Using conservative variables and conical coordinates these equations can be written as follows

$$\frac{\partial \boldsymbol{U}}{\partial t} + \frac{1}{r}\frac{\partial \left(r\left(\boldsymbol{E_c}+\boldsymbol{E_d}\right)\right)}{\partial x} + \frac{1}{r}\frac{\partial \left(r\left(\boldsymbol{F_c}+\boldsymbol{F_d}\right)\right)}{\partial y} + \frac{1}{r}\frac{\partial \left(\boldsymbol{G_c}+\boldsymbol{G_d}\right)}{\partial \varphi} + \boldsymbol{H} = 0\,. \qquad (2.1)$$

Here, $\boldsymbol{U}$ represents the vector of the conservative variables and is given as $\boldsymbol{U} = \left[\ \rho, \rho u, \rho v, \rho w, E_t\ \right]$, where the symbols ρ, u, v, w and E_t denote the fluid density, streamwise velocity, wall-normal velocity, azimuthal/spanwise velocity and total energy, respectively. The convective flux vectors ($\boldsymbol{E_c}$, $\boldsymbol{F_c}$, $\boldsymbol{G_c}$), the viscous and heat conduction terms ($\boldsymbol{E_d}$, $\boldsymbol{F_d}$, $\boldsymbol{G_d}$) and the source term ($\boldsymbol{H}$) can be calculated from the previously introduced flow quantities and pressure p using the following equations

$$\boldsymbol{E_c} = \begin{bmatrix} \rho u \\ \rho u^2 + p \\ \rho uv \\ \rho uw \\ \left(E_t + p\right) u \end{bmatrix}, \boldsymbol{F_c} = \begin{bmatrix} \rho v \\ \rho uv \\ \rho v^2 + p \\ \rho vw \\ \left(E_t + p\right) v \end{bmatrix}, \boldsymbol{G_c} = \begin{bmatrix} \rho w \\ \rho uw \\ \rho vw \\ \rho w^2 + p \\ \left(E_t + p\right) w \end{bmatrix},$$

$$\boldsymbol{E_d} = \begin{bmatrix} 0 \\ -\tau_{xx} \\ -\tau_{xy} \\ -\tau_{x\varphi} \\ -u\tau_{xx} - v\tau_{xy} - w\tau_{x\varphi} + q_x \end{bmatrix}, \boldsymbol{F_d} = \begin{bmatrix} 0 \\ -\tau_{xy} \\ -\tau_{yy} \\ -\tau_{y\varphi} \\ -u\tau_{xy} - v\tau_{yy} - w\tau_{y\varphi} + q_y \end{bmatrix},$$

$$\boldsymbol{G_d} = \begin{bmatrix} 0 \\ -\tau_{x\varphi} \\ -\tau_{y\varphi} \\ -\tau_{\varphi\varphi} \\ -u\tau_{x\varphi} - v\tau_{y\varphi} - w\tau_{\varphi\varphi} + q_\varphi \end{bmatrix},$$

$$\boldsymbol{H} = \begin{bmatrix} 0 \\ -\frac{1}{r}\sin\theta_c\left(\rho w^2 - \tau_{\varphi\varphi} + p\right) \\ -\frac{1}{r}\cos\theta_c\left(\rho w^2 - \tau_{\varphi\varphi} + p\right) \\ \frac{1}{r}\sin\theta_c\left(\rho uw - \tau_{x\varphi}\right) + \frac{1}{r}\cos\theta_c\left(\rho vw - \tau_{y\varphi}\right) \\ 0 \end{bmatrix}.$$

The total energy is computed from the internal energy i_e and the velocities as

$$E_t = \rho \left(i_e + \frac{1}{2}(u^2 + v^2 + w^2) \right) . \tag{2.2}$$

The stresses in the conical coordinate system are determined by

$$\tau_{xx} = \frac{\mu}{Re} \left(\frac{4}{3}\frac{\partial u}{\partial x} - \frac{2}{3}\frac{\partial v}{\partial y} - \frac{2}{3}\frac{1}{r}\frac{\partial w}{\partial \varphi} - \frac{2}{3}\frac{1}{r}\left(u \sin\theta_c + v\cos\theta_c\right) \right), \tag{2.3a}$$

$$\tau_{yy} = \frac{\mu}{Re} \left(\frac{4}{3}\frac{\partial v}{\partial y} - \frac{2}{3}\frac{\partial u}{\partial x} - \frac{2}{3}\frac{1}{r}\frac{\partial w}{\partial \varphi} - \frac{2}{3}\frac{1}{r}\left(u \sin\theta_c + v\cos\theta_c\right) \right), \tag{2.3b}$$

$$\tau_{\varphi\varphi} = \frac{\mu}{Re} \left(\frac{4}{3}\frac{1}{r}\frac{\partial w}{\partial \varphi} - \frac{2}{3}\frac{\partial u}{\partial x} - \frac{2}{3}\frac{\partial v}{\partial y} + \frac{4}{3}\frac{1}{r}\left(u \sin\theta_c + v\cos\theta_c\right) \right), \tag{2.3c}$$

$$\tau_{xy} = \frac{\mu}{Re} \left(\frac{\partial v}{\partial x} + \frac{\partial u}{\partial y} \right), \tag{2.3d}$$

$$\tau_{x\varphi} = \frac{\mu}{Re} \left(\frac{1}{r}\frac{\partial u}{\partial \varphi} + \frac{\partial w}{\partial x} - \frac{1}{r} w \sin\theta_c \right), \tag{2.3e}$$

$$\tau_{y\varphi} = \frac{\mu}{Re} \left(\frac{1}{r}\frac{\partial v}{\partial \varphi} + \frac{\partial w}{\partial y} - \frac{1}{r} w \cos\theta_c \right), \tag{2.3f}$$

and the heat-flux vector is given as

$$\boldsymbol{q} = -\frac{\mu}{(\gamma - 1) Re Pr M^2} \left(\frac{\partial T}{\partial x}, \frac{\partial T}{\partial y}, \frac{1}{r}\frac{\partial T}{\partial \varphi} \right) , \tag{2.4}$$

with μ as dynamic viscosity.

The conical coordinate system used for the equations above is illustrated in figure 2.1. The streamwise direction, parallel to the cone surface, is denoted by x. The wall-normal direction, orthogonal to the cone surface, is specified by y and φ represents the azimuthal direction. The local radius r can be calculated from the streamwise and wall-normal direction according to $r = x sin\theta_c + y\cos\theta_c$, with θ_c as cone half angle. The governing equations in a rectangular coordinate system, which are applied for flat-plate simulations, can be obtained from the equations in the conical coordinate system for $\theta_c = 0$ and $r \to \infty$. The equations in rectangular coordinates are, for example, discussed in Harris (1997).

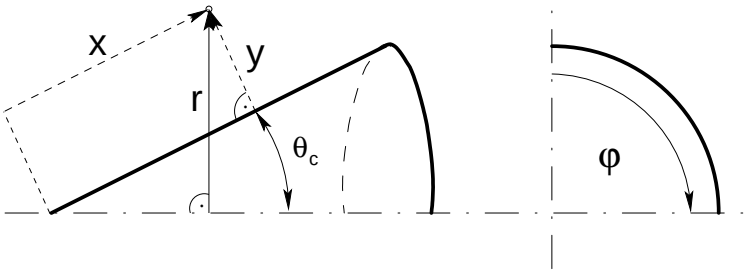

Figure 2.1: Illustration of a conical coordinate system.

The set of equations is closed with the equation of state for an ideal gas in dimensionless form,

$$p = \frac{\rho T}{\kappa M^2}, \tag{2.5}$$

and Sutherland's law is used to calculate the viscosity as a function of temperature. It has the following nondimensional form

$$\mu = T^{\frac{3}{2}} \frac{1 + \frac{C}{T^*_\infty}}{T + \frac{C}{T^*_\infty}}\,. \tag{2.6}$$

Here, $C = 110.4K$ and T^*_∞ represents the dimensional temperature of the approach flow. The viscosity is nondimensionalized by its approach-flow value. For the Mach 8 cone simulations, the viscosity is calculated using Sutherland's law with low temperature correction as follows.

$$\mu = \begin{cases} \frac{C_1}{\mu^*_\infty} \cdot T^*_1 & \text{, if } T^* < T^*_1 \\ \frac{C_1}{\mu^*_\infty} \cdot (TT^*_\infty) & \text{, if } T^* \in [T^*_1; T^*_2] \\ \frac{C_2}{\mu^*_\infty} \cdot (TT^*_\infty)^{\frac{3}{2}} \,/\, ((TT^*_\infty) + T^*_2) & \text{, if } T^* > T^*_2 \end{cases} \tag{2.7}$$

where

$$\begin{array}{ll} T^*_1 = 40.0K, & C_1 = 6.93873 \cdot 10^{-7} Ns/m^2K, \\ T^*_2 = 110.4K, & C_2 = 1.4580 \cdot 10^{-5} Ns/m^2K^{1/2}. \end{array}$$

The flow quantities are nondimensionalized with their approach-flow values, indicated by the subscript ∞, except for the pressure and the total energy, which are

scaled by the dynamic pressure $\rho_\infty^* {U_\infty^*}^2$. Furthermore, the independent variables x, y and t are nondimensionalized using a reference length scale L^* (and the approach streamwise velocity U_∞^* for t). In both Navier–Stokes codes used for the present work, this reference length scale is an arbitrary, constant value and will always be denoted by L^* throughout this report whereas all linear stability solvers applied to the different problems in this report are based on a so-called viscous length scale L_e^*, which represents an estimate for the local boundary-layer thickness

$$L_e^* = \sqrt{\frac{\nu_e^* x^*}{U_e^*}}\,. \tag{2.8}$$

Here, ν_e^* is the dimensional kinematic viscosity at the boundary layer edge (subscript e).

The nondimensionalization of the governing equations introduces the Reynolds number Re, Mach number M, Prandtl number Pr and the ratio of specific heats γ as nondimensional parameters

$$\begin{aligned} Re = \frac{\rho_\infty^* U_\infty^* L^*}{\mu_\infty^*}\,, \quad Pr = \frac{\mu^* c_{p\infty}^*}{k^*}\,, \\ M = \frac{U_\infty^*}{a_\infty^*} = \frac{U_\infty^*}{\sqrt{(\gamma-1)\, c_{p\infty}^* T_\infty^*}}, \quad \text{and} \quad \gamma = \frac{c_{p\infty}^*}{c_{p\infty}^* - R}\,, \end{aligned} \tag{2.9}$$

with $c_{p\infty}^*$, k^*, a_∞^* and R being the specific heat at constant pressure, the thermal conductivity, the speed of sound and the specific gas constant for air of the approach flow, respectively. For all simulations, the Prandtl number is assumed to be constant and has a value of 0.71. Hence, the Prandtl number relates the thermal conductivity k directly to the viscosity μ.

The Reynolds number based on the viscous length scale L_e^* is usually called local Reynolds number since it is only valid for one particular streamwise position. This Reynolds number is denoted by

$$R_x = \frac{U_e^* L_e^*}{\nu_e^*} = \sqrt{\frac{U_e^* x^*}{\nu_e^*}} \tag{2.10}$$

throughout this report.

3. Numerical Method

In this chapter, the computational methods used for all direct numerical simulations (DNS) discussed in this report are presented. The results for a flat plate (Chapter 5) have been obtained by employing the Navier–Stokes code NSCC (Navier–Stokes Compressible in C) while the cone results were computed with a new higher order code. Both codes were developed in our CFD laboratory (Harris, 1997; Laible *et al.*, 2008, 2009). Section 3.1 explains the numerical method and boundary conditions implemented in NSCC. Additional information regarding this code can also be found in von Terzi (2004) and Husmeier (2008). Note, however, that with the actual version of NSCC used in this report cone geometries cannot be calculated as in Husmeier (2008). Instead other features have been implemented, as for example full Fourier transformations in spanwise direction. The new higher order Navier–Stokes code is discussed in section 3.2.

3.1 NSCC Code

The governing equations from chapter 2 are solved on a rectangular coordinate system. An explicit fourth-order Runge–Kutta method (Ferziger, 1998) is used for time integration. Harris (1997) optimized the time integration in NSCC in order to reduce storage requirements. Applied to the following model ordinary differential equation

$$\frac{d\phi}{dt} = f\left(t, \phi\right) \ , \tag{3.1}$$

the explicit fourth-order Runge–Kutta method can be written as

$$
\begin{aligned}
&\textbf{1st substep:} \\
&\qquad \phi_1 \;&:=&\;\; \phi_n + \frac{\Delta t}{2} f\left(t, \phi_n\right) , \\
&\textbf{2nd substep:} \\
&\qquad \phi_2 \;&:=&\;\; \phi_n + \frac{\Delta t}{2} f\left(t + \frac{\Delta t}{2}, \phi_1\right) , \\
&\qquad \phi_1 \;&:=&\;\; \phi_1 + 2\phi_2 \, , \\
&\textbf{3rd substep:} \\
&\qquad \phi_2 \;&:=&\;\; \phi_n + \Delta t f\left(t + \frac{\Delta t}{2}, \phi_2\right) , \\
&\qquad \phi_1 \;&:=&\;\; \frac{1}{3}\left(-\phi_n + \phi_1 + \phi_2\right) , \\
&\textbf{4th substep:} \\
&\qquad \phi_{n+1} \;&:=&\;\; \phi_1 + \frac{\Delta t}{6} f\left(t + \Delta t, \phi_2\right) .
\end{aligned}
\tag{3.2}
$$

The symbol ":=" in equations (3.2) indicates that these equations are assignments and thus are only valid in the context of a programming language. Variables with the subscript n are from the old timestep n while variables with subscript $n+1$ are the result of the time integration (new timestep). Δt is the stepsize in time.

The spatial derivatives in streamwise and wall-normal direction (x and y) of equations (2.1), (2.3), and (2.4) are discretized using second-order one-sided finite differences inside the integration domain. These finite differences have the following form for grid point i and timestep n

$$\left(\frac{\partial \phi}{\partial x}\right)_n^{i+} \simeq \frac{-\phi_n^{i+2} + 8\phi_n^{i+1} - 7\phi_n^i}{6\Delta x} , \tag{3.3a}$$

$$\left(\frac{\partial \phi}{\partial x}\right)_n^{i-} \simeq \frac{\phi_n^{i-2} - 8\phi_n^{i-1} + 7\phi_n^i}{6\Delta x} , \tag{3.3b}$$

where $(+)$ denotes forward differencing and $(-)$ indicates backward differencing. In the literature, these stencils are usually referred to as "4th-order split" finite differences since averaging equations (3.3) leads to a standard 4th-order central difference

stencil. For every Runge–Kutta substep in equations 3.2, the integration direction (forward/backward differencing) of these one-sided stencils is altered. Altering the integration direction increases the overall accuracy of the numerical scheme. Originally, the idea of using low-order one-sided finite differences and altering the integration direction for different substeps of the time integration scheme was introduced by MacCormack (Tannehill *et al.*, 1997). He used first-order one-sided differences for the spatial derivatives and a second-order Runge–Kutta method (Heun's method) for the time integration. Although first-order one-sided differences are applied in MacCormack's method, the overall accuracy in time and space is second order. A similar behavior can also be observed in the present case. Harris (1997) showed that by applying his numerical scheme to different model equations (wave equation and diffusion equation) a third-order method can be recovered.

Equations (3.3) are only valid for first derivatives. However, in equation (2.1), also second derivatives with respect to all spatial directions and cross derivatives, second derivatives with respect to two spatial directions, are present (in the stress and heat-flux terms). In NSCC, these derivatives are computed by employing twice the finite differences for a first derivative (equations 3.3) with opposite integration direction instead of using a finite difference stencil for a second derivative directly. Harris (1997) denotes the derivatives in equation (2.1) as "outer" derivatives and the derivatives in equations (2.3) and (2.4) as "inner" derivatives.

3.1.1 Domain Boundaries

The finite difference stencils used inside the integration domain cannot be applied at the domain boundaries and at the first grid points adjacent to the boundary points since the values of all flow variables beyond the boundaries are not known. Hence, at these grid points new finite difference stencils have to be employed, which are generally referred to as "boundary closure" in the literature. For the method developed

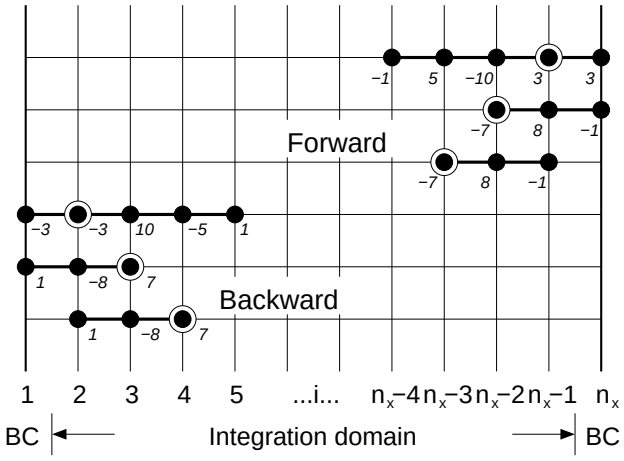

Figure 3.1: Illustration of the computational grid and the stencils implemented in NSCC for the streamwise direction x at one timestep n. (∘) denotes grid point where the spatial derivative is computed. (•) represents grid points that are used for the calculation of the spatial derivative at grid point (∘). Note that this notation follows Kloker (1993).

by Harris (1997), only the grid points adjacent to the boundary points need to be calculated by a different stencil while the boundary points are set by the boundary conditions (section 3.1.3) except for the free-stream boundary, where the boundary condition is applied to both grid points. Harris (1997) chose the following finite difference stencils for the calculation of grid points adjacent to the boundary points

$$\left(\frac{\partial\phi}{\partial x}\right)_n^2 \simeq \frac{\phi_n^5 - 5\phi_n^4 + 10\phi_n^3 - 3\phi_n^2 - 3\phi_n^1}{6\Delta x}\,, \tag{3.4a}$$

$$\left(\frac{\partial\phi}{\partial x}\right)_n^{n_x-1} \simeq \frac{-\phi_n^{n_x-4} + 5\phi_n^{n_x-3} - 10\phi_n^{n_x-2} + 3\phi_n^{n_x-1} + 3\phi_n^{n_x}}{6\Delta x}\,. \tag{3.4b}$$

Note that for these stencils, averaging with the corresponding stencil from equations (3.3) results again in a fourth-order finite difference stencil. An illustration of the computational grid and the stencils implemented in NSCC for the streamwise direction x is given in figure 3.1. In this figure, (∘) denotes the grid point where the spatial derivative is computed while (•) indicates all grid points that are used for the calculation of the spatial derivative at grid point (∘). Figure 3.1 also shows the coefficients used for the calculation of a particular finite difference stencil.

3.1.2 Spanwise Discretization

The spanwise domain is assumed to be periodic and therefore, transformed into spectral space using Fast Fourier transforms. This has an implication on the calculation of any spanwise derivative since in spectral space, a derivative with respect to z for Fourier mode k at timestep n is defined as

$$\left(\widetilde{\frac{\partial\phi}{\partial z}}\right)_n^k \simeq \beta_k \widetilde{\phi}_n^k \quad \text{and} \quad \left(\widetilde{\frac{\partial\phi}{\partial z}}\right)_n^k \simeq -\beta_k \widetilde{\phi}_n^k \tag{3.5}$$

for cosine and sine modes, respectively. Here, the spanwise wavenumber β_k is obtained from

$$\beta_k = \frac{2\pi k}{\lambda_z}\,. \tag{3.6}$$

The spanwise wave length λ_z determines the spanwise domain extent of the DNS.

NSCC has two options for the Fourier transformations: (i) All flow variables (i.e. u-velocity, v-velocity, etc.) are assumed to be symmetric to the centerline, except for the spanwise velocity w, which is antisymmetric. Symmetric quantities are then transformed into Fourier space using a Fourier cosine transformation and antisymmetric variables (w) are transformed by a Fourier sine transformation. Thus, only one-half spanwise wave length λ_z has to be computed for this configuration. (ii) No symmetry is assumed and therefore, all variables are transformed using a full Fourier transformation. This option requires the computation of the entire wave length λ_z in spanwise direction.

The Fourier transformations in NSCC are based on the VFFTPK library, which can be downloaded from netlib (http://www.netlib.org/vfftpack/). According to this library and its implementation in NSCC, a Fourier cosine transformation into spectral

space and its back transformation into physical space are given by

physical→spectral:

$$\widetilde{\phi}_k^c = \mathcal{F}(\phi)_k^c \quad \sim \quad \frac{1}{2(n_z-1)}\left[\phi_0^c + 2\sum_{l=1}^{n_z-1}\phi_l^c \cos\left(\frac{\pi k l}{n_z-1}\right)\right] \tag{3.7a}$$

spectral→physical:

$$\phi_l^c = \mathcal{F}^{-1}\left(\widetilde{\phi}\right)_l^c \quad \sim \quad \widetilde{\phi}_0^c + 2\sum_{k=1}^{K-1}\widetilde{\phi}_k^c \cos\left(\frac{\pi k l}{n_z-1}\right) \tag{3.7b}$$

for $k = 0, ..., K-1$ and $l = 0, ..., n_z - 1$, respectively. $\widetilde{\phi}_k^c$ represent the Fourier amplitudes for mode k. Moreover, n_z indicates the number of grid points used for resolving the spanwise direction in physical space over the interval $[0, (n_z-1)\Delta z]$ with

$$\Delta z = \frac{\lambda_z}{2(n_z-1)} \tag{3.8}$$

and K represents the number of modes in Fourier space (for the simulations $n_z = 2K-1$).

The Fourier sine transformation to spectral space and its back transformation into physical space are as follows

physical→spectral:

$$\widetilde{\phi}_k^s = \mathcal{F}(\phi)_k^s \quad \sim \quad -\frac{1}{(n_z-1)}\sum_{l=1}^{n_z-1}\phi_l^s \sin\left(\frac{\pi k l}{n_z-1}\right) \tag{3.9a}$$

spectral→physical:

$$\phi_l^s = \mathcal{F}^{-1}\left(\widetilde{\phi}\right)_l^s \quad \sim \quad -2\sum_{k=1}^{K-1}\widetilde{\phi}_k^s \sin\left(\frac{\pi k l}{n_z-1}\right) \tag{3.9b}$$

for $k = 0, ..., K-1$ and $l = 0, ..., n_z - 1$, respectively.

In contrast to a symmetric simulation where only one-half of the spanwise wave length has to be calculated, an asymmetric simulation requires the entire spanwise wave length as computational domain. Hence, for symmetric simulations n_z represents the number of grid points in one-half wave length, whereas for asymmetric simulations,

this number depicts the grid points in one full spanwise wave length. In this case, the grid spacing in spanwise direction is therefore obtained from

$$\Delta z = \frac{\lambda_z}{(n_z - 1)}. \tag{3.10}$$

The full Fourier transformation for an asymmetric simulation are implemented in NSCC according to

physical→spectral:

$$\widetilde{\phi}_0 \sim \frac{1}{2n_z} \sum_{l=0}^{n_z-1} \phi_l \tag{3.11a}$$

$$\widetilde{\phi}_k^c \sim \frac{1}{n_z} \sum_{l=0}^{n_z-1} \phi_l \cos\left(\frac{2\pi kl}{n_z}\right) \tag{3.11b}$$

$$\widetilde{\phi}_k^s \sim \frac{1}{n_z} \sum_{l=0}^{n_z-1} \phi_l \sin\left(\frac{2\pi kl}{n_z}\right) \tag{3.11c}$$

spectral→physical:

$$\phi_l \sim \widetilde{\phi}_0 + \sum_{k=1}^{K-1} \left[\widetilde{\phi}_k^c \cos\left(\frac{2\pi kl}{n_z}\right) + \widetilde{\phi}_k^s \sin\left(\frac{2\pi kl}{n_z}\right)\right] \tag{3.11d}$$

with $k = 0, ..., K-1$ and $l = 0, ..., n_z - 1$. As for the symmetric case, K denotes the number of Fourier modes. The entire storage space in NSCC for the Fourier modes is however $2K-1$ since the cosine modes and the sine modes have to be stored separately.

The representation of the spanwise direction in Fourier space has one disadvantage: Nonlinear terms in the governing equations (chapter 2) cannot be easily calculated in Fourier space. Thus, for the computation of these terms, the governing equations are transformed into physical space and thereafter, transformed back into spectral space. This approach is commonly referred to as "pseudo-spectral" (Canuto *et al.*, 1988).

3.1.3 Boundary Conditions

At the inflow, the conservative quantities ρ, ρu_i and E_t, obtained from the similarity solution of a compressible flat-plate boundary layer, are specified. The no-slip and

no-penetration conditions are used at the wall except for the disturbance hole/slot. In addition, the wall is assumed to be adiabatic for the base flow, whereas temperature fluctuations at the wall are assumed to vanish. At the outflow, a buffer domain technique (Meitz & Fasel, 2000) is implemented to avoid reflections of disturbance waves from the outflow boundary. At the free-stream boundary, all total flow quantities are separated into the mean and disturbance quantities. For the mean flow quantities, a von Neumann condition is applied, whereas for the disturbance quantities, an exponential decay condition is employed, which was derived for compressible flow using linear stability considerations (Thumm, 1991). Harris (1997) provides details on the implementation of these boundary conditions in NSCC.

3.2 New Higher Order Code

In the new higher order code (Laible *et al.*, 2008, 2009), the Navier–Stokes equations are integrated in time using the explicit fourth-order Runge–Kutta method. The implementation of this method in the code follows exactly from Harris (1997) as explained in the previous section (equation 3.2).

For the spatial differentiation inside the computational domain, several different options are available. In this section, only the options that were used for the simulations presented in chapter 6 and 7 are discussed (for more detail, see Laible *et al.*, 2008, 2009). The interior spatial discretization is mainly based on high-order accurate finite differences. In particular, the inviscid fluxes (convective terms $\boldsymbol{E_c}$ and $\boldsymbol{F_c}$ in equation 2.1) are divided in an upwind flux and a downwind flux using van Leer's splitting (van Leer, 1982). Then 9^{th}-order grid centered upwind differences (Zhong, 1998) are applied to evaluate the derivatives for these fluxes in x and y-direction. These grid centered upwind differences are derived using a factor σ, which prescribes

the degree of upwinding,

$$\left(\frac{\partial \phi}{\partial x}\right)_n^i = \sum_{k=i-N}^{i+N} c_k\left(\sigma\right)\phi_n^k - \sigma\overline{\Delta x}\left(\frac{\partial^{(2N)}\phi}{\partial x^{(2N)}}\right)_n^i + \ldots . \tag{3.12}$$

For $\sigma = 0$, the upwind scheme reduces to a standard central difference scheme. The c_k's in equation (3.12) are the stencil coefficients, which are dependent on the factor σ. σ is obtained from an eigenvalue analysis of the discretized (in space) linear wave equation (Zhong, 1998). For the 9^{th}-order upwind scheme ($N = 5$), Laible *et al.* (2008) obtained a value of $\sigma = -1500$ in order to stabilize the numerical scheme. $\overline{\Delta x}$ is the averaged grid spacing over the stencil interval and has the order of $2N - 1$. The parameter N determines the number of grid points used for the stencil. Moreover, equation (3.12) clearly shows that for $\sigma \neq 0$ an additional error term is introduced, which reduces the order of the centered upwind difference scheme by one when compared to the central difference scheme with the same number of grid points.

The derivatives of the viscous terms ($\boldsymbol{E_d}$ and $\boldsymbol{F_d}$ in equation 2.1) and the source term ($\boldsymbol{H}$) are calculated using 8^{th}-order central differences in streamwise direction and wall-normal direction. It is important to note that the second derivatives in the viscous terms are calculated directly instead of applying twice a first derivative stencil. This is in contrast to the method by Harris introduced in section 3.1 and improves the stability of the numerical scheme (Zhong, 1998).

All finite difference stencils are derived on a non-uniform grid. The coefficients (c_k's in equation 3.12) are obtained from a Lagrange polynomial interpolation (Zhong & Tatineni, 2003). For a stencil based on N grid points with coordinates x_i and node values ϕ_i, the $N - 1$ degree polynomial is given by

$$P_N(x) = \sum_{i=1}^{N} l_i(x)\phi_i, \quad \text{with} \quad l_i(x) = \frac{\prod_{l=1,l\neq i}^{N}(x - x_l)}{\prod_{l=1,l\neq i}^{N}(x_i - x_l)}\,. \tag{3.13}$$

For example, a second derivative at grid point x_i can be calculated by differentiating

the polynomial $P_N(x)$ twice according to

$$\left(\frac{d^2\phi(x)}{dx^2}\right)_{x=x_i} = \left(\frac{d^2P_N(x)}{dx^2}\right)_{x=x_i} = \sum_{j=1}^{N} b_{i,j}\phi_j \,, \tag{3.14}$$

where the coefficients $b_{i,j}$ have different values for different grid points with index i (non-uniform grid), and are given by

$$b_{i,j} = \frac{d^2}{dx^2}\left(l_j(x)\right)_{x=x_i} \,. \tag{3.15}$$

3.2.1 Domain Boundaries

Since boundary closures based on high-order finite difference schemes may develop oscillations and hence, are usually unstable, Laible used different methods in order to stabilize the numerical scheme at the boundaries. Figures 3.2 and 3.3 summarize Laible's approach for the grid centered upwind difference stencils used for the discretization of the convective terms. In streamwise direction the numerical scheme is mainly stabilized by employing standard central difference stencils with reduced order up to the last three points where the discretization is switched to one-sided 5^{th}-order finite differences. Although the order is reduced from 9^{th}-order upwind finite differences to one-sided 5^{th}-order finite differences near the outflow, only a limited upstream effect of the lower-order numerical scheme is expected since this numerical scheme is utilized for supersonic and hypersonic transition simulations. Near the inflow such boundary treatment is not required since the initial condition is known upstream of the inflow boundary of the high-order DNS (more details can be found in section 3.2.3). Therefore, grid centered upwind finite differences can be applied up to the first grid point of the computational domain.

For the discretization of the viscous terms (second derivatives) near the inflow, the same approach as for the convective terms was chosen. The flow field is known upstream of the inflow and hence, high-order central difference stencils can be used up to the inflow. Near the outflow however, one-sided difference stencils based on the

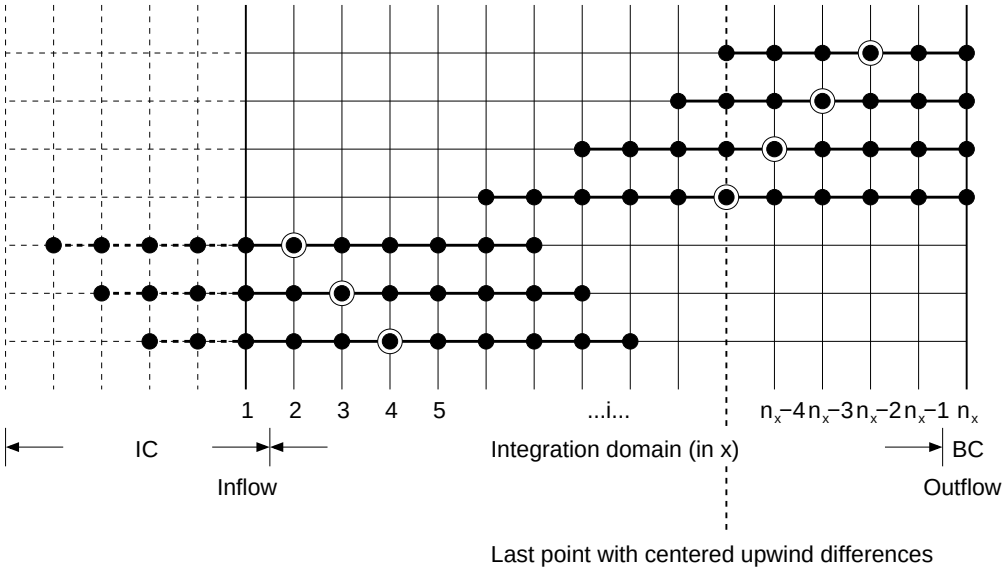

Figure 3.2: Illustration of the computational grid and the stencils implemented in the new high-order code by Laible (Laible *et al.*, 2008, 2009) for the inviscid terms ($\boldsymbol{E_c}$ and $\boldsymbol{F_c}$ in equation 2.1) in streamwise direction x at one timestep n. (∘) denotes grid point where the spatial derivative is computed. (•) represents grid points that are used for the calculation of the spatial derivative at grid point (∘).

same number of grid points as the central difference stencils are employed. Thus, the order of the numerical scheme utilized as boundary closure for the viscous terms near the outflow does not need to be as strongly reduced as for the convective terms to stabilize the overall numerical scheme.

In order to maintain high-order boundary closures in wall-normal direction, Laible follows an approach suggested by Zhong & Tatineni (2003). At the wall, the interior high-order finite difference schemes (convective and viscous) are coupled with high-order boundary closures using one-sided finite differences (figure 3.3). To ensure stable boundary schemes, the grid is clustered near the wall according to the following function:

$$y_j = \frac{\arcsin\left(-\eta \cos\left(\pi j / 2n_y\right)\right)}{\arcsin\left(\eta\right)}. \tag{3.16}$$

Here, j denotes the grid point index in wall-normal direction, n_y is the total number of grid points in this direction and the parameter η determines the degree of grid

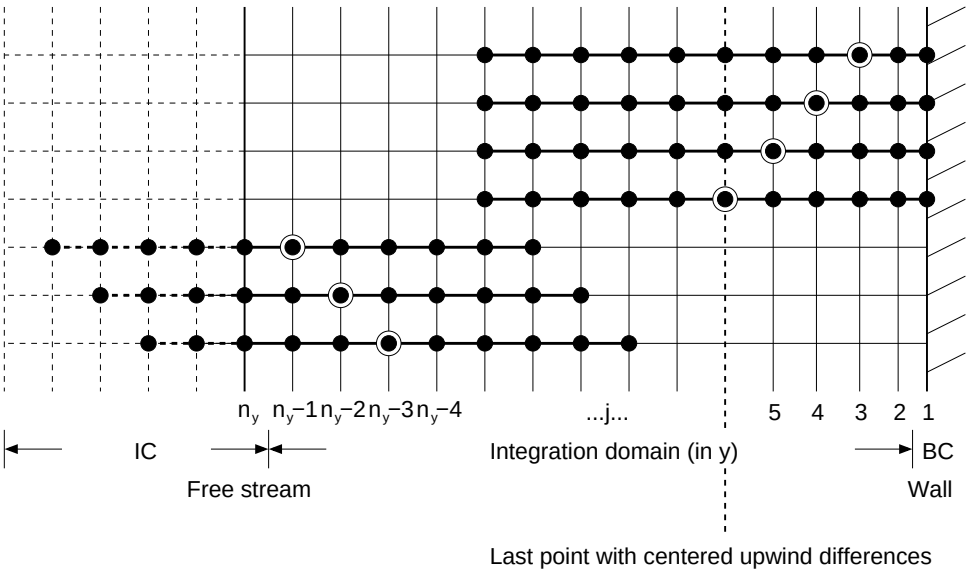

Figure 3.3: Illustration of the computational grid and the stencils implemented in the new high-order code by Laible (Laible *et al.*, 2008, 2009) for the inviscid terms ($\boldsymbol{E_c}$ and $\boldsymbol{F_c}$ in equation 2.1) in wall-normal direction y at one timestep n. (∘) denotes grid point where the spatial derivative is computed. (•) represents grid points that are used for the calculation of the spatial derivative at grid point (∘).

stretching. Note that stretching is only applied at the wall boundary and not (like in Zhong & Tatineni, 2003) at the wall and free-stream boundary. Applying grid stretching only at the wall is advantageous for boundary layer simulations, since typically a rather strong grid stretching away from the wall is employed. The free stream does not need to be as highly resolved as the region close to the wall. The resulting numerically unstable boundary closure at the free stream is circumvented by enforcing the Dirichlet boundary condition (section 3.2.4), not only on the free stream boundary point, but also at the points next to the boundary. Hence as at the inflow, high-order one-sided finite differences are avoided at the free stream.

3.2.2 Azimuthal Discretization

The azimuthal direction in the high-order code by Laible was assumed to be periodic and therefore transformed into Fourier space using the VFFTPK library as discussed

in section 3.1.2. Hence, all spatial derivatives with respect to the azimuthal direction were calculated according to equation (3.5). Moreover, all flow quantities are assumed to be symmetric with respect to the centerline except for the azimuthal velocity w, which is antisymmetric. Since the same library for the Fast Fourier Transformation (FFT) as in NSCC was also implemented in the new high-order code, the definition of the Fourier transformation follows equations (3.7) and (3.9). However, Laible applies a different scaling to all Fourier modes with $k \neq 0$. In his case, these Fourier modes have a value that is twice the magnitude of the modes defined in equations (3.7) and (3.9). For example, the transformation into spectral space from equation (3.7) can therefore be recast to

$$\widetilde{\phi}_0^c = \mathcal{F}(\phi)_0^c \sim \frac{1}{2(n_z-1)} \left[\phi_0^c + 2 \sum_{l=1}^{n_z-1} \phi_l^c \right] \tag{3.17}$$

for the "0^{th}" Fourier mode and

$$\widetilde{\phi}_k^c = \mathcal{F}(\phi)_k^c \sim \frac{1}{(n_z-1)} \left[\phi_0^c + 2 \sum_{l=1}^{n_z-1} \phi_l^c \cos\left(\frac{\pi k l}{n_z-1} \right) \right] \tag{3.18}$$

for all higher modes with $k \neq 0$.

3.2.3 Simulation Strategy and Initial Condition

In this section, the strategy is explained how to obtain appropriate initial conditions (IC) for cone simulations presented in this report. In contrast to flat-plate boundary layers, no similarity solution exists for a cone boundary layer if the transverse curvature terms are considered (Malik & Spall, 1991). Thus, a different strategy, when compared to flat-plate simulations, has to be found to obtain an accurate IC for a cone. This strategy is demonstrated in figure 3.4. In a precursor simulation, using a finite volume code developed by Gross (Gross & Fasel, 2002, 2008), the steady base flow for the entire cone geometry including the nose tip is calculated (figure 3.4a). This finite volume code solves the Navier–Stokes equations on a generalized coordi-

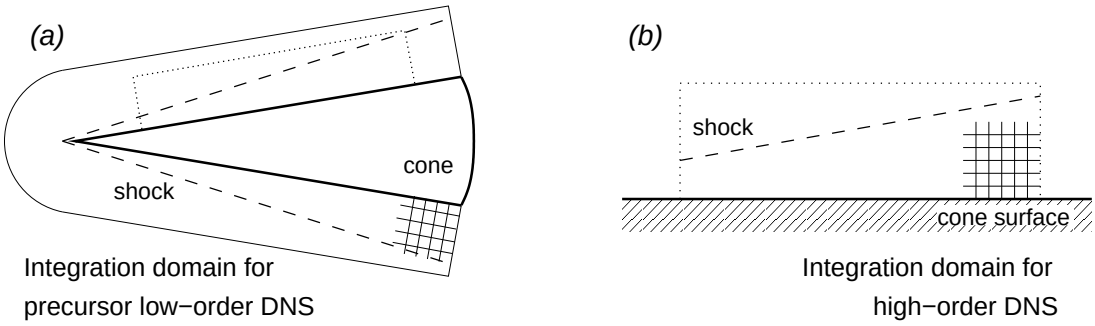

Figure 3.4: Illustration of the simulation strategy used for cone simulations: (a) Integration domain for the precursor simulations of the steady base flow using a coarse grid and a low-order numerical scheme. Note the nose tip of the cone is included in this simulation. (b) Integration domain for the high-order simulations using the code developed by Laible. Initial Condition (IC) from the precursor DNS is interpolated on a new computational grid.

nate system. The convective fluxes are discretized using a second-order symmetric total variation diminishing (TVD) upwind scheme while the viscous terms are calculated with a second-order accurate control volume approach. The time integration is based on an implicit Euler. This code can accurately predict the entire steady flow field for a cone. However, for unsteady transition simulations, the numerical scheme is too diffusive for capturing the correct spatial development of instability waves with a reasonable number of grid points. Therefore, a smaller part of the computational domain from the precursor simulation is extracted for the actual transition simulations, for which the high-order code developed by Laible (figure 3.4b) is employed. The flow field of this smaller domain is then interpolated on a new computational grid suitable for the high-order computations. Note that in this smaller domain the shock is also included. If the high-order finite differences as described in section 3.2 were used for the calculation of the shock, strong oscillations would be introduced. To avoid such oscillations, in the code by Laible, the order of the interior numerical integration scheme is strongly reduced in the near-shock region.

3.2.4 Boundary Conditions

The inflow is separated into two regions: a subsonic region ($M < 1$) close to the wall and a supersonic/hypersonic region ($M > 1$). In the supersonic/hypersonic region, Dirichlet conditions for u, v, w, T, p and ρ are specified (e.g. obtained from the precursor calculation) while for the subsonic region, a non-reflecting boundary condition is adopted as suggested by Poinsot & Lele (1992). On the cone surface, the no-penetration ($v = 0$) and the no-slip ($u = 0, w = 0$) conditions are enforced. The wall is set to be adiabatic for the steady base flow and temperature fluctuations are assumed to vanish for the unsteady simulations. At the outflow, a buffer domain technique is applied, where finite amplitude disturbances are ramped to zero (see Meitz & Fasel, 2000). Since for the simulations presented in chapter 6, the free stream is located above the oblique shock, Dirichlet conditions (for u, v, w, T, p, ρ) can be enforced at this boundary.

4. Compressible Linear Stability Theory

The spatial and temporal evolution of infinitesimal small disturbances in a boundary layer is governed by linear stability theory (LST). In all simulations discussed in this report, the boundary layer is forced through a hole or disturbance slot in the wall using small disturbance amplitudes. Hence, the initial disturbance development in the boundary layer for these simulations should follow linear stability behavior. In order to validate whether the Navier–Stokes solvers used for such simulations can capture the initial linear disturbance development accurately, results of the DNS are compared to theoretical predictions of LST. Furthermore, results from LST can also be utilized to identify possible Craik-type resonances (Craik, 1971). Some basic concepts of LST are introduced in the following sections. The main ideas and results of LST summarized in this chapter are obtained from Mack (1969).

4.1 Characterization of Disturbances

In linear stability theory (LST), disturbances have the form

$$\phi'(x,y,z,t) = \hat{\phi}(y)\exp\left(i\left(\alpha x + \beta z - \omega t\right)\right) . \tag{4.1}$$

This is a general equation for a plane wave travelling at a specific wave angle ψ with respect to the streamwise direction x. The disturbance amplitude $\hat{\phi}$ is only dependent on the wall-normal direction y. The wave angle is given by

$$\psi = \arctan\left(\frac{\beta}{\alpha_r}\right) , \tag{4.2}$$

with

$$\alpha_r = \frac{2\pi}{\lambda_x} \text{ and } \beta = \frac{2\pi}{\lambda_z} \tag{4.3}$$

as streamwise and spanwise/azimuthal wavenumbers, respectively. The streamwise wavenumber α_r is the real part of the complex wavenumber α in equation (4.1). If

the streamwise wavenumber α is assumed to be complex

$$\alpha = \alpha_r + i\alpha_i \,, \tag{4.4}$$

disturbances grow spatially with α_i as streamwise amplification rate. In the case of spatial LST, the disturbance frequency ω is real while for temporal LST, where disturbances grow temporally, ω is complex and α is real. Disturbances with a negative value of α_i (positive ω_i) experience streamwise (temporal) amplification while for positive values of α_i (negative ω_i), disturbances decay. Disturbances that neither grow nor decay are referred to as neutral. As already indicated in equation (4.3), the spanwise or azimuthal wavenumber β is always real. For a cone, the spanwise wavenumber β is dependent on the so-called azimuthal mode number k_c, which represents the ratio of the cone circumference and the azimuthal wave length λ_z at the cone surface. Figure 4.1 illustrates that for $k_c = 1$ the azimuthal wave length λ_z

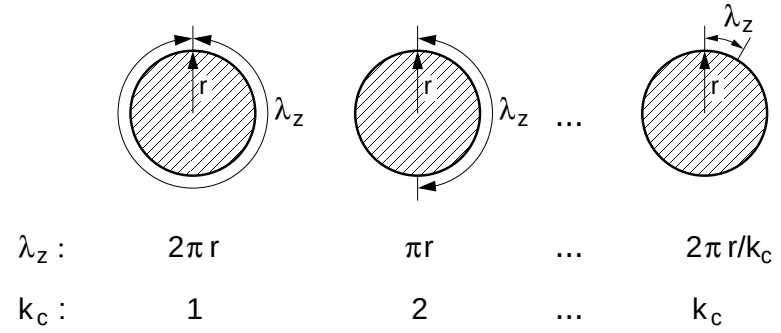

Figure 4.1: Definition of azimuthal mode number and azimuthal wave length for a cone.

corresponds to the cone circumference. In general for a cone, the azimuthal wave length λ_z can be calculated from

$$\lambda_z\,(x) = \frac{2\pi r\,(x)}{k_c}\,. \tag{4.5}$$

The cone radius r is a function of the streamwise direction x

$$r\,(x) = x\sin\,(\theta_c)\;. \tag{4.6}$$

Note that in the framework of LST, k_c can only have integer values and consequently, only a discrete set of azimuthal wavenumbers β can exist. This is in contrast to a flat plate (with infinite dimension in z-direction), where the spanwise wavenumber β can in principle take any value.

The streamwise and spanwise/azimuthal wavenumbers are nondimensionalized using the viscous length scale L_e^*,

$$\alpha = \alpha^* L_e^* \text{ and } \beta = \beta^* L_e^* . \tag{4.7}$$

The nondimensionalization of the streamwise direction x with L_e^* results in the local Reynolds number as introduced by equation (2.10)

$$R_x = \frac{x^*}{L_e^*} = \sqrt{\frac{U_e^* x^*}{\nu_e^*}} .$$

For the frequency, there are two commonly used nondimensionalizations, which are as follows:

$$\omega = 2\pi \frac{f^* L_e^*}{U_e^*} \quad \text{and} \quad F = \frac{\omega}{R_x} = 2\pi \frac{f^* \nu_e^*}{{U_e^*}^2} . \tag{4.8}$$

In the literature, F is often called "reduced" frequency and in contrast to ω, is independent of the viscous length scale L_e^*. If the boundary layer edge conditions are constant, a constant value of F represents a constant dimensional frequency f^*. This is not the case for ω since this frequency is proportional to $\sqrt{x}$.

4.2 Linearization of the Governing Equations

For the derivation of the linear stability equations, all flow quantities are decomposed into a mean flow (denoted by capital letters) and a disturbance component (denoted by $'$). The mean flow is assumed to be parallel ($V = 0$, $U = U(y)$ and $T = T(y)$)

and two-dimensional ($W = 0$):

$$u = U(y) + u', \tag{4.9a}$$

$$v = v', \tag{4.9b}$$

$$w = w', \tag{4.9c}$$

$$p = 1 + p', \tag{4.9d}$$

$$T = T(y) + T', \tag{4.9e}$$

$$\rho = \frac{1}{T(y)} + \rho'. \tag{4.9f}$$

Note that in contrast to the Navier–Stokes equations for the DNS (equation 2.1), pressure is nondimensionalized by its boundary edge value p_e^* instead of the dynamic pressure and the mean-flow pressure is assumed to be constant in wall-normal direction (boundary-layer assumption). The velocities are nondimensionalized by U_e^*, temperature by T_e^*, density by ρ_e^* and viscosity by μ_e^*. As length scale, L_e^* (equation 2.8) is used. Furthermore, it is assumed that the dynamic viscosity and thermal conductivity are only functions of temperature. This is appropriate since here a calorically perfect gas with constant Prandtl number $Pr = 0.71$ is investigated and the viscosity is given by Sutherland's law. A Taylor series approximation for the viscosity and conductivity, where all higher-order terms for the temperature disturbance are neglected, yields

$$\mu = \mu(T) + \frac{d\mu(T)}{dT}T' \quad \text{and} \quad k = k(T) + \frac{dk(T)}{dT}T'. \tag{4.10}$$

The decompositions in equations (4.9) and (4.10) are then substituted into the compressible Navier–Stokes equations (for a flat plate here, since all curvature and divergence terms are neglected for the linear stability analysis). If the resulting equations are linearized and the mean flow is subtracted, the disturbance equations for the continuity, x-momentum, y-momentum, z-momentum and energy are obtained (Mack, 1969; Balakumar & Malik, 1992):

continuity

$$\frac{\partial \rho'}{\partial t} + \frac{1}{T}\left(\frac{\partial u'}{\partial x} + \frac{\partial v'}{\partial y} + \frac{\partial w'}{\partial z}\right) + v'\frac{d\left(T^{-1}\right)}{dy} + U\frac{\partial \rho'}{\partial x} = 0\,, \tag{4.11}$$

x-momentum

$$\begin{aligned}\left(\frac{\partial u'}{\partial t} + U\frac{\partial u'}{\partial x} + v'\frac{dU}{dy}\right) = &-\frac{T}{\gamma M_e^2}\frac{\partial p'}{\partial x} + \frac{T}{R_x}\left[\mu\left(\frac{\partial^2 u'}{\partial x^2} + \frac{\partial^2 u'}{\partial y^2} + \frac{\partial^2 u'}{\partial z^2}\right)\right.\\ &+\frac{\mu}{3}\left(\frac{\partial^2 u'}{\partial x^2} + \frac{\partial^2 v'}{\partial x \partial y} + \frac{\partial^2 w'}{\partial x \partial z}\right) + \frac{d\mu}{dT}\frac{dT}{dy}\left(\frac{\partial u'}{\partial y} + \frac{\partial v'}{\partial x}\right)\\ &\left.+\frac{d\mu}{dT}\left(\frac{d^2U}{dy^2}T' + \frac{dU}{dy}\frac{\partial T'}{\partial y}\right) + \frac{d^2\mu}{dT^2}\frac{dT}{dy}\frac{dU}{dy}T'\right]\,,\end{aligned} \tag{4.12}$$

y-momentum

$$\begin{aligned}\left(\frac{\partial v'}{\partial t} + U\frac{\partial v'}{\partial x}\right) = &-\frac{T}{\gamma M_e^2}\frac{\partial p'}{\partial y} + \frac{T}{R_x}\left[\mu\left(\frac{\partial^2 v'}{\partial x^2} + \frac{\partial^2 v'}{\partial y^2} + \frac{\partial^2 v'}{\partial z^2}\right)\right.\\ &+\frac{\mu}{3}\left(\frac{\partial^2 u'}{\partial x \partial y} + \frac{\partial^2 v'}{\partial y^2} + \frac{\partial^2 w'}{\partial y \partial z}\right) + \frac{d\mu}{dT}\left(2\frac{dT}{dy}\frac{\partial v'}{\partial y} + \frac{dU}{dy}\frac{\partial T'}{\partial x}\right)\\ &\left.-\frac{2}{3}\frac{d\mu}{dT}\frac{dT}{dy}\left(\frac{\partial u'}{\partial x} + \frac{\partial v'}{\partial y} + \frac{\partial w'}{\partial z}\right)\right]\,,\end{aligned} \tag{4.13}$$

z-momentum

$$\begin{aligned}\left(\frac{\partial w'}{\partial t} + U\frac{\partial w'}{\partial x}\right) = &-\frac{T}{\gamma M_e^2}\frac{\partial p'}{\partial z} + \frac{T}{R_x}\left[\mu\left(\frac{\partial^2 w'}{\partial x^2} + \frac{\partial^2 w'}{\partial y^2} + \frac{\partial^2 w'}{\partial z^2}\right)\right.\\ &\left.+\frac{\mu}{3}\left(\frac{\partial^2 u'}{\partial x \partial z} + \frac{\partial^2 v'}{\partial y \partial z} + \frac{\partial^2 w'}{\partial z^2}\right) + \frac{d\mu}{dT}\frac{dT}{dy}\left(\frac{\partial w'}{\partial y} + \frac{\partial v'}{\partial x}\right)\right]\,,\end{aligned} \tag{4.14}$$

energy

$$\begin{aligned}\left(\frac{\partial T'}{\partial t} + U\frac{\partial T'}{\partial x} + v'\frac{dT}{dy}\right) = &-\left(\gamma - 1\right)T\left(\frac{\partial u'}{\partial x} + \frac{\partial v'}{\partial y} + \frac{\partial w'}{\partial z}\right)\\ &+\frac{\gamma T}{Pr R_x}\left[\mu\left(\frac{\partial^2 T'}{\partial x^2} + \frac{\partial^2 T'}{\partial y^2} + \frac{\partial^2 T'}{\partial z^2}\right) + \frac{d\mu}{dT}\frac{d^2T}{dy^2}T' + 2\frac{d\mu}{dT}\frac{dT}{dy}\frac{\partial T'}{\partial y} + \frac{d^2\mu}{dT^2}\left(\frac{dT}{dy}\right)^2 T'\right]\\ &+\frac{\gamma(\gamma-1)TM_e^2}{R_x}\left[2\mu\frac{dU}{dy}\left(\frac{\partial u'}{\partial y} + \frac{\partial v'}{\partial x}\right) + \frac{d\mu}{dT}\left(\frac{dU}{dy}\right)^2 T'\right]\,.\end{aligned} \tag{4.15}$$

The equation of state is

$$p' = \frac{T'}{T} + \rho' T \,. \tag{4.16}$$

The boundary conditions are

$$\begin{aligned} y = 0: &\qquad u' = 0, v' = 0, w' = 0, \text{ and } T' = 0\,, \\ y \to \infty: &\qquad \text{all disturbances are bounded}\,. \end{aligned}$$

These equations further simplify if their solutions are limited to plane harmonic waves in the form of equation 4.1. The disturbance quantities are then replaced by

$$\begin{bmatrix} u' \\ v' \\ w' \\ \rho' \\ T' \\ p' \end{bmatrix} = \begin{bmatrix} \hat{u} \\ \alpha\hat{v} \\ \hat{w} \\ \hat{\rho} \\ \hat{T} \\ \hat{p} \end{bmatrix} \exp\left(i\left(\alpha x + \beta z - \omega t\right)\right) . \tag{4.18}$$

Hence, the linearized Navier–Stokes equations can be recast to the following eigenvalue problem:

continuity

$$i\left(U\alpha - \omega\right)\hat{\rho} + \frac{1}{T}\left(i\alpha\hat{u} + \alpha\frac{d\hat{v}}{dy} + i\beta\hat{w}\right) + \frac{d(T^{-1})}{dy}\alpha\hat{v} = 0\,, \tag{4.19}$$

***x*-momentum**

$$\begin{aligned} i\left(U\alpha - \omega\right)\hat{u} + \frac{dU}{dy}\alpha\hat{v} = &-\frac{iT\alpha\hat{p}}{\gamma M_e^2} + \frac{T}{R_x}\left[\mu\left(\frac{d^2\hat{u}}{dy^2} - \left(\alpha^2 + \beta^2\right)\hat{u}\right)\right. \\ &+\frac{\mu}{3}\left(i\alpha^2\frac{d\hat{v}}{dy} - \alpha^2\hat{u} - \alpha\beta\hat{w}\right) + \frac{d\mu}{dT}\frac{dT}{dy}\left(\frac{d\hat{u}}{dy} + i\alpha^2\hat{v}\right) \\ &\left.+\frac{d\mu}{dT}\left(\frac{d^2U}{dy^2}\hat{T} + \frac{dU}{dy}\frac{d\hat{T}}{dy}\right) + \frac{d^2\mu}{dT^2}\frac{dT}{dy}\frac{dU}{dy}\hat{T}\right]\,, \end{aligned} \tag{4.20}$$

***y*-momentum**

$$i\left(U\alpha - \omega\right)\hat{v} = -\frac{T}{\alpha\gamma M_e^2}\frac{d\hat{p}}{dy} + \frac{T}{R_x}\left[\mu\left(\frac{d^2\hat{v}}{dy^2} - \left(\alpha^2 + \beta^2\right)\hat{v}\right)\right.$$

$$+\frac{\mu}{3}\left(i\frac{d\hat{u}}{dy}+\frac{d^2\hat{v}}{dy^2}+i\frac{\beta}{\alpha}\frac{d\hat{w}}{dy}\right)+\frac{d\mu}{dT}\left(2\frac{dT}{dy}\frac{d\hat{v}}{dy}+i\frac{dU}{dy}\hat{T}\right)$$
$$-\frac{2}{3}\frac{d\mu}{dT}\frac{dT}{dy}\left(i\hat{u}+\frac{d\hat{v}}{dy}+i\frac{\beta}{\alpha}\hat{w}\right)\Bigg], \tag{4.21}$$

z-momentum

$$i\left(U\alpha-\omega\right)\hat{w}=-\frac{iT\beta\hat{p}}{\gamma M_e^2}+\frac{T}{R_x}\left[\mu\left(\frac{d^2\hat{w}}{dy^2}-\left(\alpha^2+\beta^2\right)\hat{w}\right)\right.$$
$$\left.+\frac{\mu}{3}\left(i\alpha\beta\frac{d\hat{v}}{dy}-\alpha\beta\hat{u}-\beta^2\hat{w}\right)+\frac{d\mu}{dT}\frac{dT}{dy}\left(\frac{d\hat{w}}{dy}+i\alpha^2\hat{v}\right)\right], \tag{4.22}$$

energy

$$i\left(U\alpha-\omega\right)\hat{T}+\frac{dT}{dy}\alpha\hat{v}=-\left(\gamma-1\right)T\left(i\alpha\hat{u}+\alpha\frac{d\hat{v}}{dy}+i\beta\hat{w}\right)$$
$$+\frac{\gamma T}{PrR_x}\left[\mu\left(\frac{d^2\hat{T}}{dy^2}-\left(\alpha^2+\beta^2\right)\hat{T}\right)+\frac{d\mu}{dT}\left(\frac{d^2T}{dy^2}\hat{T}+2\frac{dT}{dy}\frac{d\hat{T}}{dy}\right)+\frac{d^2\mu}{dT^2}\left(\frac{dT}{dy}\right)^2\hat{T}\right]$$
$$+\frac{\gamma(\gamma-1)TM_e^2}{R_x}\left[2\mu\frac{dU}{dy}\left(\frac{d\hat{u}}{dy}+i\alpha^2\hat{v}\right)+\frac{d\mu}{dT}\left(\frac{dU}{dy}\right)^2\hat{T}\right], \tag{4.23}$$

equation of state

$$\hat{p}=\frac{\hat{T}}{T}+\hat{\rho}T. \tag{4.24}$$

The boundary conditions are

$$y=0: \qquad \hat{u}=0,\hat{v}=0,\hat{w}=0, \text{ and } \hat{T}=0\,,$$
$$y\to\infty: \qquad \text{all eigenfunctions are bounded}\,.$$

4.3 Inviscid Theory

To simplify the numerical procedure for solving the eigenvalue problem introduced above, Mack (1969) applied a coordinate transformation to the linear stability equations. For the inviscid case ($R_x\to\infty$), this transformation is especially advantageous because then the three-dimensional eigenvalue problem can be reduced to a

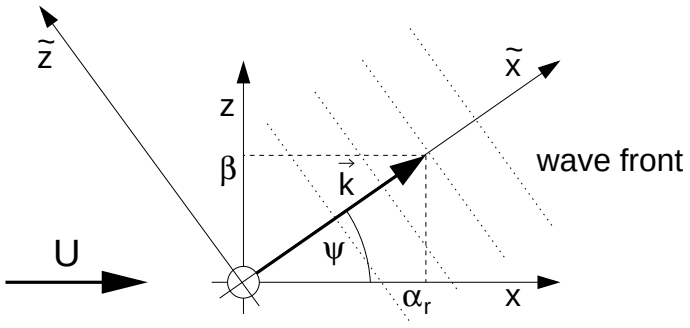

Figure 4.2: Illustration of the tilde coordinate system introduced by Mack (1969) in order to reduce the the three-dimensional inviscid eigenvalue problem to a two-dimensional form. Here, in contrast to the more general approach of Mack (1969), only a two-dimensional boundary layer is considered.

two-dimensional one. Figure 4.2 illustrates the rotated coordinate system $(\tilde{x}, y, \tilde{z})$ according to Mack. In this coordinate system, the $\tilde{x}$-axis is in the direction of the wave propagation (perpendicular to the wave front) while the x-axis is in the direction of the free stream. The angle between the x- and $\tilde{x}$-axes is the wave angle ψ. Since the $\tilde{z}$-axis is along the wave front of the harmonic wave, equation (4.1) reduces to

$$\phi'(\tilde{x}, y, t) = \hat{\phi}(y) \exp\left(i\left(|\vec{k}|\tilde{x} - \omega t\right)\right), \tag{4.26}$$

with

$$\tilde{x} = \cos(\psi)\, x + \sin(\psi)\, z\,, \tag{4.27}$$

and

$$\cos(\psi) = \frac{\alpha_r}{|\vec{k}|} \text{ and } \sin(\psi) = \frac{\beta}{|\vec{k}|}\,, \tag{4.28}$$

where $\vec{k}$ represents the wavenumber vector

$$\vec{k} = \begin{bmatrix} \alpha_r \\ \beta \end{bmatrix}. \tag{4.29}$$

Hence, in the stability equations, all derivatives of the disturbance quantities are zero with respect to $\tilde{z}$. Note, for convenience, in equation (4.26) and in the following discussion the temporal approach of LST is used. The disturbance frequency ω is

therefore assumed to be complex and α is real ($\alpha = \alpha_r$)

$$\omega = \omega_r + i\omega_i = \alpha_r \left(c^r_{ph,x} + i c^i_{ph,x} \right) , \tag{4.30}$$

with $c^r_{ph,x}$ denoting the phase speed in streamwise direction (x) and $\alpha_r c^i_{ph,x}$ representing the temporal amplification rate.

The transformation relations for the eigenfunctions defined by equation (4.18) between both coordinate systems are as follows:

$$\tilde{\hat{u}} = \hat{u} + \tan(\psi)\,\hat{w}\,, \tag{4.31a}$$

$$\tilde{\hat{v}} = \hat{v}\,, \tag{4.31b}$$

$$\tilde{\hat{w}} = -\tan(\psi)\,\hat{u} + \hat{w}\,, \tag{4.31c}$$

$$\tilde{\hat{p}} = \hat{p}\,, \tag{4.31d}$$

$$\tilde{\hat{T}} = \hat{T}\,, \tag{4.31e}$$

$$\tilde{\hat{\rho}} = \hat{\rho}\,. \tag{4.31f}$$

4.3.1 Neutral Solutions

Dropping the viscous terms and transforming the stability equations into the new coordinate system leads to the two-dimensional inviscid stability equations. Mack (1969) states that there are several forms of the inviscid equations that are helpful to address different properties of the inviscid case. Lees & Lin (1946), for example, derived the compressible version of the Rayleigh equation

$$\frac{d}{dy}\left[\frac{(U - c_{ph,x})\,\frac{d\tilde{\hat{v}}}{dy} - \frac{dU}{dy}\tilde{\hat{v}}}{\left(1 - \tilde{M}^2_{rel}\right) T} \right] = \frac{|\vec{k}|^2}{T}\,(U - c_{ph,x})\,\tilde{\hat{v}}\,, \tag{4.32}$$

where $\tilde{M}_{rel}$ denotes the relative Mach number

$$\tilde{M}_{rel} = \frac{U - c_{ph,x}}{\sqrt{T}}\,\tilde{M}_e\,, \tag{4.33}$$

and $\tilde{M}_e$ is the Mach number in the tilde coordinate system

$$\tilde{M}_e = M_e \cos(\psi) \,. \tag{4.34}$$

The physical meaning of $\tilde{M}_{rel}$ can be better understood if neutral disturbances are considered ($c^i_{ph,x} = 0$). In this case, $\tilde{M}_{rel}$ represents the local Mach number of the mean flow relative to the phase velocity in the direction of the wave propagation

$$\tilde{M}_{rel} = \frac{U^*(y) - c^*_{ph,x}}{a^*(y)} \cos(\psi) \,. \tag{4.35}$$

Moreover, $\tilde{M}_{rel}$ is a function of the wall-normal direction y.

Equation (4.32) is a second-order differential equation for the wall-normal velocity eigenfunction $\tilde{\hat{v}}$ with two boundary conditions:

$$\tilde{\hat{v}}(0) = 0 \;\text{ and }\; \tilde{\hat{v}} \text{ bounded as } y \to \infty \,. \tag{4.36}$$

Using

$$\xi(y) = \frac{1}{\left(1 - \tilde{M}^2_{rel}\right) T} \,, \tag{4.37}$$

equation (4.32) can be rewritten in the following form (Henningson & Schmid, 2001)

$$\frac{d}{dy}\left[\xi(y) \frac{d\tilde{\hat{v}}}{dy}\right] = \left[\frac{\frac{d}{dy}\left(\xi(y) \frac{dU}{dy}\right)}{U - c_{ph,x}} + \frac{|\vec{k}|^2}{T}\right] \tilde{\hat{v}} \,. \tag{4.38}$$

In this form, it is straight forward to recognize the singularity for $U(y_c) = c_{ph,x}$ ($\tilde{M}_{rel} = 0$) in equation (4.38) for a neutral disturbance. The wall-normal position y_c of the singularity is called "critical layer". A solution for equation (4.38) according to Frobenius' method can only exist at y_c if the singularity is regular. Therefore, the quantity

$$\frac{d}{dy}\left(\xi(y) \frac{dU}{dy}\right) = \frac{d}{dy}\left(\frac{1}{T} \frac{dU}{dy}\right) \tag{4.39}$$

has to vanish at the critical layer. The wall-normal position (critical layer), where this quantity has a value zero, is also called "generalized inflection point". Furthermore, as

proven by Lees & Lin (1946), **a generalized inflection point somewhere within the boundary layer is a necessary and sufficient condition for the existence of a neutral, inviscid subsonic disturbance**. The terminology "subsonic" in the previous statement stems from a classification of neutral disturbances based on $\tilde{M}_{rel}$ at the boundary layer edge ($U = T = 1$ for $y \geq \delta$) introduced by Lees & Lin (1946):

$$|\tilde{M}_{rel}\,(y \geq \delta)\,| < 1 \quad \left(c_{ph,x} > 1 - \frac{1}{\tilde{M}_e}\right) \;:\; \text{subsonic}\,, \tag{4.40a}$$

$$|\tilde{M}_{rel}\,(y \geq \delta)\,| = 1 \quad \left(c_{ph,x} = 1 - \frac{1}{\tilde{M}_e}\right) \;:\; \text{sonic}\,, \tag{4.40b}$$

$$|\tilde{M}_{rel}\,(y \geq \delta)\,| > 1 \quad \left(c_{ph,x} < 1 - \frac{1}{\tilde{M}_e}\right) \;:\; \text{supersonic}\,. \tag{4.40c}$$

In addition, Lees & Lin (1946) could show that **a generalized inflection point at a wall-normal position y_c greater than y_0, where y_0 is the point at which $c_{ph,x} = 1 - \frac{1}{\tilde{M}_e}$, is a necessary condition for the existence of an amplified disturbance**. The amplification rate is related to the difference in phase speed $c_{ph,x}\,(y_c) - c_{ph,x}\,(y_0)$; that is, as $c_{ph,x}\,(y_c) \rightarrow c_{ph,x}\,(y_0)$, $\alpha_r c^i_{ph,x} \rightarrow 0$. This is however only true for a particular type of disturbances, the so-called "first-mode" disturbances, which are an extension of the incompressible Tollmien-Schlichting instability waves. Further information on amplified disturbances can be found in section 4.3.2.

Mack (1969) first realized that different types of disturbances exist, which are solutions of the inviscid stability problem. If the compressible version of the Rayleigh equation (equation 4.32) is recast in terms of the disturbance pressure eigenfunction instead of wall-normal velocity

$$\frac{d^2\tilde{\hat{p}}}{dy^2} - \frac{d}{dy}\left[\ln\left(\tilde{M}^2_{rel}\right)\right]\frac{d\tilde{\hat{p}}}{dy} - |\vec{k}|^2\left(1 - \tilde{M}^2_{rel}\right)\tilde{\hat{p}} = 0\,, \tag{4.41}$$

one can see that this equation changes its behavior when $(1 - \tilde{M}_{rel})$ changes its sign. If the second term on the left-hand side is neglected (which is possible for large $|\vec{k}|^2$ according to Mack, 1969), the remaining equation is elliptical in nature for $\tilde{M}_{rel} < 1$ and a wave equation for $\tilde{M}_{rel} > 1$. Hence, multiple solutions can exist when $\tilde{M}_{rel} > 1$

("region of supersonic relative flow") somewhere in the boundary layer since there is an infinite sequence of wave lengths which satisfy the boundary conditions. Moreover, Lees & Lin (1946) provided the theorem that **there is only a unique wavenumber corresponding to one phase speed for the neutral subsonic disturbance if** $\tilde{M}_{rel} < 1$ **throughout the entire boundary layer**.

Mack (1969) termed the multiple solutions of the inviscid stability problem modes. The different modes can be distinguished by the number of zeros in their pressure eigenfunction. If there is no zero in the pressure eigenfunction of a neutral subsonic disturbance, the disturbance is a so-called "first mode" while one zero in the pressure eigenfunction indicates a "second mode". In general, an n^{th} mode of a neutral subsonic disturbance has $n-1$ zeros in its pressure eigenfunction. For insulated wall boundary layers, the second mode and the higher modes only appear for a free-stream Mach number of 2.2 and higher.

A further consequence of a region of supersonic relative flow ($\tilde{M}_{rel} > 1$) in the boundary layer is the existence of another class of disturbance waves that are independent of the generalized inflection point. These disturbances are characterized by having phase velocities in the range

$$1 \leq c_{ph,x} \leq 1 + \frac{1}{\tilde{M}_e} \tag{4.42}$$

and were first discovered by Mack (1969). For a phase velocity greater than unity, equation (4.38) does not have a singularity since the streamwise velocity U has a maximal value of one in the free stream ($U(y \geq \delta) = 1$). Because of the absence of a singularity and therefore a critical layer, Mack (1969) referred to these disturbances as "regular neutral solutions".

A summary of all neutral, plane disturbances for the inviscid stability problem of a boundary layer is presented in figure 4.3. As already mentioned before (equations 4.40), disturbances can be classified according to their phase velocity. There are mainly two different groups of disturbances. Disturbances that result from the

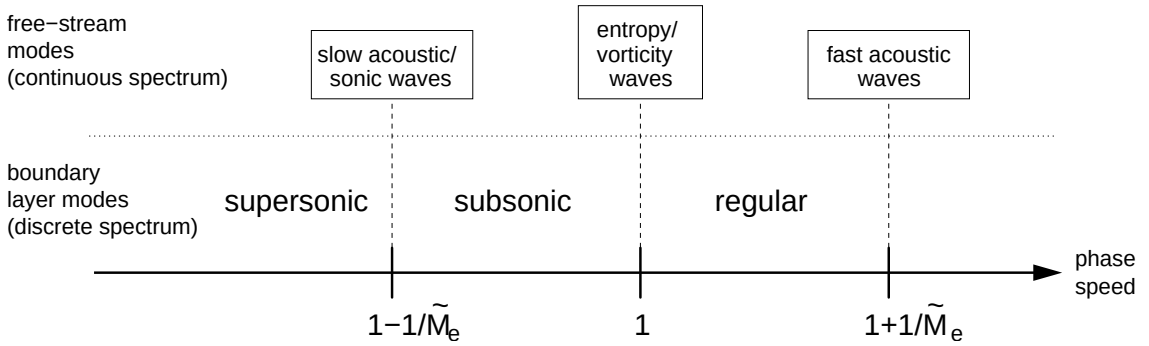

Figure 4.3: Classification of neutral, plane disturbances according to their phase speed $c_{ph,x}$.

boundary layer and are therefore commonly termed "boundary-layer modes" (discrete spectrum) and disturbances that are travelling in the free stream (continuous spectrum). The boundary-layer modes consist of the supersonic, subsonic and regular disturbances as discussed by Mack (1969) while the free-stream modes are of acoustical, entropic and vortical nature. "Slow" acoustic waves have the phase speed $c_{ph,x} = 1 - 1/\tilde{M}_e$ and propagate upstream relative to the free stream. Entropy and vorticity waves propagate with the free stream and "fast" acoustic waves ($c_{ph,x} = 1 + 1/\tilde{M}_e$) travel downstream relative to the free stream.

4.3.2 Amplified and Damped Solutions

The previous section introduced the main classes of neutral disturbances for a high-speed boundary layer. The primary interest of linear stability theory, however, is on amplified disturbances since these disturbances will eventually transition the flow to turbulence. Figures 4.4a and 4.4b (all data presented in the figures of this chapter are digitized from Mack, 1969) show the real and imaginary part of the complex eigenvalue $c^r_{ph,x} + ic^i_{ph,x}$ as a function of the streamwise wavenumber for two-dimensional disturbances. These diagrams are typical for low and moderate supersonic Mach numbers up to Mach 4.4 (Mack, 1969). The streamwise wavenumbers of neutral subsonic disturbances and neutral regular disturbances are also included in this figure. α_{sn}

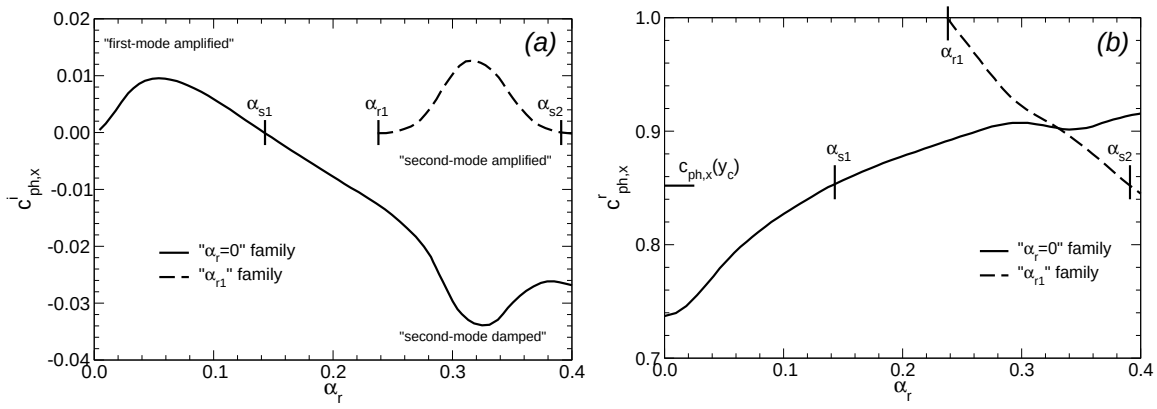

Figure 4.4: Complex phase speed of two-dimensional disturbances as a function of streamwise wavenumber α_r for $M_e = 3.8$, insulated wall and free-stream temperature $T_e^* = 80K$: (a) imaginary part $c^i_{ph,x}$, (b) real part $c^r_{ph,x}$. Reproduced from Mack (1969), figure 11.6.

denotes the streamwise wavenumber of the neutral subsonic mode n. For example, a first-mode neutral subsonic disturbance has the streamwise wavenumber α_{s1} and a second-mode neutral subsonic disturbance has α_{s2} as its streamwise wavenumber. A similar nomenclature is used by Mack for the regular neutral disturbances. α_{r1} represents a first-mode regular neutral solution while α_{rn} would denote a n^{th}-mode regular neutral solution. The distinction between different regular neutral modes is according to the zeros (phase change) in the pressure eigenfunction as discussed for the subsonic neutral solutions in the previous section.

The eigenvalues for $c^i_{ph,x} \neq 0$ in figure 4.4a lie on two separate curves and therefore, form two distinct "families" of solutions. Mack (1969) states that it is easier to discuss the inviscid amplified or damped solutions in terms of these families than in terms of modes as for the neutral solutions from the previous section. He distinguishes between different families according to their origin in the complex phase speed diagram. For example in figure 4.4a, the solid curve originates from $\alpha_r = 0$ with a phase speed of $c_{ph,x} = 1 - 1/M_e$ while the dashed curve starts at α_{r1} with $c_{ph,x} = 1$. Since the mode characteristics change along these eigenvalue curves and are often not well defined, it

is not possible to assign one curve to a particular mode. For example, on the dashed curve between α_{r1} and α_{s2} in figure 4.4a, the pressure eigenfunctions for the different eigenvalues change from a "first-mode regular neutral"-type eigenfunction with zero phase change to a "second-mode subsonic neutral"-type eigenfunction with one phase jump. Because of this phase change, typical for second-mode neutral solutions (regular and subsonic), Mack (1969) terms the amplified disturbances between α_{r1} and α_{s2} "second-mode amplified solutions". The solutions on the solid curve starting at $\alpha_r = 0$ are called "first-mode amplified solutions" in the region between $\alpha_r = 0$ and α_{s1} and "second-mode damped solutions" near the minimum between α_{r1} and α_{s2}. Again, this distinction is based on the phase change in the pressure eigenfunction of the different solutions.

An important result of Mack's numerical investigations is that first-mode amplified solutions have a phase speed $c_{ph,x}$ between the phase speed for a sonic disturbance $c_{ph,x}(y_0) = 1 - 1/\tilde{M}_e$ and the phase speed at the critical layer (generalized inflection point) $c_{ph,x}(y_c)$, hence

$$c_{ph,x}(y_0) < c_{ph,x} < c_{ph,x}(y_c)\,. \tag{4.43}$$

As a consequence of this restriction, the amplification rate of first-mode amplified solutions is directly related to the difference in phase speed $\Delta c_{ph,x} = c_{ph,x}(y_c) - c_{ph,x}(y_0)$. Figure 4.5a shows $c_{ph,x}(y_c)$ and $c_{ph,x}(y_0)$ as a function of edge Mach number M_e for several different free-stream temperatures T_e^*. For all curves, the difference $\Delta c_{ph,x}$ has a minimum near $M_e = 1.6$ while for larger Mach numbers the difference increases and finally levels off. The maximal temporal amplification rate $(\alpha_r c^i_{ph,x})_{max}$ for two-dimensional first-mode amplified disturbances exhibits a very similar behavior with a minimum near Mach 1.5. The influence of the phase difference $\Delta c_{ph,x}$ on the amplification rate of first-mode disturbances suggests that anything that changes $c_{ph,x}(y_c)$ or $c_{ph,x}(y_0)$ affects the amplification rate of first-mode disturbances. For example, by increasing the free-stream temperature and keeping the wall insulated,

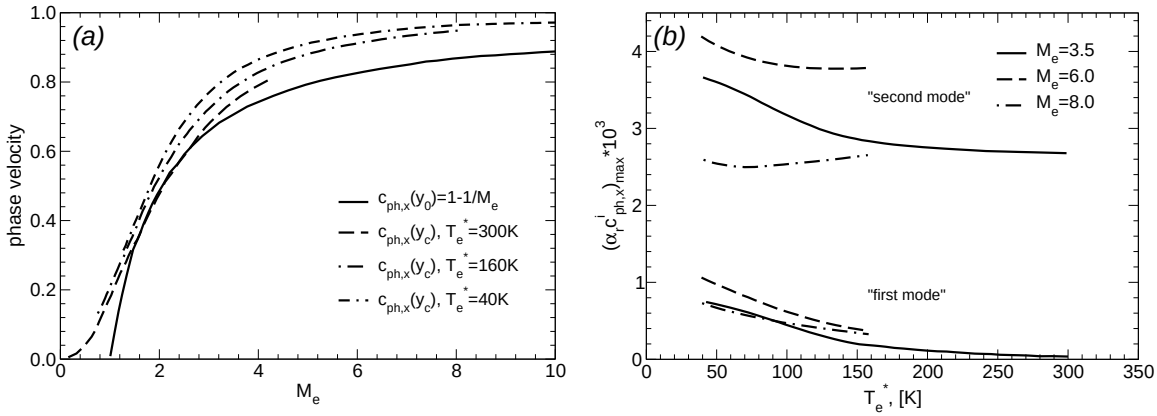

Figure 4.5: Effect of free-stream temperature on the stability behavior of a supersonic/hypersonic boundary layer with insulated wall: (a) Phase velocities as function of Mach number M_e, (b) maximum amplification rates of two-dimensional first- and second-mode amplified disturbances for different Mach numbers. Reproduced from Mack (1969), figures 11.13 and 11.14.

the curve for $c_{ph,x}(y_c)$ moves closer to $c_{ph,x}(y_0)$ (figure 4.5a). Note that $c_{ph,x}(y_0) = 1 - 1/\tilde{M}_e$ is not dependent on the free-stream temperature and therefore, stays constant.

The maximal amplification rate as a function of the free-stream temperature is depicted in figure 4.5b for several Mach numbers. Clearly, as expected from figure 4.5a, an increase in free-stream temperature reduces the temporal amplification rate of first-mode amplified disturbances. Also shown in figure 4.5b are the maximal amplification rates for second-mode amplified disturbances. The effect of the free-stream temperature on a second-mode amplified disturbance can be either stabilizing or destabilizing depending on the Mach number. Since second-mode neutral disturbances (regular or subsonic) are primarily a result of the supersonic relative flow region ($\tilde{M}_{rel} > 1$), the amplification rates of second-mode amplified disturbances are mainly influenced by the wall-normal extent of this region. Therefore, anything that changes the thickness of the supersonic relative flow region also affects second-mode (and higher) amplified disturbances. Figure 4.5b further indicates that for two-dimensional disturbances, second-mode amplified solutions have always the highest amplification rates when compared to first-mode amplified solutions for Mach numbers $M_e \geq 2.2$.

So far, only the stability behavior of two-dimensional disturbances have been discussed in this section. Results for three-dimensional disturbances can be obtained from the two-dimensional stability equations in the tilde coordinate system from figure 4.2. In this coordinate system, the Mach number $\tilde{M}_e$ of the mean flow in direction of the wave propagation is defined by equation (4.34) with ψ as the wave angle ($\tilde{M}_e = M_e \cos(\psi)$). The change of the Mach number $\tilde{M}_e$ with respect to the wave angle ψ has direct implications on first-mode and second-mode amplified disturbances. The phase speed of a sonic disturbance $c_{ph,x}(y_0) = 1 - 1/\tilde{M}_e$ decreases as ψ increases from $0°$ to $90°$ while the phase speed of the critical layer $c_{ph,x}(y_c)$ remains unchanged since the mean velocity and temperature profiles are fixed. Consequently, the difference $\Delta c_{ph,x} = c_{ph,x}(y_c) - c_{ph,x}(y_0)$ increases and this leads to a destabilization of first-mode amplified disturbances. At the same time, the wall-normal thickness of the supersonic relative flow region decreases with $\tilde{M}_e$ (equation 4.33) yielding a stabilization of second-mode and higher-mode amplified disturbances. Both trends are illustrated in figure 4.6 for a Mach 8.0 boundary layer with an insulated wall and a free-stream temperature of $T_e^* = 50K$. This figure shows the temporal amplification rate as a function of the streamwise wavenumber. For two-dimensional waves, the amplified region of the first three modes are merged (solid line) and second-mode amplified disturbances are most unstable. With increasing wave angle ψ, first-mode amplified disturbances are destabilized until they reach their highest amplification rate at about $\psi = 56°$. Since the streamwise wavenumber α_r approaches zero for $\psi \to 90°$, the decrease in α_r eventually outweighs the increase in amplification rate due to the increase of $c_{ph,x}(y_c) - c_{ph,x}(y_0)$ and therefore, $\alpha_r c^i_{ph,x}$ starts to decrease with further increase of ψ (graph for $\psi = 60°$ in figure 4.6). As expected, the second-mode and third-mode amplified solutions are stabilized with increasing ψ. At about $\psi = 45°$, only the first two unstable regions are still visible while at $\psi = 60°$, the second-mode unstable region has completely vanished.

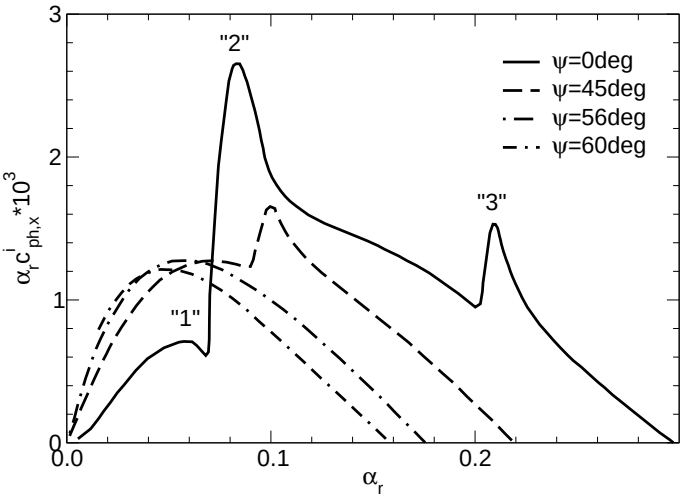

Figure 4.6: Amplification rate as function of wavenumber for three-dimensional disturbances at $M_e = 8.0$, insulated wall and free-stream temperature $T_e^* = 50K$. Reproduced from Mack (1969), figure 11.18.

4.4 Viscous Theory

In order to investigate the influence of viscous effects on the stability behavior of a high-speed boundary layer the complete linearized Navier–Stokes equations (equation 4.19 to 4.24) have to be solved numerically. As for the inviscid case, Mack (1969) transformed equations (4.19) to (4.24) into the rotated (tilde) coordinate system illustrated in figure 4.2. In this coordinate system, the governing equations reduce to a "nearly two-dimensional form". Despite the existence of the $\tilde{z}$-momentum equation, the three-dimensional form of the governing equations differs only from the two-dimensional form in a dissipation term in the energy equation involving the velocity component parallel to the wave front ($\tilde{w}'$). Mack (1969) showed that, by neglecting this dissipation term, only a small error in the calculation of the maximal temporal amplification rate for oblique disturbances is introduced, while the computational cost is considerable reduced since only two-dimensional equations have to be solved. Today, neglecting this dissipation term and therefore, reducing the three-dimensional problem to a two-dimensional form is not necessary since the computational resources

increased significantly in the last 40 years.

The terminology introduced for the inviscid case is also used for the viscous theory. In particular, a first-mode amplified solution of the inviscid stability problem has a viscous counterpart, which is termed "viscous first-mode amplified disturbance" in this section. The same convention is also employed for second-mode amplified disturbances. The distinction between viscous first-mode and viscous second-mode disturbances is again based on the phase change in the pressure eigenfunction as explained in section 4.3.1. However, for the viscous problem, it is even harder to assign a disturbance a particular mode characteristic, especially for high Mach numbers.

In the following sections, the main results of viscous linear stability theory are summarized.

4.4.1 Amplified and Damped Solutions

Mack (1969) reports that, depending on the Mach number, the wave angle and the mode type (first or second mode) of the disturbance, viscosity can have both, a stabilizing and destabilizing effect. In figure 4.7, neutral stability curves for two-dimensional disturbances are plotted against $1/R_x$ for different Mach numbers from 1.6 to 3.8. The streamwise wavenumbers α_{s1} for two-dimensional neutral subsonic disturbances at $1/R_x = 0$ denote the inviscid limit for the different Mach numbers.

At all Mach numbers, the neutral stability curves in figure 4.7 approach the inviscid limit for $R_x \rightarrow \infty$. For the inviscid case, the region between $\alpha_r = 0$ and α_{s1} includes first-mode amplified solutions as discussed for Mach 3.8 in figure 4.4a. Hence, it can be concluded that the neutral stability curves in figure 4.7 define the boundary of the viscous counterpart of a first-mode amplified region. At Mach 1.6, for low Reynolds numbers, the unstable region is at higher streamwise wavenumbers than the inviscid limit. Thus, for this Mach number and at low Reynolds numbers, viscosity destabilizes disturbances with streamwise wavenumber larger than α_{s1} and

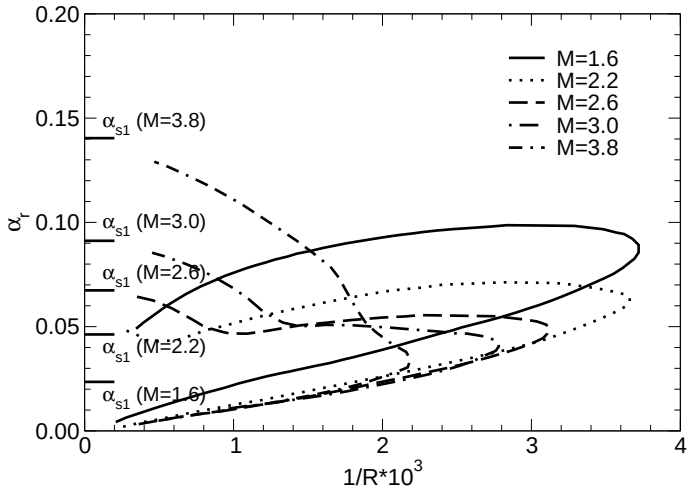

Figure 4.7: Neutral stability curves for two-dimensional disturbances as a function of inverse of local Reynolds number $1/R_x$ and streamwise wavenumber α_r for several different Mach numbers (insulated wall and free-stream temperature $T_e^* = 80K$). Reproduced from Mack (1969), figure 12.2.

stabilizes disturbances for lower streamwise wavenumber. This destabilizing effect decreases with increasing Mach number. At $M_e = 3.8$, for example, viscosity only stabilizes viscous first-mode amplified disturbances at all finite Reynolds numbers.

Figure 4.8 provides a clearer picture of the influence of viscosity on the stability behavior of viscous first (figure 4.8a) and second-mode (figure 4.8b) amplified two-dimensional disturbances. In this figure, the maximal temporal amplification rate $(\alpha_r c^i_{ph,x})_{max}$ is plotted against local Reynolds number R_x for several Mach numbers. As explained in figure 4.7, at low supersonic Mach numbers ($M_e = 1.6$, 2.2, and 2.6), viscosity has a destabilizing effect on viscous first-mode disturbances for low Reynolds numbers in figure 4.8a. At Mach 3.0, this effect disappears and viscosity stabilizes for all finite Reynolds numbers. Viscous second-mode amplified disturbance (figure 4.8b), on the other hand, are always stabilized by viscosity.

The destabilizing effect of viscosity on first-mode disturbances decreases with increasing wave angle. Therefore, three-dimensional first-mode disturbances are less destabilized than two-dimensional first-mode disturbances. Figure 4.9 shows the

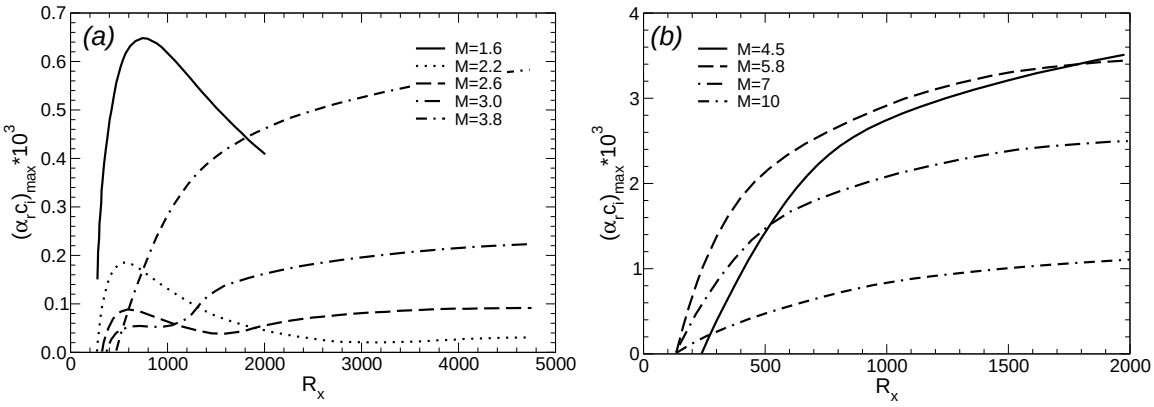

Figure 4.8: Maximal temporal amplification rate $(\alpha_r c^i_{ph,x})_{max}$ of two-dimensional disturbances as a function of local Reynolds number for first-mode-type amplified disturbances (a) and second-mode-type amplified disturbances (b) (insulated wall and free-stream temperature $T_e^* = 80K$ for a and $50K$ for b). Reproduced from Mack (1969), figures 12.10 and 12.12.

maximal temporal amplification rate of inviscid and viscous first and second-mode amplified solutions as a function of edge Mach number. The thin lines represent the inviscid limit. While inviscid, two-dimensional second-mode amplified disturbances are always more amplified than two-dimensional, inviscid first-mode disturbances for Mach numbers larger than 2.2; this is not the case if three-dimensional, inviscid first-mode amplified disturbances are considered. The curve for two-dimensional, inviscid second-mode disturbances intersects the curve for three-dimensional, inviscid first-mode solutions at about $M_e = 2.66$. Viscosity strongly reduces the amplification rates of second-mode amplified disturbances. Below of about $M_e = 3.0$, first-mode disturbances become destabilized by viscosity. Since the destabilizing influence of viscosity decreases with increasing obliqueness, the wave angle decreases for viscous first-mode amplified disturbances for decreasing Mach numbers. The Mach number where the curve for two-dimensional, viscous second-mode solutions intersects with the curve for viscous first-mode solutions is approximately at $M_e = 4.0$.

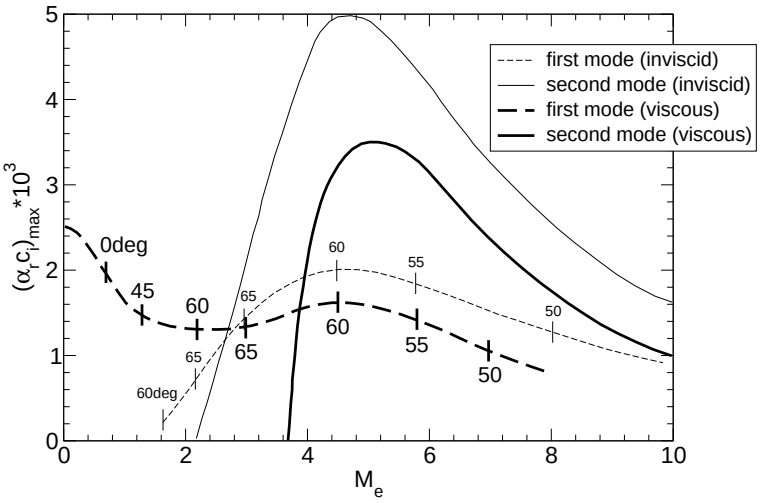

Figure 4.9: Effect of Mach number on the maximal temporal amplification rate of most unstable inviscid and viscous first and second-mode-type amplified disturbances at $R_x = 1500$. Wave angles of first-mode amplified solutions are specified for selected Mach numbers. Reproduced from Mack (1969), figures 11.11, 11.21, and 13.18.

4.4.2 Eigenvalue Diagram

The final figure discussed in this chapter (figure 4.10) demonstrates the complex phase speed $c^r_{ph,x} + ic^i_{ph,x}$ of two-dimensional disturbances as a function of streamwise wavenumber α_r for the viscous linear stability problem at Mach number 3.8. The inviscid limit from figure 4.4 is also included for comparison. Recent studies of compressible linear stability theory (Fedorov, 2003; Tumin, 2007) introduced new concepts and terminology that can be explained using figure 4.10.

The dispersion relation in figure 4.10a is very similar to the inviscid case although the local Reynolds number is low ($R_x = 850$). There are two solutions with one solution originating from the slow acoustic wave spectrum $c_{ph,x} = 1 - 1/M_e$ and the other originating from the fast acoustic wave spectrum $c_{ph,x} = 1 + 1/M_e$. These are the viscous counterparts of the $\alpha_r = 0$ family and the α_{r1} family of solutions from figure 4.4. Fedorov (2003) and Tumin (2007) denote the family of solutions from the slow acoustic wave spectrum "slow mode" or "mode S" and consequently, the family

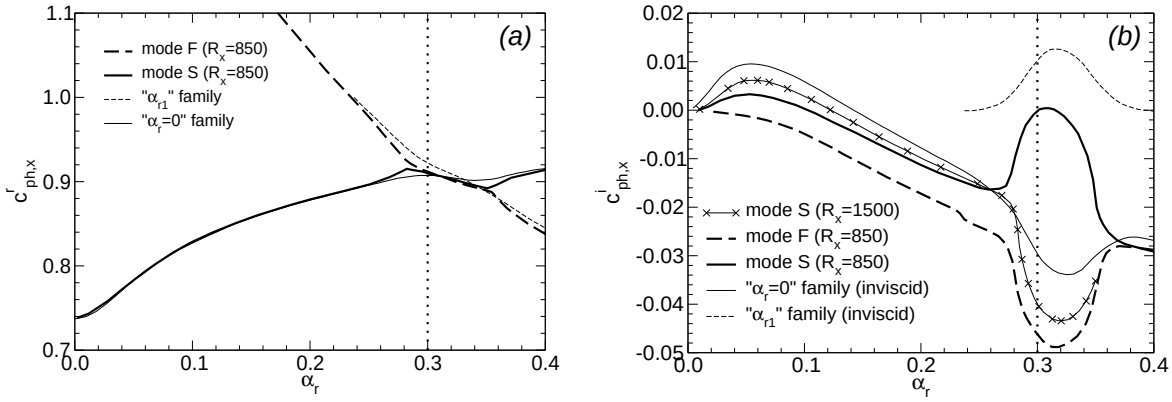

Figure 4.10: Complex phase speed of two-dimensional disturbances as a function of streamwise wavenumber α_r for $M_e = 3.8$, insulated wall and free-stream temperature $T_e^* = 80K$: (a) real part $c^r_{ph,x}$, (b) imaginary part $c^i_{ph,x}$. Reproduced from Mack (1969), figure 12.17.

of solutions from the fast acoustic wave spectrum "fast mode" or "mode F". This notation will also be used throughout this report.

The phase speed of mode S and mode F change with streamwise wavenumber α_r and coincide at about $\alpha_r = 0.3$, which is called point of "synchronism" (Fedorov & Khokhlov, 2002). Any point where two families of solutions coincide in their phase speed $c^r_{ph,x}$ is termed "synchronism" by Fedorov (2003) and Tumin (2007). Hence, for example, mode S is synchronized with the slow acoustic wave spectrum at $\alpha_r = 0.0$, while mode F is synchronized with the fast acoustic wave spectrum for the same streamwise wavenumber. The "synchronism" mechanism between mode S and mode F at $\alpha_r = 0.3$ leads to the amplification of one of those modes and produces for the current Mach number ($M_e = 3.8$) the second mode unstable region. Figure 4.10b shows $c^i_{ph,x}$ versus the streamwise wavenumber α_r for both modes at two different local Reynolds numbers and for the inviscid case. At $R_x = 850$, mode S contains the viscous first-mode amplified solutions and the viscous second-mode amplified solutions while mode F is damped throughout the entire wavenumber regime. At $R_x = 1500$, the picture changes and mode S contains only the viscous first-mode amplified solution while mode F, which is not shown, develops into a viscous second-

mode amplified disturbance, just as predicted by the inviscid theory. If the Reynolds number is further increased the curves for mode S and mode F approach the inviscid limit.

As a final conclusion for this chapter, it is important to note that there exists a misunderstanding in the research comunity about first-mode and second-mode unstable regions. As discussed for figure 4.10b, both regions are not always a result of two amplified independent families of disturbances (mode S and mode F). Even for the inviscid case at high Mach numbers, the second-mode unstable region (and even higher-mode unstable regions) can be contained within one family of solutions (the family originating from $c_{ph,x} = 1 - 1/M_e$). This fact, for example, is illustrated in figure 4.6 (for 0 deg) of the last section.

5. Transition to Turbulence Via Oblique Breakdown in a Flat-Plate Boundary Layer at Mach 3

In a recent series of numerical studies Mayer *et al.* (2007) and Mayer & Fasel (2008) showed that oblique breakdown might have been present in the experiments by Kosinov and co-workers (Kosinov *et al.*, 1994) and suggested that oblique breakdown might be the most dominant nonlinear mechanism (Mayer *et al.*, 2009*a*) for supersonic boundary layers. However, a nonlinear mechanism is only relevant for the transition process if this mechanism can indeed completely transition a laminar boundary layer to turbulence. Hence, the following chapter discusses the final question: Does oblique breakdown lead to a fully developed turbulent boundary layer? In this chapter, the entire transition path initiated by a pair of oblique time-harmonic waves at low amplitudes is studied in detail. The flow conditions for this study are explained in section 5.1. The forcing amplitudes are low enough so that the early disturbance development can be compared to linear stability theory (section 5.2). The known origin and characteristics of the disturbances introduced facilitate a more reliable interpretation of the results at the later nonlinear stages. In section 5.3, the characteristics of the oblique breakdown mechanism are studied for the early and late nonlinear stages. Finally, in section 5.4, it is assessed whether a fully turbulent flow can be reached and sustained.

5.1 Physical Problem and Computational Setup

The simulations in this chapter are a continuation of the earlier studies by Mayer (2004) and Husmeier *et al.* (2005) of flat-plate boundary layer at Mach 3. The physical conditions of the simulations match the Princeton wind-tunnel conditions (Graziosi & Brown, 2002): the unit Reynolds number formed with the free-stream velocity and free-stream viscosity at the inflow is $Re = 2.181 \times 10^6 m^{-1}$ and the free-stream

temperature is $T^*_\infty = 103.6K$.

Figure 5.1a illustrates the computational setup for all simulations discussed in this chapter. The earlier simulation by Mayer (2004) and Husmeier *et al.* (2005) is denoted as CASE 1. CASE 3 and 4 are the main focus of this chapter and CASE 2, 5, 6 & 7 are used as grid, domain height and domain width studies. The overall resolution increases from CASE 1 to CASE 7. An example for the grid of CASE 3 & 4 is shown in figure 5.1b. The grid is clustered in the streamwise direction using a fifth-order polynomial (figure 5.1c) and in the wall-normal direction using a third-order polynomial (figure 5.1e). The computational grid in physical space consists of a total of roughly 212 million grid points for CASE 3 & 4 (see table 5.1 for the other cases). The inflow of the domain for all cases is located at $x^*_0 \simeq 0.258m$ downstream of the leading edge of the plate, whereas the outflow ranges from approximately 11.3 to 14.5 streamwise wave lengths λ_x of the oblique fundamental disturbance waves in the linear regime, i.e. $x^*_L \simeq 1.145m$ for CASE 3 & 4. The domain height for CASE 3 & 4 is chosen as $y^*_H \simeq 0.030m \approx 5$ boundary layer thicknesses δ (laminar) at the outflow, such that even with the high increase in boundary layer thickness caused by the transition process no turbulent flow structures reach the free-stream boundary. Pseudo-spectral discretization using Fourier modes (Canuto *et al.*, 1988) is employed in the spanwise direction of the computations. For CASE 1-6, the flow is assumed to be symmetric to the centerline ($z^* = 0.0m$) of the flat plate with respect to the streamwise velocity u, wall-normal velocity v, density ρ and temperature T and antisymmetric with respect to the spanwise velocity w, whereas for CASE 7, the symmetry condition is removed.

Time-harmonic disturbances with a fundamental frequency of about $f^* = 6.36kHz$ ($F = 3 \times 10^{-5}$) are introduced through a blowing and suction slot located between $x^*_1 \simeq 0.394m$ and $x^*_2 \simeq 0.452m$ ($x_2 - x_1 \approx \lambda_x$). A discrete wave pair of instability waves with equal but opposite wave angle is excited for all cases, except for CASE 4, where also a two-dimensional wave with the fundamental frequency and a very low

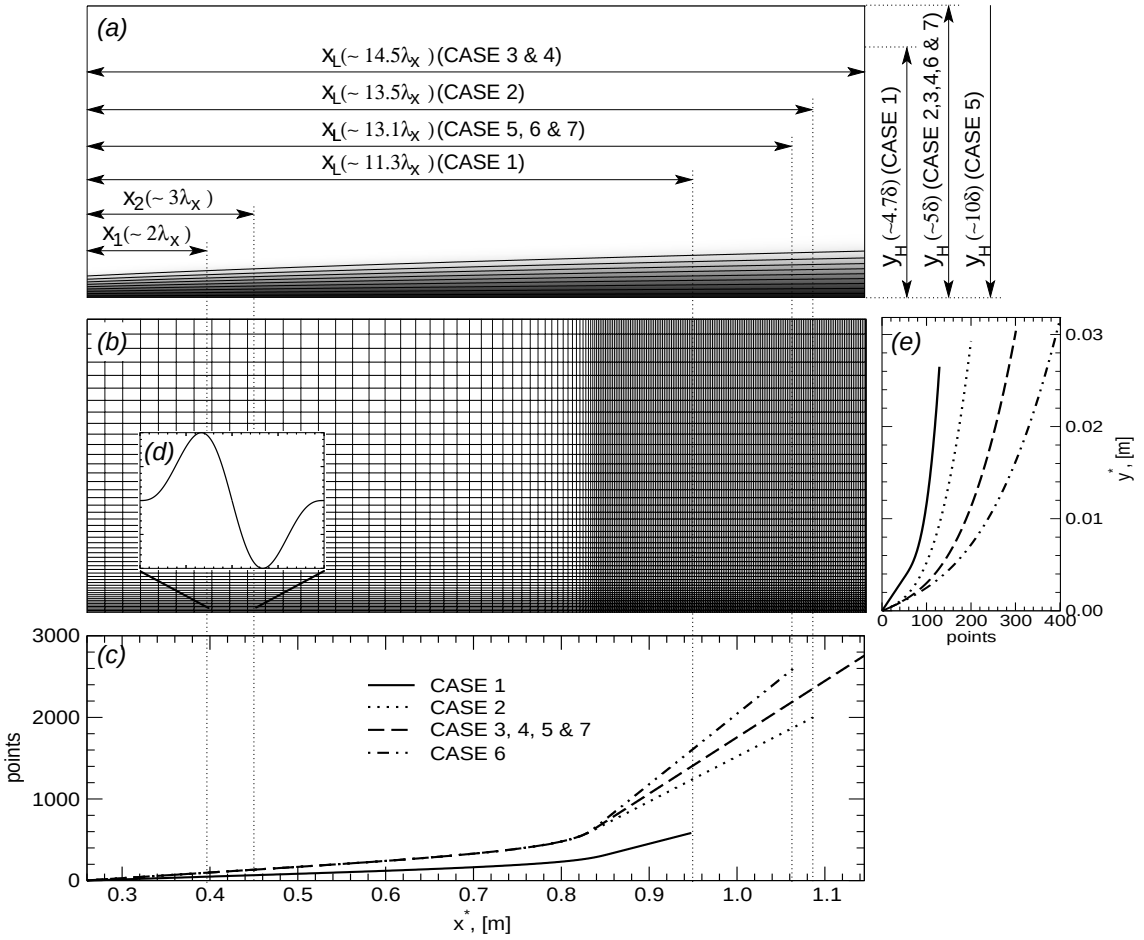

Figure 5.1: Computational setup for all cases: (a) computational domain, (b) grid used for CASE 3, for clarity only every 14th point in x and every 6th point in y are plotted, (c) grid clustering in the streamwise direction, (d) blowing and suction velocity profile v_p over the disturbance slot, (e) grid stretching in the wall-normal direction; M=3.0, T^*_∞=103.6K, flat plate.

disturbance amplitude is additionally forced to initialize waves that are not directly generated through the nonlinear wave interactions of the forced wave pair. The spanwise wavenumber of $\beta^* \simeq 211.52m^{-1}$ for this wave pair is chosen to be such that the generated instability waves experience strong amplification as predicted by LST throughout the entire computational domain. This spanwise wavenumber determines also the domain width of all simulations, i.e. $z_W^* = \lambda_z^* = 2\pi/\beta^* \simeq 0.03m$. The major differences between the setup for all cases are summarized in table 5.1.

5.2 Linear Regime

The linear transition regime is studied using both numerical simulations and several theoretical approaches. This section will discuss results from LST, PSE and DNS. The linear stability solvers from Mack (Mack, 1965, 1987) and Tumin (Tumin, 2007, 2008) are employed. The latter utilizes a single-domain Chebyshev spectral collocation method (Malik, 1990; Tumin, 2007) to solve for the entire spectrum for a single disturbance frequency at a given streamwise position in the flow and for a prescribed spanwise wavenumber. Tumin's solver was adjusted to the Intel® Math Kernel Library (based on LAPACK) for the solution of the generalized, nonsymmetric eigenvalue problem. The spectra for the physical flow conditions discussed in this chapter are shown in figure 5.2 for two frequencies and two spanwise wavenumbers at the streamwise position $x^* = 0.5m$ ($R_x = 1044$).

Figure 5.2a,b show the two-dimensional eigenvalue spectra (vanishing β) for the frequencies $f^* = 6.36kHz$ and $f^* = 84.78kHz$. Two horizontal lines illustrated by the circles in both figures represent the acoustic wave modes. Tumin (2007) denotes the spectrum on the left side as the fast acoustic wave spectrum and on the right side as the slow acoustic wave spectrum. These continuous spectra originate from streamwise wavenumbers α_r corresponding to the phase velocities $c_{ph,x} = 1 \pm 1/M$. The vertical line of circles in figure 5.2 indicates the continuous vorticity and entropy

	CASE 1	CASE 2	CASE 3	CASE 4	CASE 5	CASE 6	CASE 7
Forcing properties:							
$A_{[1,0]}$	0.0	0.0	0.0	1.0E−4	0.0	0.0	0.0
$A_{[1,\pm1]}$	3.0E−3	3.0E−3	3.0E−3	3.0E−3	3.0E−3	3.0E−3	3.0E−3
Domain size:							
x_L $[m]$	0.948	1.087	1.145	1.145	1.050	1.065	1.050
y_H $[m]$	0.026	0.029	0.030	0.030	0.059	0.032	0.030
Grid size and FFT's:							
n_x	585	2001	2757	2757	2101	2601	2101
n_y	130	200	301	301	391	401	301
K	64	101	128	128	128	128	128
n_z	127	201	255	255	255	255	513
$n_x \times n_y \times n_z$	9.7E6	80.4E6	211.6E6	211.6E6	200.9E6	266E6	323.8E6
symmetry in z?	yes	yes	yes	yes	yes	yes	no
Grid resolution (at outflow):							
points per $\lambda_x^{[1,1]}$	~ 170	~ 350	~ 440	~ 440	~ 440	~ 550	~ 440

Table 5.1: Main simulation parameters that differ between all cases. Note that the notation $[h, k]$ is used in order to identify a particular wave according to its frequency h and its spanwise wavenumber k. h denotes multiples of the fundamental forcing frequency $f^* = 6.36kHz$ and k multiples of the smallest spanwise wavenumber $\beta^* = 211.52m^{-1}$; M=3.0, T^*_∞=103.6K, flat plate.

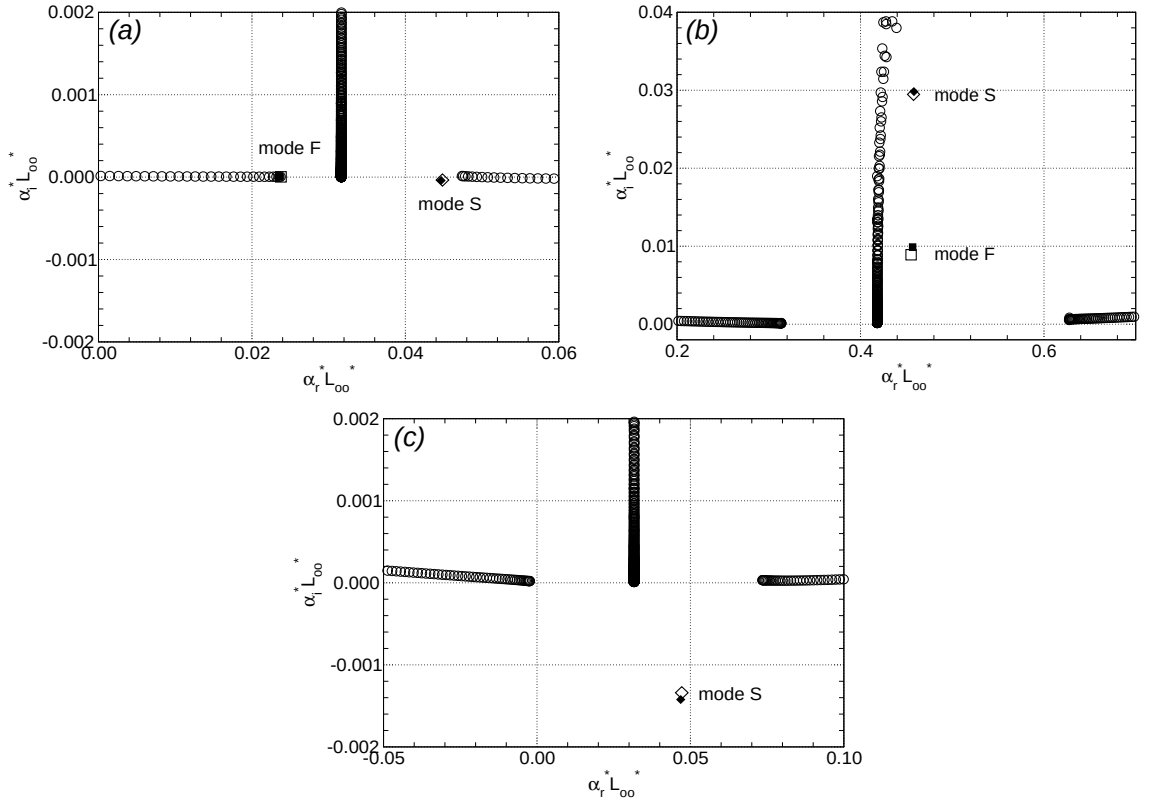

Figure 5.2: Eigenvalue spectra at $x^* = 0.5m$ ($R_x = 1044$). Results denoted by ($\circ$, $\Diamond$, $\Box$) are obtained from Tumin's solver (DNS solution as base flow) whereas results denoted by ($\blacklozenge$, $\blacksquare$) are from Mack's solver (similarity solution as base flow). (a) $f^* = 6.36kHz$ ($F = 3.0 \times 10^{-5}$, $\omega = 0.03132$), 2D ($\beta \sim 10^{-8}$), (b) $f^* = 84.78kHz$ ($F = 40.0 \times 10^{-5}$, $\omega = 0.4176$), 2D ($\beta \sim 10^{-8}$), (c) $f^* = 6.36kHz$ ($F = 3.0 \times 10^{-5}$, $\omega = 0.03132$), 3D ($\beta = 0.102$); M=3.0, T^*_∞=103.6K, flat plate.

spectra ($c_{ph,x} = 1$). Very close to the acoustic wave spectra are two discrete modes in figure 5.2a with mode F (fast mode) originating from the fast acoustic wave spectrum and mode S (slow mode) originating from the slow acoustic wave spectrum. These modes can be distinguished from the continuous spectrum by their eigenfunctions (see for example figure 5.4a).

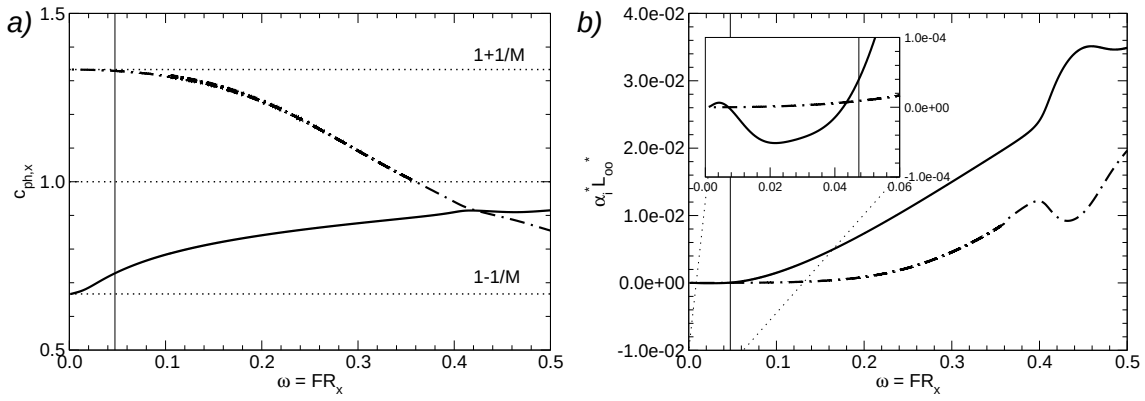

Figure 5.3: Stability behavior of both discrete eigenmodes (—: mode S, -.-: mode F) from the spectrum in figure 5.2 as a function of nondimensionalized angular frequency ω (equation 4.8) at $R_x = 1044$ ($\beta \sim 10^{-8}$): (a) phase velocity $c_{ph,x}$, (b) streamwise amplification rate α_i. Vertical solid line highlights the outflow boundary of the longest simulation (CASE 3) discussed in this chapter. The insert in (b) shows a close-up of the amplified region; M=3.0, T^*_∞=103.6K, flat plate.

By changing the disturbance frequency or the streamwise position for the calculation of the spectrum, both discrete modes are moving through the complex α plane as illustrated by figure 5.2b. Here, both modes are clearly separate from the continuous spectra and are strongly damped. A similar trend can be observed when the spanwise wavenumber is increased as shown in figure 5.2c. Tracking the eigenvalues of mode F and mode S with changing disturbance frequency at a constant streamwise position R_x leads to figure 5.3. This figure shows the phase velocities of both modes as a function of the nondimensionalized frequency ω. Note that ω is dependent on the streamwise position and on the frequency (equation 4.8). The phase velocities, however, are only a function of ω meaning that changing the frequency for a con-

stant streamwise position will result in the same phase-velocity plot as changing the streamwise position for a constant frequency (Ma & Zhong, 2003). This is not true for the amplification rate α_i in figure 5.3b.

The phase velocity and amplification rate development in figure 5.3 show some of the typical behavior as discussed for Mach 3.8 in section 4.4. For $\omega \to 0$, mode S synchronizes with the slow acoustic wave spectrum and mode F synchronizes with the fast acoustic wave spectrum represented by the horizontal lines at $c_{ph,x} = 1-1/M$ and $c_{ph,x} = 1+1/M$, respectively. For increasing frequency ω, the phase velocity of mode S increases and for mode F decreases until they coincide at a specific frequency ($\omega \simeq 0.44$ in figure 5.3a). This coincidence between the phase velocities of both discrete modes results from a "synchronism" mechanism (Fedorov & Khokhlov, 2002, and section 4.4), which can amplify one of the discrete modes. For higher Mach numbers, usually mode S is amplified leading to the so-called second-mode unstable region. In figure 5.3b, the "synchronism" amplifies mode F. The increase in amplification for this mode is however too small in order to generate a second-mode unstable region as can be expected when figure 4.9 is considered.

The "synchronism" mechanism between both discrete modes has also a strong effect on their eigenfunctions. Figure 5.4 demonstrates how the eigenfunctions of both modes change with increasing frequency ω. When the phase velocities of both modes coincide, their eigenfunction profiles become very similar as apparent in the pressure disturbance in figure 5.4c.

For the setup of the simulations discussed in this chapter, it is important to know whether the synchronization point at $\omega \simeq 0.44$ is located within the computational domain since this mechanism could have an influence on the nonlinear stages of transition and therefore, on oblique breakdown. In contrast to higher Mach numbers, the synchronization point at Mach 3 is at a large value for the frequency ω. Figure 5.5, for example, illustrates how this value decreases with increasing Mach number. Note that this figure does not show the exact location where the phase velocities of both

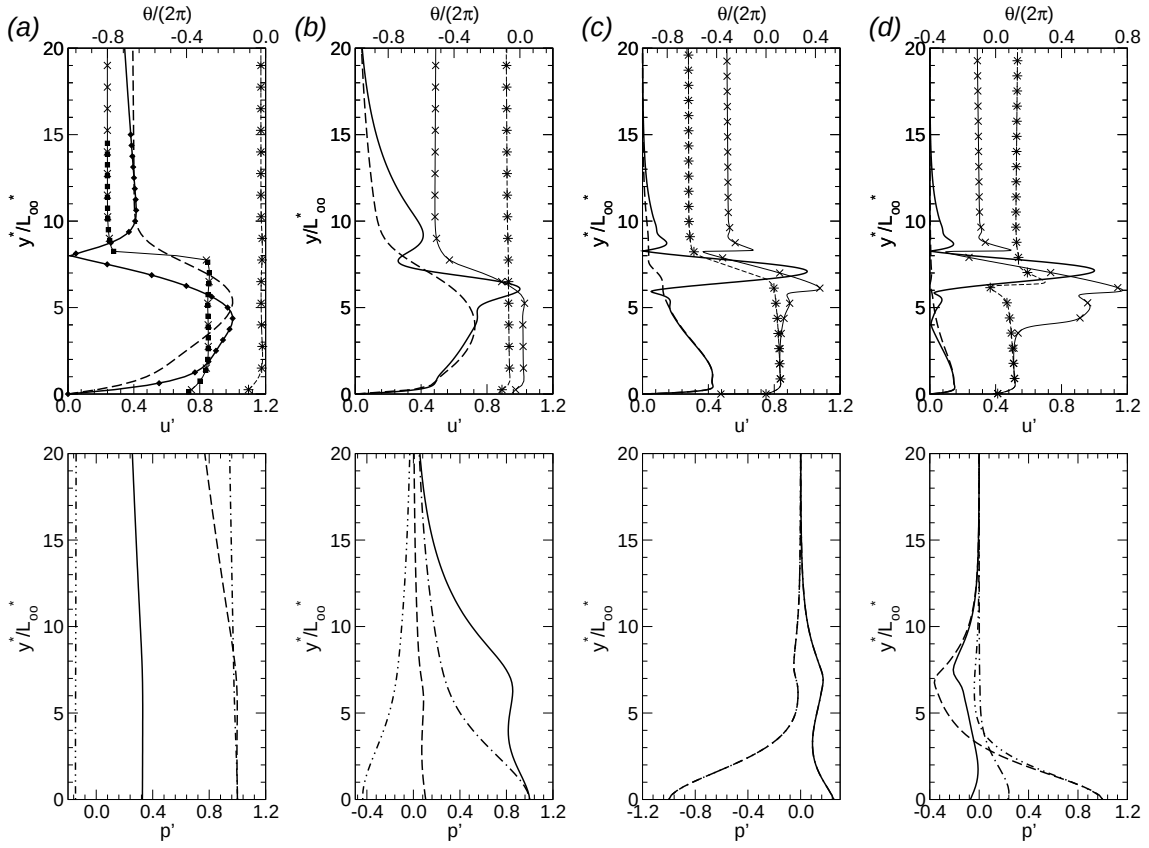

Figure 5.4: Eigenfunctions of the u-velocity and the pressure disturbance for $R_x = 1044$ and $\beta \sim 10^{-8}$ from Tumin's solver (Tumin, 2007, 2008): *u-velocity*: amplitude (—) and phase (-×-) of mode S, amplitude (- -) and phase (-∗-) of mode F, *pressure*: real part (—) and imaginary part (- -) of mode S, real part (-.-) and imaginary part (-..-) of mode F. (a) $\omega = 0.03132$ ($f^* = 6.36kHz$, $F = 3.0 \times 10^{-5}$), results denoted by (♦, ■) are from Mack's solver (Mack, 1965) for comparison, (b) $\omega = 0.2088$ ($f^* = 42,39kHz$, $F = 20.0 \times 10^{-5}$), (c) $\omega = 0.4176$ ($f^* = 84.78kHz$, $F = 40.0 \times 10^{-5}$), (d) $\omega = 0.4915$ ($f^* = 100.00kHz$, $F = 47.08 \times 10^{-5}$); M=3.0, T^*_∞=103.6K, flat plate.

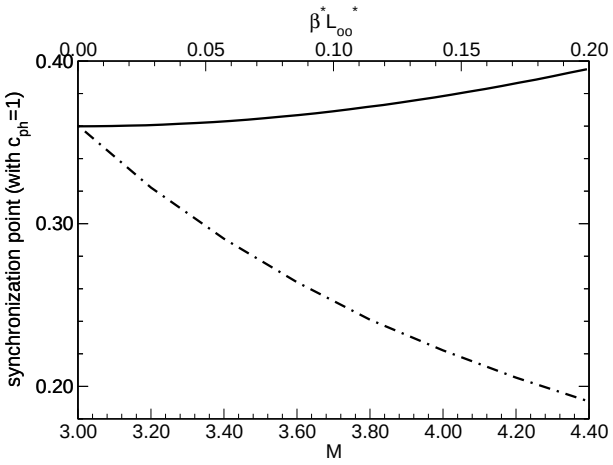

Figure 5.5: Angular frequency ω at the synchronization point of mode F with the entropy and vorticity continuous spectrum as a function of Mach number M for two-dimensional disturbances (-.-) and as a function of spanwise wavenumber β (—) for Mach 3 at $R_x = 1044$. According to Mack (1969), a second-mode unstable region exists for $M \gtrsim 3.8$ (see figure 4.9). M=3.0, T^*_∞=103.6K, flat plate.

discrete modes coincides, but rather the location where mode F coalesces with the entropy and vorticity continuous spectrum ($c_{ph,x} = 1$ in figure 5.3a). The vertical lines in figure 5.3 indicate the position of the outflow for the simulation with the largest streamwise domain size (CASE 3). Clearly, the synchronization point is far downstream of the outflow and hence, will not play any role in the transition process for a flat-plate boundary layer at Mach 3. With increasing spanwise wavenumber this point even moves to higher values of ω (figure 5.5). Thus, it can be concluded that oblique breakdown, initiated for a spanwise wavenumber of $\beta^* = 211.52m^{-1}$ and a frequency of $f^* = 6.36kHz$ ($F = 3.0 \times 10^{-5}$), is only caused by mode S and thus, mode F is not of interest for the interpretation of the simulation data in the following sections.

For the rest of this section, the emphasis is on the stability behavior of mode S and whether the simulations can correctly reproduce its downstream behavior. The amplification rate of mode S is strongly dependent on the spanwise wavenumber. As demonstrated in figure 5.2c, mode S moves to higher streamwise amplification

rates and becomes separated from the slow acoustic wave spectrum for a spanwise wavenumber of $\beta^* = 211.52m^{-1}$ and a frequency $f^* = 6.36kHz$ when compared to the spectrum for two-dimensional disturbances with the same disturbance frequency in figure 5.2a. Note, also the origins of the slow and fast acoustic spectra move to different streamwise wavenumbers since their corresponding streamwise phase velocities change according to $c_{ph,x} = 1 \pm 1/(M\cos(\psi))$ with ψ being the wave angle (section 4.3).

Tracking the eigenvalues of mode S in figure 5.2 yields the stability diagrams in figure 5.6. In figure 5.6, contour levels of the amplification rate α_i are plotted for different disturbance frequencies and at different streamwise positions for a given spanwise wavenumber. The solid lines constitute the stability diagram for the spanwise wavenumber $\beta^* \simeq 211.52m^{-1}$ and the dashed line in figure 5.6a indicates the neutral curve for the corresponding two-dimensional instability waves. Figure 5.6b shows contour levels of α_i at constant local Reynolds number $R_x = 750$ and figure 5.6c for a constant frequency $f^* = 6.36kHz$. The computational domains for CASE 1, 2, 3 & 4 are also included in these figures. Instability waves (modes S) with the frequency of interest for the DNS ($6.36kHz$) are amplified throughout the computational domain as can be seen in figure 5.6c. Therefore, linear stability suggests that, for the flow conditions and the domain of interest, transition may be triggered by these oblique instability waves.

In addition to the oblique breakdown simulations, two DNS with a considerably decreased forcing amplitude were performed such that the linear regime is maintained throughout the computational domain. These simulations facilitate a comparison of the DNS results to LST (with parallel flow assumption) and to PSE. The PSE calculations were conducted using NOLOT (Hein *et al.*, 1996) during a stay at the Institut für Aerodynamik und Gasdynamik (IAG) in Stuttgart, Germany. Figure 5.7 compares the complex streamwise wavenumber α from the DNS to LST and PSE for a constant frequency of 3.0×10^{-5} ($6.36kHz$) at two different spanwise wavenumbers

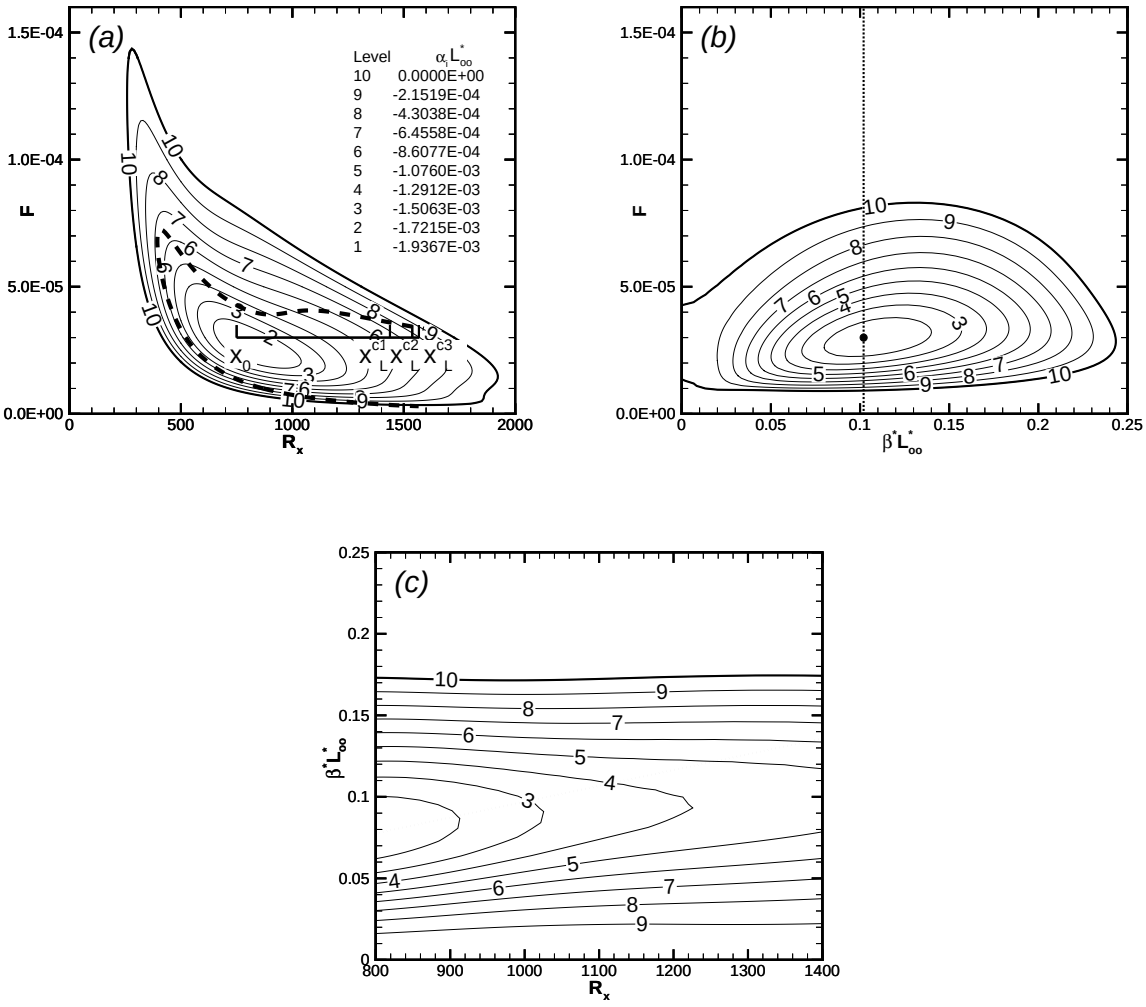

Figure 5.6: Contours of constant amplification rate α_i obtained from LST (Mack's solver): (a) for constant spanwise wavenumber $\beta^* \simeq 211.52m^{-1}$, dashed line indicates neutral curve for two-dimensional waves, (b) for constant local Reynolds number $R_x = 750$ ($x^* = x_0^* \simeq 0.258m$) (c) for constant frequency $f^* = 6.36kHz$ ($F = 3.0 \times 10^{-5}$). Horizontal solid line in (a) and dotted lines in (b) and (c) indicate computational setup; M=3.0, T^*_∞=103.6K, flat plate.

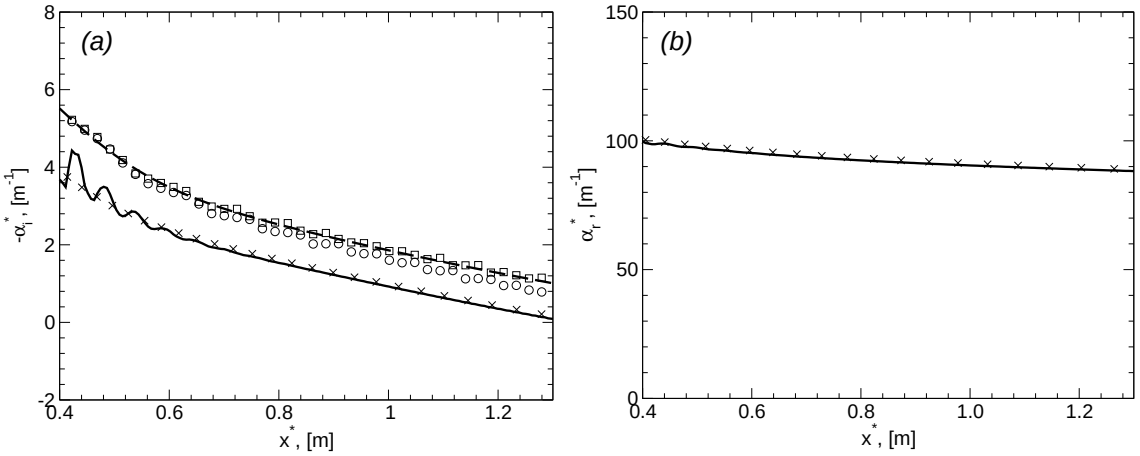

Figure 5.7: Streamwise development of the complex streamwise wavenumber α obtained by LST using Mack's solver ($\times$: $\beta^* = 211.52m^{-1}$), PSE using NOLOT (- -: $\beta^* = 196.2m^{-1}$) and DNS (low forcing amplitude) for $F = 3.0 \times 10^{-5}$ ($6.36kHz$): (a) streamwise amplification rate α_i, (b) streamwise wavenumber α_r. For the DNS, α is calculated using two different criteria, the wall pressure (—: $\beta^* = 211.52m^{-1}$) and the maximum in the wall-normal amplitude distribution of the u-velocity disturbance ($\circ$: $\beta^* = 211.52m^{-1}$, $\square$: $\beta^* = 196.2m^{-1}$); M=3.0, T^*_∞=103.6K, flat plate.

($\beta^* = 196.2m^{-1}$ and $\beta^* = 211.52m^{-1}$). From the DNS data, the complex streamwise wavenumber was calculated (see equation 4.4). The streamwise amplification rate α_i in figure 5.7a is computed using either the wall-pressure disturbance amplitude (Eissler & Bestek, 1996; Ma & Zhong, 2003) or the maximum in the wall-normal amplitude distribution for the u-velocity. As observed in previous investigations for supersonic flat-plate boundary layers (Thumm *et al.*, 1989; Eissler & Bestek, 1996; Husmeier *et al.*, 2005), the amplification rate based on the latter predicts stronger growth rates than LST and this behavior was attributed to non-parallel effects by the authors. The excellent agreement between DNS and PSE results in figure 5.7a further corroborates this statement. Note that PSE is a nonlocal stability analysis, which accounts for non-parallel effects. When using the wall-pressure disturbance for the computation of the amplification rate α_i, the agreement between LST and DNS data improves significantly. This improvement confirms that different criteria are differently affected by non-parallel effects as already observed for incompressible

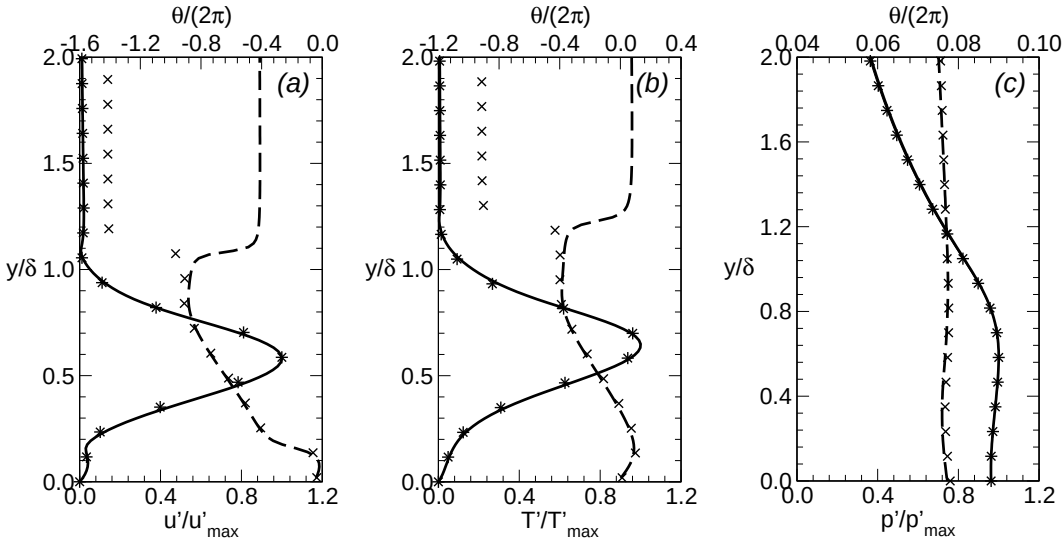

Figure 5.8: Comparison of wall-normal amplitude and phase distribution obtained from DNS (reduced forcing amplitude) with the eigenfunctions from LST for (a) u-velocity disturbance, (b) temperature disturbance and (c) pressure disturbance at $x^* = 0.5m$ and $\beta^* = 211.52m^{-1}$. DNS: (—) amplitude distribution, (- -) phase distribution; Tumin's stability solver (DNS profiles as base flow): ($\star$) amplitude distribution, ($\times$) phase distribution; M=3.0, T^*_∞=103.6K, flat plate.

boundary layers by Fasel & Konzelmann (1990).

The last figure for this section (figure 5.8) compares the wall-normal amplitude and phase distribution for the velocity, temperature and pressure from the DNS to results obtained by LST using Tumin's stability solver at $x^* = 0.5m$, $\beta^* = 211.52m^{-1}$ and $f^* = 6.36kHz$. The amplitude distributions from both, linear theory and DNS, are normalized by their respective maximum values within the boundary layer. The excellent agreement between all results substantiates that the linear eigenbehavior of the unstable mode in figure 5.2c is correctly reproduced in the DNS. Furthermore, the agreement with theory confirms that the disturbances introduced via the blowing and suction slot indeed initiate a pair of oblique instability waves and that these waves are dominant for the present setup.

5.3 From the Weakly Nonlinear Regime to the Late Nonlinear Stages

In the last section, it was demonstrated that, for a laminar flat-plate boundary layer at Mach 3 with $T^*_\infty = 103.6K$ and an adiabatic wall, transition can only be initiated

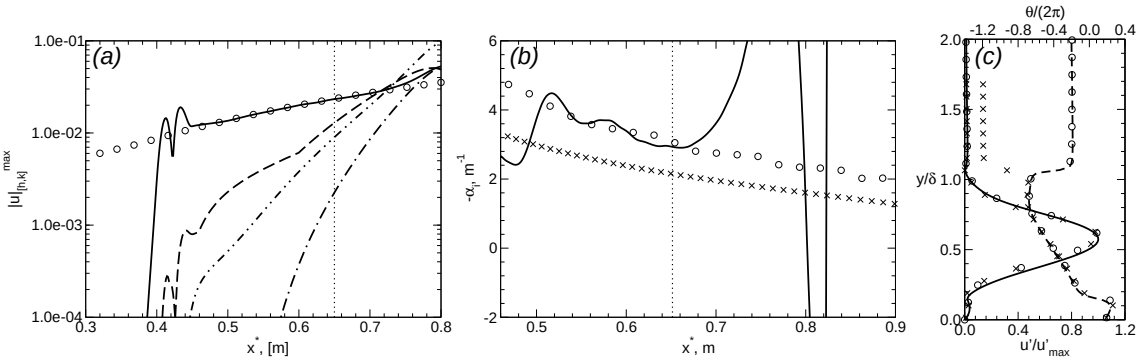

Figure 5.9: Initial disturbance development of the forced oblique instability wave with $f^* = 6.36kHz$ and $\beta^* = 211.52m^{-1}$ for cases with the high forcing amplitude (*lines*), a DNS with reduced forcing amplitude (∘) and for LST (×). (a) streamwise development of maximum u-velocity disturbance: (—) $[1, \pm 1]$ (- -) $[0, \pm 2]$ (-..) $[1, \pm 3]$ (-.-) $[0, \pm 4]$ (b) amplification rate α_i calculated using the maximum of the u-velocity disturbance as criterion, (b) wall-normal amplitude and phase distribution of the streamwise velocity perturbation at $x^* = 0.65m$ (vertical dotted line in a and b); M=3.0, T^*_∞=103.6K, flat plate.

by a slow mode (mode S). For a frequency of $6.36kHz$ and a spanwise wavenumber of $\beta^* = 211.52m$, this mode experiences strong streamwise amplification and therefore, was forced in all simulations discussed below. The forcing amplitude was chosen as 0.3% of the free-stream velocity U_∞ for all cases. In addition, the wall temperature, even in the fully turbulent region, was fixed to the adiabatic wall temperature of the laminar boundary layer, i.e. $T_w = T_{ad}$.

To verify whether the transition process initiated in the simulations indeed passes through all transition regimes typical for a low-disturbance environment, figure 5.9b compares the streamwise amplification rate α_i obtained from the maximum in the wall-normal amplitude distribution of the streamwise velocity disturbance from figure 5.9a (—) with results from LST (Mack's solver) and the DNS with a reduced

forcing amplitude from the previous section. The streamwise amplification rate in figure 5.9b for the cases with the high forcing amplitude is either contaminated by acoustic disturbances or by the fast mode (see also the validation case in Eissler & Bestek, 1996) since its streamwise distribution exhibits an oscillation. For the simulation with the reduced forcing amplitude from the previous section, these modulations are weaker since the disturbance slot was positioned farther upstream when compared to the location of the disturbance slot for all simulations with the higher forcing amplitude. As a consequence, the amplitude levels of the damped acoustic disturbances or the damped fast mode were very small in the region of interest for the simulation with the small forcing amplitude (see figure 5.7a). Note a receptivity study as in Tumin *et al.* (2007) would provide more detailed information about the absolute amplitude values of the fast mode and the continuous part of the spectrum right downstream of the disturbance slot. Such a study, however, is beyond the scope of this chapter. Nevertheless, figure 5.9 confirms that in all cases with a large forcing amplitude the linear regime is correctly reproduced by all DNS results presented in this chapter.

The early nonlinear stages of oblique breakdown are dominated by the nonlinear interaction of a wave–vortex triad composed by the forced oblique discrete modes $[1, \pm 1]$ and the steady vortex modes $[0, \pm 2]$ (Fasel *et al.*, 1993; Chang & Malik, 1994) as demonstrated by the streamwise development of the wall-normal maximum for the streamwise velocity in figure 5.9a. It is important to note that the $[0, \pm 2]$ modes are generated directly by the forced oblique modes $[1, \pm 1]$ and grow mainly through nonlinear interaction with these oblique modes (Chang & Malik, 1994). This is in contrast to the incompressible case where the growth of the $[0, \pm 2]$ modes is caused by transient growth (Berlin *et al.*, 1999).

The wave–vortex triad also clearly dominates the flow structures in the early nonlinear stages of oblique breakdown. Figure 5.10 shows contours of streamwise velocity disturbance at two different wall-normal positions between $x^* = 0.546m$ and

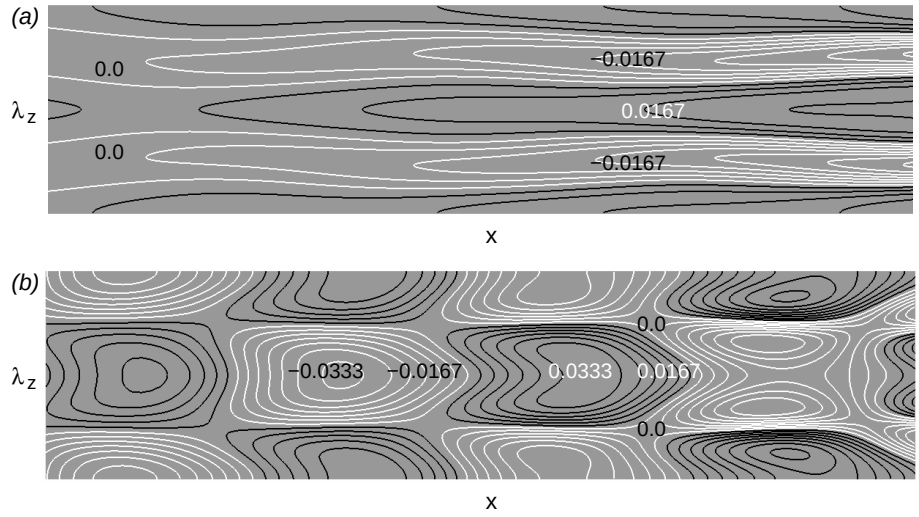

Figure 5.10: Contours of streamwise velocity disturbance illustrating flow structures in the early stage of oblique breakdown between $x^* = 0.546m$ and $x^* = 0.670m$: (a) close to the wall at $y^* \simeq 0.9mm$, (b) farther away at $y^* \simeq 2.3mm$; M=3.0, T^*_∞=103.6K, flat plate.

$x^* = 0.670m$. Close to the wall at $y^* \simeq 0.9mm$ longitudinal regions of low and high streamwise velocity develop and are amplified in streamwise direction while for higher wall-normal positions (at $y^* \simeq 2.3mm$) the typical wave pattern of two superimposed oblique instability waves is visible. Hence, the influence of the vortex modes $[0, \pm 2]$ on the contours of streamwise velocity disturbance is more significant closer to the wall while for higher wall-normal positions the initially forced wave pair $[1, \pm 1]$ is dominant. The wall-normal dependency of the flow structures in the contours of streamwise velocity disturbance is caused by the absolute amplitude level of modes $[0, \pm 2]$ and $[1, \pm 1]$ and their wall-normal amplitude distribution. The maximum in the wall-normal amplitude distributions of modes $[0, \pm 2]$ is closer to the wall than for modes $[1, \pm 1]$ (see also Mayer, 2004).

Instantaneous flow structures identified by the Q-criterion (Hunt *et al.*, 1988) in figure 5.11 confirm the structures shown in figure 5.10. Q is related to the second invariant of the velocity gradient tensor. Positive values of Q reveal flow regions where rotation dominates the flow field. Again, the flow structures in figure 5.11a

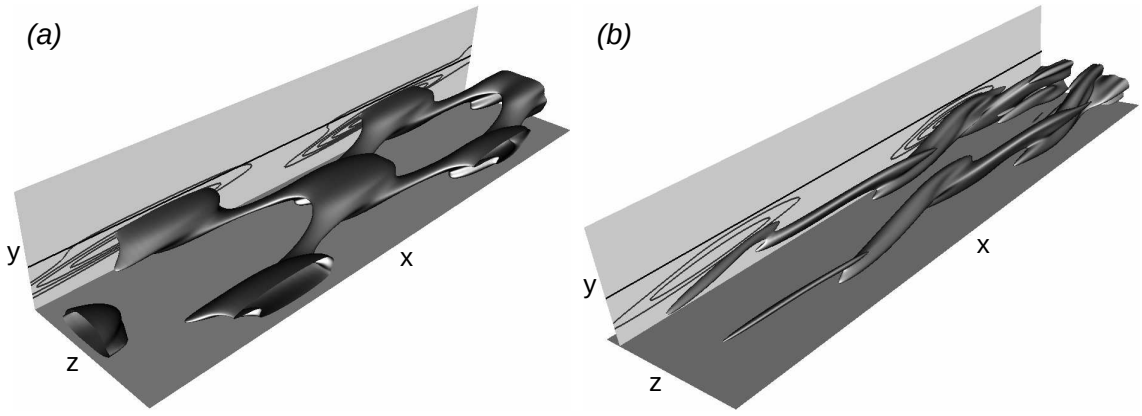

Figure 5.11: Flow structures identified by the Q-criterion: (a) $Q = 10$ between $x^* = 0.546m$ and $x^* = 0.670m$, (b) $Q = 100$ between $x^* = 0.670m$ and $x^* = 0.798m$. Also shown are the boundary layer thickness indicated by a solid black horizontal line and contours (between -0.1 and -0.001) of streamwise velocity disturbance for a constant spanwise position (in (a) at $z^* \simeq 0.0149m = \lambda_z/2$ and in (b) at $z^* \simeq 0.0114m \simeq 0.38\lambda_z$); M=3.0, T^*_∞=103.6K, flat plate.

represent the superposition of two oblique waves. The legs connecting the staggered maxima in figure 5.11a denote constant phase lines for both modes indicating that two waves (here $[1, \pm 1]$) with equal but opposite wave angle travel downstream. Also shown in figure 5.11 are the boundary layer thickness indicated by a solid black line and contours of streamwise velocity disturbance (between -0.1 and -0.001) for one constant spanwise position (in (a) at $z^* \simeq 0.0149m = \lambda_z/2$ and in (b) at $z^* \simeq 0.0114m \simeq 0.38\lambda_z$). When comparing the contours of streamwise velocity disturbance in figures 5.10 and 5.11, the Q-criterion predicts similar flow structures.

The characteristic disturbance amplitude curves for the early and late nonlinear stages of oblique breakdown is shown in figure 5.12. This figure demonstrates the streamwise development of the maximum u-velocity disturbance for various spanwise wavenumbers from CASE 1 and CASE 2 for modes that are directly created through nonlinear wave interactions of the wave–vortex triad. The nonlinear generation of higher-harmonic modes in time and spanwise direction follows a particular pattern as found for a Mach 1.6 boundary layer (Thumm, 1991; Fasel *et al.*, 1993): Modes

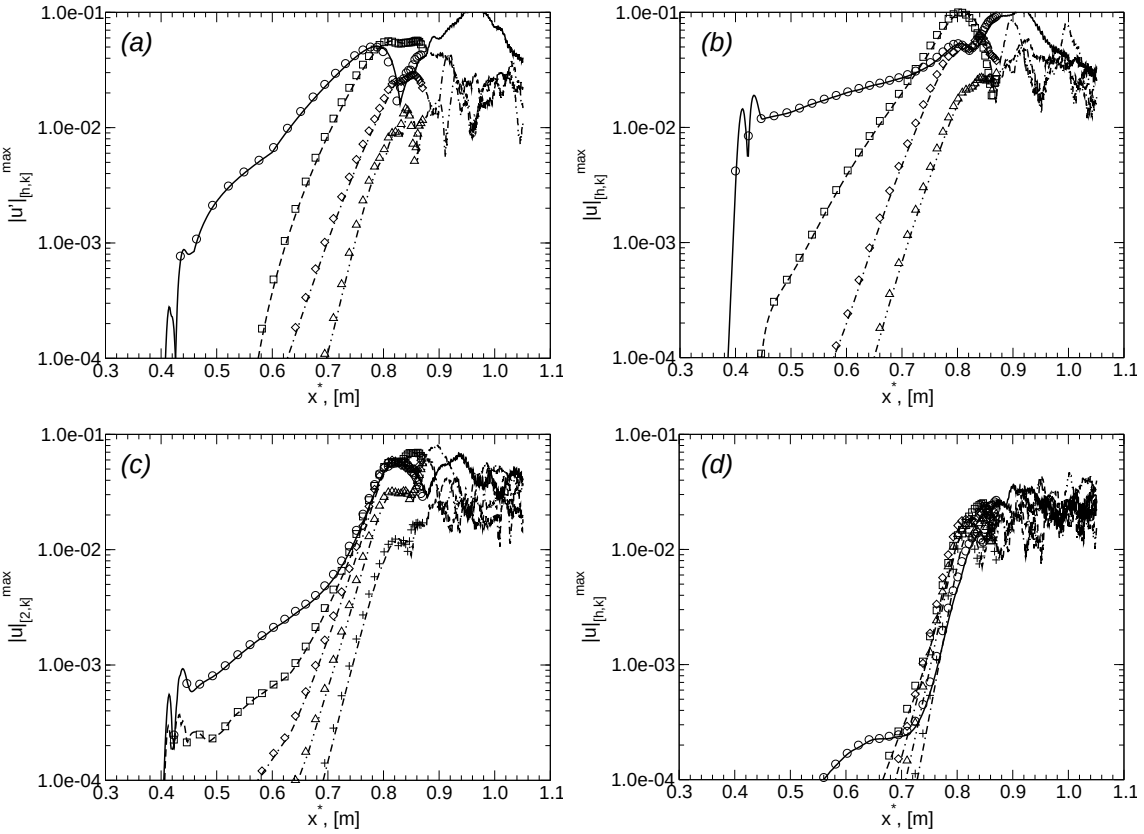

Figure 5.12: Streamwise development of the maximum u-velocity disturbance for different spanwise wavenumbers from CASE 1 (*symbols*) and CASE 2 (*lines*): (a) stationary modes ((∘, —): $[0, \pm 2]$, (□, - -): $[0, \pm 4]$, (◊, -.-): $[0, \pm 6]$, (△, -..): $[0, \pm 8]$), (b) modes with the fundamental frequency ((∘, —): $[1, \pm 1]$, (□, - -): $[1, \pm 3]$, (◊, -.-): $[1, \pm 5]$, (△, -..): $[1, \pm 7]$), (c) modes with the first higher-harmonic frequency ((∘, —): $[2, \pm 0]$, (□, - -): $[2, \pm 2]$, (◊, -.-): $[2, \pm 4]$, (△, -..): $[2, \pm 6]$, (+, -..): $[2, \pm 8]$), (d) modes with the second higher-harmonic frequency ((∘, —): $[3, \pm 1]$, (□, - -): $[3, \pm 3]$, (◊, -.-): $[3, \pm 5]$, (△, -..): $[3, \pm 7]$, (+, -..): $[3, \pm 9]$); M=3.0, T^*_∞=103.6K, flat plate.

with odd spanwise wavenumbers k are only generated for odd harmonic frequencies h, while modes with even spanwise wavenumbers are generated only for even frequencies h resulting in an even value for the sum of h and k.

The forced modes $[1, \pm 1]$ initially develop linearly up to about $x^* = 0.7m$ (see figure 5.9a and figure 5.12b). At roughly this position, modes $[0, \pm 2]$ and $[1, \pm 3]$ reach amplitude levels that are comparable to the levels of modes $[1, \pm 1]$. This event marks the end of the early nonlinear stage. A short distance downstream, at about $x^* = 0.8m$, higher harmonic modes reach amplitude levels of the same order of magnitude as the original wave–vortex triad and nonlinear saturation sets in. Note that the maximum of the u-velocity fluctuation does not directly display the energy transfer between separate modes. Nevertheless, it still reveals important events in the transition process of oblique breakdown, especially when modes that are not direct descendants of the wave–vortex triad are considered. These modes are generated by round-off errors due to the limited machine precision and their streamwise and spanwise amplitude development is displayed for the subharmonic frequency in figures 5.13a and 5.13b and for the fundamental frequency in figures 5.13c and 5.13d. Note that for other frequencies, which are not integer multiples of the fundamental frequency, similar amplitude distributions can be observed.

The streamwise amplitude development of all modes in figures 5.13a and 5.13c exhibit similar features as for the modes in figure 5.12. Up to about $x^* = 0.8m$, all modes experience streamwise amplitude growth while they start to saturate farther downstream. However, one major difference to figure 5.12 is a sudden increase in the streamwise growth rate for all modes at about $x^* = 0.9m$. The spanwise amplitude distributions in figures 5.13b and 5.13d broaden significantly in streamwise direction with the peak amplitude at small spanwise wavenumbers. An explanation for the initial growth up to $x^* = 0.8m$ of disturbances with frequencies that are no longer integer multiples of the fundamental frequency may be provided by the new resonance triads discussed in Mayer *et al.* (2009*a*) where all three instability waves possess a

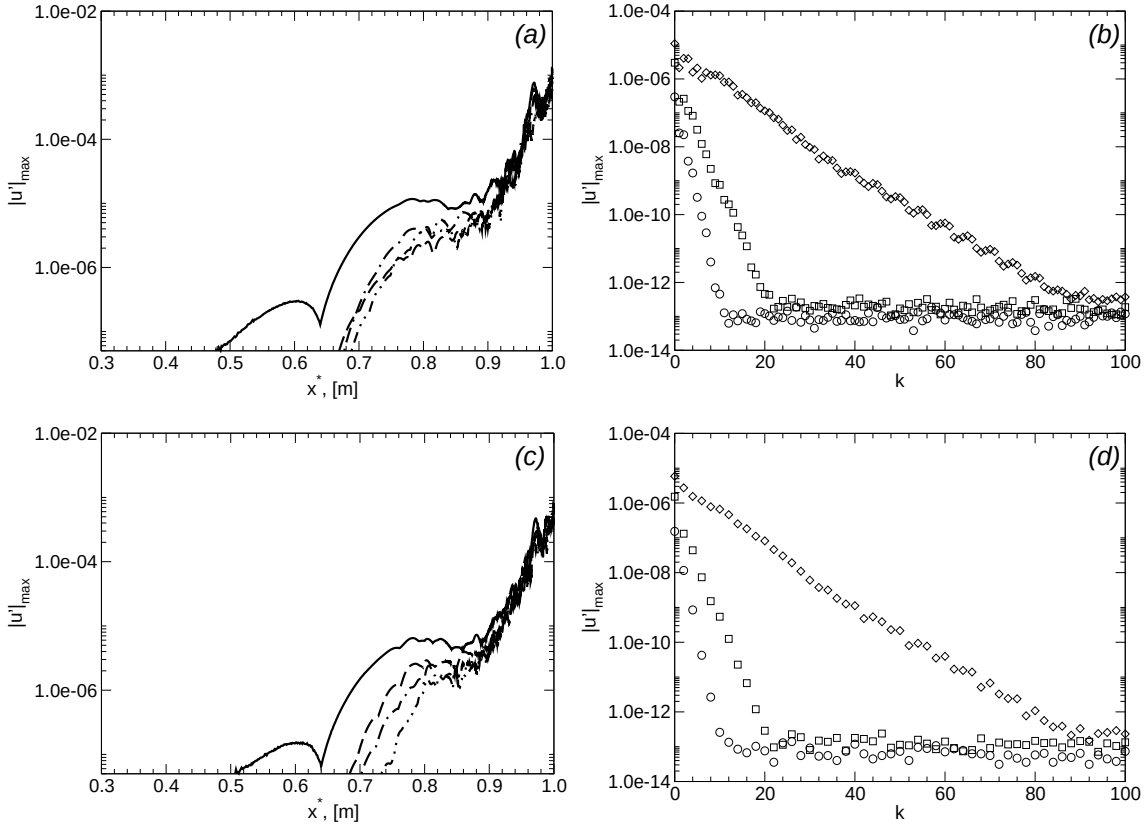

Figure 5.13: Streamwise (a,c) and spanwise (b,d) amplitude development for modes that are not directly generated by the wave–vortex triad ($[1, \pm 1]$ and $[0, \pm 2]$) from CASE 3: (a,b) subharmonic frequency, (c,d) fundamental frequency. For (a): (—) $[0.5, 0]$, (- -) $[0.5, \pm 1]$, (-.-) $[0.5, \pm 2]$, (-..) $[0.5, \pm 3]$. For (c): (—) $[1, 0]$, (- -) $[1, \pm 2]$, (-.-) $[1, \pm 4]$, (-..) $[1, \pm 6]$. For (b,d): ($\circ$) $x^* = 0.6m$, ($\square$) $x^* = 0.7m$, ($\diamond$) $x^* = 0.8m$; M=3.0, T^*_∞=103.6K, flat plate.

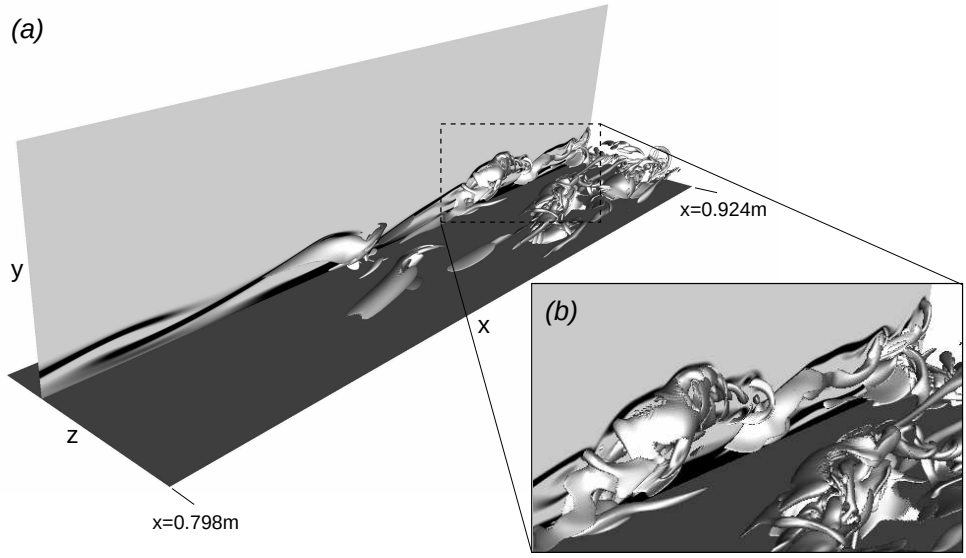

Figure 5.14: Flow structures identified by the Q-criterion for $Q = 15000$ (CASE 3) between $x^* = 0.798m$ and $x^* = 0.924m$. Also shown are contours of spanwise vorticity at $z^* \simeq -0.0087m$. (a) Entire three-dimensional view, (b) close-up of the breakdown region confirming that the Q-criterion predicts similar structures as illustrated by the spanwise vorticity; M=3.0, T^*_∞=103.6K, flat plate.

different disturbance frequency.

In the following figures, flow structures are shown for the region between $x^* = 0.798m$ and $x^* = 0.97m$ in order to highlight key features in the flow field that could be related to the sudden increase in the streamwise growth rate at about $x^* = 0.9m$ for all modes in figure 5.13 that are not directly generated by the wave–vortex triad. The instantaneous three-dimensional isosurfaces for $Q = 15000$ in figure 5.14a reveal that the longitudinal structures from figure 5.11 are lifted up from the wall and breakup into small-scale structures, which are similar to hairpin-like vortices. A close-up view of these flow structures is given in figure 5.14b. Contours of spanwise vorticity at $z^* \simeq -0.0087m$ in figure 5.14 further corroborate that the Q-criterion clearly identifies the relevant flow structures.

The contours of spanwise vorticity for various spanwise positions in figure 5.15 provide a detailed view of the breakup region and the downstream development of the

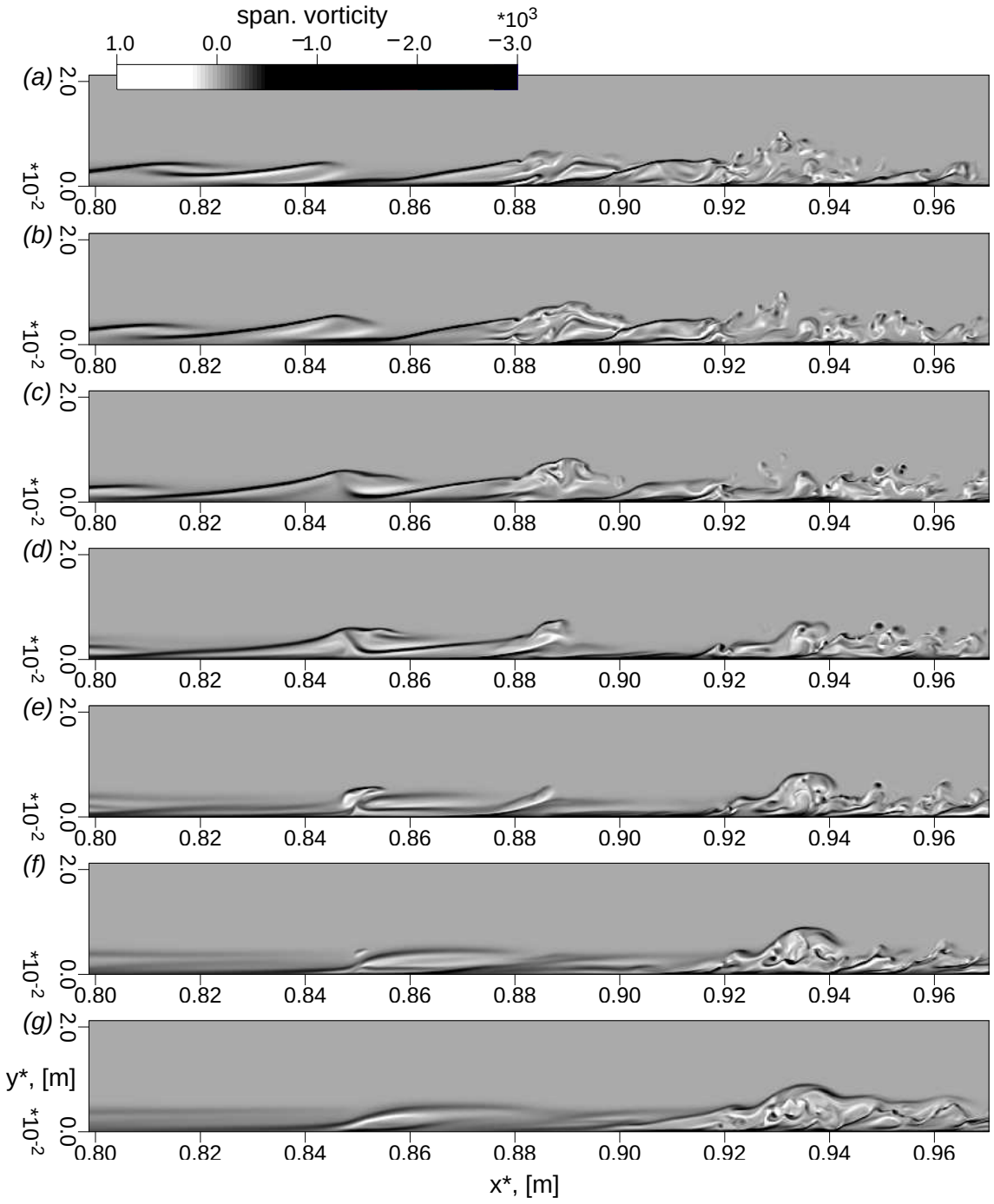

Figure 5.15: Contours of spanwise vorticity at various spanwise positions for one time instant from CASE 3: (a) $z^* \simeq -0.0087m$, (b) $z^* \simeq -0.0076m$, (c) $z^* \simeq -0.0064m$, (d) $z^* \simeq -0.0052m$, (e) $z^* \simeq -0.0041m$, (f) $z^* \simeq -0.0029m$, (g) $z^* \simeq -0.0017m$; M=3.0, T^*_∞=103.6K, flat plate.

small-scale structures. Note that the streamwise extent in this figure reaches farther downstream than in figure 5.14. The contour levels are chosen such that the contrast in these plots is significantly increased. Figure 5.15 reveals rope-like structures (region of high shear) that coincide with the position of the longitudinal structures from the previous figure. The tip of these rope-like structures is lifted up from the wall and again breaks up into smaller scales. This breakup is further exemplified by the temporal evolution of contours of spanwise vorticity at $z^* \simeq -0.0087m$ in figure 5.16. At this spanwise position, the breakup region extends from about $x^* \simeq 0.84m$ to $x^* \simeq 0.9m$. The sudden increase in streamwise amplification of all modes downstream of $x^* \simeq 0.9m$ in figure 5.13 seems to be linked to the breakup into smaller scales. Downstream of this position the entire flow is rapidly contaminated by small-scale structures as demonstrated in figure 5.17 and the final breakdown to turbulence is initiated.

The flow structures in figures 5.14 to 5.17 are symmetric with respect to the centerline of the plate. This is to be expected since these figures are obtained from CASE 3, in which symmetry is enforced by the computational setup. If the symmetry condition is not enforced as for CASE 7, the picture does not change as demonstrated by figure 5.18. This figure illustrates contours of streamwise velocity u of the first higher Fourier mode in spanwise direction from CASE 7 for the sine and cosine modes (equation 3.11), respectively. The minimum and maximum of the contour levels in figure 5.18a and b are different in order to emphasize the flow structures. The influence of asymmetric modes on oblique breakdown initiated by two oblique waves with exactly the same amplitude and phase is limited since these modes are only generated by the round-off error of the calculation. In CASE 3, the streamwise position of the final breakup into small-scale structures denotes the location where all modes with frequency unequal to integer multiples of the forcing frequency are strongly amplified. In CASE 7, a similar behavior can be observed. At exactly the same streamwise position (where the breakup into small-scale structures occurs)

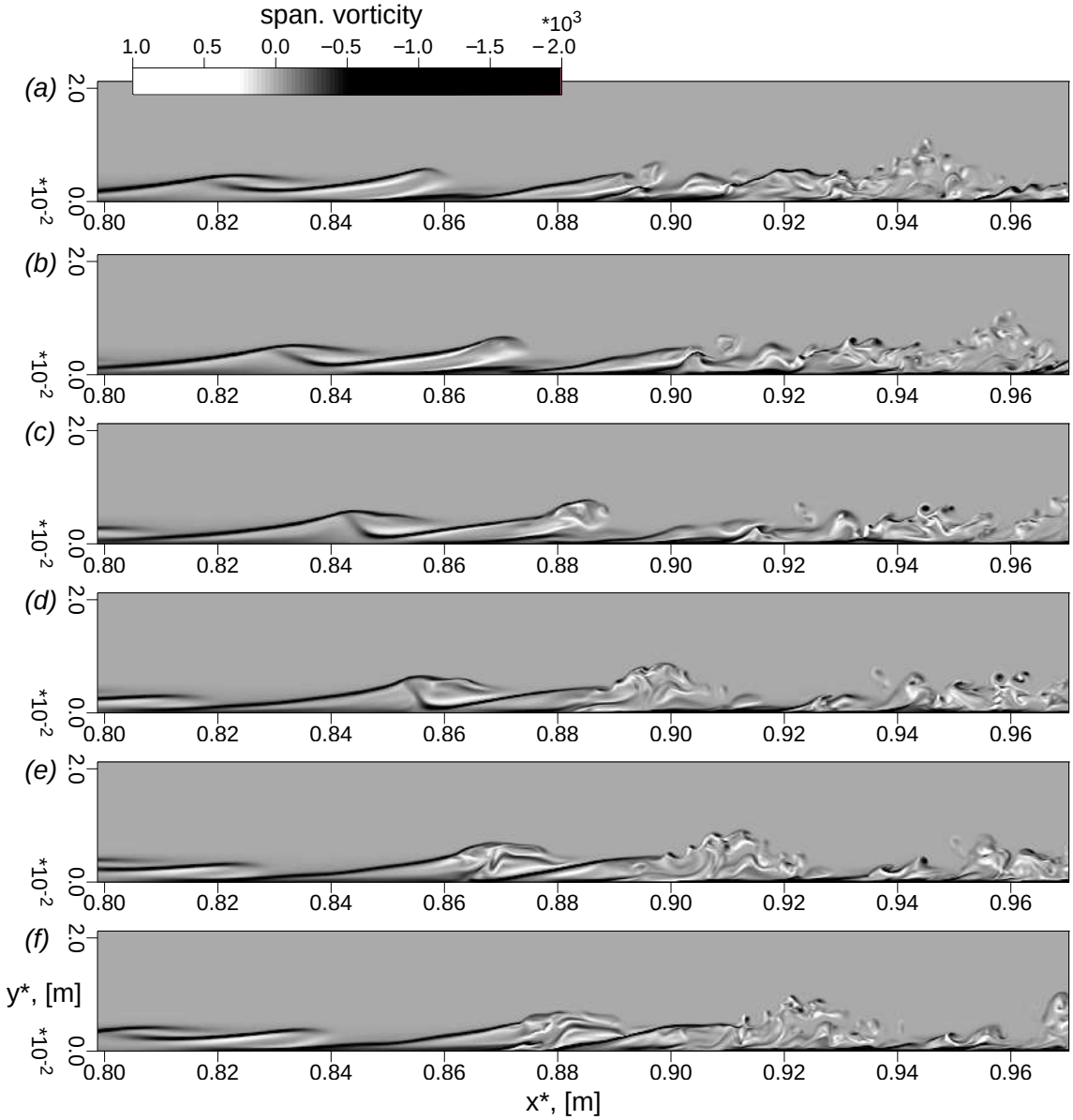

Figure 5.16: Contours of instantaneous spanwise vorticity at one particular spanwise positions ($z^* \simeq -0.0087m$) for various time instants highlighting the breakup into smaller structures (CASE 3): (a) $t = \frac{3}{20}T$, (b) $t = \frac{6}{20}T$, (c) $t = \frac{9}{20}T$, (d) $t = \frac{12}{20}T$, (e) $t = \frac{15}{20}T$, (f) $t = \frac{18}{20}T$; M=3.0, T^*_∞=103.6K, flat plate.

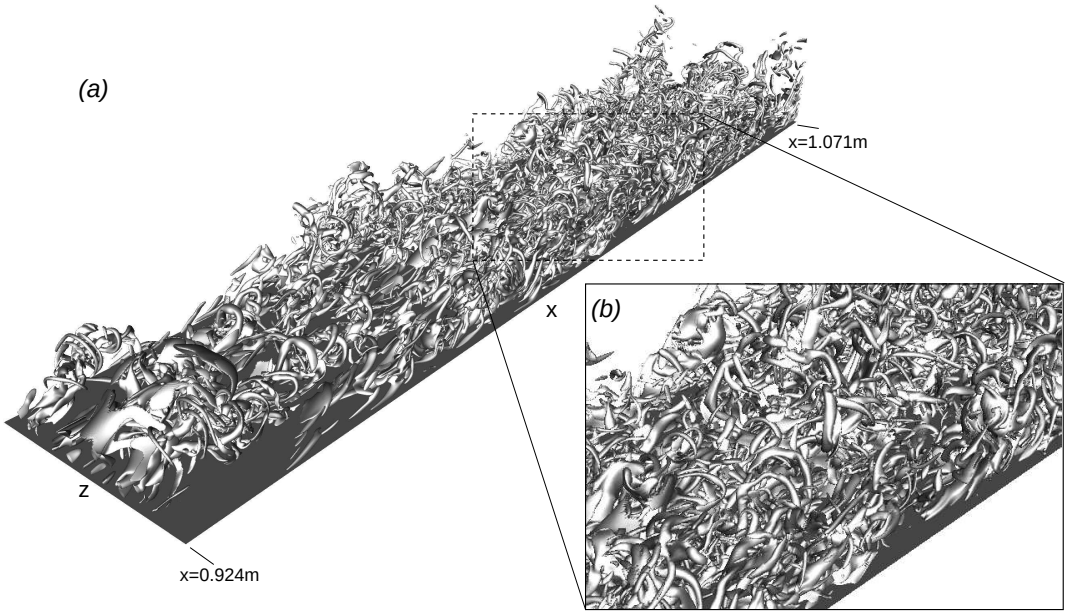

Figure 5.17: Flow structures identified by the Q-criterion for $Q = 20000$ (CASE 3) between $x^* = 0.924m$ and $x^* = 1.071m$. (a) Entire three-dimensional view, (b) close-up of the early turbulent region; M=3.0, T^*_∞=103.6K, flat plate.

the asymmetric modes also start to be amplified as illustrated by figure 5.18a. The amplitude values of the streamwise velocity for the sine mode in figure 5.18a provide a measure for the magnitude of asymmetry in CASE 7. For the u-velocity, this mode is set to zero in CASE 3. Since the contour levels for the sine mode in figure 5.18a are more than 10 orders of magnitude smaller than the contour levels for the cosine mode, CASE 7 remains symmetric even after the breakup into small-scale structures. This is true over the entire domain length of CASE 3. It is however visible that the asymmetric modes are strongly amplified in downstream direction and will eventually reach high amplitude values.

5.4 Final Breakdown to Turbulence

In the previous section a detailed description of the breakup into small-scale structures for oblique breakdown was given and therefore, the different transition regimes from

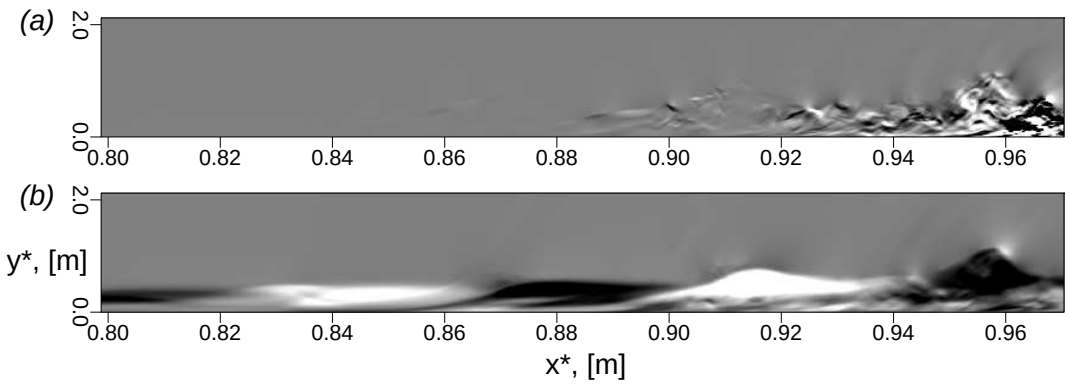

Figure 5.18: Contours of instantaneous streamwise velocity u obtained from CASE 7 for the first higher Fourier mode in spanwise direction: (a) sine mode, contour levels from −1.0E−12 to 1.0E−12, (b) cosine mode, contour levels from −0.1 to 0.1; M=3.0, T^*_∞=103.6K, flat plate.

the early nonlinear regime to the breakdown were discussed. Figure 5.17 clearly illustrates that the breakup is accompanied by a rapid spreading of small-scale structures over the entire flow field downstream of a particular streamwise position ($x^* \simeq 0.9m$). Close to this position, the time signal however is still periodic although the flow field exhibits features of a turbulent boundary layer (small-scale structures). Thus, the final breakdown to turbulence did not occur yet. All cases listed in table 5.1, except of CASE 1, which has a very small streamwise domain extent, lead to the same results for the early and late nonlinear transition stages. The different grid resolutions and domain heights of the different cases mainly affect the final breakdown to turbulence. Therefore, this section will also assess what resolution is necessary in order to obtain a converged solution for the entire transition process of oblique breakdown at Mach 3.

In order to check when periodicity breaks down in the simulations, figure 5.19 compares the streamwise development of the wall-normal maximum for the u-velocity disturbance obtained from a Fourier transformation of the time-dependent flow data for CASE 2, CASE 3 and CASE 4. Note that CASE 4 only differs from CASE 3 in the forcing input. In CASE 4, additionally to the oblique instability waves with frequency $f^* = 6.36kHz$, a two-dimensional instability wave with one order of mag-

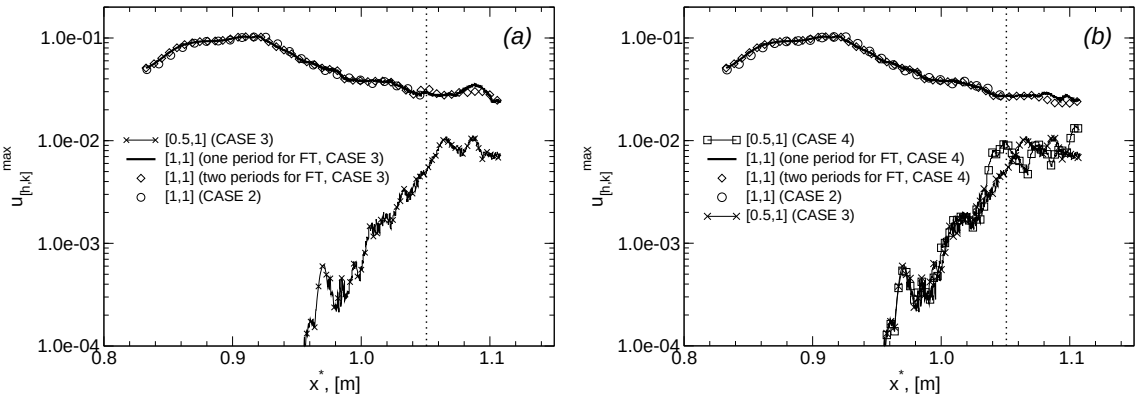

Figure 5.19: Streamwise development of the wall-normal maximum of the streamwise velocity u for selected Fourier modes: (a) CASE 3, (b) CASE 4; the dotted line marks the end of the domain of CASE 2. The notation $[h, k]$ is used to identify a particular wave according to its frequency h and its spanwise wavenumber k. h denotes multiples of the fundamental frequency and k multiples of the smallest spanwise wavenumber; M=3.0, T^*_∞=103.6K, flat plate.

nitude smaller amplitude but the same forcing frequency as the oblique waves was also introduced. Forcing a two-dimensional instability wave initializes waves that can otherwise not be directly generated through the nonlinear wave interactions of the forced wave pair and, therefore, are generated only at the level of round-off errors. As a consequence of the additional perturbation, the disturbance spectrum should be broader earlier for this simulation.

For figure 5.19, two different Fourier transforms have been performed using either a time signal with the length of one period of the forcing frequency or two periods. If the flow field remained periodic in time, the Fourier-modes from both time signals would develop identically in the streamwise direction. As can be seen in figure 5.19, this is not the case for CASE 3 & 4. Just downstream of the end of the domain of the simulation CASE 2 ($x^* = 1.05$), highlighted by a dotted vertical line in figure 5.19, the streamwise amplitude distribution of the initially forced mode $[1, \pm 1]$ differs for the two time signals. Hence, CASE 3 and CASE 4 clearly lose their periodicity close to the end of the computational domain. This is further emphasized by figure 5.20,

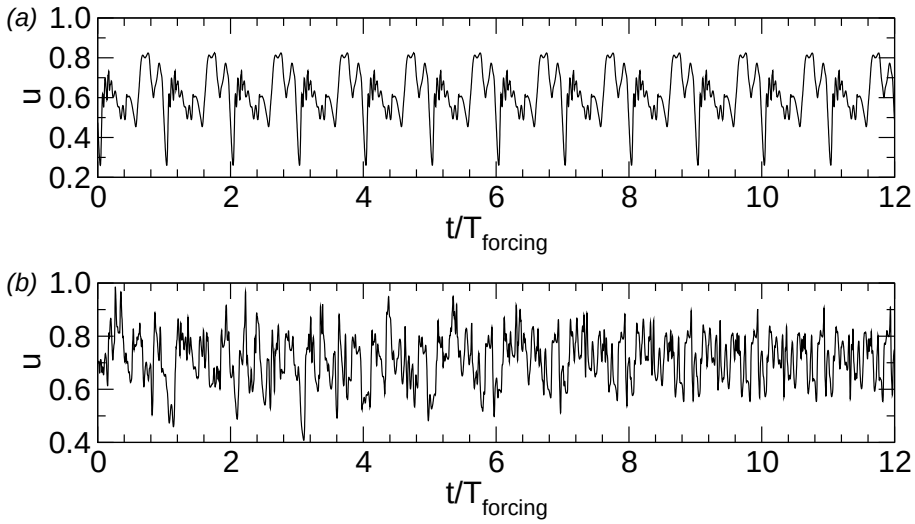

Figure 5.20: Temporal evolution of the streamwise velocity at $y = 2.15mm$ ($y^+ \simeq 50$) for CASE 3: (a) $x^* = 0.942m$, (b) $x^* = 1.104$; M=3.0, T^*_∞=103.6K, flat plate.

which shows the original time-signal (12 forcing periods) for CASE 3 for two different streamwise positions at the wall-normal location $y = 2.15mm$ ($y^+ \simeq 50$). At $x^* = 0.942m$ (figure 5.20a), the signal is still strongly periodic whereas farther downstream, at $x^* = 1.104$ (figure 5.20b), a more random behavior becomes apparent. As figure 5.13 from the previous section, figures 5.19 and 5.20b illustrate the growth of disturbances with frequencies that are no longer integer multiples of the fundamental forcing frequency. In figure 5.19, for example, the subharmonic disturbances reach amplitude levels comparable to the initially forced waves $[1, \pm 1]$ in proximity to the end of the computational domain.

With the loss of the periodicity in CASE 3, one missing piece of evidence for the final breakdown to turbulence is found. Another piece of evidence is the streamwise decay of the skin-friction coefficient after the strong increase caused by transition. Figure 5.21a demonstrates that CASE 3 indeed experiences a decay in skin friction. All disturbances with a non-harmonic frequency (with respect to the original forcing frequency) start to saturate right after the skin-friction coefficient c_f drops in figure 5.21a. This is shown for the subharmonic frequency in figure 5.19. Hence, the

decay of the skin-friction coefficient is most likely linked to the loss of periodicity. Once, the periodicity in time is lost and the peak in skin friction is surpassed downstream of $x^* = 1.05$, the transition process ends and the flow has reached a turbulent state.

The skin-friction coefficient in figure 5.21a is calculated from

$$c_f = \frac{2\overline{\mu}\frac{\partial \overline{u}}{\partial y}|_{y=0}}{Re}\,, \tag{5.1}$$

where the Reynolds number Re is based on an arbitrary reference length L^* and the flow quantities in the free stream. Note that symbols with an overline $\overline{\phi}$ represent the Reynolds-average, i.e. time and spanwise averaged flow quantities, throughout this chapter

$$\overline{\phi} = \frac{1}{\lambda_z}\frac{1}{\Delta t}\int_0^{\lambda_z}\int_{t_0}^{t_0+\Delta t}\phi\,(t,z)\,dtdz\,. \tag{5.2}$$

Furthermore, fluctuations about the mean of a Reynolds-averaged quantity $\overline{\phi}$ are denoted by ϕ' and fluctuations about the mean of a Favre-averaged quantity $\overline{\rho\phi}/\overline{\rho}$ are denoted by ϕ''. Note that in some figures the interval for the time average is indicated by the number of forcing periods $T_{forcing}$.

Also included in figure 5.21a are different values of the skin-friction coefficient from other numerical simulations published in the literature for turbulent supersonic flow (Guarini *et al.*, 2000; Maeder *et al.*, 2001) and a theoretical correlation for the fully-developed turbulent regime given by White (1991). This correlation is valid for non-adiabatic wall boundary conditions and has the following form

$$c_f \sim \frac{0.455}{\left(S\ln\left[\frac{0.06}{S}Re_{xe}\frac{\mu_e}{\mu_w}\sqrt{\frac{T_e}{T_w}}\right]\right)^2}\,, \tag{5.3}$$

where subscript e refers to edge conditions and subscript w to wall conditions. The factor S can be obtained from

$$S = \frac{\left(\frac{\overline{T}_{aw}}{T_e} - 1\right)^{\frac{1}{2}}}{\arcsin(A) + \arcsin(B)}\,, \tag{5.4}$$

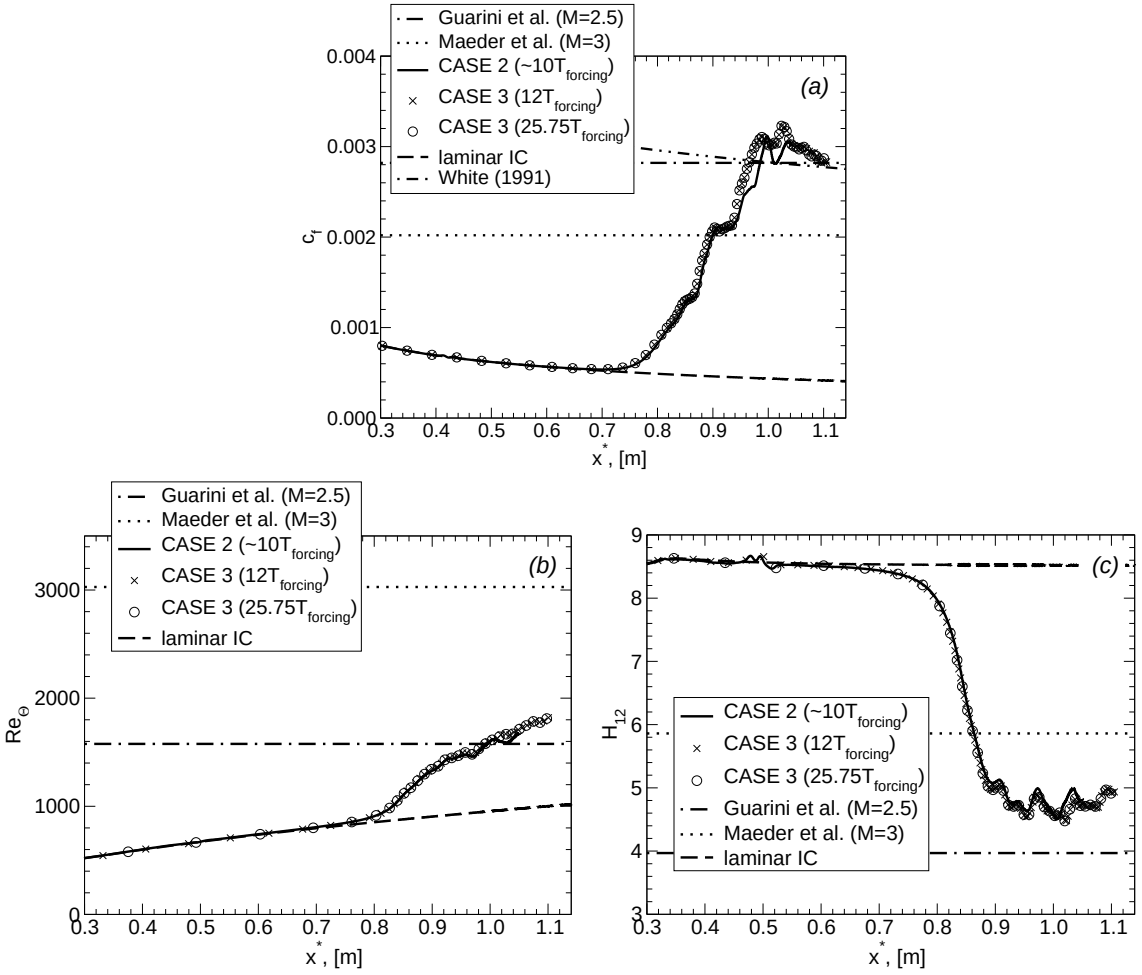

Figure 5.21: Streamwise development of selected mean-flow properties from CASE 2 and CASE 3 in comparison to different values published in the literature for turbulent supersonic flow (Guarini *et al.*, 2000; Maeder *et al.*, 2001) and theoretical models (White, 1991): (a) skin-friction coefficient c_f, (b) Reynolds number based on momentum thickness Θ, (c) shape factor H_{12}. Note that for CASE 2 and 3 the interval for the time average is indicated by the number of forcing periods $T_{forcing}$; M=3.0, T^*_∞=103.6K, flat plate.

with A and B defined as

$$A = \frac{2a^2 - b}{\sqrt{b^2 + 4a^2}} \quad \text{and} \quad B = \frac{b}{\sqrt{b^2 + 4a^2}}\,, \tag{5.5}$$

where a and b are given by

$$a = \sqrt{\frac{\gamma - 1}{2} M_e^2 \frac{T_e}{\overline{T}_w}} \quad \text{and} \quad b = \left(\frac{\overline{T}_{aw}}{\overline{T}_w} - 1 \right), \tag{5.6}$$

respectively. Note that $\overline{T}_{aw}$ denotes the adiabatic wall-temperature for a turbulent boundary layer at the same flow conditions. Since this value is not known, it has to be estimated using the turbulent recovery factor (White, 1991; Roy & Blottner, 2006)

$$r_{turb} \sim (Pr)^{\frac{1}{3}} \sim 0.9\,. \tag{5.7}$$

The streamwise development of the skin friction coefficient for CASE 3 in figure 5.21a approaches the theoretical estimate given by White's correlation (White, 1991) towards the end of the computational domain. Moreover, the value computed by Guarini *et al.* (2000) using a Temporal Direct Numerical Simulation (TDNS) for a Mach 2.5 turbulent boundary layer is close to the DNS results. TDNS, with some assumptions, computes an approximation of a fully-developed turbulent boundary layer at a given streamwise location in the limit of a vanishing extent of the streamwise domain size. The data can then be used for comparison of skin-friction coefficients with data obtained via a full spatial DNS, if a location can be found where the Reynolds number based on the momentum thickness Re_θ and the shape factor H_{12} for both simulations are in close enough agreement. Figures 5.21b and 5.21c confirm that the TDNS can be used as a rough estimate. These figures show the streamwise development of the Reynolds number based on the momentum thickness Re_θ and the shape-factor H_{12} for CASE 2, CASE 3 and TDNS reference data from the literature. Both the Reynolds number and the shape-factor are close to values from Guarini *et al.* (2000) at the end of the computational domain, but do not exactly match. A better agreement cannot be expected since both simulations differ in the

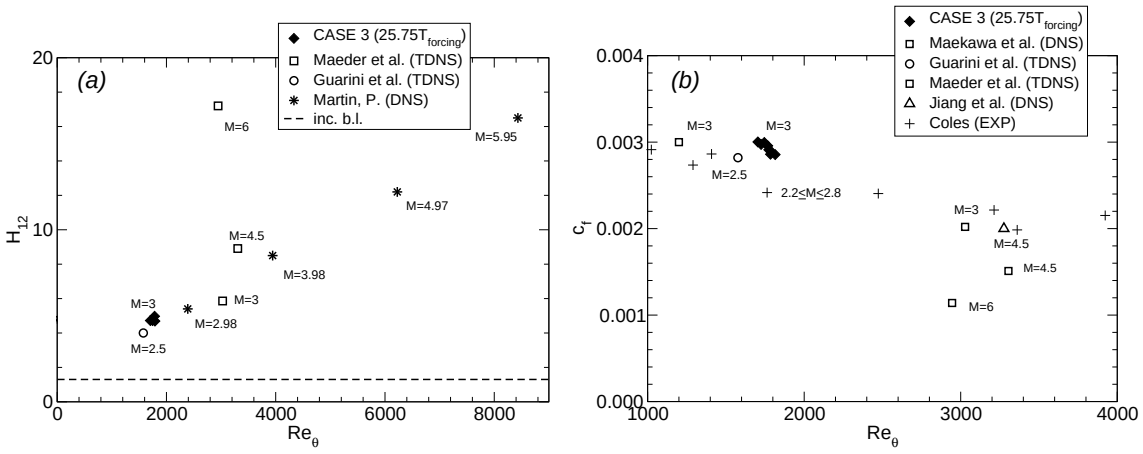

Figure 5.22: Comparison of selected mean-flow properties from CASE 3 starting from $x^* = 1.047m$ to values published in literature for supersonic and hypersonic turbulent flat-plate boundary layers (Guarini *et al.*, 2000; Maeder *et al.*, 2001; Jiang *et al.*, 2006; Maekawa *et al.*, 2007; Martin, 2007; Coles, 1954): (a) shape factor H_{12} vs. Re_θ, (b) skin friction coefficient c_f vs. Re_θ; M=3.0, T^*_∞=103.6K, flat plate.

flow speed and in the wall-temperature boundary condition. The TDNS of Maeder *et al.* (2001), although at the same Mach number, approximates the flow with a considerably higher momentum thickness, i.e. a location farther downstream than in simulations presented in this chapter. Consequently, their data should deliver a lower skin-friction coefficient, which is indeed the case.

Figure 5.22 shows the skin-friction coefficient and the shape factor as a function of the Reynolds number based on momentum thickness for the region downstream of the peak in skin friction of CASE 3 together with several additional temporal and full spatial DNS and experiments of supersonic and hypersonic turbulent boundary layers published in the literature (Guarini *et al.*, 2000; Maeder *et al.*, 2001; Jiang *et al.*, 2006; Maekawa *et al.*, 2007; Martin, 2007; Coles, 1954). When compared to these results, CASE 3 can be regarded as reaching realistic values for mean-flow properties of a wall-cooled supersonic turbulent boundary layer close to the end of the computational domain. In order to compare computed values of the skin-friction coefficient for different Mach numbers and wall-temperature boundary conditions, it is common

(Pirozzoli *et al.*, 2004) to transform the compressible skin-friction coefficient c_f at a given local Reynolds number Re_x into an incompressible reference value $c_{f,i}$ at an incompressible reference Reynolds number $Re_{x,i}$ using the van Driest II transformation (White, 1991; Roy & Blottner, 2006). These transformations are as follows:

$$c_{f,i} = F_c c_f \quad \text{and} \quad Re_{x,i} = F_x Re_x \,, \tag{5.8}$$

where F_c represents the skin-friction transformation function and F_x denotes the Reynolds number transformation function. Both functions can be computed from equation (5.4) according to

$$F_c = S^2 \quad \text{and} \quad F_x = \frac{\mu_e}{\mu_w} F_c^{-1} \,. \tag{5.9}$$

The transformed skin friction for CASE 3 is shown in figure 5.23a. For reference purposes, the friction coefficient for a Blasius boundary layer

$$c_{f,i}^B = \frac{0.664}{\sqrt{Re_{x,i}}} \,, \tag{5.10}$$

and a correlation by White (1991) for the estimate of the friction coefficient of an incompressible turbulent boundary layer

$$c_{f,i}^W = \frac{0.455}{\ln^2 (0.06 Re_{x,i})} \tag{5.11}$$

are also included in this figure. As seen in figure 5.23a, results for CASE 3 are approaching the theoretical curve of equation (5.11) for an incompressible turbulent boundary layer. This gives further confidence that CASE 3 transitioned to a turbulent state.

To assess whether CASE 3 indeed predicts a representative streamwise skin-friction distribution independent of grid and time-averaging influences, and typical for an oblique breakdown transition scenario at Mach 3, the skin-friction coefficients of the other simulation cases (CASE 1-2, 4-6) listed in table 5.1 are compared to CASE 3 in figure 5.23b. Clearly, all simulations, except for CASE 2, experience

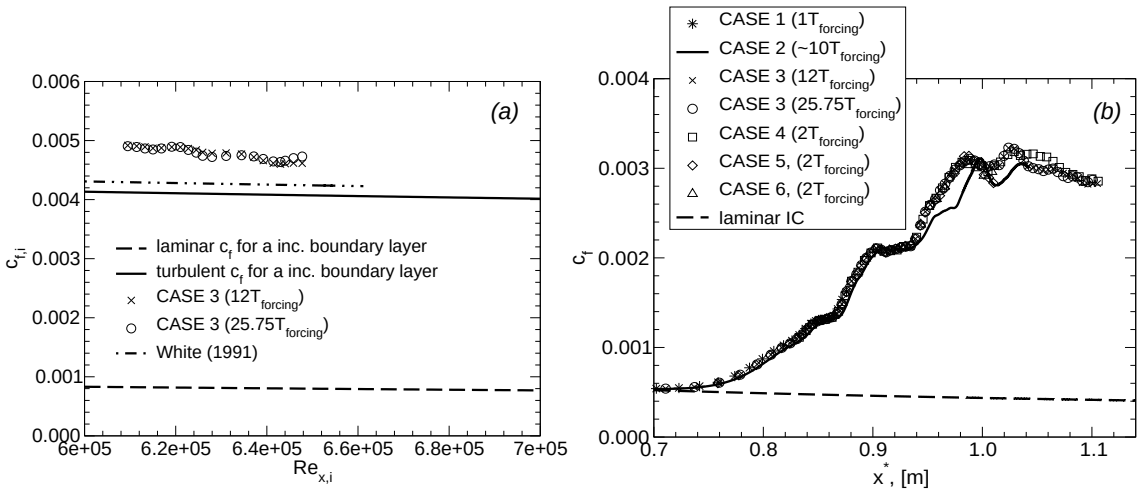

Figure 5.23: Streamwise development of skin-friction coefficient for all simulations: (a) van Driest II transformed in order to compare with incompressible, turbulent skin-friction predictions. Simulation data is taken downstream of the streamwise position $x^* = 1.047m$ ($Re_{x,i} = 609479$) where the skin-friction coefficient starts to decay, (b) for the later stages of transition in order to assess the influence of different computational grid configurations and the length of the interval for time-averaging; M=3.0, T^*_∞=103.6K, flat plate.

identical streamwise growth in skin friction up to the maximal value. Moreover, in the transitional regime the skin friction is also independent of the interval length used for the time-averaging (denoted by the number of forcing periods $T_{forcing}$) since here, the flow is still periodic. Hence, the plateaus at approximately $x^* \simeq 0.86m$ and $x^* \simeq 0.9m$ and the valley at $x^* \simeq 1.0m$ seem to be a characteristic feature of oblique breakdown initiated by only two oblique instability waves. It is very important to note that these features correlate with the findings from the previous section. The first plateau at about $x^* \simeq 0.86m$ is close to the streamwise position where the first breakup occurs in figure 5.16 while the second plateau marks the second breakup followed by the generation of hairpin-like vortices. The latter plateau also coincides with streamwise location where all disturbance modes that are not direct descendants of the wave–vortex triad start significantly to grow in figure 5.13. An imprint of the valley at $x^* \simeq 1.0m$ for the skin-friction coefficient in figure 5.23b can also be found

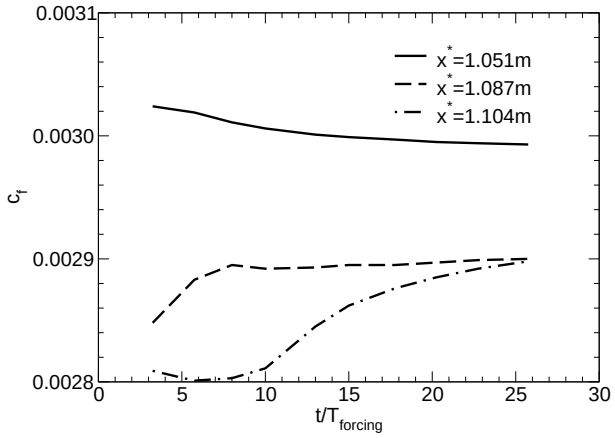

Figure 5.24: Skin-friction coefficient for CASE 3 as a function of interval length for time-averaging indicated by the number of forcing periods $T_{forcing}$ at three different streamwise positions; M=3.0, T^*_∞=103.6K, flat plate.

in the streamwise distribution of these modes in figure 5.13.

The skin-friction distributions in figure 5.23b deviate downstream of the maximum at about $x^* \simeq 1.04m$ for CASE 3 and CASE 4. Although in CASE 4, an additional two-dimensional mode ($[1, 0]$) with the fundamental frequency is forced in order to broaden the disturbance spectrum, final breakdown to turbulence is not enhanced when compared to CASE 3. For CASE 4, the skin-friction coefficient in figure 5.23b is computed from time-averaged data with only two forcing periods as interval length for the averaging. Figure 5.24 demonstrates that a larger interval length is required for time-averaging in order to obtain convergence for CASE 3. For the first two streamwise positions reported in figure 5.24 convergence is achieved within 25 forcing cycles while for the last position ($x^* = 1.104m$) CASE 3 could be longer averaged.

An overview of the grid resolution in near-wall units utilized for CASE 3 and 4 and some main characteristic quantities as maximum in skin-friction coefficient are listed in table 5.2. When compared to other numerical simulations in the literature, CASE 3 and 4 have sufficient resolution close to the outflow boundary for a supersonic turbulent boundary layer. (Note that CASE 5 has an even higher domain height as CASE 3 and CASE 6 has a finer grid resolution in wall-normal and streamwise

	Pirozzoli *et al.*	Guarini *et al.*	CASE 3	Maeder *et al.*	Jiang *et al.*
M	2.25	2.5	3	3	4.5
$Re_\Theta\|_{max}$	4250	1600	1829	3000	3300
$C_f\|_{max}$	0.003	0.003	0.0032	0.002	0.002
$(x_L - x_0)^+$	19099	2269	20363	549	9584
y_H^+	3479	875	698	1176	1290
z_W^+	1671	1134	341	314	192
Δx^+	14.50	8.86	3.32	2.96	6.00
Δy_w^+	1.05	0.48	0.49	–	0.63
Δz^+	6.56	5.91	1.35	1.74	1.50

Table 5.2: Grid resolution and domain size from CASE 3 (inner length scale taken at $x^* = 1.087m$) compared to other simulations in the literature; M=3.0, T_∞^*=103.6K, flat plate.

direction than CASE 3.)

For CASE 3, wall-normal distributions of the Reynolds-averaged streamwise velocity ($\overline{U}$), Favre averaged streamwise velocity ($\overline{\rho U}/\overline{\rho}$) and Reynolds-averaged temperature ($\overline{T}$) are presented in figure 5.25 using outer scaling at different streamwise positions. For comparison, one profile from CASE 2 is also plotted in figures 5.25b and 5.25c at position $x^* \simeq 0.996m$. This profile matches the corresponding profile from CASE 3 perfectly in the outer part of the boundary layer. Close to the wall, however, differences become apparent, which is to be expected since the skin-friction coefficient does also not agree for both cases in figure 5.23b. The difference in the mean-flow profiles between CASE 2 and CASE 3 in figure 5.25 is most likely caused by the different wall-normal stretching in both simulations since the grid resolution at the wall is exactly the same for both simulations. Note that it is common in simulations of turbulent boundary layers to use strong grid stretching in wall-normal direction. For the simulations presented here, such a grid stretching is not applicable because it would be unlikely, if not impossible, to compute a correct disturbance eigenfunction in the linear regime of the transition process. Since the goal of the present investigation is to compute through the entire transition process, a more conservative approach to

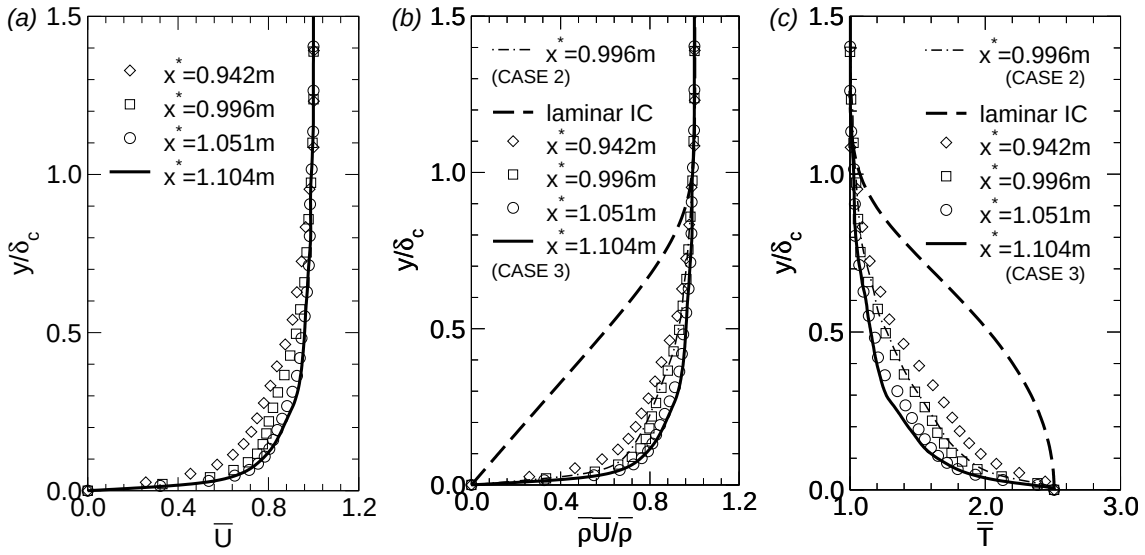

Figure 5.25: Wall-normal distribution of several mean-flow quantities from CASE 2 and CASE 3 at different streamwise positions: (a) Reynolds-averaged streamwise velocity, (b) Favre-averaged streamwise velocity, (c) Reynolds-averaged temperature. δ_c denotes boundary layer thickness obtained from the Reynolds-averaged streamwise velocity $\overline{U}$; M=3.0, T^*_∞=103.6K, flat plate.

wall-normal stretching had to be employed.

With increasing downstream position, all mean-flow profiles in figure 5.25 become fuller when compared to the laminar initial condition denoted by IC. For the last two downstream locations $x^* \simeq 1.051m$ and $x^* \simeq 1.104m$, the change in the profile shape is not as pronounced as for the upstream positions. These two positions are downstream of the maximum in skin friction in figure 5.23b (see also table 5.3) and therefore, the mean-flow profiles should be close to turbulent boundary layer profiles. For convenience, table 5.3 summarizes selected mean-flow properties at all downstream locations utilized for figure 5.25 and succeeding figures.

Using the van Driest transformation

$$U_c = \int_0^{\bar{u}} \sqrt{\frac{\overline{T}_w}{\overline{T}}} du \tag{5.12}$$

for the mean-flow profiles in figure 5.25 allows for comparison with incompressible similarity profiles of turbulent boundary layers. The van Driest transformed stream-

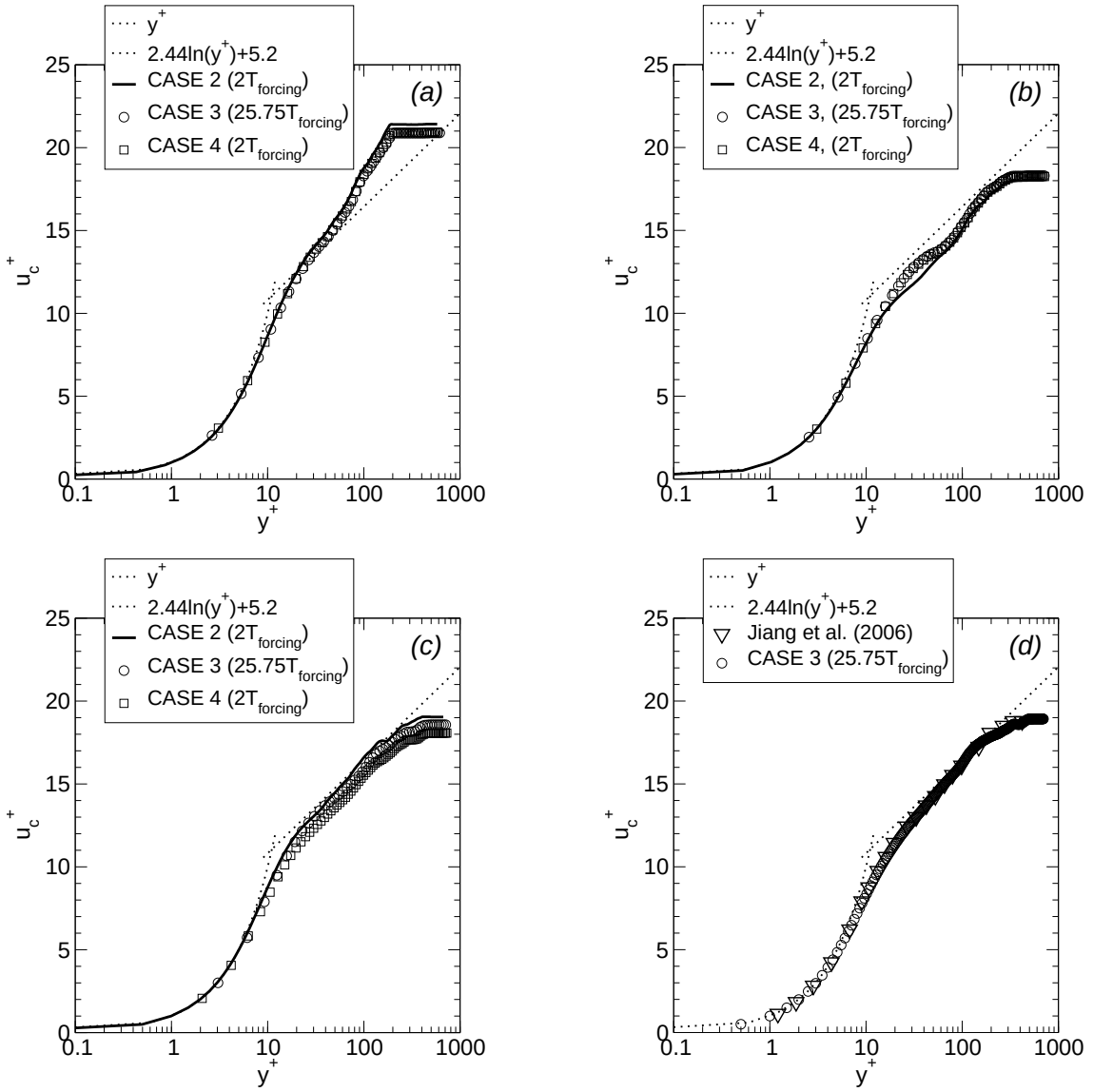

Figure 5.26: Van Driest transformed streamwise velocity normalized by wall-shear velocity for different streamwise positions: (a) $x^* = 0.942m$, (b) $x^* = 0.996m$, (c) $x^* = 1.05m$, (d) $x^* = 1.104m$; for clarity only every fourth point is shown, except for (d) where every point is plotted to illustrate the near-wall resolution; M=3.0, T^*_∞=103.6K, flat plate.

	upstream of c_f^{max}		downstream of c_f^{max}		
x^* $[m]$	0.942	0.996	1.051	1.087	1.104
Re_x	2.041E6	2.165E6	2.292E6	2.378E6	2.416E6
$Re_{x,i}$	–	–	6.125E5	6.383E6	6.481E6
Re_θ	1458	1594	1714	1774	1827
H_{12}	4.704	4.606	4.721	4.961	4.935
c_f	2.317E−3	3.055E−3	2.993E−3	2.900E−3	2.898E−3
$c_{f,i}$	–	–	4.878E−3	4.710E−3	4.730E−3
δ^* $[mm]$	9.074	11.477	15.680	17.714	18.402

Table 5.3: Summary of mean-flow properties at five different streamwise locations for CASE 3; M=3.0, T^*_∞=103.6K, flat plate.

wise velocity in near-wall units is plotted in figure 5.26 for different streamwise positions. Also included is the theoretical similarity profile for incompressible turbulent boundary layers, which follows the form

$$U_c^+ = \frac{1}{\kappa} \ln\left(y^+\right) + C\,. \tag{5.13}$$

For the von Kármán constant κ, typically a value of $\kappa = 0.41$ is used while the constant C is about 5.2 (Roy & Blottner, 2006).

Downstream of the peak in skin friction c_f, the van Driest transformed velocity approaches the theoretical curves in figures 5.26c and 5.26d. This behavior is also reported by Jiang *et al.* (2006), who investigated transition initiated by oblique breakdown in a flat-plate boundary layer at Mach 4.5. Their van Driest transformed mean velocity profile is compared to CASE 3 in figure 5.26d. Note that in figure 5.26 not every point in wall-normal direction is plotted except for figure 5.26d, which therefore illustrates the near wall resolution of CASE 3 ($\Delta y^+ \simeq 0.49$).

The first part of this section corroborated that oblique breakdown can lead to a turbulent flow by collecting two important pieces of evidence: (1) The loss of periodicity of the flow and (2) a clear decay of the skin friction in downstream direction after reaching a peak value at about $x^* \simeq 1.05m$. So far, however, only mean-flow data for CASE 3 were discussed and compared to theoretical predictions for

supersonic turbulent flows and results from other numerical simulations. The focus of the following discussion is on turbulent statistics that are based on fluctuation quantities as for example the turbulent Mach number or r.m.s. values.

It is common in the literature to check the accuracy of simulations of turbulent boundary layers by analyzing one-dimensional power spectra of velocity components at given streamwise and wall-normal positions. Such results are displayed in figure 5.27 for $y^+ \simeq 49$ at different streamwise locations. The spectra were computed using Fourier transforms and the following relation

$$E_{\alpha\alpha} = \overline{\mathcal{F}(\alpha)\,\mathcal{F}(\alpha)}\,, \tag{5.14}$$

where $\mathcal{F}(\alpha)$ symbolizes the Fourier transform of the velocity component α. In figure 5.27, α represents either the streamwise, wall-normal or spanwise velocity, i.e. u, v or w, respectively. Note that for the calculation of the power spectra in the spanwise direction (figures 5.27a, 5.27c and 5.27e) the overline in equation (5.14) indicates only a time average (Reynolds average) whereas for the computation of the power spectra in time (figures 5.27b, 5.27d and 5.27f) only a spanwise average is used.

In figure 5.27, all velocity components experience an energy decline as predicted by theory (Heisenberg, 1948) (dashed and dashed-dotted lines). For the calculation of the energy spectra in CASE 2 (figures 5.27a and 5.27b), only a limited amount of temporal data were available and, hence, the curves are not as smooth as for CASE 3 (figures 5.27c-f). Nevertheless, the energy decay in the spanwise direction close to the end of the computational domain (at $x^* = 1.051m$ in figure 5.27a) seems to be sufficient in CASE 2 whereas in figure 5.27b the lower resolution in the streamwise direction leads to a premature drop in energy for high frequencies. The higher resolution in the spanwise and streamwise directions for CASE 3 improves the power spectra (at $x^* = 1.051m$ in figures 5.27c, d and at $x^* = 1.087m$ in figures 5.27e, f). Figures 5.27c and 5.27e show a drop of the order of six decades in the spanwise direction while figures 5.27d and 5.27f show a drop of more than four decades.

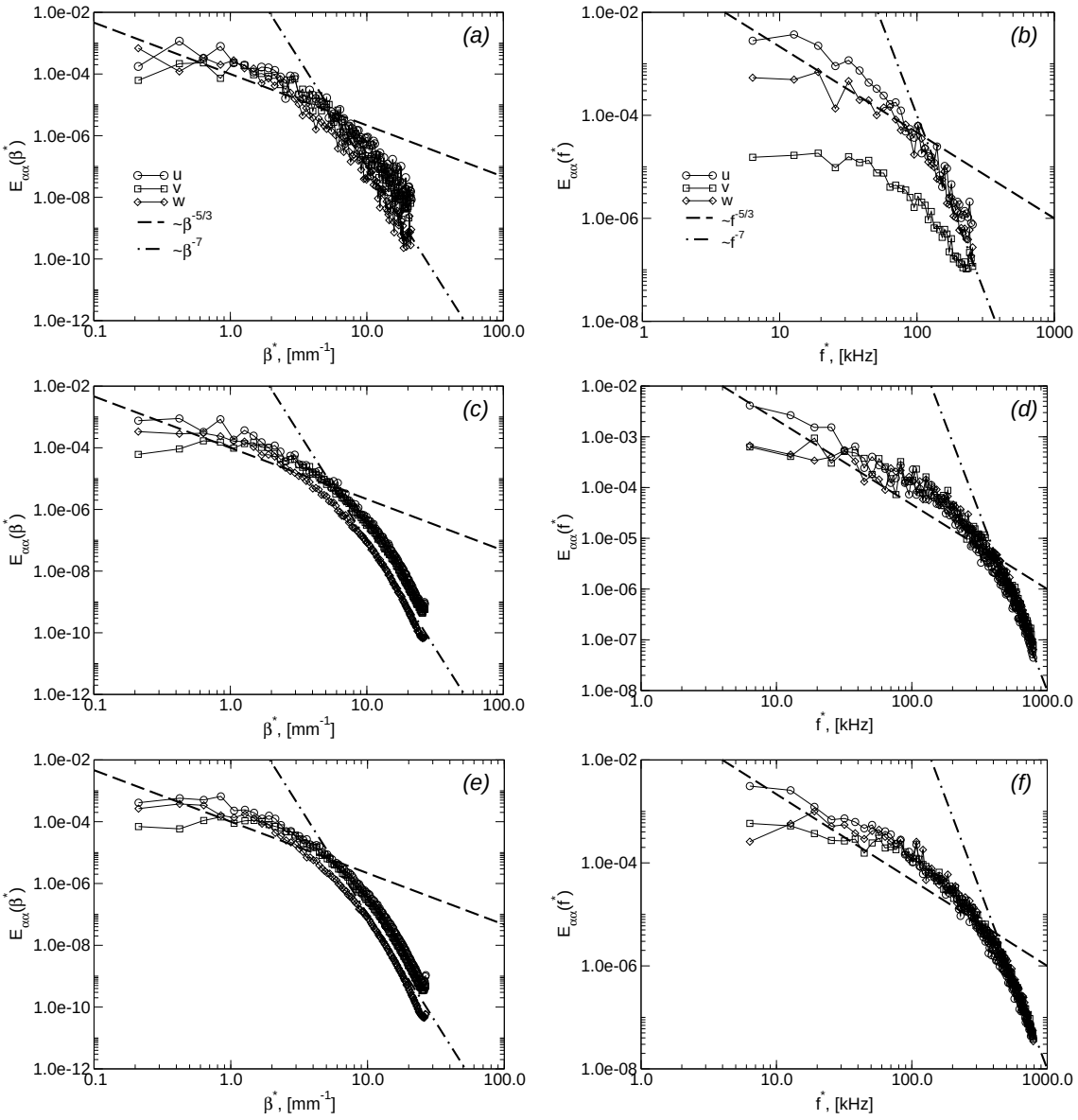

Figure 5.27: One-dimensional lateral (left) and temporal (right) power spectra $E_{\alpha\alpha}$ for velocity components from CASE 2 and CASE 3 at $y^+ \simeq 49$: (a) $x^* = 1.051m$ (CASE 2), (b) $x^* = 1.051m$ (CASE 2), (c) $x^* = 1.051m$ (CASE 3), (d) $x^* = 1.051m$ (CASE 3), (c) $x^* = 1.087m$ (CASE 3), (d) $x^* = 1.087m$ (CASE 3); lines denote theoretical reference data from Heisenberg (1948); M=3.0, T^*_∞=103.6K, flat plate.

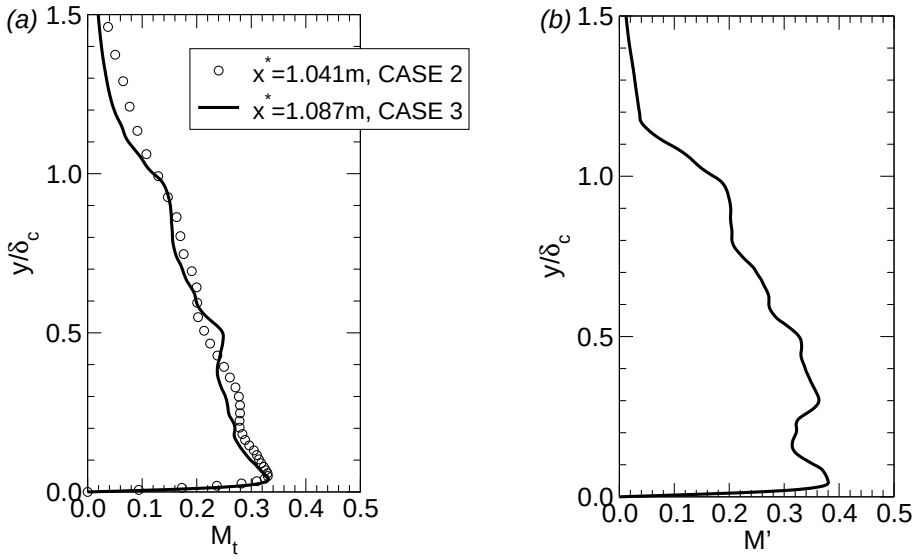

Figure 5.28: Wall-normal distribution of turbulent Mach number M_t (a) and fluctuation Mach number M' (b) at different streamwise positions from CASE 3 and CASE 2; M=3.0, T^*_∞=103.6K, flat plate.

One convenient measure of compressibility effects in a turbulent boundary layer is the fluctuation Mach number M'. A similar quantity widely used in the literature is the turbulent Mach number M_t. These are defined as

$$M' = \sqrt{\overline{\left(M - \overline{M}\right)^2}} \quad \text{and} \quad M_t = \frac{\sqrt{\overline{u''u''} + \overline{v''v''} + \overline{w''w''}}}{\overline{a}}\,. \tag{5.15}$$

Turbulence is only weakly affected by compressibility effects for a fluctuation Mach number smaller than about 0.3 (Morkovins hypothesis, see Fernholz & Finley, 1980). Note that different threshold values have been reported in the literature (Guarini *et al.*, 2000). For the simulations discussed in this chapter, the fluctuation Mach number exceeds a value of 0.3 only slightly, as can be seen in figure 5.28b. As a consequence, Morkovin's hypothesis is likely to hold and comparison of statistical values of the turbulence with incompressible data after proper transformation is justified.

For simulation CASE 3, the wall-normal distribution, for both the turbulent Mach number and the fluctuation Mach number, exhibits another peak close to the boundary layer edge. A similar peak is also present in the r.m.s. value of the streamwise

velocity fluctuation u'' in figure 5.29a. This peak might be caused by the strong coherent structures visible in the spanwise average of the wall-normal density gradient in figure 5.30. Although the turbulent Mach number for CASE 2 looks smoother in figure 5.29a, the r.m.s. value of the streamwise velocity fluctuation shows a similar peak as CASE 3 close to the boundary layer edge.

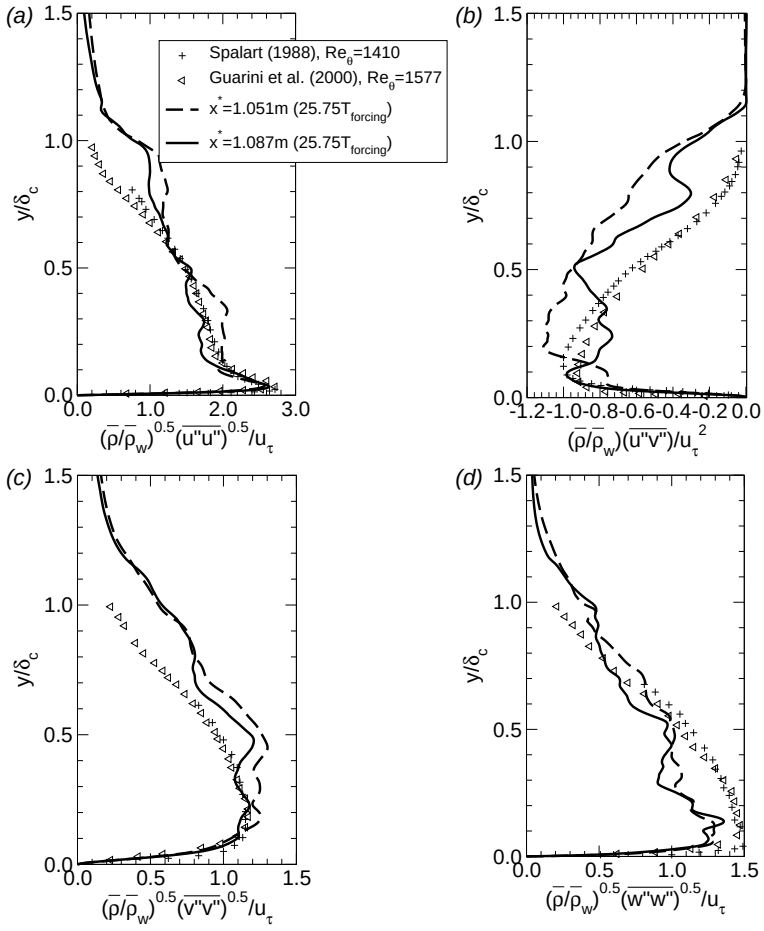

Figure 5.29: Wall-normal distribution of r.m.s. values for (a) streamwise, (b) wall-normal and (c) spanwise velocity at $x^* = 1.051m$ and $x^* = 1.087m$ for CASE 3; M=3.0, T^*_∞=103.6K, flat plate.

For CASE 3, figure 5.29 compares the r.m.s. values of all velocity components (Favre average) to profiles published in the literature from DNS of an incompressible turbulent boundary layer (Spalart, 1988) and the previously mentioned DNS by

Guarini *et al.* (2000) of a compressible turbulent boundary layer at Mach 2.5. The profiles for CASE 3 and of Guarini *et al.* (2000) are rescaled employing Morkovin's density scaling. Except for the peak at the boundary layer edge, the r.m.s. value for the streamwise velocity fluctuation matches the distribution from Guarini *et al.* (2000) and Spalart (1988) at $x^* = 1.087m$ while the r.m.s. values for the other velocity components have not yet reached the corresponding reference data. This suggests that the flow is turbulent, but still may not yet be fully developed.

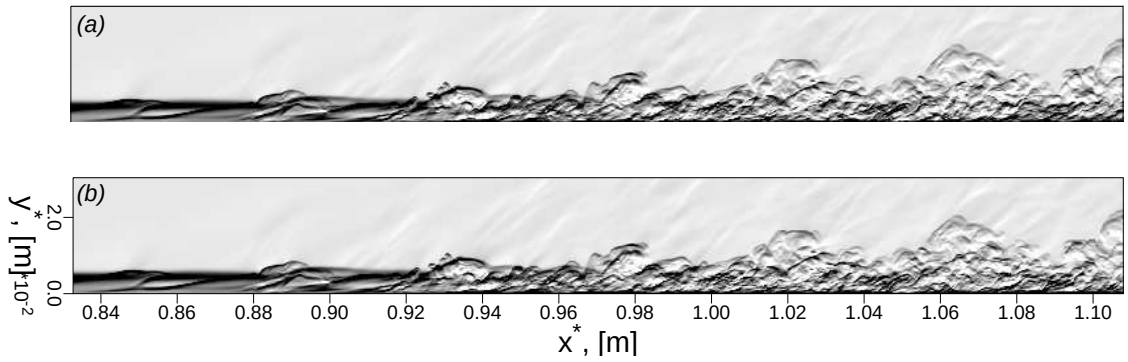

Figure 5.30: Contours of spanwise averaged wall-normal density gradient $\partial\rho/\partial y$ at two different instances one fundamental forcing period apart (CASE 3): (a) t_1, (b) $t_2 = t_1 + T_{forcing}$; M=3.0, T^*_∞=103.6K, flat plate.

In the last figure of this section (figure 5.31), a topview (x-z plane) of contours of instantaneous density is given for two different wall-normal positions. This figure illustrates the break-up region and the early turbulent region close to the wall (figure 5.31a) and farther away (figure 5.31b). Dark regions denote high density and brighter regions denote low density flow. Two-dimensional coherent structures seem to appear in figure 5.31b. These structures are also present in figure 5.30 and repeat with half the wave length of the initially forced oblique fundamental waves. The strong coherence might be an explanation for the overshoot of the skin friction in figure 5.21a and figure 5.23 when compared with the turbulent reference data.

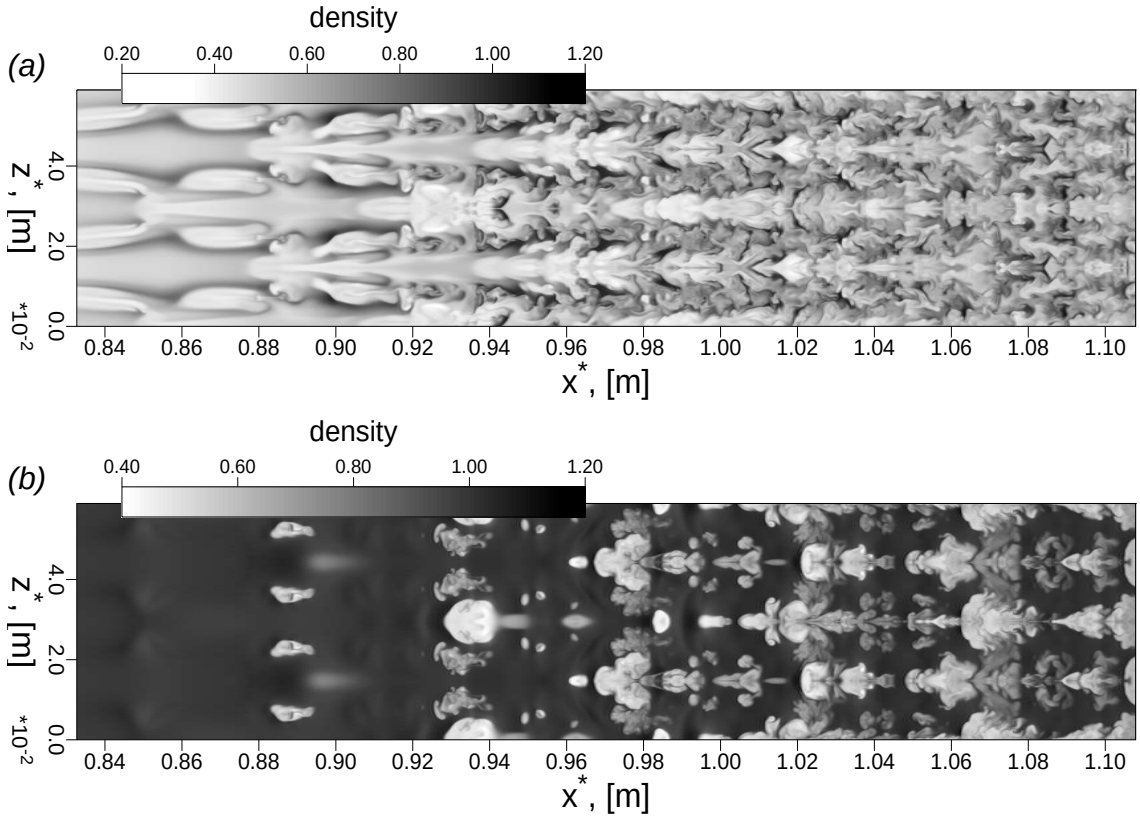

Figure 5.31: Topview of contours of instantaneous density ρ for two wall-normal positions (two wave lengths in spanwise direction): (a) $y^* \simeq 2.2mm$ (corresponds to $y^+ \simeq 49$ at $x^* = 1.087m$), (b) $y^* \simeq 7.0mm$ (corresponds to $y^+ \simeq 163$ at $x^* = 1.087m$); M=3.0, T^*_∞=103.6K, flat plate.

5.5 Summary of Mach 3 Oblique Breakdown Simulations

In this chapter, direct numerical simulation of the complete transition path of oblique breakdown in a supersonic flat-plate boundary layer at Mach 3 was discussed. The transition process was initiated by a discrete pair of oblique instability waves at low disturbance amplitudes with frequency $f^* = 6.36kHz$. The downstream development of this wave pair and the concomitant process of laminar to turbulent transition was studied from the linear regime to the final breakdown to turbulence. Linear theory predicts and the DNS confirms that oblique instability waves with the frequency of interest and the spanwise wavenumber $\beta^* = 211.52m^{-1}$ are strongly amplified

throughout the computational domain and can trigger oblique breakdown for the computational setup and realistic experimental conditions.

The early nonlinear transition regime exhibited the typical characteristics for oblique breakdown: The wavenumber spectrum filled up rapidly in the spanwise and streamwise direction and the well known pattern of nonlinear wave interactions initiated by the forced oblique wave pair was observed. Typical flow structures for the early stages of oblique breakdown were also identified. These structures were predominantly longitudinal structures with a rope-like shape in the sideview (x-y-plane). In the later stages of transition, the tip of these structures was lifted up from the wall and broke down to small-scale structures. The breakup region extended from about $x^* \simeq 0.84m$ to $x^* \simeq 0.9m$ of the computational setup. Close to the end of this breakup region (downstream of $x^* \simeq 0.9m$) a sudden increase in streamwise amplification of all modes that are not direct descendants of the original oblique wave pair occurred. This increase in streamwise amplification seemed to be linked to the breakup into small scales. Downstream of $x^* \simeq 0.9m$ the entire flow was rapidly contaminated by small-scale structures and the final breakdown to turbulence was initiated. In an ideal environment, where oblique breakdown is initiated by two oblique waves with exactly the same amplitude and phase, the influence of asymmetric modes on oblique breakdown is only limited. Hence, up to the early turbulent regime, oblique breakdown is mainly symmetric with respect to the spanwise direction. In the DNS using full Fourier transformation in spanwise direction, asymmetric modes were however amplified in downstream direction and may have eventually reached high amplitude values in the later turbulent region.

The DNS data provided strong evidence that a fully turbulent flow was reached. The most important results are: (1) The turbulent and fluctuating Mach numbers were sufficiently low such that Morkovin's hypothesis holds and the comparison of properly transformed data with results obtained for incompressible turbulent boundary layers is justified. (2) The decay of the skin-friction coefficient in the streamwise

directions approached correlations and comparable data for turbulent boundary layers in the literature. (3) A loss of periodicity in the time signals for the investigated setup occurred downstream of the peak in skin friction. (4) A logarithmic region in the van Driest transformed mean streamwise velocity profile was formed. (5) The power spectra of velocity components exhibited well-known theoretical scaling laws. In conclusion, the DNS data clearly demonstrated that oblique breakdown is a viable path to sustained turbulence.

6. Transition in a Mach 8 Boundary Layer on a Sharp Cone: Spatial Direct Numerical Simulations

6.1 Physical Problem and Flow Parameters

The cone geometry and flow parameters used for this investigation are the same as in the experiments by Stetson *et al.* (1983*b*). The semi-vertex angle of the cone is $\theta_c = 7^\circ$ and the cone is considered "sharp" with a nose radius $r^*_{nose} = .038mm$. The length of the model used in the experiments, $L^* = 1.016m$, is used as the reference length for the present calculations. The global Reynolds number is $3,333,333$ corresponding to a unit Reynolds number of 3.28×10^6 $1/m$. The free stream Mach number and temperature are 7.95 and 53.35 K. A summary of the conditions of the approach flow and after the shock is given in table 6.1. Although the boundary layer edge conditions are not constant for the flow over a sharp cone, the variation is small for the computed flow, and in the context of the presented research the after-shock conditions are considered constant. Figure 6.1 shows the edge Reynolds number varies by less than 0.5% as a function of streamwise coordinate.

Table 6.1: Approach Flow Conditions

	Approach Flow	Behind Shock
M[-]	7.95	6.8
Re[-]	3,333,333	4,760,000
T_∞[K]	53.35	71.00

6.2 Pulse Simulations

Disturbances were introduced into the flow through a forcing slot. The disturbances were forced for a short duration by a "pulse" in time. This type of forcing introduces a broad spectrum of frequencies in one or multiple specified azimuthal modes. The

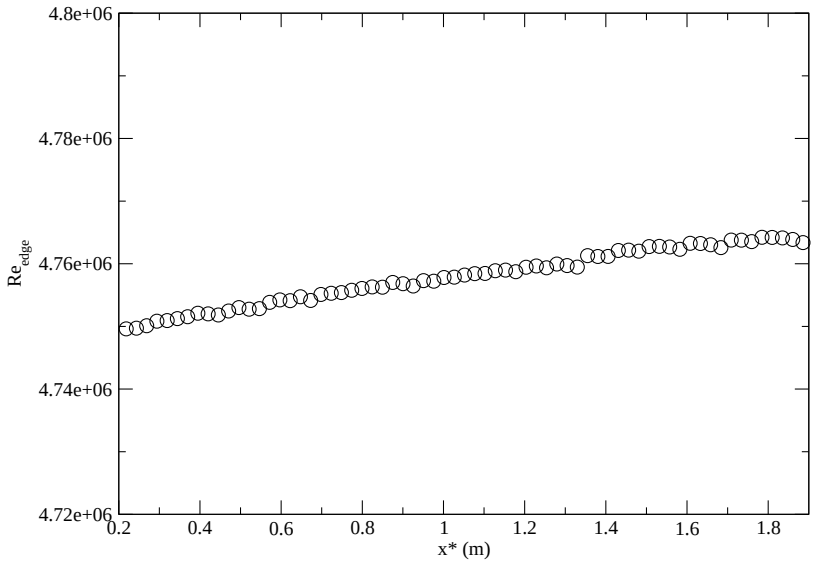

Figure 6.1: Boundary layer edge Reynolds number as a function of downstream position for the computed baseflow. Sharp cone, $M = 7.95$, $T = 53.35K$.

purpose of these simulations was to compare stability behavior extracted from the simulations against linear stability calculations as well as to guide the selection of frequencies for continuous forcing simulations (discussed in section 6.4). The first step is to validate the mean flow. Comparison of steady baseflow profiles at $R_x = 2024$ with Mangler transformed similarity solutions and profiles obtained from the finite volume code are presented in figure 6.2.

To simulate linear unstable waves with $k_c = 0$ (defined in Chapter 4), a low amplitude ($A_{in} = 10^{-6}$) axisymmetric pulse is introduced into the flow which develops into a two-dimensional wave packet containing a broad spectrum of frequencies. The Fourier spectrum of the pulse, taken in the center of the disturbance strip, is shown in figure 6.3 and illustrates the broad range of frequencies produced by the forcing. Using temporal Fourier decomposition, the streamwise evolution of amplitude and phase information can be extracted for discrete frequencies. The growth rate and streamwise wave number of a given mode are calculated as

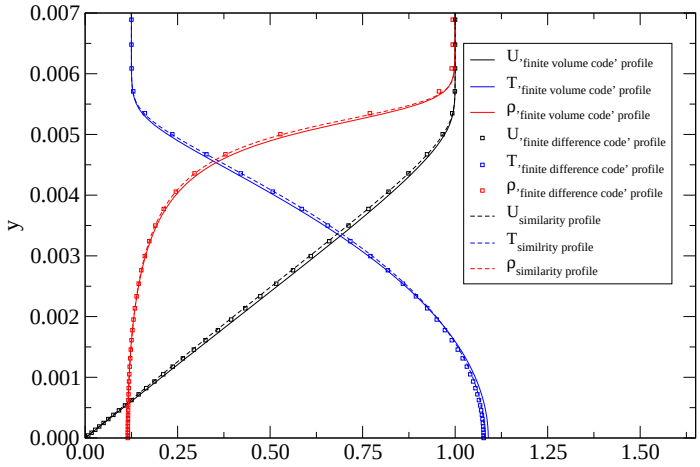

Figure 6.2: Comparison of meanflow profiles at $R_x = 2024$ with similarity solutions and profiles obtained in the precursor calculation (finite volume code). Note that for visualization purposes, T has been scaled by a factor of 0.2. Sharp cone, $M = 7.95$, $T = 53.35K$.

$$\alpha_i = -\frac{\partial}{\partial x}\left(\ln\frac{A(x)}{A_0}\right)\frac{R_x}{R_e}, \qquad \alpha_r = \frac{\partial}{\partial x}(\theta(x)). \tag{6.1}$$

Comparison of the real and imaginary parts of the streamwise wave number with results from Tumin's LST solver are given in figure 6.4 for $f^* = 73.782kHz$. The growth rates from DNS are computed based on the wall-normal maximum of the u-velocity disturbance. Overall, the agreement is reasonable. There are deviations in both the real and imaginary parts of the streamwise wave number which may be due to non-parallel effects which are neglected in the context of LST.

The streamwise distribution of the N-factors, which are computed as $\ln(\frac{A_n(x)}{A_{n,0}})$, of several frequencies are given in figure 6.5. As reported by Schneider (2001*a*), N-factors corresponding to transition in experiments range between approximately 5 and 10 depending on the background disturbances present in the particular wind tunnel. For the present DNS, the wave to first reach an N-factor of 5.5 has frequency $F = 9.1 \times 10^{-5}$ ($f^* = 79.255kHz$). Based on the linear growth, this frequency was chosen as the primary disturbance wave for controlled transition simulations discussed

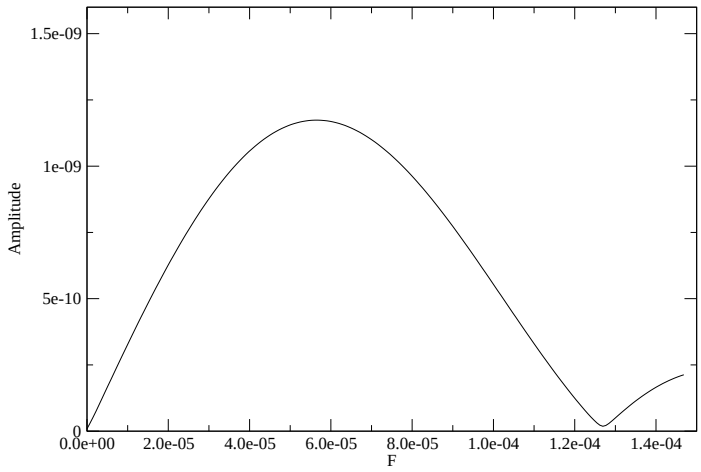

Figure 6.3: Fourier spectrum (amplitude as a function of frequency) of the disturbance input in the v-velocity for the low-amplitude 2D pulse simulation. Sharp cone, $M = 7.95$, $T = 53.35K$.

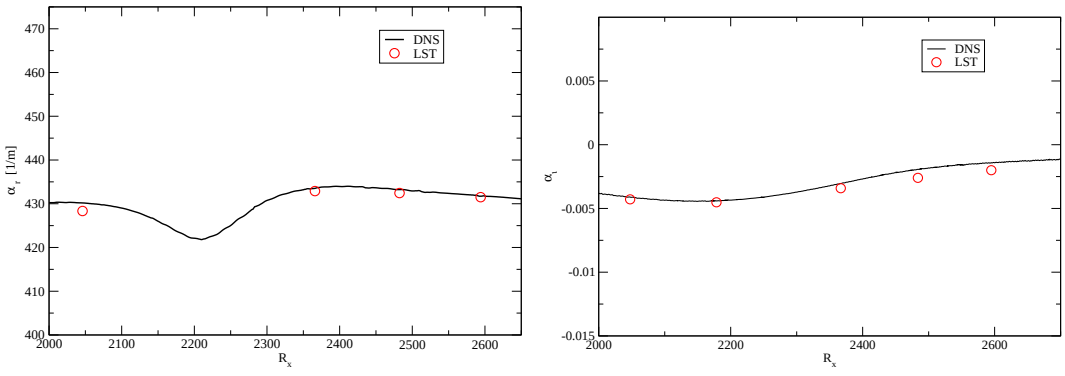

Figure 6.4: Comparison of DNS data with LST data from Tumin's solver for a low-amplitude 2D pulse *a)* Streamwise wave number, α_r (left) *b)* Growth rate, α_i (right). Sharp cone, $M = 7.95$, $T = 53.35K$.

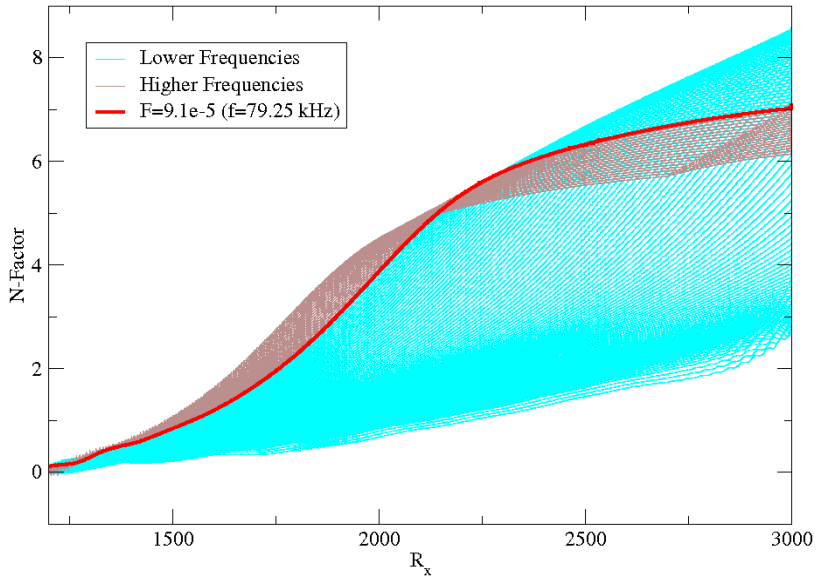

Figure 6.5: The downstream amplitude development (N-factor) of several frequencies from 2-D pulse DNS. $F = 9.1 \times 10^{-5}$ ($f^* = 79.255kHz$) is the first to reach an N-factor of 5.5. Sharp cone, $M = 7.95$, $T = 53.35K$.

in section 6.4. The relatively low N-factor is chosen because disurbances will be forced at large amplitudes for simulations of nonlinear transition.

6.2.1 Nonlinear Growth of Low-Frequencies

In the growth curves for u-velocity disturbances obtained from 2-D pulse simulations it was apparent that several low-frequency waves experienced a rapid increase in growth rate. For example, in figure 6.6, at approximately $R_x = 2000$, several low-frequencies (a representative band is colored in red, modes 1-30 corresponding to frequencies $5.48 * 10^{-7} < F < 1.6 * 10^{-5}$) suddenly become strongly amplified. Given that the amplitude of the initial pulse-disturbance for this simulation was low ($A_{in} = 10^{-6}$), it was expected that the disturbance development should remain linear for the extent of the computational domain (because products of disturbances are of negligible amplitude). Thus, such rapid growth of frequencies well below those that LST predicts to be strongly amplified is clearly worth exploring further.

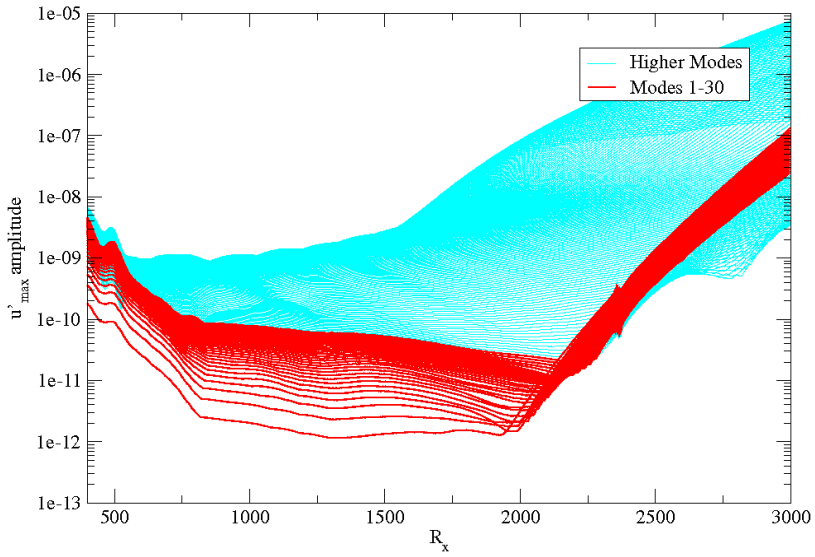

Figure 6.6: Streamwise development of several disturbance frequencies (all with $k_c = 0$) shown by u-velocity disturbance amplitudes. Low-frequencies, $5.3 * 10^{-7} < F < 1.6 * 10^{-5}$, are colored in red with higher frequencies in gray. Forcing amplitude $A_{in} = 10^{-6}$. Sharp cone, $M = 7.95$, $T = 53.35K$.

To confirm that the rapid growth is indeed caused by nonlinear interactions, the effect of the initial pulse amplitude was studied. Figure 6.7 shows the amplitude development for a pulse with $A_{in} = 10^{-9}$ and $A_{in} = 10^{-3}$. For the sufficiently low amplitude of 10^{-9}, the sudden change in growth rate is no longer observed until very close to the end of the computational domain (note that the "noisy" data in this simulation is due to the fact that the amplitudes are sufficiently low they are near the order of round-off error). As the amplitude is increased to 10^{-3}, the shift in growth rate occurs even further upstream relative to the $A_{in} = 10^{-6}$ case and the low-frequencies reach amplitudes similar to those of the most amplified disturbances in the simulations. Clearly, this sudden increase in growth rate is strongly related to the initial forcing amplitude which is an indicator that nonlinearity plays a key role.

As a comparison, wall-pressure disturbance amplitudes are also presented for the highest amplitude simulation in figure 6.8. In the wall-pressure, the increase in growth rate is not as sudden and the amplitudes (relative to the most amplified modes)

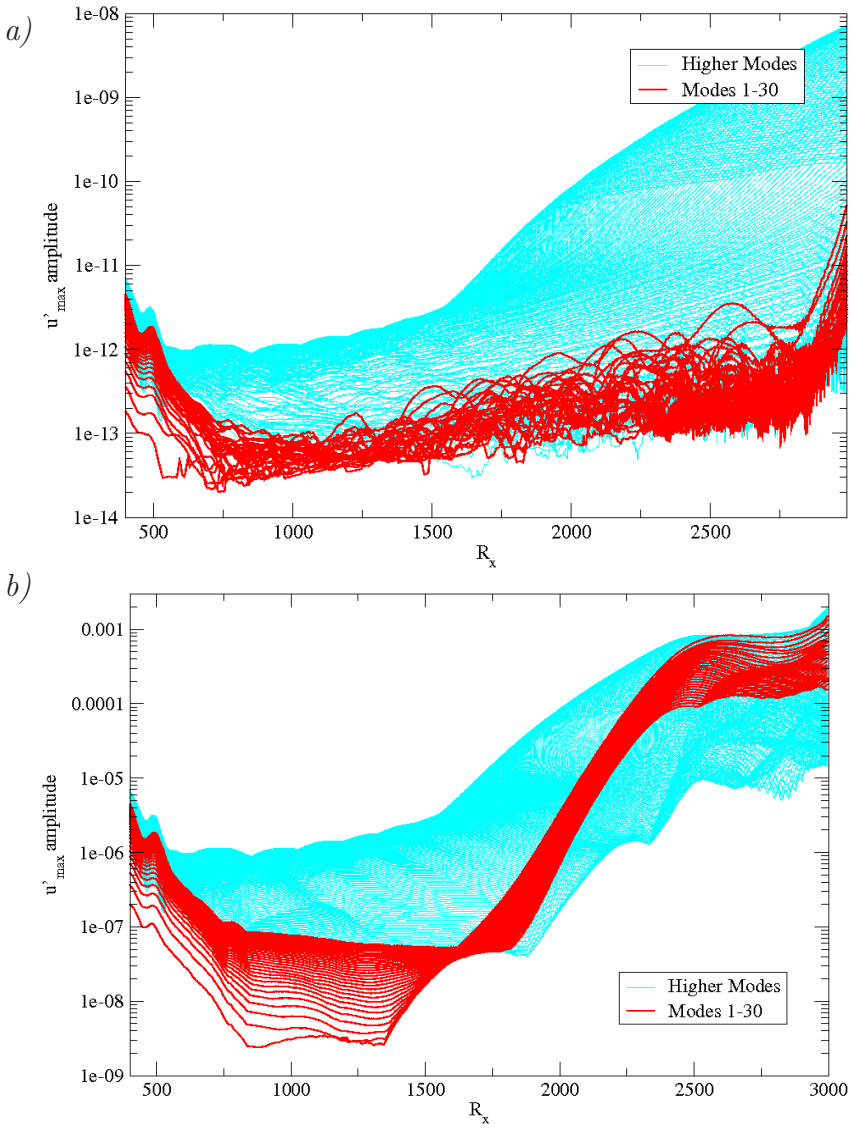

Figure 6.7: Streamwise development of several disturbance frequencies (all with $k_c = 0$) shown by u-velocity disturbance amplitudes for two different pulse amplitudes. Low-frequencies ,$5.48{*}10^{-7} < F < 1.6{*}10^{-5}$, are colored in red with higher frequencies in gray. *a)* Forcing amplitude $A_{in} = 10^{-9}$ *b)* Forcing amplitude $A_{in} = 10^{-3}$. Sharp cone, $M = 7.95$, $T = 53.35K$.

are not as high. The wall-normal u-velocity disturbance amplitude distributions for $F = 5.48 * 10^{-7}$ are shown at several downstream locations in figure 6.9. There is a clear change in the overall shape of the eigenfunction upstream and downstream of

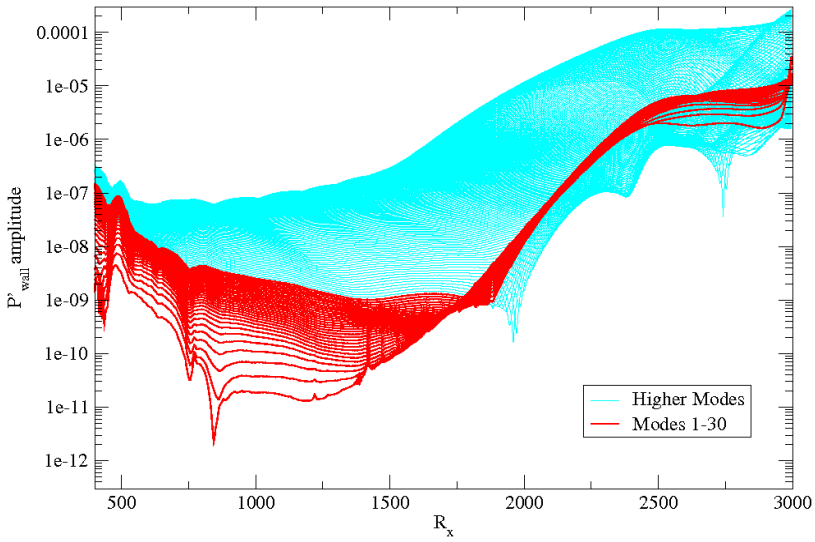

Figure 6.8: Streamwise development of several disturbance frequencies (all with $k_c = 0$) given by wall-pressure disturbance amplitudes. Low-frequencies ,$5.48 * 10^{-7} < F < 1.6 * 10^{-5}$, are colored in red with higher frequencies in gray. Forcing amplitude $A_{in} = 10^{-3}$. Sharp cone, $M = 7.95$, $T = 53.35K$.

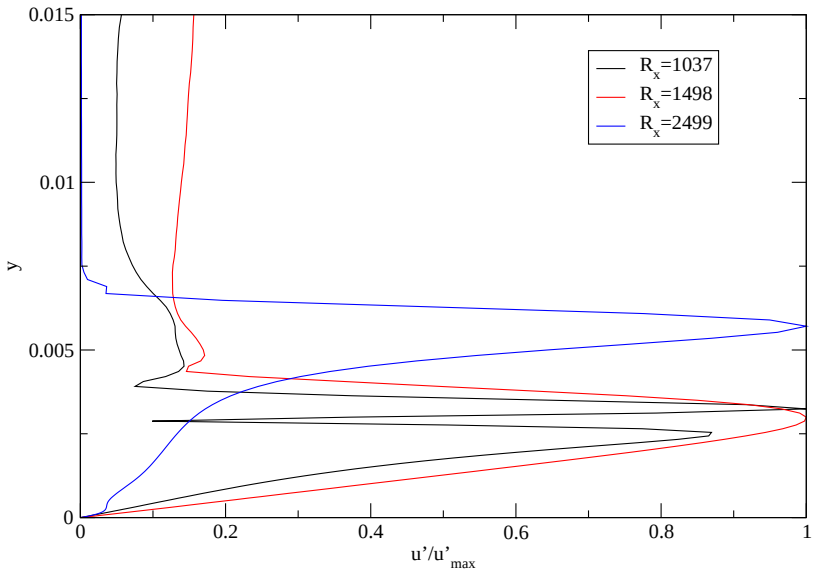

Figure 6.9: Wall normal amplitude distributions of u-velocity disturbances at several downstream locations for $F = 5.48 * 10^{-7}$. Forcing amplitude $A_{in} = 10^{-6}$. Sharp cone, $M = 7.95$, $T = 53.35K$.

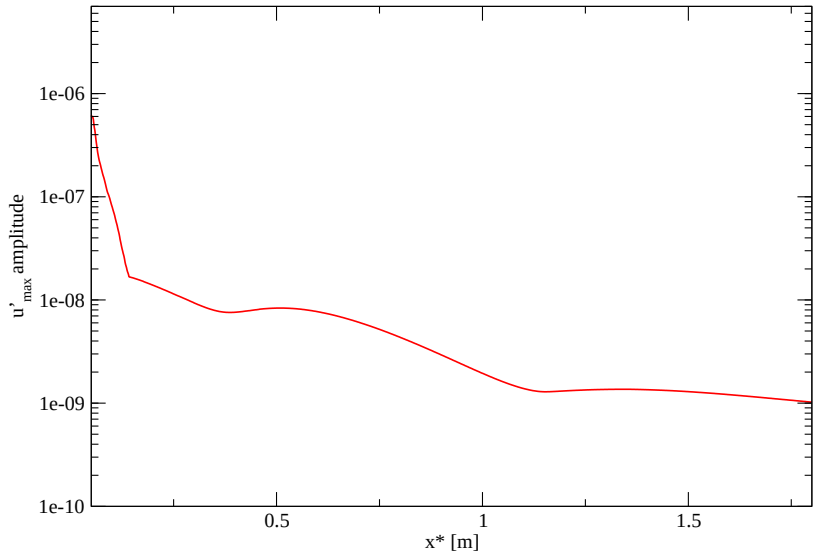

Figure 6.10: Streamwise evolution of the u-velocity disturbance amplitude for a single mode, $F = 5.48 * 10^{-7}$, continuously forced with wall-normal blowing and suction. Forcing amplitude $A_{in} = 10^{-6}$. Sharp cone, $M = 7.95$, $T = 53.35K$.

the shift in growth rate.

6.2.2 Continuous Forcing of Low Frequency Waves

To further confirm that this rapid growth is indeed a nonlinear mechanism, simulations with continuous forcing were performed. Initially, only a single mode is forced ($F = 5.48 * 10^{-7}$) with an amplitude of 10^{-6}. As expected from LST, this low frequency disturbance is damped throughout the domain (see figure 6.10).

The next step was to force two disturbance waves and attempt to duplicate the rapid shift in growth rate observed when a broad spectrum of disturbances were present. A "primary" disturbance wave was chosen with $F = 8.23 * 10^{-5}$ because it is the wave with the highest amplitude at the point of the rapid growth of the low-frequency modes from the pulse simulation with $A_{in} = 10^{-6}$ (see figure 6.6). In order to reduce the computational time necessary for the disturbance to travel to the end of the domain, the low-frequency wave was chosen as $F = 5.48 * 10^{-6}$, a factor

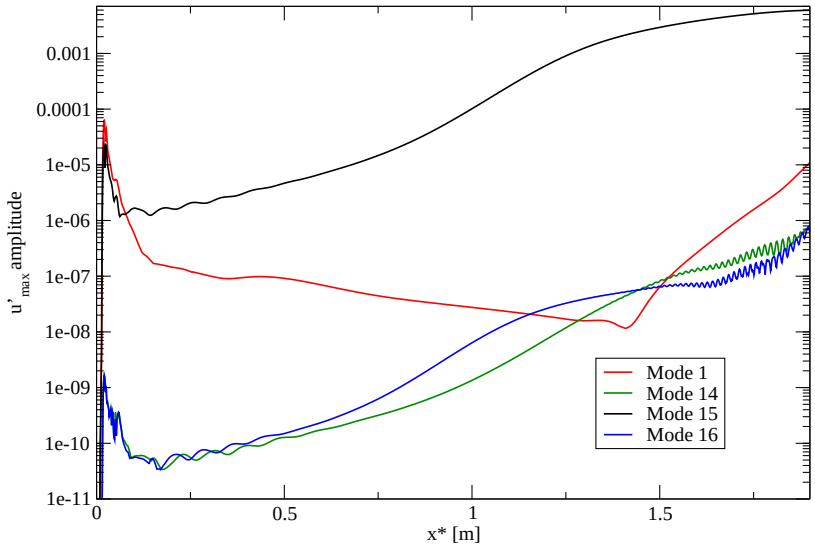

Figure 6.11: Streamwise evolution of the u-velocity disturbance amplitude for continuous forcing of 2 modes,$F = 5.48 * 10^{-6}$-mode 1,0 and $F = 8.23 * 10^{-5}$-mode 15,0, continuously forced with wall-normal blowing and suction. Forcing amplitude $A_{1,0} = A_{15,0} = 10^{-4}$. Sharp cone, $M = 7.95$, $T = 53.35K$.

of ten larger than the lowest frequency plotted in figure 6.6 (which was investigated as the single forced disturbance). This frequency is still well below those that LST predicts to be strongly amplified and is within the band of modes that were suddenly amplified in the pulse simulations.

The streamwise development of u-velocity disturbance amplitudes is shown in figure 6.11. The fundamental frequency, mode 1 in the figure, corresponds to the low-frequency disturbance, while the high frequency "primary" wave is mode 15. Both disturbances were forced with an amplitude of 10^{-4}. Initially, mode 1 is damped. However, just downstream of the point where modes 14 and 16 (which are nonlinearly generated due to the forcing of modes 1 and 15) reach the amplitude of mode 1, the low-frequency wave suddenly becomes strongly amplified. The amplification of the low-frequency only after additional modes have surpassed its amplitude is an indication of a possible 3-wave interaction - or resonance triad.

Three wave interactions, known as resonance triads, are a nonlinear mechanism

Table 6.2: Streamwise Wave Numbers.

Frequency Harmonic	Streamwise wave number
1	23.2
14	395.1
15	418.9
16	445.3

which is possible in equations with quadratic nonlinearities (such as the Navier-Stokes equations). The resonance conditions for such an interaction (equation 6.2) are given by relations between the streamwise, spanwise and temporal wave numbers which ensure that two waves quadratically interacting will produce the third wave.

$$\begin{aligned} \alpha_r^1 + \alpha_r^2 &= \alpha_r^3 \\ \beta^1 + \beta^2 &= \beta^3 \\ \omega_r^1 + \omega_r^2 &= \omega_r^3 \end{aligned} \tag{6.2}$$

For the present simulations, all the waves involved are axisymmetirc and thus $\beta = 0$. For this situation, the resonance condition only requires that the frequency and streamwise wave number conditions are met. Since the frequency is directly related to the Fourier harmonic (or mode number in the previously discussed simulations), the resonance condition on the frequency is automatically met between modes 1, 14 and 15 or 1, 15 and 16 in figure 6.11. The only remaining condition is on the streamwise wave number. The streamwise wave numbers for the four disturbance modes are listed in table 6.2. The resonance condition on the streamwise wave number is close to being met considering either of two triads - modes 1, 14 and 15 or modes 1, 15 and 16. However, between modes 1,14 and 15 the resonance condition is more closely fulfilled as $\alpha_r^{1,0} + \alpha_r^{14,0} \approx 418$ which is almost exactly the wave number of mode 15.

The final step in confirming the existence of this resonance triad was performing a simulation where all three waves were forced. Figure 6.12 shows the evolution of u-velocity disturbance amplitudes with mode 1 forced at an amplitude of 10^{-8} and

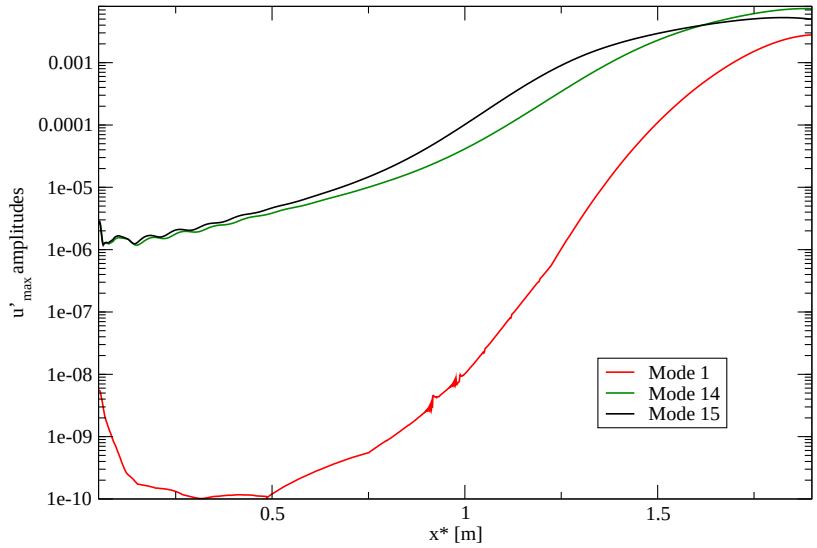

Figure 6.12: Streamwise evolution of the u-velocity disturbance amplitude for continuous forcing of 3 modes,$F = 5.48 * 10^{-6}$-mode 1,0, $F = 7.67 * 10^{-5}$-mode 14,0 and $F = 8.23 * 10^{-5}$-mode 15,0, continuously forced with wall-normal blowing and suction. Forcing amplitude $A_{1,0} = 10^{-8}$ $A_{14,0} = A_{15,0} = 10^{-4}$. Sharp cone, $M = 7.95$, $T = 53.35K$.

modes 14 and 15 forced with amplitudes of 10^{-5}. For this disturbance environment, the low-frequency wave is rapidly amplified after only a short downstream distance and remains amplified for the rest of the computational domain. This is yet a further confirmation that the sudden growth of low-frequency waves in the pulse simulations is caused by resonance triads made up of axisymmetric waves. In the broad disturbance spectrum of the pulse simulations, different interactions in the band of relatively high (second mode) frequencies appear to cause a resonance which leads to rapid, nonlinear growth of a band of low frequency waves.

6.2.3 Effect on Oblique Waves

To address the question of whether or not a similar rapid growth of low-frequency oblique waves ($k_c \neq 0$) occurs, a pulse simulation where a broad range of frequencies were seeded at $k_c = 20$ was performed. Given that the low-frequency growth has

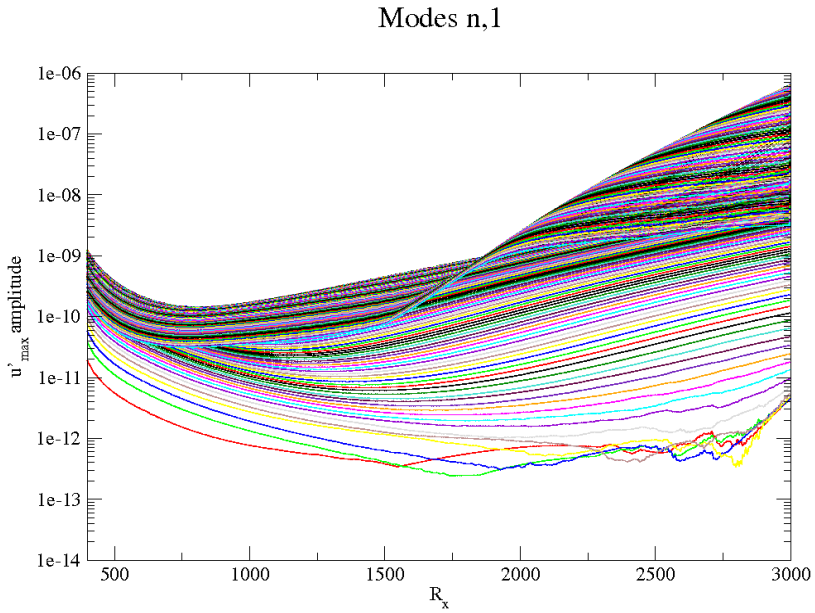

Figure 6.13: Streamwise evolution of the u-velocity disturbance amplitudes of modes n,1 ($k_c = 20$) for a three-dimensional pulse disturbance. Forcing amplitude $A_{in} = 10^{-6}$. Sharp cone, $M = 7.95$, $T = 53.35K$.

been demonstrated to likely be caused by resonance triads, it seems unlikely that such interaction would occur for three waves with the same k_c and $k_c \neq 0$ due to the inability to fulfill the resonance condition on the azimuthal wave number. This assumption is confirmed by the results presented in figure 6.13 which show the development u-velocity disturbance amplitudes for several frequencies with $k_c = 20$.

An additional simulation, in which both modes (n,0) and modes (n,1) are forced simultaneously by a pulse disturbance was performed. Note that for mode (n,k), n corresponds to multiples of some fundamental frequency (which is based on the total simulation time), and k corresponds to multiples of the fundamental azimuthal mode number (which is $k_c = 20$ for this case). This simulation showed that rapid growth of oblique, low-frequency waves occurs in the presence of axisymmetric disturbances. Figure 6.14 shows the development of u-velocity disturbances for both the axisymmetric and oblique waves. It is clear that the oblique waves are heavily influenced by the axisymmetric waves as low-frequencies experience rapid growth at exactly the

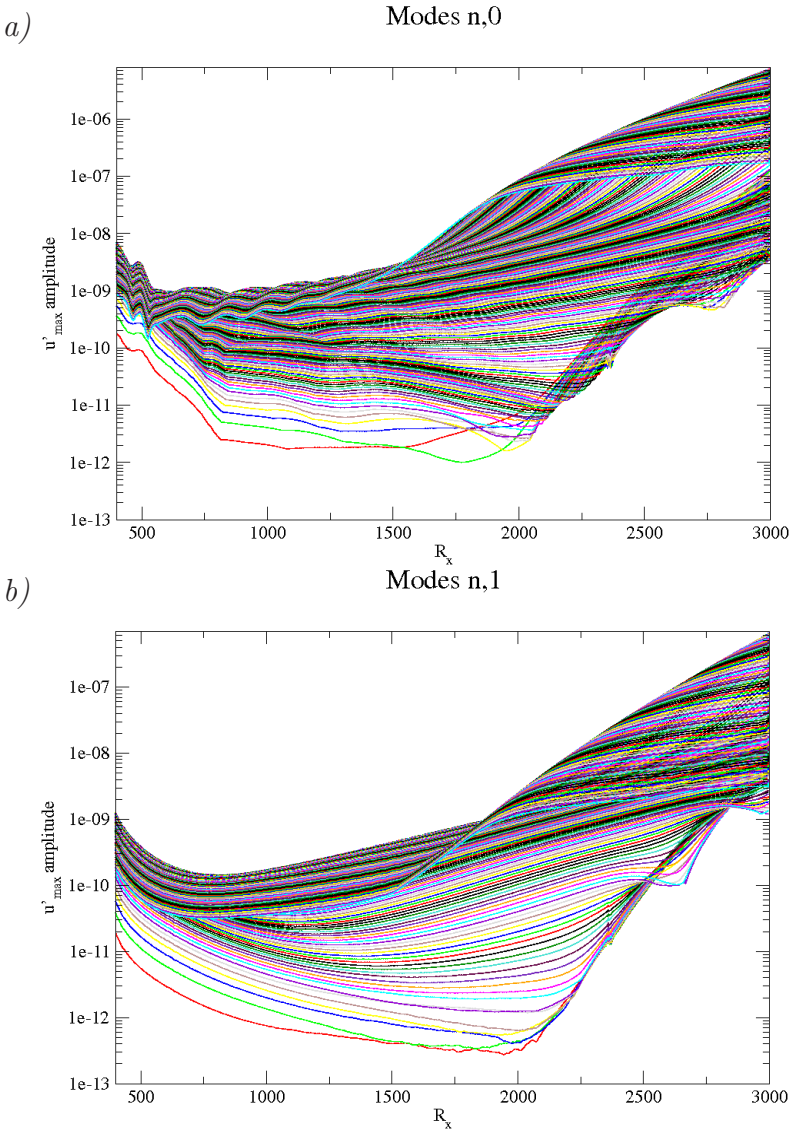

Figure 6.14: Streamwise evolution of the u-velocity disturbance amplitudes with modes (n,0) and (n,1) forced simultaneously by a pulse disturbance. Forcing amplitude $A_{in} = 10^{-6}$. In the presence of axisymmetric disturbances, low-frequency oblique waves experience rapid growth at $\sim R_x = 2000$ *a)* Modes n,0 *b)* Modes n,1 ($k_c = 20$). Sharp cone, $M = 7.95$, $T = 53.35K$.

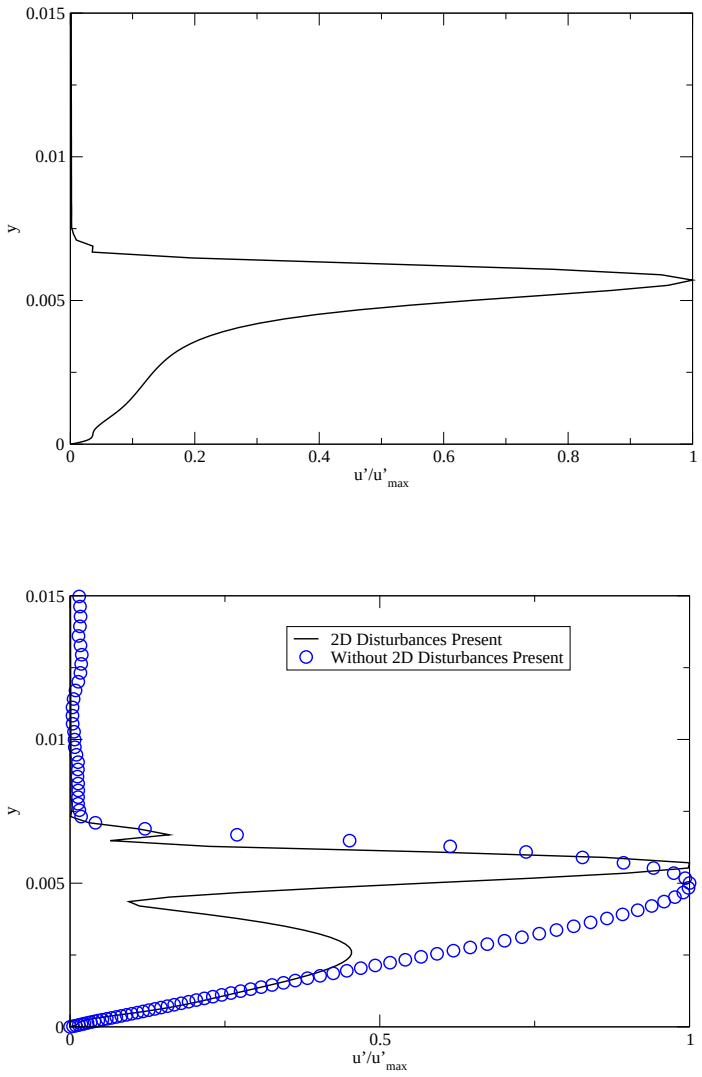

Figure 6.15: Wall-normal u-velocity disturbance amplitude distributions at $R_x = 2499$ for *a)* Mode 1,0 ($F = 5.48 * 10^{-7}$), (top) *b)* Mode 1,1 ($k_c = 20$, $F = 5.48 * 10^{-7}$), (bottom). Open symbols are without the presence of 2D disturbances (modes n,0). Solid line is with 2D disturbances present. Forcing amplitudes $A_{in}^{n,0} = A_{in}^{n,1} = 10^{-6}$. Sharp cone, $M = 7.95$, $T = 53.35K$.

same point that the phenomena occurs for the axisymmetric disturbances.

Figure 6.15 shows the drastic changes in the wall-normal amplitude distributions of u-velocity disturbances for a low-frequency ($F = 5.48 * 10^{-7}$) oblique disturbance wave at $R_x = 2499$ when axisymmetric disturbances are present. For reference, the amplitude distribution of the axisymmetric mode is plotted for the same frequency at the same location. Clearly, this nonlinear mechanism can have a large influence on both axisymmetric and oblique disturbances.

6.2.4 Preliminary Summary of Pulse Simulations

Simulations using a pulse (in time) type disturbance input were performed for axisymmetric waves to extract stability data for comparison with LST. Wall-normal amplitude distributions as well as streamwise wave numbers and growth rates showed good agreement with results from Tumin's LST solver. In the pulse simulations it was apparent that low frequency waves underwent a sudden and rapid increase in growth rate after a certain streamwise location. The point of this sudden growth shifted upstream for increasing pulse amplitude. This phenomenon was thoroughly investigated and determined to be the result of resonance triads caused by a difference interaction of two high-frequency, second mode waves within the most unstable band expected from LST. These two-waves interact with a third, low-frequency wave causing rapid amplification of the low-frequency. Similar behavior was not observed in simulations of pulse type disturbance for one specific higher azimuthal mode ($k_c = 20$) presumably because the resonance condition on the spanwise wave number was no longer met. However, in the presence of two-dimensional disturbances, low-frequency oblique waves also become strongly amplified at the same streamwise position as the onset of the amplification for the two-dimensional modes. The sudden increase in growth rate is accompanied by a change in character of the wall-normal amplitude distribution of the oblique mode.

6.3 Three-Dimensional Wave Packets

6.3.1 Simulation Setup

In order to observe which nonlinear mode interactions become dominant with a broad spectrum disturbance environment, wave packets were introduced into the boundary layer. The wave packets were created by a short duration pulse disturbance in the wall normal velocity from a small hole in the cone surface (analogous to the incompressible experiments by Medeiros & Gaster (1999)). The impulse type disturbance in time and space creates a broad spectrum of frequencies and azimuthal modes (wave angles). These disturbances convect downstream and initially grow or decay according to linear theory. At some point, after the amplitudes have grown large enough, nonlinear interactions begin occurring. No particular nonlinear mechanism is forced, and thus the wave packet can be considered as a model for natural transition that would occur with a broad spectrum of disturbances.

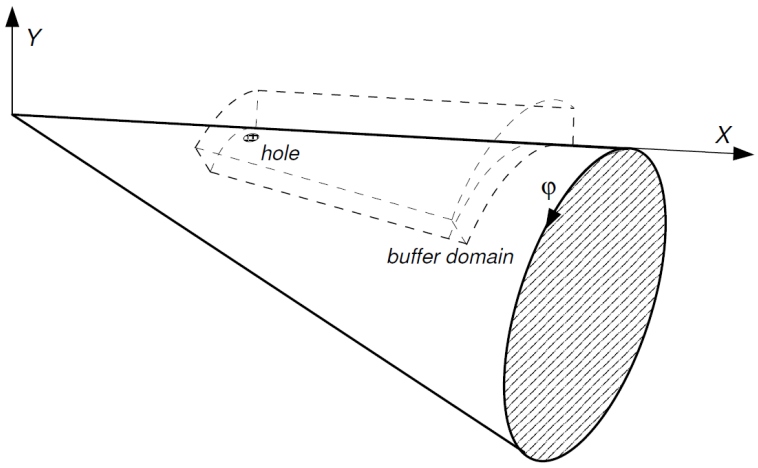

Figure 6.16: Schematic of the physical domain used for the wave packet simulations. The physical domain used for the simulations extends from $x^* \approx .11m$ to $x^* \approx 1.86m$ ($718 < R_x < 2957$). Sharp cone, $M = 7.95$, $T = 53.35K$.

A schematic of the physical domain used for the simulations is shown in figure 6.16. The computational domain extends in the streamwise direction from $x^* \approx .11m$

to $x^* \approx 1.86m$ ($718 < R_x < 2957$), not including the buffer domain applied to the outflow. The azimuthal extent of the domain is 1/3 of the cone's circumference. The large azimuthal domain is required due to the high degree of azimuthal spreading as the wavepacket travels downstream. The hole through which the wave packet is initially generated is approximately circular with a diameter of $d^* = 13.14mm$.

A stability diagram for axisymmetric waves ($k_c = \beta = 0$) computed with Mack's stability solver is shown in figure 6.17. Since two-dimensional second mode waves are most amplified for Mach 8, it is expected that the initial development of the wave packets (given that the most amplified frequencies are seeded) should be according to the 2D stability diagram shown below. Additionally, slightly oblique waves (low k_c) will exhibit similar stability behavior to the two-dimensional waves.

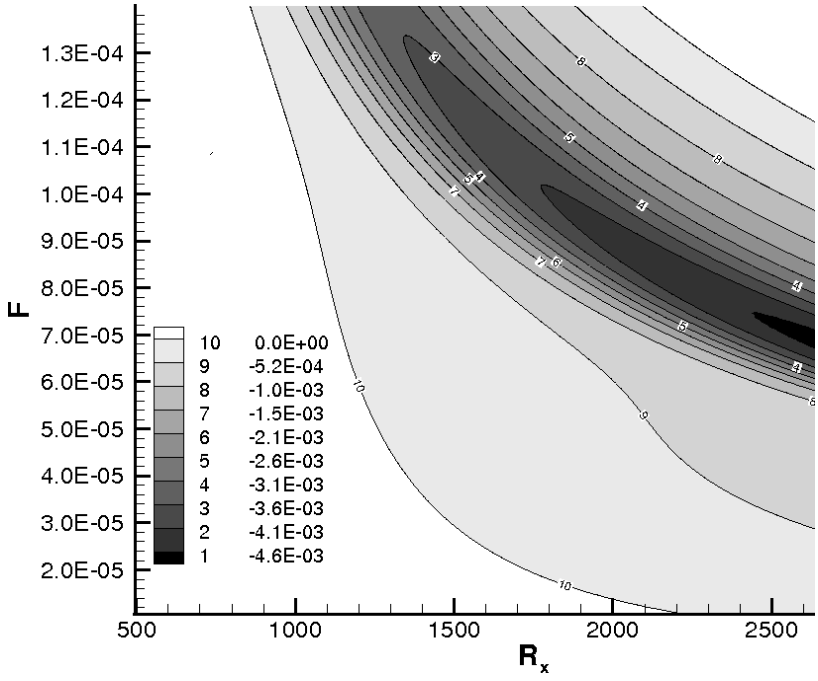

Figure 6.17: Stability diagram for axisymmetric waves shown as contours of constant amplification rate, α_i, in the reduced frequency-local Reynolds number plane. Sharp cone, $M = 7.95$, $T = 53.35K$.

6.3.2 Low Amplitude Wave Packet

A wave packet forced with an initial amplitude of 10^{-5} was introduced into the flow. The main purpose is to allow for comparison with higher forcing amplitude simulations that will produce strong nonlinear interactions. A disturbance spectrum taken over the center of the forcing hole is shown in figure 6.18 detailing the broad frequency spectrum introduced by the pulse disturbance. The range of azimuthal mode numbers introduced is somewhat narrow, however it should be noted that near the upstream edge of the cone, the local circumference is quite small and thus even waves with small k_c can have strongly oblique wave angles.

The disturbance spectrums plotted by contours of wall pressure amplitude in the frequency-azimuthal mode number plane at two downstream locations are shown in figure 6.19. Due to the low amplitude of the initial pulse that produced the wave packet, the amplification of disturbance modes should be governed by LST. As expected, the most dominant disturbances are two-dimensional and the frequency decreases in downstream direction as the boundary layer grows. Waves with small k_c) at similar frequencies are also strongly amplified. There is some evidence of weak nonlinear interactions in the final downstream location as "legs" begin to appear in the spectrum reaching to slightly lower frequencies. However, the amplitudes are quite low relative to the strongest modes.

The development of the structure of the wave packet is shown in physical space in figure 6.20 by contours of wall pressure disturbance on the cone surface at several time instances. The early stages of the development of the wave packet feature a strong 2D wave in the center and oblique waves in the tail. There is also a component traveling in front of the main disturbances which is most likely the "fast" acoustic waves which move at a speed $1+\frac{1}{M}$. The main component of the wave packet remains two-dimensional, but there is a small amount of azimuthal modulation towards the end of the domain.

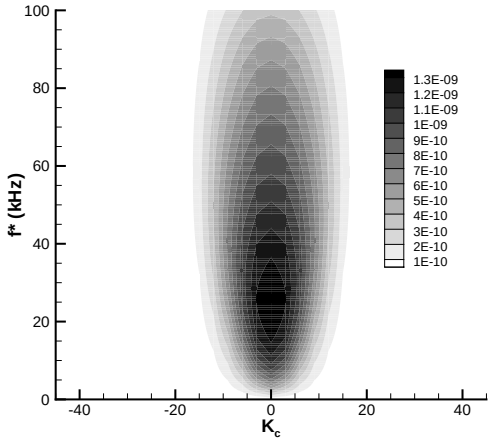

Figure 6.18: Disturbance spectrum showing amplitudes of wall-pressure disturbances in the frequency-azimuthal mode number plane in the center of the forcing hole. A broad spectrum of frequencies and azimuthal modes are introduced into the flow. Sharp cone, $M = 7.95$, $T = 53.35K$.

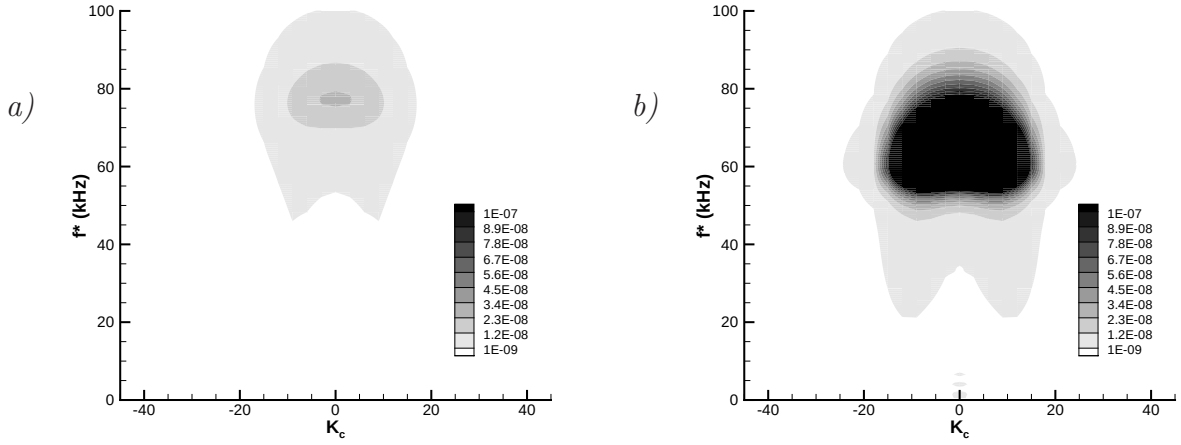

Figure 6.19: Wall-pressure disturbance spectrums for the low amplitude wave packet ($A_{in} = 10^{-5}$). *a)* $x^* = 1.107m$ ($R_x = 2277$) *b)* $x^* = 1.847m$ ($R_x = 2943$). Sharp cone, $M = 7.95$, $T = 53.35K$.

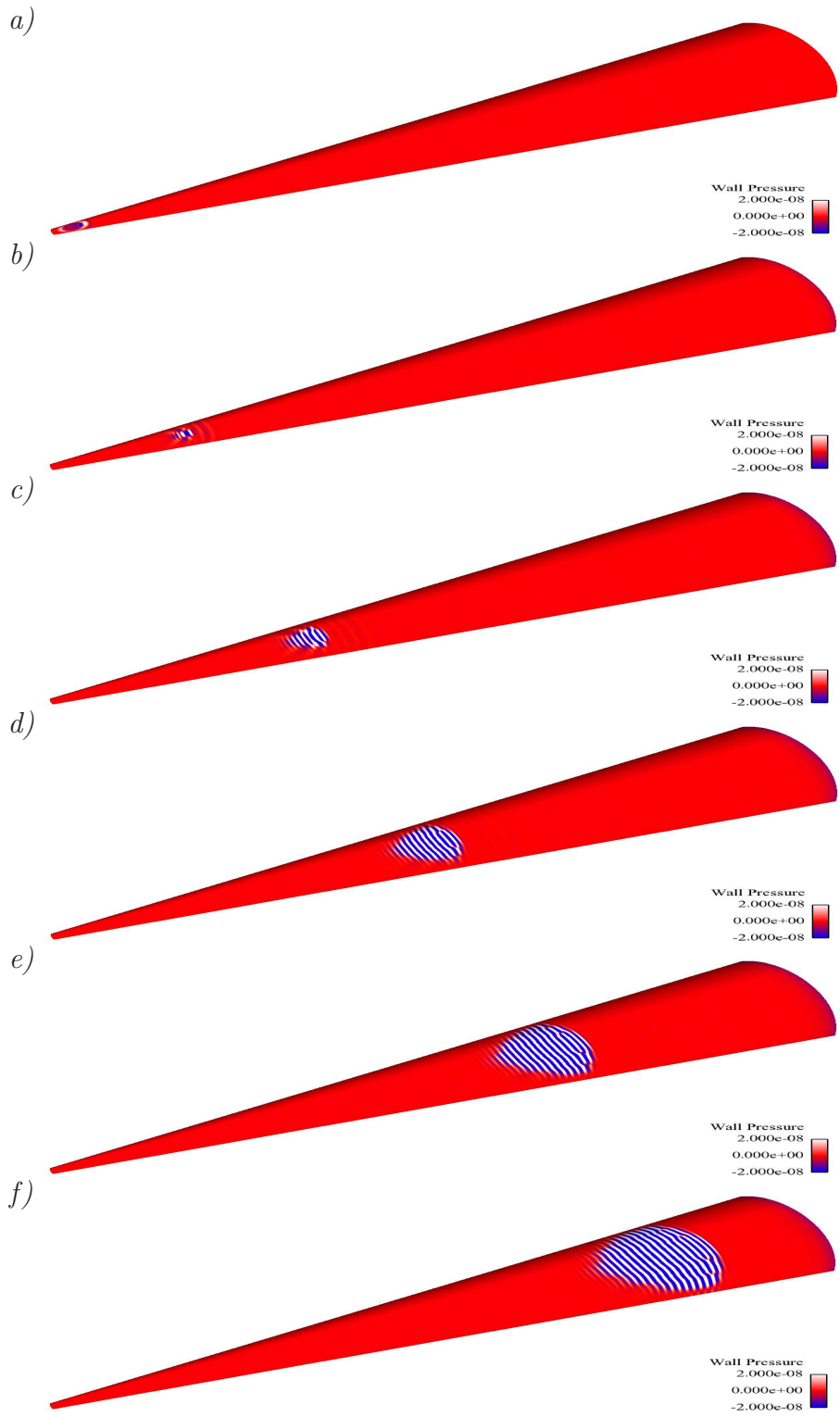

Figure 6.20: Development of wall pressure disturbances in the low-amplitude wave packet on the cone's surface. *a)* t=.02 ($t^* = 17.4 * 10^{-3} ms$) *b)* t=.1 ($t^* = .087 ms$) *c)* t=.2 ($t^* = .174 ms$) *d)* t=.3 ($t^* = .261 ms$) *e)* t=.4 ($t^* = .349 ms$) *f)* t=.5 ($t^* = .436 ms$). Sharp cone, $M = 7.95$, $T = 53.35 K$.

6.3.3 High Amplitude Wave Packet

In order to observe the relevant nonlinear interactions that occur with a broad spectrum of disturbances, a wave packet with amplitude 10^{-2} was simulated. The initial amplitude is small enough that the downstream development of the wave packet is initially governed by LST but large enough that by the end of the computational domain there are strong nonlinear interactions occurring. Figure 6.21 shows contours of the wall pressure disturbance in the frequency-azimuthal mode number plane at $x^* = .89m$ ($R_x = 2042$), $x^* = 1.01m$ ($R_x = 2175$), and $x^* = 1.13m$ ($R_x = 2301$). The structure of the spectrum is similar to the the low amplitude wave packet, and generally follows expected behavior from LST. The most amplified waves are axisymmetric. Weakly three dimensional waves are also amplified, but not as strongly as the 2D modes. Note that the dimensional frequency range of $50 - 100kHz$ seen in the DNS corresponds to a reduced frequency range of approximately $5.8 * 10^{-5} < F < 1.18 * 10^{-4}$.

Figure 6.22 presents wall pressure disturbance spectrums further downstream at $x^* = 1.25m$ ($R_x = 2421$), $x^* = 1.37m$ ($R_x = 2535$), $x^* = 1.61m$ ($R_x = 2749$), and $x^* = 1.85m$ ($R_x = 2947$). The disturbances grow as they travel downstream and eventually reach amplitudes that initiate strong nonlinear interactions. The spectrum initially broadens as the disturbances spread to higher azimuthal modes. The disturbances also seem to spread to slightly lower frequencies which creates 2 "legs" extending downward from the main disturbance. At $x^* = 1.37m$, the spectrum continues to broaden and a low frequency, 2D component appears in the spectrum. At the next location, $x^* = 1.61m$, a higher harmonic of the 2D disturbance component appears and the disturbances continue to spread to higher azimuthal modes near the most amplified frequency. Notably absent is evidence of subharmonic resonance which was reported in the Mach 6 experiments by Bountin *et al.* (2008). Figure 6.23 shows the wall pressure disturbance spectrum at $x^* = 1.85m$ ($R_x = 2947$), with the contour

levels adjusted to be more appropriate for the disturbance levels at this location. With these contour levels, the only relevent disturbances appear to be within a narrow band of frequencies.

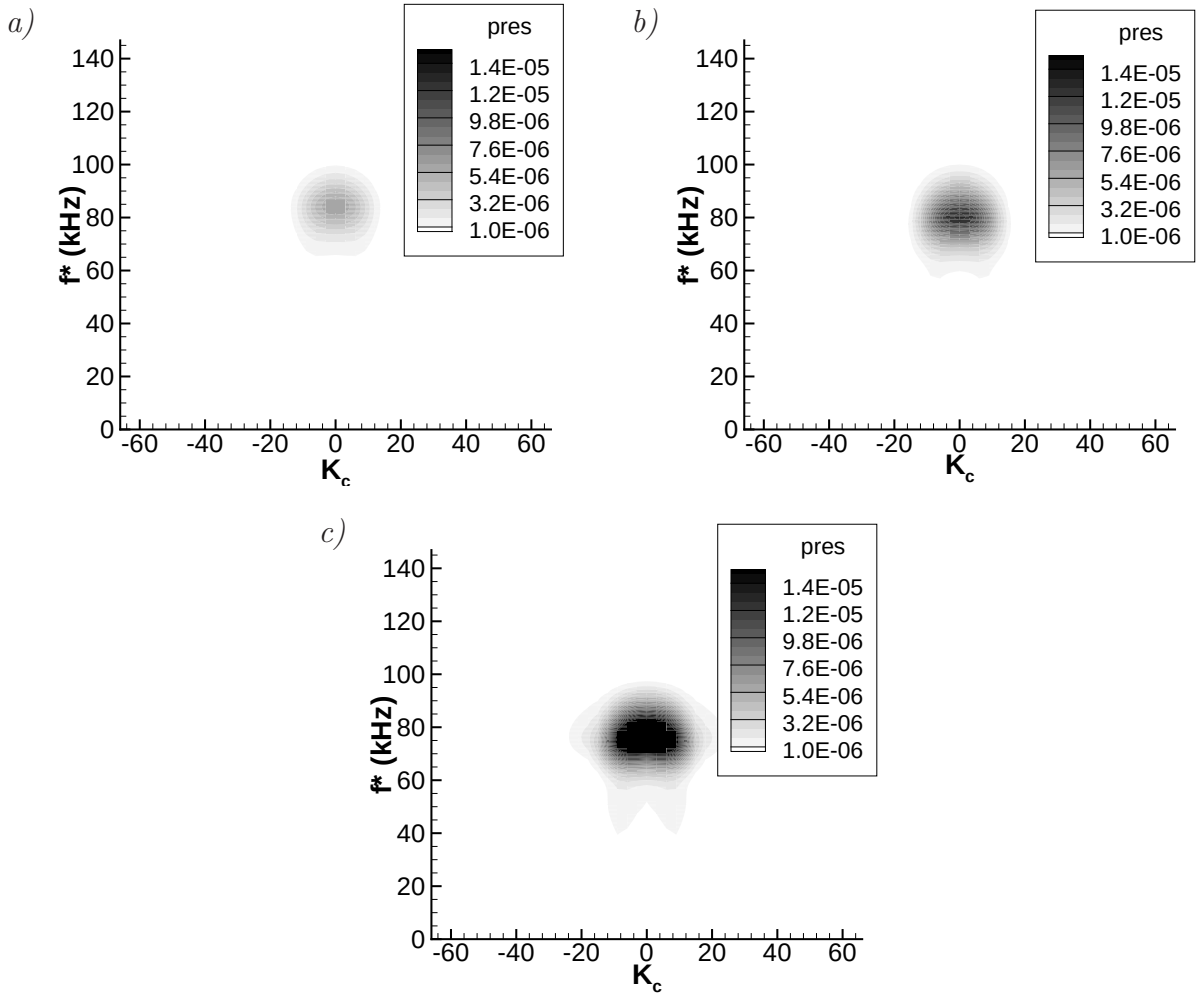

Figure 6.21: Disturbance spectrums of the high-amplitude wave packet shown in contours of wall-pressure disturbance amplitudes in the frequency-azimuthal mode number plane at different downstream locations. Disturbance development is primarily linear for these locations with a narrow band of amplified two-dimensional and slightly oblique waves. *a)* $x^* = .89m$ $(R_x = 2042)$ *b)* $x^* = 1.01m$ $(R_x = 2175)$ *c)* $x^* = 1.13m$ $(R_x = 2301)$. Sharp cone, $M = 7.95$, $T = 53.35K$.

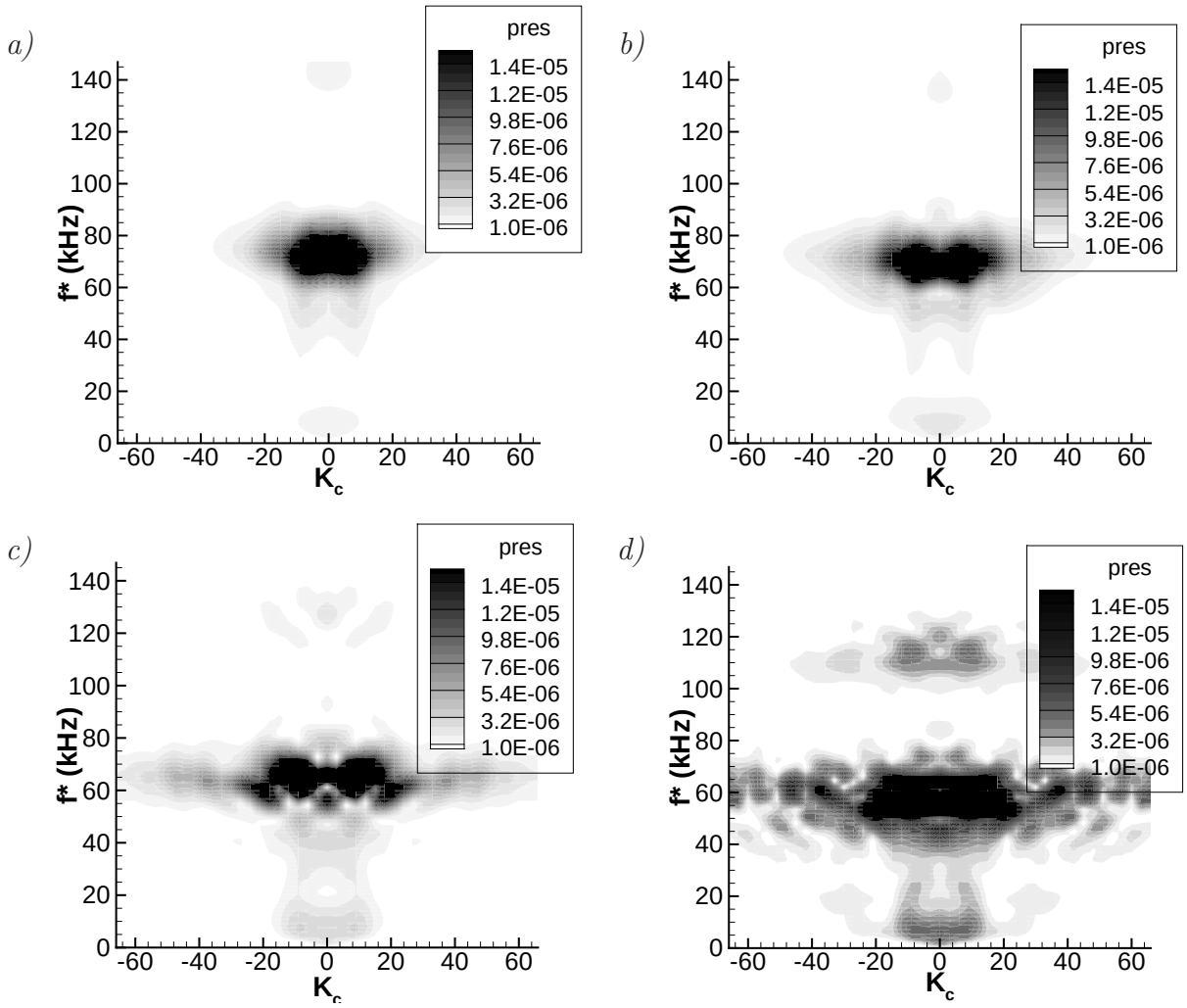

Figure 6.22: Wall-pressure disturbance spectrums of the high-amplitude wave packet at locations farther downstream. Nonlinear interactions begin occurring and become quite strong by the final downstream position. The modes with the most sudden increase in amplitude, an indicator of strong nonlinear growth, are higher azimuthal harmonics in the band of amplified frequencies. *a)* $x^* = 1.25m$ ($R_x = 2421$) *b)* $x^* = 1.37m$ ($R_x = 2535$) *c)* $x^* = 1.61m$ ($R_x = 2749$) *d)* $x^* = 1.85m$ ($R_x = 2947$). Sharp cone, $M = 7.95$, $T = 53.35K$.

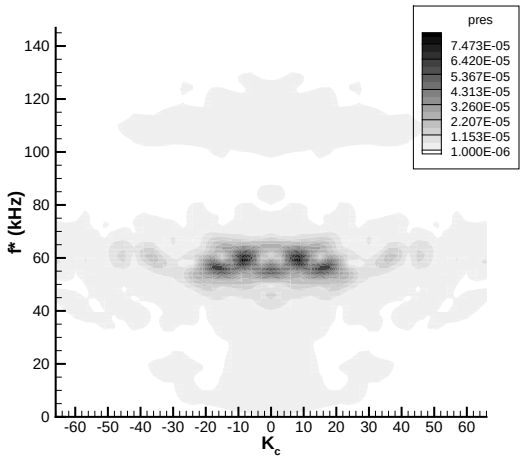

Figure 6.23: Wall-pressure disturbance spectrum of the high-amplitude wave packet at $x^* = 1.85m$ ($R_x = 2947$) with contour levels adjusted. Sharp cone, $M = 7.95$, $T = 53.35K$.

The generation of frequency harmonics and higher azimuthal modes are clear indications of strong nonlinear interactions. The strongest nonlinear interaction, identified by the modes which show sharp increases in amplitude from one downstream position to the next, is the spreading of disturbances to higher azimuthal modes in a relatively narrow band of frequencies. This feature of the spectrum suggests that fundamental resonance between 2D and 3D waves may be the dominant nonlinear interaction for these flow conditions.

The development of the wave packet in physical space on the cone's surface (Figure 6.24) is presented by visualizing contours of wall pressure disturbance. These visualizations give a general picture of the physical extent of the wavepacket and how it develops and grows as it travels downstream. The initial structure of the packet is very similar to the low amplitude case (figure 6.20). The packet is two-dimensional in the center with lower amplitude oblique wave components evident near the azimuthal edges and especially at the tail. The packet spreads in the azimuthal direction and stretches in the streamwise direction as it travels downstream.

The streamwise stretching is due to the superposition of several modes with differing phase velocities. As the wave packet reaches downstream locations where nonlinear interactions start occurring, it becomes increasingly modulated in the spanwise direction. The wavelength of the spanwise modulation is rather large, but near the end of the computational domain there is evidence of shorter azimuthal-wavelength modulations of the main two-dimensional wave front. These are most likely due to the side peaks at high wave numbers evident in the disturbance spectrums in Fourier space.

Detailed views of the late-stage physical structure of the wave packet on the cone surface are shown in Figure 6.25. Wall pressure contours (left) and vortical structures in the wave packet identified with isosurfaces of $Q = 50$ (right) near the end of the computational domain. The Q-surfaces are colored with contours of azimuthal vorticity. The general structure of the packet is similar regardless of the disturbance quantity. The short wave length spanwise modulations are clearly evident in the vorticity contours. It is also apparent that there is a clearly dominant streamwise wavelength associated with the wave packet. At the later downstream locations, the physical nature of the packet is quite different when compared to the low-amplitude case (figure 6.20). Most notable are oblique disturbances emanating from the tail which do not appear in the low-amplitude case.

The space/time evolution of the wave packet is also presented by several instantaneous snapshots of the streamwise distribution of wall-pressure disturbances at the centerline of the wave packet. The initial development of the disturbances is shown in figure 6.26. The nondimensional time differential between each snapshot is $\Delta t = .1$ corresponding to a physical time of $\Delta t^* \approx 0.087ms$. The dashed lines represent an approximate location for the tail and front of the wavepacket. An estimate for the convection speed of the front and tail for the time interval shown in 6.26 can be computed by noting the change in x-location of each end of the wavepacket at each interval Δt. An approximation for the speed of the tail is $\sim 873m/s$ and the speed of the

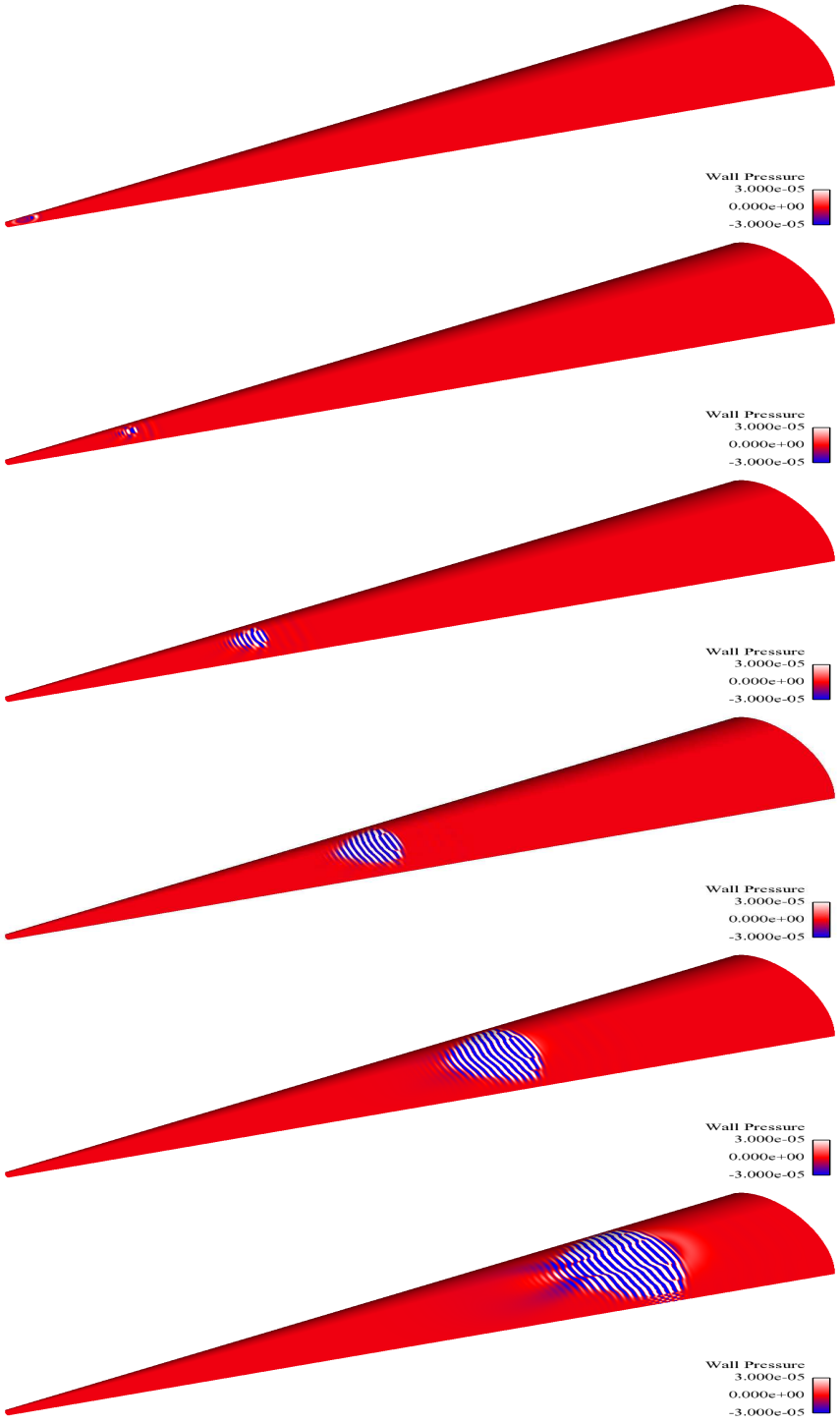

Figure 6.24: Instantaneous contours of wall pressure disturbances in the high-amplitude wave packet on the cone surface illustrating the development of the physical structure of the wave packet and the extent to which it spreads by the time it has reached the end of the computational domain. Sharp cone, $M = 7.95$, $T = 53.35K$.

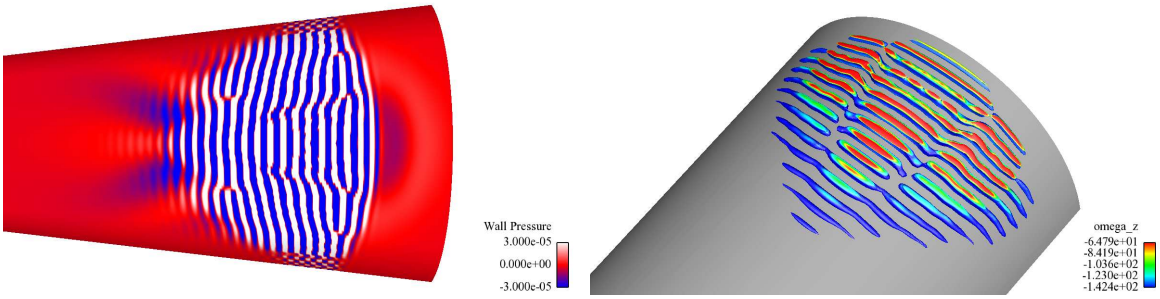

Figure 6.25: (Left) Detailed view of the wall pressure disturbances near the downstream end of the computational domain. (Right) Isosurfaces of $Q = 50$ colored with contours of azimuthal vorticity. The two-dimensional structure of the wavepacket is strongly modulated in the azimuthal direction. Clearly evident in the vorticity contours are the shorter azimuthal wavelength modulations of the structure near the front of the wave packet. Sharp cone, $M = 7.95$, $T = 53.35K$.

front is $\sim 1164m/s$. Since the lines passing through the tail and front of the packet remain straight, it is clear that speeds of the front and tail remain approximately constant. It should be noted that $1164m/s$ corresponds to a nondimensional speed of 1 while $873m/s$ corresponds to a nondimensional speed of .75. One would expect the dominant modes in the wave packet to have phase speeds between $1 - \frac{1}{M} = .875$ and 1. One possible explanation for the low speed of the tail is that these waves have much lower amplitudes than the dominant waves of the packet and therefore it is reasonable to assume that they are most likely oblique waves (which according to LST are less amplified) and thus the phase speed in the streamwise direction would be less than $1 - \frac{1}{M}$ accounting for the wave angle.

The continued space/time development in the centerline of the wave packet is presented in 6.27. Time increases vertically along the left colum and continues to increase going up the right colum. Each frame corresponds to an increase in time of $\Delta t^* \approx 0.087ms$. The left colum ranges from time .8 to 1.2 ($.698ms < t^* < 1.047ms$) and the right from time 1.3 to 1.7 ($1.135ms < t^* < 1.484ms$). It is apparent that as the wave packet develops an increasing number of modes reach amplitudes significant enough to modulate the overall spatial distribution of disturbance. By the final time

instances shown, the character of the packet has changed significantly and there seems to be a highly modulated structure at the front of the packet. This is most likely due to the strong nonlinear interactions which are apparent from the disturbance

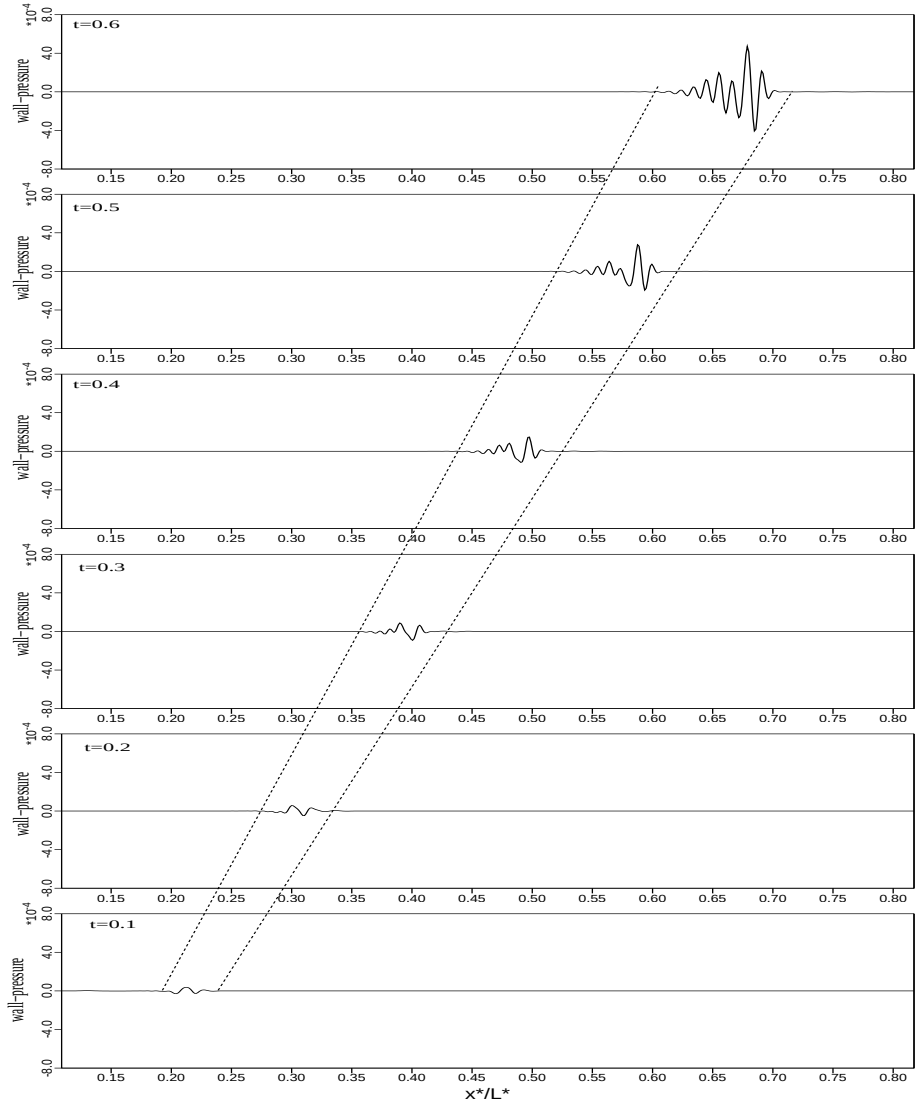

Figure 6.26: Instantaneous snapshots of the streamwise distribution of wall-pressure disturbancesthe in the centerline of the high-amplitude wave packet showing the initial development of the wave packet from $.1 < t < .6$ ($.087ms < t^* < .522ms$). The nondimensional time difference between each frame (time increasing in the vertical direction) is 0.1 corresponding to $\Delta t^* \approx 0.087ms$. Sharp cone, $M = 7.95$, $T = 53.35K$.

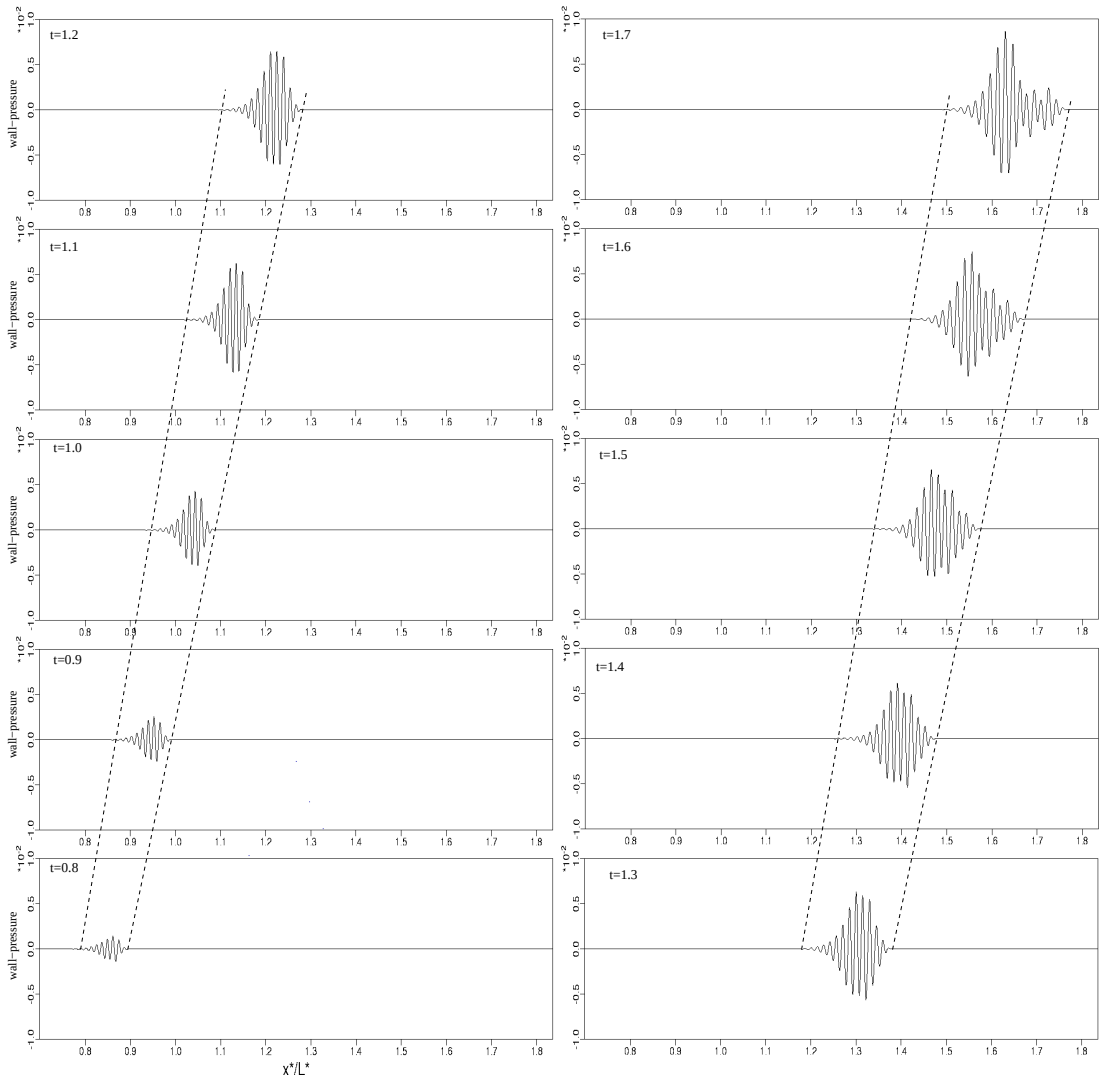

Figure 6.27: Instantaneous snapshots of the streamwise distribution of wall-pressure disturbances in the centerline of the high-amplitude wave packet from (left) time .8 to 1.2 ($.698ms < t^* < 1.047ms$) (right) time 1.3 to 1.7 ($1.135ms < t^* < 1.484ms$). At the later time instances the structure of the front of the packet is highly modulated due to nonlinear interactions. Sharp cone, $M = 7.95$, $T = 53.35K$.

spectrums.

As a comparison, the disturbance spectrums of the high-amplitude wave packet are also shown as contours of the maximum u-velocity disturbance. Note that the y-location where the u-disturbance amplitude is taken is chosen independently for each mode based on the position of the maximum in the wall-normal disturbance amplitude distribution for each mode. Figure 6.28 shows spectrums at the same downstream locations as the wall pressure spectrums (figure 6.21) for the early development of the disturbance modes. The overall structure of the spectrum is similar to the wall-pressure disturbance spectrums, however there is a notable low frequency component that is first visible at $x^* = 1.01m$ ($R_x = 2175$) and is quite apparent by $x^* = 1.13m$ ($R_x = 2301$).

The low frequencies are amplified in approximately the same band of azimuthal modes as the main disturbance component. This component of the disturbance spectrum appears much stronger in the u-velocity in comparison to wall-pressure, where it is not evident at all until $x^* = 1.37m$ ($R_x = 2535$), and still remains at small amplitude levels relative to the strongest disturbances even at the last downstream location. It seems likely that these high amplitude disturbances are caused by the resonance triads identified previously in the pulse simulations (section 6.2). The low frequency modes, which should not be strongly amplified according to LST, appear to grow due to an interaction between a pair of unstable waves within the band of amplified frequencies. As was previously discussed (see section 6.2), the interactions seem to be most relevent for two-dimensional disturbances but are capable of spreading to higher azimuthal modes. This notion is supported by the observation that the maximum frequency difference within the band of strongly amplified disturbances (centered at $\sim 75kHz$ for $x^* = 1.13m$) roughly corresponds to the highest "low" frequency ($\sim 15kHz$) apparent in the spectrum at this position. This is a further confirmation of the existence of the resonance triads given a broad spectrum, 3D disturbance environment.

Disturbance spectrums of u-velocity are also shown further downstream (6.29) at locations corresponding to the wall-pressure spectrums in figure 6.22. At these locations, the strong low-frequency component is apparent. At the final downstream location, $x^* = 1.85m$ ($R_x = 2947$), the low frequency disturbances are a dominant

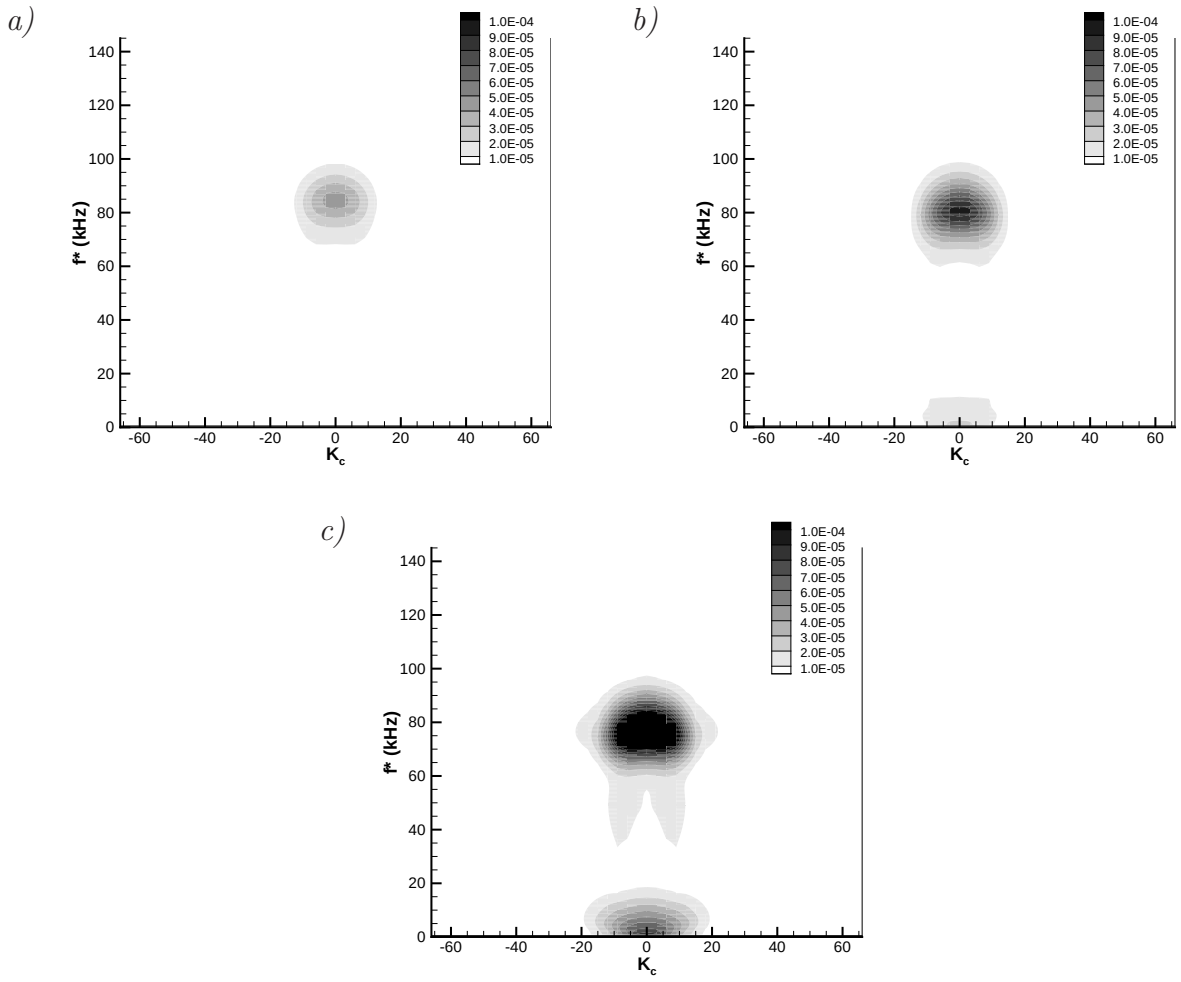

Figure 6.28: Disturbance spectrums of the high-amplitude wave packet shown in contours of u-velocity disturbance amplitudes in the frequency-azimuthal mode number plane at different downstream locations. The y-location at which the disturbances amplitudes are shown is picked based on the maximum in the wall-normal u-velocity amplitude distribution computed for each mode. *a)* $x^* = .89m$ ($R_x = 2042$) *b)* $x^* = 1.01m$ ($R_x = 2175$) *c)* $x^* = 1.13m$ ($R_x = 2301$). Sharp cone, $M = 7.95$, $T = 53.35K$.

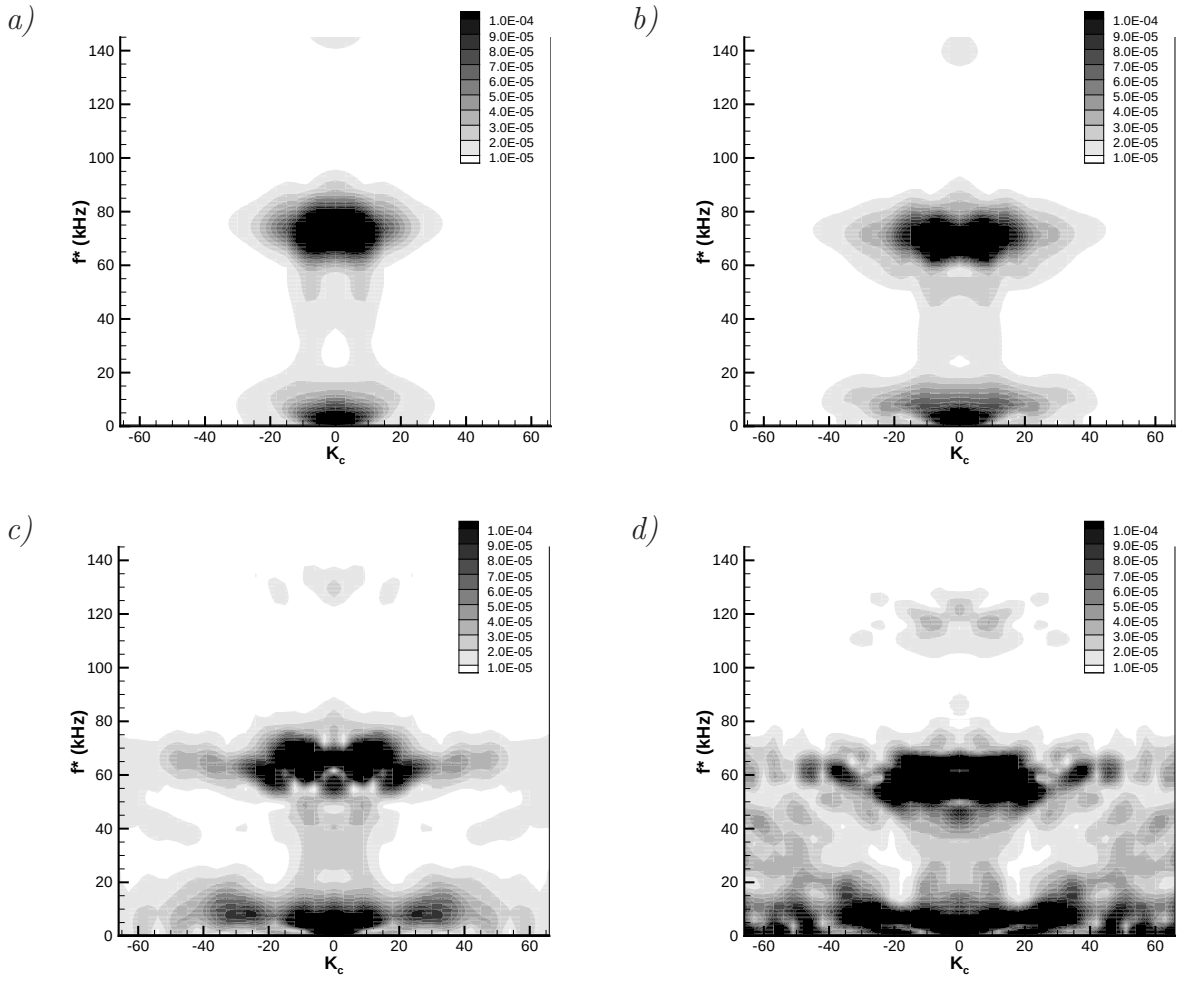

Figure 6.29: u-velocity disturbance spectrums of the high-amplitude wave packet at locations farther downstream. A low-frequency disturbance component appears much stronger in u-velocity compared to wall-pressure. By the final downstream location, the amplitudes of the low-frequency components are comparable to the maximum amplitudes in the entire disturbance spectrum. *a)* $x^* = 1.25m$ $(R_x = 2421)$ *b)* $x^* = 1.37m$ $(R_x = 2535)$ *c)* $x^* = 1.61m$ $(R_x = 2749)$ *d)* $x^* = 1.85m$ $(R_x = 2947)$. Sharp cone, $M = 7.95$, $T = 53.35K$.

feature in the spectrum.

6.3.4 Preliminary Summary of Wave Packet Simulations

Both low amplitude ($A_{in} = 10^{-5}$) and high amplitude ($A_{in} = 10^{-2}$) wave packets were introduced into the flow. The development of the disturbance spectra of the low amplitude wave packet showed no evidence of strong nonlinear interactions. The most amplified disturbances remained two-dimensional ($k_c = 0$) throughout the domain. At the final downstream location, the spectrum has spread to higher azimuthal modes within the band of unstable frequencies. The amplitude of modes with $k_c = 20$ is within one order of magnitude of the largest disturbances. There are also relatively low amplitude "legs" stretching to lower frequencies at small k_c. The physical nature of the wave packet is highly 2D in the center with oblique waves in the tail (especially in the initial development). In the initial stages of the development of the wave packet, the wave angles appear to be of 45° or greater (see figure 6.20 b). This is likely due to the fact that even at small azimuthal mode numbers, the wave angles can be large due to the small local circumference of the cone. As the packet travels downstream the 2D component becomes dominant.

The high amplitude wave packet initially develops similarly to the low amplitude case. However, as the amplitudes grow, strong nonlinear interactions become apparent. Based on the wall pressure disturbance, the strongest nonlinear growth appears to be in waves with $k_c > 20$ within the primary band of unstable frequencies. The generation of the second harmonic of the most dominant frequencies, as well as a low frequency component are also evident, but fairly weak. This suggests that fundamental resonance of 2D and 3D waves may be a dominant mechanism for these flow conditions. Spectra of u-velocity disturbances show similar behavior as wall-pressure with the exception of the low-frequency component becoming much more pronounced. The low-frequencies reach amplitudes similar to those of the strongest disturbance

modes in the spectrum. The low-frequency band of disturbances spreads to nearly all higher azimuthal mode numbers resolved in the simulation. These disturbances may be related to the resonance triads discussed in section 6.2 which appear to be caused by an interaction of two modes that are close in frequency. The physical structure of the nonlinear wave packet is generally two-dimensional with oblique waves evident in the tail. By the end of the computational domain the wave structures have become modulated in the azimuthal direction.

6.4 Controlled Transition Simulations

6.4.1 Disturbance Generation and Post Processing

The simulations presented in this chapter feature controlled disturbance input generated by time harmonic wall-normal blowing and suction over a disturbance strip near the upstream end of the computational domain. The generation of these disturbances is governed by a boundary condition for the v-velocity at the wall,

$$v(x, y = 0, \varphi, t) = A(x_p)cos(-\omega t + \theta)cos(k_c\varphi), \tag{6.3}$$

with x_p defined as

$$x_p = \frac{2x - (x_2 + x_1)}{x_2 - x_1} \quad -1 < x_p < 1. \tag{6.4}$$

The streamwise distribution for the velocity, $A(x_p)$, is a fifth order polynomial representing a dipole which is smooth everywhere including the endpoints (see Harris (1997)) and is shown schematically in figure 6.30.

The disturbances are tracked in the downstream direction according to their mode numbers n and k, where n corresponds to the harmonic in time and k corresponds to the multiple of the fundamental azimuthal mode number. Since Fourier modes are used in the azimuthal discretization (see section 3.2), the time dependent behavior of each azimuthal mode is output separately for each azimuthal mode from the code.

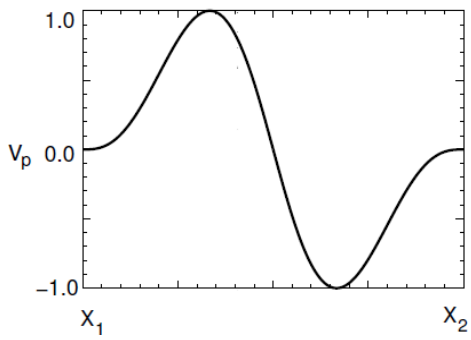

Figure 6.30: Schematic of the streamwise velocity distribution in the forcing slot used for inputting controlled disturbances.

In order to decompose the time history into temporal Fourier harmonics, fast Fourier transforms are employed in post-processing according to

$$\begin{aligned}\hat{\phi}_0 &\sim \frac{1}{2n_t}\sum_{t=0}^{n_t-1}\phi_t \\ \hat{\phi}_n &\sim \frac{1}{n_t}(\sum_{t=0}^{n_t-1}\phi_t cos(\frac{2\pi nt}{n_t}) + \sum_{t=0}^{n_t-1}\phi_t sin(\frac{2\pi nt}{n_t})).\end{aligned} \tag{6.5}$$

In equation 6.5, $\hat{\phi_{0,0}}$ represents a time and azimuthal averaged flow quantity. The average flow field is used to calculate the skin friction coefficient,

$$c_f = 2\frac{\bar{\mu_w}}{Re_{edge}}\frac{\partial\bar{u}}{\partial y}|_w. \tag{6.6}$$

The computed skin friction can be compared with the theoretical turbulent value suggested by White (1991),

$$c_{f,plate} \approx \frac{.455}{S^2 ln^2(\frac{.06\bar{\mu}_e}{S\mu_w}Re_x\sqrt{\frac{T_e}{T_w}})}, \tag{6.7}$$

with

$$S = \frac{1}{\arcsin A \arcsin B}\sqrt{\frac{\bar{T_w}}{\bar{T_e}}} - 1 \tag{6.8}$$

and A and B are defined by

$$A = \frac{2a^2 - b}{\sqrt{b^2 + 4a^2}} \qquad B = \frac{b}{\sqrt{b^2 + 4a^2}}$$
$$a = \sqrt{\frac{\gamma - 1}{\gamma} M_e^2 \frac{\bar{T}_e}{\bar{T}_w}} \qquad b = \frac{\bar{T_{aw}}}{\bar{T}_w} - 1. \tag{6.9}$$

The overbar represents an average flow quantity while the subscript w denotes the wall values and the subscript e denotes the boundary layer edge values. However, the adiabatic wall temperature ($\bar{T_{aw}}$), is not known and must be estimated according to the turbulent recovery factor, $r_{turb} \sim Pr^{1/3} \sim 0.9$. An additional correction factor must also be included because the skin friction estimate is only applicable for flows over a flat plate. For a cone, White (1991) suggests the correction $c_{f,cone} = 1.15 * c_{f,plate}$.

Within the context of fluid dynamics simulations, it is also useful to look at flow structures which can be visualized by isosurfaces of the Q-criterion. According to Hunt *et al.* (1988), Q relates the strain rate and rotation rate with positive Q values denoting higher rotation rate than strain rate and thus identifying a vortex core. Q is defined as the second invariant of the velocity gradient tensor and can be computed according to

$$Q = \frac{1}{2}(W_{ij}W_{ij} - S_{ij}S_{ij}), \quad S_{ij} = \frac{1}{2}(\frac{\partial u_i}{\partial x_j} + \frac{\partial u_j}{\partial x_i}), \quad W_{ij} = \frac{1}{2}(\frac{\partial u_i}{\partial x_j} - \frac{\partial u_j}{\partial x_i}). \tag{6.10}$$

6.4.2 Fundamental Resonance Mechanism

The wave packet simulations (see section 6.3) provided evidence of possible fundamental resonance between two-dimensional and three-dimensional waves. Fundamental (K or Klebanoff type) breakdown, first shown experimentally for incompressible flows by Klebanoff *et al.* (1962), is a secondary instability mechanism governed by a two-dimensional primary wave (mode (1,0)) which interacts nonlinearly with a symmetric pair of oblique waves at the same frequency (modes (1,±1)). A wave number diagram

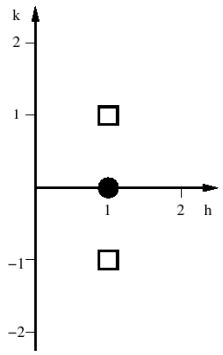

Figure 6.31: Wave number diagram for fundamental resonance. Frequency harmonic, h, on the abscissa and azimuthal mode number, k, on the ordinate. Closed symbols represent the primary disturbance and open symbols the secondary disturbance.

for this mechanism is presented in figure 6.31. Fundamental resonance can be studied in a numerical simulation or experiment by seeding both the primary and secondary disturbance waves (modes (1,0) at a amplitude, and (1,1) at a low amplitude). Nonlinear interaction causes the oblique secondary waves to rapidly amplify. The large amplitude two-dimensional primary wave becomes modulated in the spanwise direction as the oblique disturbances reach large amplitudes. This modulation leads to the formation of so-called Λ-vortices which appear in an aligned pattern due to the common frequency of the two and three-dimensional disturbances. The tips of the Λ structures begin lifting from the surface while the legs go towards the wall and hairpin structures appear on the tip of the Λ vortices. Eventually, the structures break down to smaller scales as the flow reaches a fully turbulent state.

6.4.3 Parameter Study

The strength of fundamental resonance will depend strongly on the wave angle of the secondary disturbance wave. The cone geometry complicates this issue because for a constant azimuthal mode number the wave angle changes in the downstream direction. In the context of the numerical simulations, only a specific azimuthal

mode number can be forced. Thus, a parameter study was performed to determine the azimuthal mode number with the strongest resonant growth. The primary, two-dimensional disturbance wave, was chosen based on the linear behavior discussed in section 6.2. The parameter study consisted of a series of low-resolution simulations in which different azimuthal-modes ($10 < k_c < 60$) were forced at a low amplitude in addition to a two-dimensional primary disturbance at a moderate amplitude.

A summary of the results of these simulations is presented in figure 6.32. The streamwise evolution of the amplitude of mode (1,1) for different azimuthal mode numbers is shown as well as the linear behavior which was extracted from simulations only forcing mode (1,1) at a low amplitude. Several of these modes depart from their linear behavior and experience resonant growth. Waves with moderately high azimuthal mode numbers ($40 < k_c < 52$) experience the strongest resonant growth. The effect of the amplitude of the primary disturbance, mode (1,0), was also studied. Figure 6.32 presents the amplitude development of mode (1,1) ($k_c = 50$) for several different primary wave amplitudes. As expected within the context of secondary instability theory, the onset and strength of the fundamental resonance is entirely dependant on the amplitude of the primary wave. With increasing primary wave amplitude, the resonance location moves upstream. From this information, it is also possible to explain the broad side bands appearing in the wave packet spectra (see section 6.3) near the most dominant axisymmetric frequency. Although higher $k_c's$ have stronger resonant growth, due to the initial linear behavior they have much lower amplitudes at the resonance location than less oblique waves. Thus, in the wave packet the initial oblique component of the spectrum appears at relatively low wave numbers and higher azimuthal modes begin appearing somewhat further downstream.

Figure 6.33 contains a comparison of the secondary growth rate ($-\sigma_i$) after resonance of mode (1,1) at $R_x = 2225$. At this position it is clear that the strongest resonant growth is for $k_c = 46$. It is also useful to look at contours of $-\sigma_i$ in the $K_c - R_x$ plane (figure 6.33) to understand the growth at different downstream locations. From

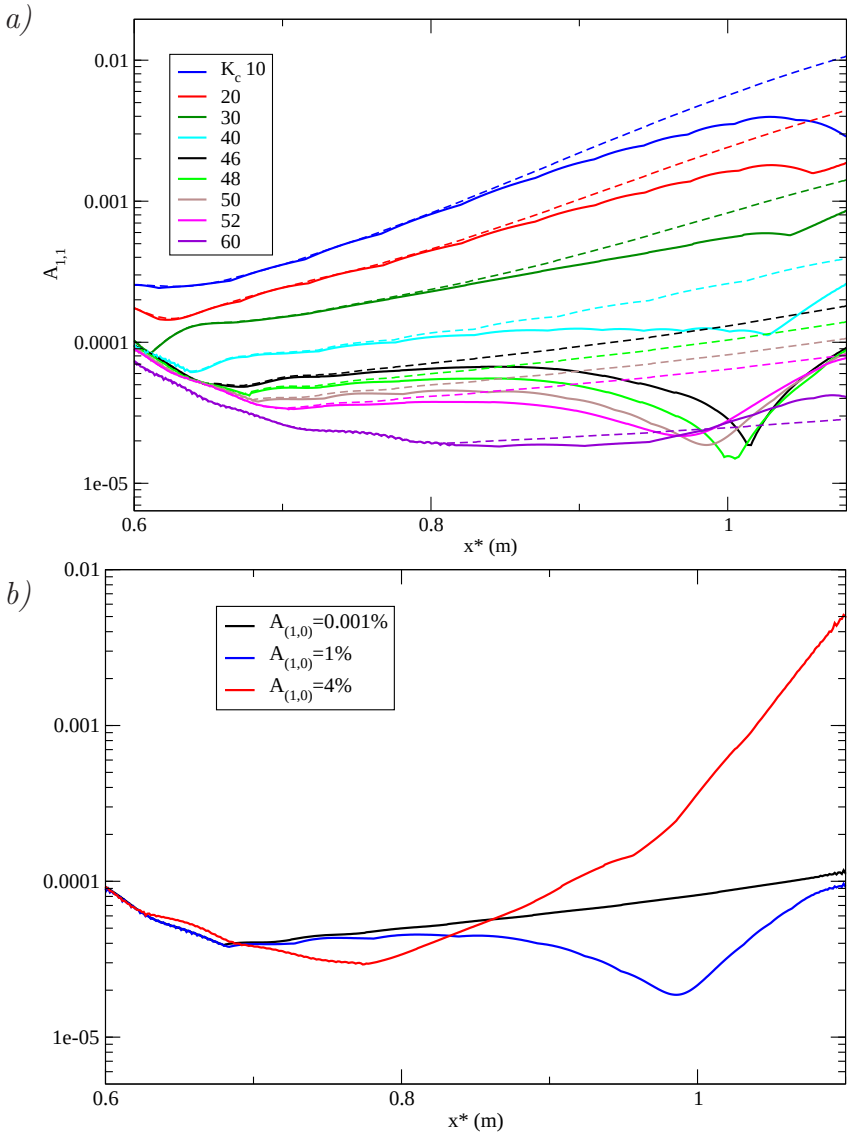

Figure 6.32: *a)* Downstream development of ρ'_{max} amplitudes illustrates departure from linear behavior and the onset of fundamental resonance with the strongest growth for azimuthal modes $40 < k_c < 52$. *b)*Comparison of amplitude development of mode (1,1) for $k_c = 50$ with different primary wave (1,0) amplitudes shows that as the amplitude of primary wave is increased the resonance point moves upstream. Sharp cone, $M = 7.95$, $T = 53.35K$.

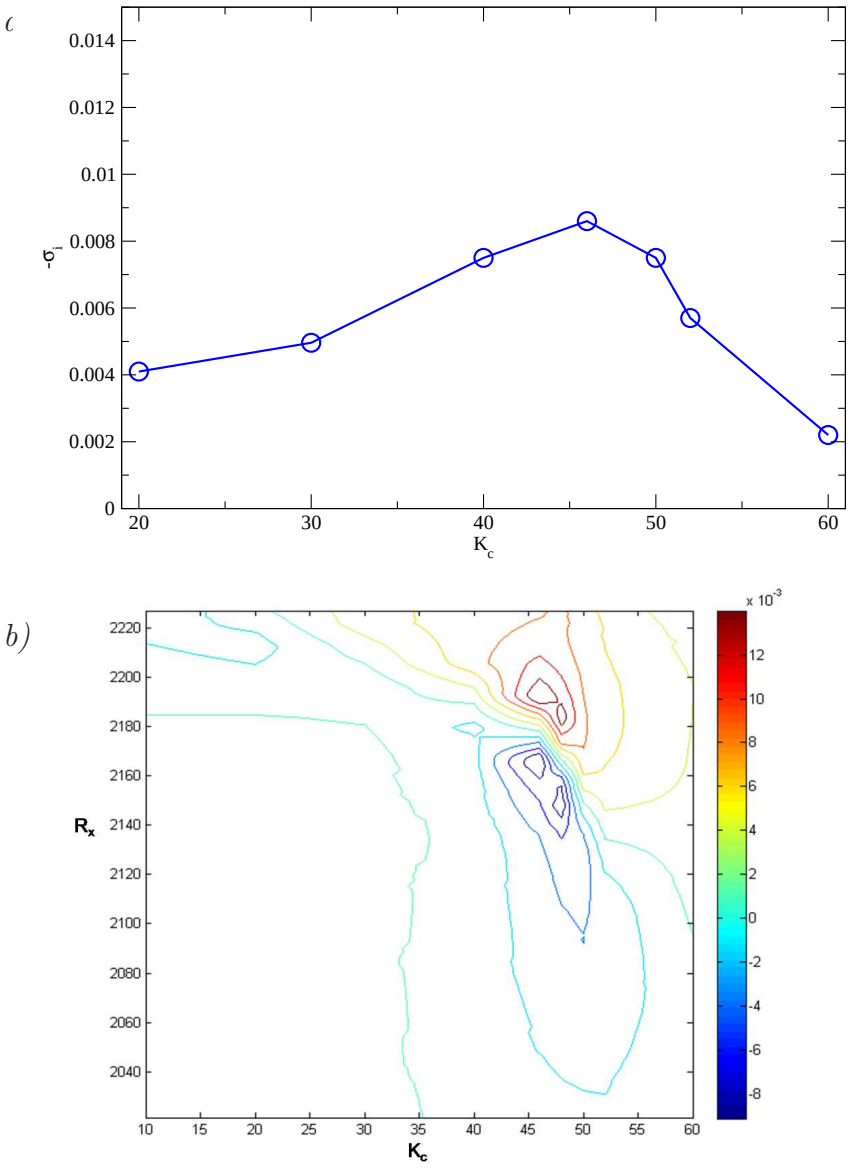

Figure 6.33: *a)* The growth rate of mode (1,1), $-\sigma_i$, after resonance ($R_x = 2225$) shows the strongest resonant growth is for $k_c < 46$. *b)* Contours of the secondary growth rate in the $K_c - R_x$ plane show strong resonant growth for $40 < k_c < 50$ beginning near $R_x = 2180$. Sharp cone, $M = 7.95$, $T = 53.35K$.

this plot, it is also apparent that the strongest resonance is for $40 < K_c < 50$ and that the resonance begins near $R_x \approx 2180$.

6.4.4 Breakdown Simulations: Fundamental Breakdown

Based on the results of the parameter study, a series of simulations with increased resolution were performed forcing both an axisymmetric mode (1,0) with non-dimensional frequency $F = 9.1 \times 10^{-5}$ as well as a symmetric pair of oblique waves at the same frequency (modes $(1, \pm 1)$) with azimuthal mode number $k_c = 46$. A summary of the simulations is presented in table 6.3.

Name	Nx	Ny	Nz (modes)	Grid size	Domain length in x [m]	$A_{1,0}$	$A_{1,1}$
FB1	2000	300	16	$19.8e^6$	$0.5 < x* < 1.433$	$4e^{-2}$	$1e{-}3$
FB2	2000	300	33	$39e^6$	$0.5 < x* < 1.433$	$4e^{-2}$	$1e{-}3$
FB3	2000	300	33	$39e^6$	$0.5 < x* < 1.433$	$4e^{-2}$	$1e{-}2$
FB4	3500	300	82	$171.15e^6$	$0.55 < x* < 1.47$	$5e^{-2}$	$5e{-}2$
FB5	2400	300	55	$39.6e^6$	$1.04 < x* < 1.52$	n/a	n/a
FB6	3000	300	82	$73.8e^6$	$1.04 < x* < 1.53$	n/a	n/a

Table 6.3: Summary of parameters used in the spatial simulations. Sharp cone, $M = 7.95$, $T = 53.35K$.

The downstream development of the u-velocity disturbance amplitudes for simulation *FB1* is shown in figure 6.34. The onset of fundamental resonance is apparent. Modes (1,1) and (0,1) grow nonlinearly and eventually overtake the primary disturbance wave (1,0). There is also a generation of higher harmonics, modes (2,0) and (2,1), which was observed in the experiments by Stetson & Kimmel (1992*b*). When modes (0,1) and (1,0) approach the amplitude of the primary disturbance, mode (1,0), all higher modes rapidly grow as the transition process becomes strongly nonlinear. Flow structures identified by isosurfaces of Q=200 (figure 6.35) show the characteristic aligned Λ-structures developing and the formation of hairpin vortices near the end of the domain. The structures show that the flow remains extremely coherent.

The average skin friction coefficient (figure 6.34) shows an initially strong increase just before $x^* = 0.8m$. However, the skin friction surprisingly decreases sharply to almost the laminar value before slightly rising again near the end of the computational domain. In order to rule out a lack of adequate azimuthal resolution, simulation *FB2* was performed with 33 modes. Figure 6.36 shows identical behavior of the skin friction and amplitude development when compared to simulation *FB1*. Thus, it can be concluded that the spanwise resolution in simulation *FB1* was adequate.

Careful examination of the streamwise evolution of the skin friction and disturbance amplitudes revealed that the peak in the skin friction corresponds to the streamwise location where mode (1,0) saturates and starts decreasing in amplitude. The skin friction rises again only after many higher modes reach amplitudes within one to two orders of magnitude of the strongest disturbances. Due to the initial decay of mode (1,1) the amplitude at the resonance point is nearly two orders of magnitude lower than the initial forcing and therefore it only exceeds the amplitude of the primary disturbance near the end of the computational domain. To further confirm the dependence of the initial rise in the skin friction solely on mode (1,0), a simulation only allowing one higher azimuthal mode was performed. The development of the amplitudes and skin friction are presented in figure 6.37. As predicted, the skin friction initially rises identically to simulations FB1 and FB2. Thus, simulation *FB3* was performed with the initial amplitude of the secondary disturbance (mode (1,1)) increased to 10^{-2}.

Figure 6.38 shows the development of u-velocity disturbance amplitudes for simulation *FB3*. In comparison to *FB2*, mode (1,1) reaches a large amplitude further upstream (due to the increased initial amplitude) which causes stronger nonlinear interactions and growth of higher modes. The average skin-friction coefficient (see figure 6.38) still includes the initial rise associated with the large amplitude 2D disturbances, and a subsequent fall associated with its saturation. However, the fall is not as drastic and the skin friction coefficient again rises rapidly at $x^* \approx 1.25m$ as higher

modes experience strong amplification and reach large amplitudes. The saturation and decrease in amplitude of the 2D modes is likely due to energy being transferred to three-dimensional modes.

The flow visualizations (figure 6.39) reveal remarkable similarities to fundamental

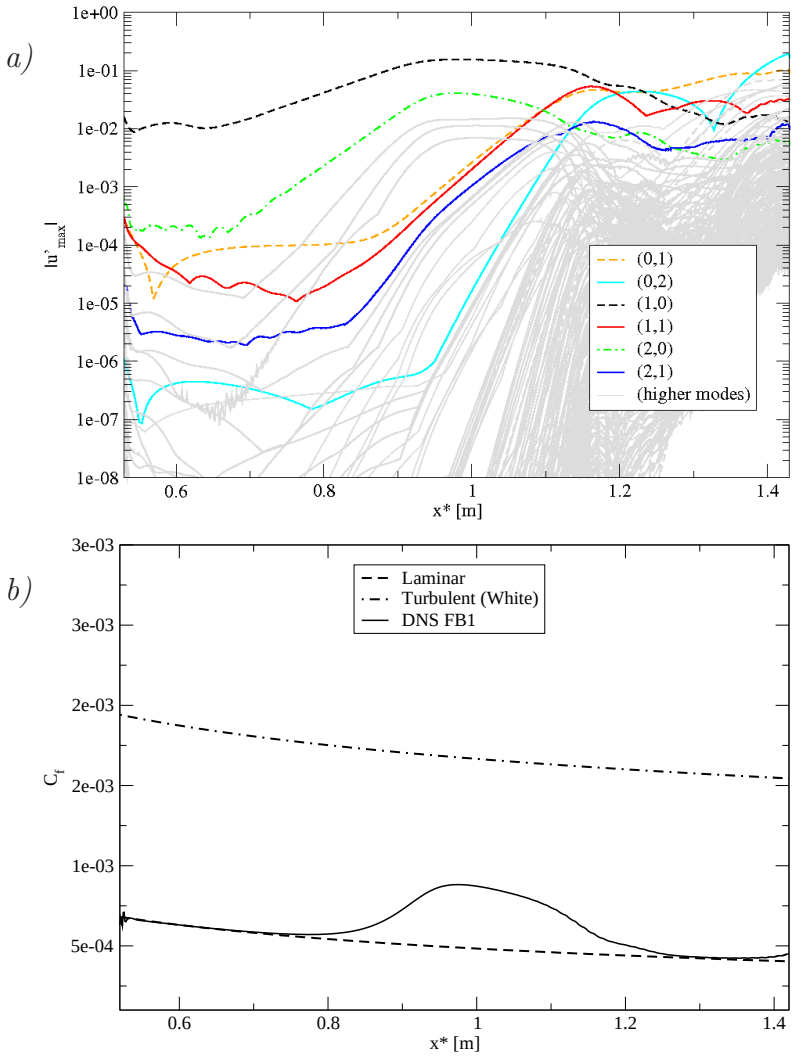

Figure 6.34: *a)* Streamwise development of u-velocity disturbance amplitudes for simulation *FB1* show the onset of transition via fundamental resonance. Modes (0,1) and (1,1) grow nonlinearly and overtake the primary wave (1,0). *b)* Time and azimuthal averaged skin friction coefficient, c_f, first rises in response to the large amplitude 2-D disturbance. However it then falls again due to saturation of mode (1,0). Sharp cone, $M = 7.95$, $T = 53.35K$.

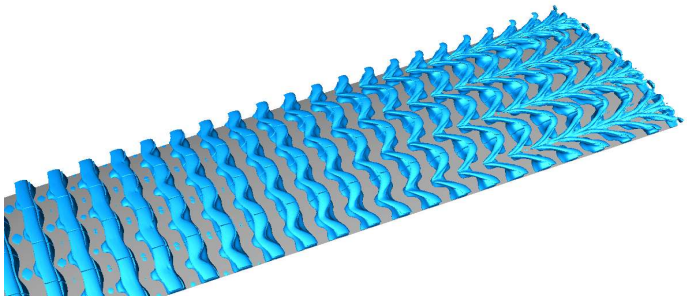

Figure 6.35: Flow structures identified by isosurfaces of Q=200 for simulation *FB1*. Λ-vortices develop and hairpin vortices begin forming at the tip of the Λ structures near the end of the domain. Sharp cone, $M = 7.95$, $T = 53.35K$.

breakdown in incompressible flows (c.f. Kachanov (1994)). The 2-D disturbance becomes modulated in the azimuthal direction as oblique waves experience nonlinear amplification. This modulation eventually forms the characteristic aligned Λ-vortex pattern with the tips lifting from the cone surface. The contours of azimuthal vorticity in the symmetry plane (figure 6.39) show the shear layer "rolling up" as the flow breaks up into smaller scales and becomes less coherent. One key feature of this transition process is the vast extent in the downstream direction over which it takes place (relative to the incompressible case). The formation and eventual breakup of the Λ-structures occurs over quite a large number of fundamental wave lengths.

In an attempt to completely eliminate the dip in skin friction, as well as to reach a fully turbulent state by the end of the computational domain, simulation *FB4* was performed with increased forcing amplitudes of both the primary and secondary disturbances. Both modes (1,0) and (1,1) were forced with $A_{1,0} = A_{1,1} = 5{*}10^{-2}$ and the extent of the downstream domain was increased slightly (see table 6.3). Results from simulation *FB4* showed particularly interesting behavior. Downstream development of the u-velocity disturbance amplitudes and skin friction coefficient are presented in figure 6.40. It appears that the high amplitude forcing mode (1,1) generates a high amplitude mode (0,2) which becomes the most dominant disturbance for this simulation. This alters the development of the disturbances and also produces mode

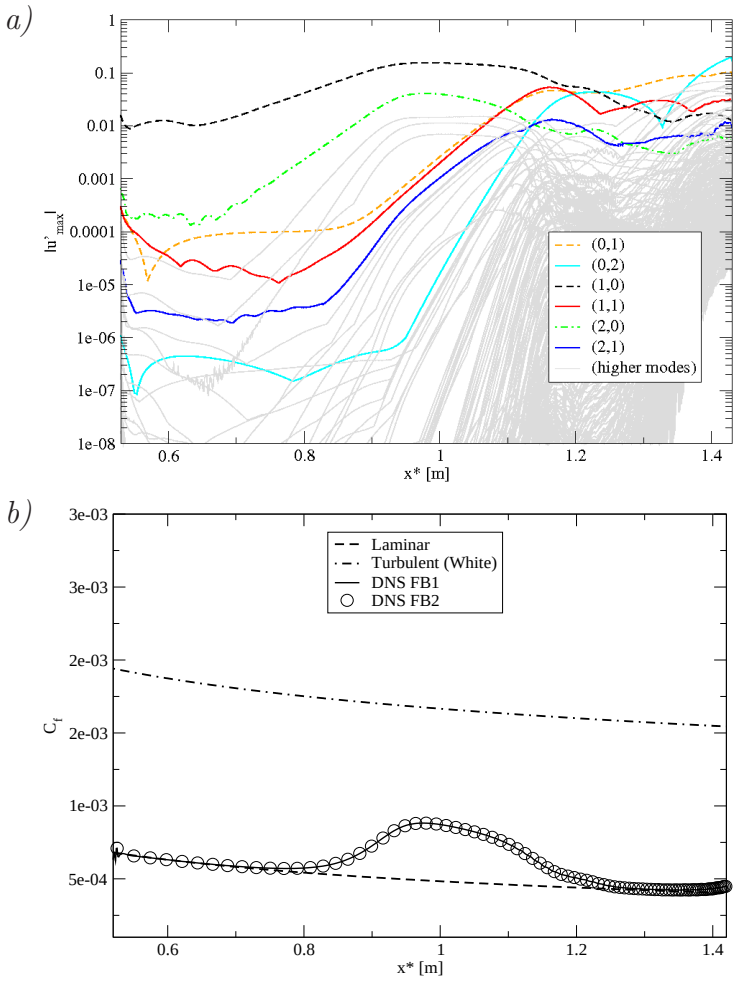

Figure 6.36: *a)* Streamwise development of u-velocity disturbance amplitudes for simulation *FB2* *b)* Time and azimuthal averaged skin friction coefficient, c_f, shows identical behavior to the lower resolution simulation FB1. Sharp cone, $M = 7.95$, $T = 53.35K$.

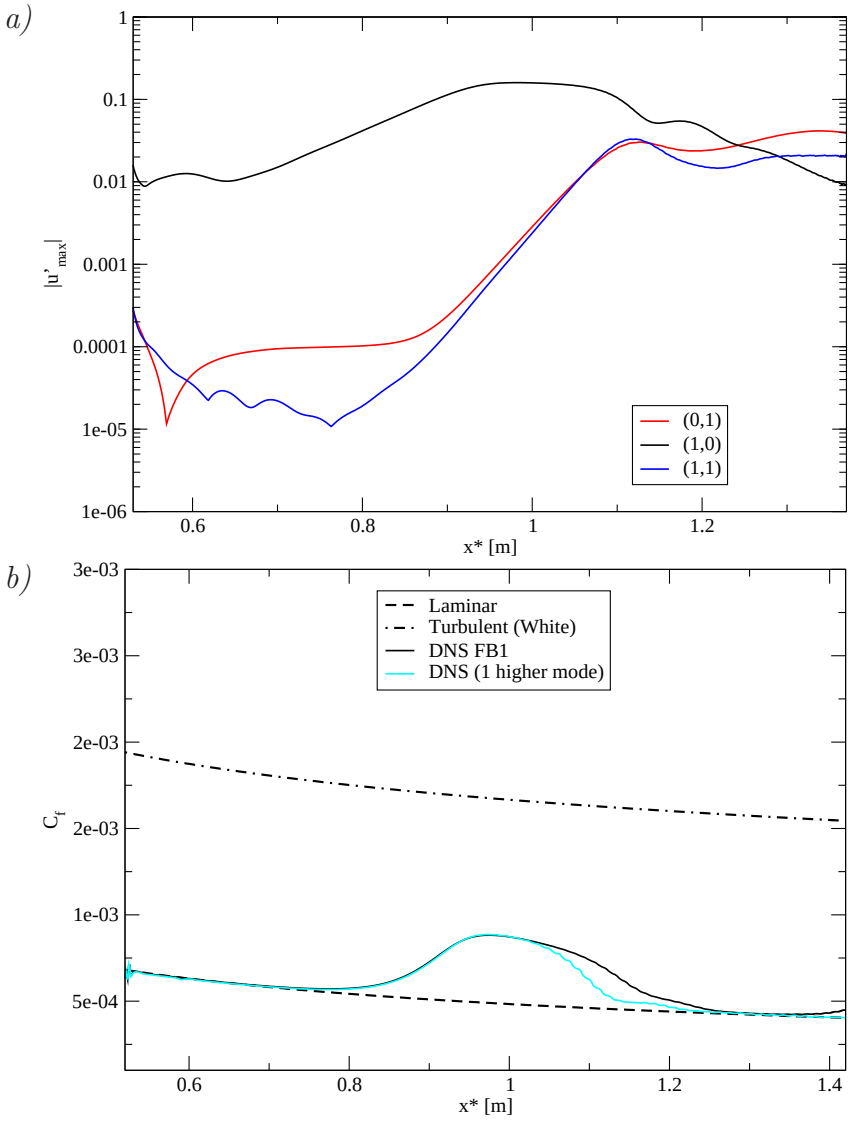

Figure 6.37: *a)* Streamwise development of u-velocity disturbance amplitudes for fundamental resonance only allowing only one higher azimuthal mode. *b)* Average skin friction coefficient for fundamental resonance simulation allowing only one higher spanwise mode. The initial rise is only governed by the primary, 2D disturbance wave. Sharp cone, $M = 7.95$, $T = 53.35K$.

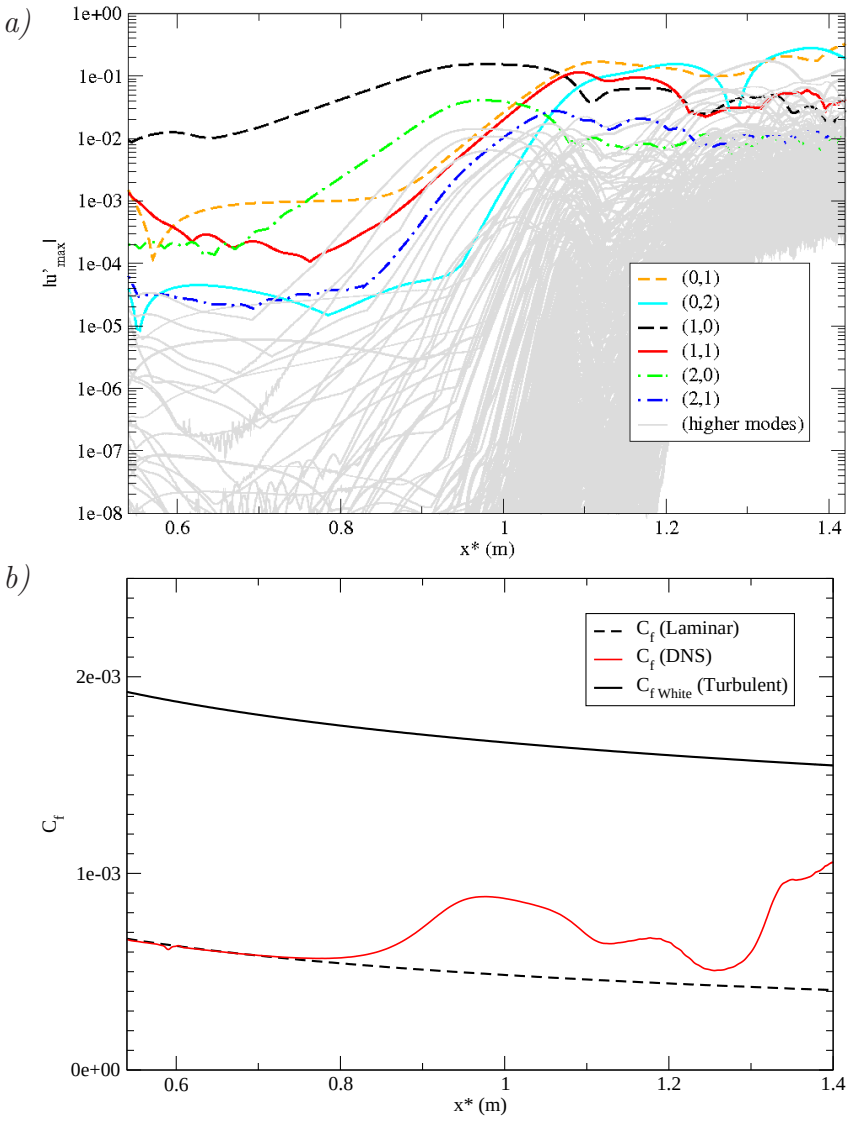

Figure 6.38: *a)* The streamwise development of u-velocity disturbance amplitudes for simulation *FB3*. Increased initial amplitude of the secondary wave causes it to overtake the primary wave further upstream compared to simulation *FB2*. *b)* Averaged skin friction coefficient, c_f, for simulation *FB3*. $A_{1,0} = 4 * 10^{-2}$, $A_{1,1} = 10^{-2}$. Sharp cone, $M = 7.95$, $T = 53.35K$.

a)

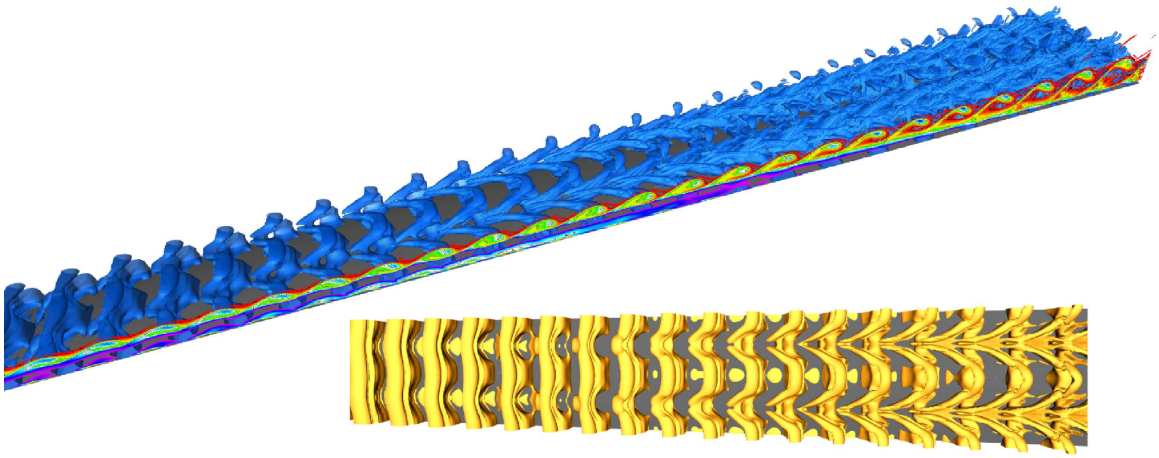

b)

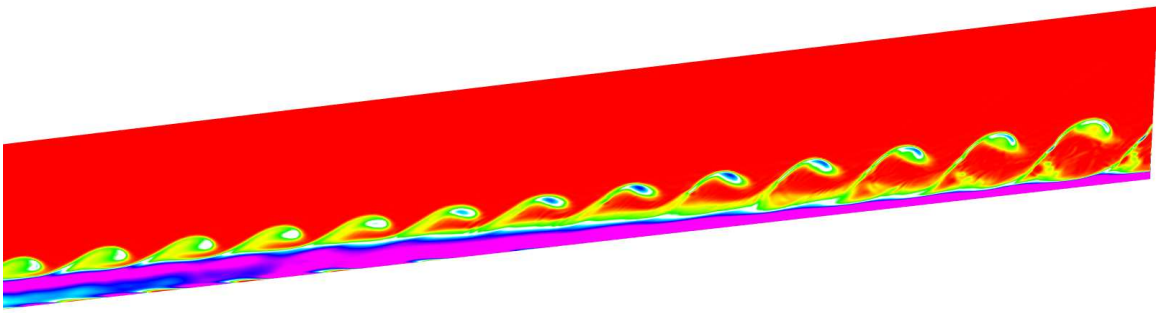

Figure 6.39: *a)* (top) Instantaneous flow visualization with isosurfaces of the Q-vortex identification criterion (Q=300) and countours of azimuthal vorticity in the symmetry plane. Λ-structures develop and begin breaking up into small scales as the flow transitions. (bottom) Top view of the flow visualized with isosurfaces of Q=300 clearly showing the development of Λ-structures. *b)* Contours of azimuthal vorticity in the symmetry plane show the shear layer "rolling up." Sharp cone, $M = 7.95$, $T = 53.35K$.

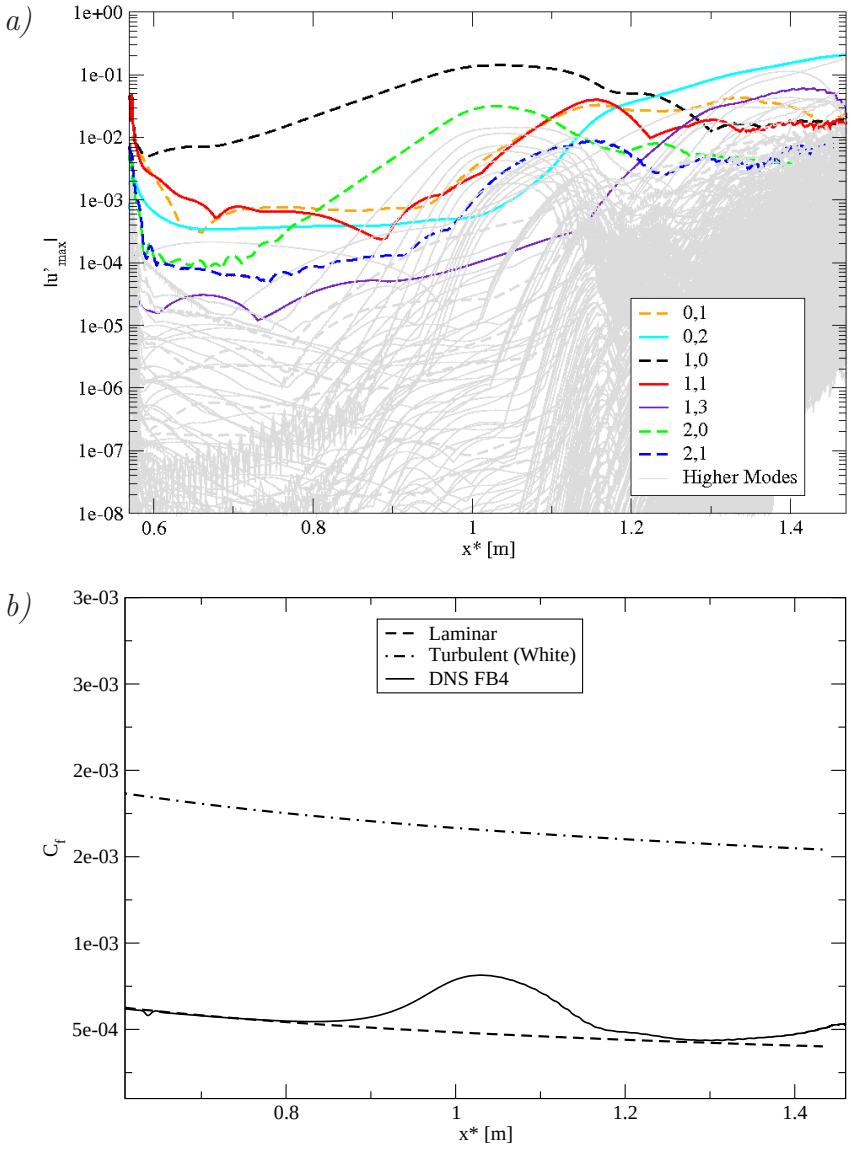

Figure 6.40: *a)* Streamwise development of u-velocity disturbance amplitudes for simulation *FB4*. $A_{1,0} = A_{1,1} = 5 * 10^{-2}$. *b)* Averaged skin friction coefficient for simulation *FB4* demonstrates that the increased amplitude forcing has delayed the transition process in simulation *FB4*. Sharp cone, $M = 7.95$, $T = 53.35K$.

(1,3). Since modes (0,2) and (1,3) are the signature modes of oblique breakdown, it seems that forcing mode (1,1) at such a large amplitude triggers an oblique beakdown mechanism which competes with the fundamental breakdown. The net result is that the entire transition process is delayed. The bulk of higher modes, which reached large amplitude at $x^* \approx 1.2m$ in simulation *FB3*, only begin their rapid nonlinear growth near the end of the domain at $x^* \approx 1.4m$. Therefore, the flow is farther from turbulence in simulation *FB4* compared to previous simulations (as is clear from the average skin friction in figure 6.40).

6.4.5 Time Dependent Inflow Continuation

With the goal of progressing deeper into the transitional regime, simulations *FB5 and FB6* were performed based on the results of simulation *FB3*. In these simulations, rather than forcing disturbances through wall blowing and suction, disturbances are forced directly at the inflow boundary using the results of simulation *FB3*. The wall-normal amplitude and phase distributions of all flow quantities were extracted at $x^* = 1.044m$ from simulation *FB3* for modes (0,1), (0,2), (1,0), (1,1), (1,2), (2,0), (2,1) and (2,2). At the inflow, these unsteady disturbances are then superposed with the steady baseflow boundary condition. Equation 6.11 governs the inflow boundary condition for each disturbance wave used for these simulations. $A(y)$ and $\theta(y)$ represent the amplitude and phase distributions for each disturbance quantity extracted from simulatin *FB3*. ϕ is a placeholder for any primitive variable (u, v, T, ρ, P or w). Figure 6.41 contains a schematic of the setup for these continuation simulations using time dependent inflow forcing.

$$\phi(y)_{inflow} = A(y)sin(\omega t + \theta(y))cos(k_c\varphi) \tag{6.11}$$

Clearly, at $x^* = 1.044m$ in simulation *FB3* there are many other large amplitude disturbances. However, due to computational expense the entire disturbance

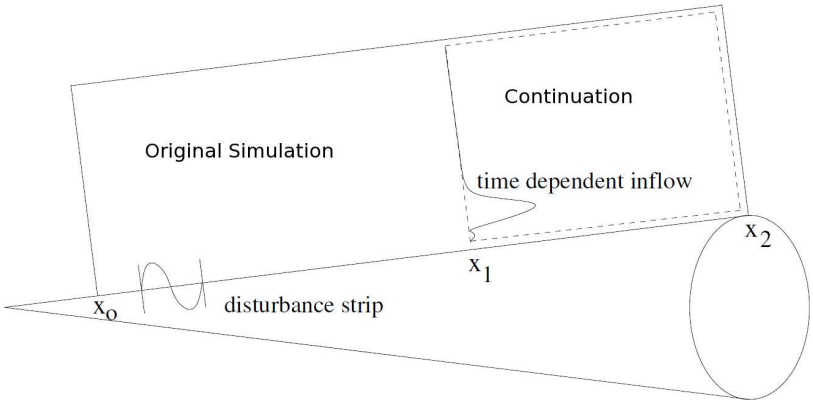

Figure 6.41: Schematic of continuation strategy using time dependent inflow boundary condition (simulations *FB5* and *FB6*).

field cannot be forced at the inflow. The relevent modes were chosen by their disturbance amplitudes at this streamwise location. This clearly represents an assumption regarding the initial condition for simulations *FB5 and FB6*. The development of u-velocity disturbance amplitudes for simulation *FB5* are presented in figure 6.42. All higher modes are immediately generated and begin to grow rapidly. The average skin friction (figure 6.42) demonstrates similar behavior to simulation *FB3*. Note that the skin friction for simulation *FB3* drops dramatically due to the buffer domain applied at the outflow. However, there are discrepancies between the skin friction for simulations *FB3* and *FB5* due to the fact that only a small number of disturbances were introduced at the inflow and not the complete disturbance field. The skin friction rises more rapidly and approaches more closely the turbulent values suggested by White (1991). Since only eight disturbance waves were forced based on the disturbance environment from simulation *FB3*, the other disturbances are "naturally" generated based on the nonlinear interactions in the governing equations. This allows for enhanced nonlinear interactions slightly further upstream when compared to simulation *FB3*.

To confirm the results of simulation *FB5* and to determine if the behavior in the skin friction after $x^* \approx 1.4m$ is due to a lack of adequate resolution, simulation *FB6*

was performed with increased x-resolution and an increased number of azimuthal modes (see table 6.3). The skin friction, plotted in figure 6.43, initially develops almost identically for both cases. However, in the late stages some discrepancy is present. The differences, as well as the lack of smoothness or apparent convergence of the skin friction may be due to the fact that the flow is losing periodicity and Fourier transforms over a single period fo the fundamental disturbance wave were used for the averaging.

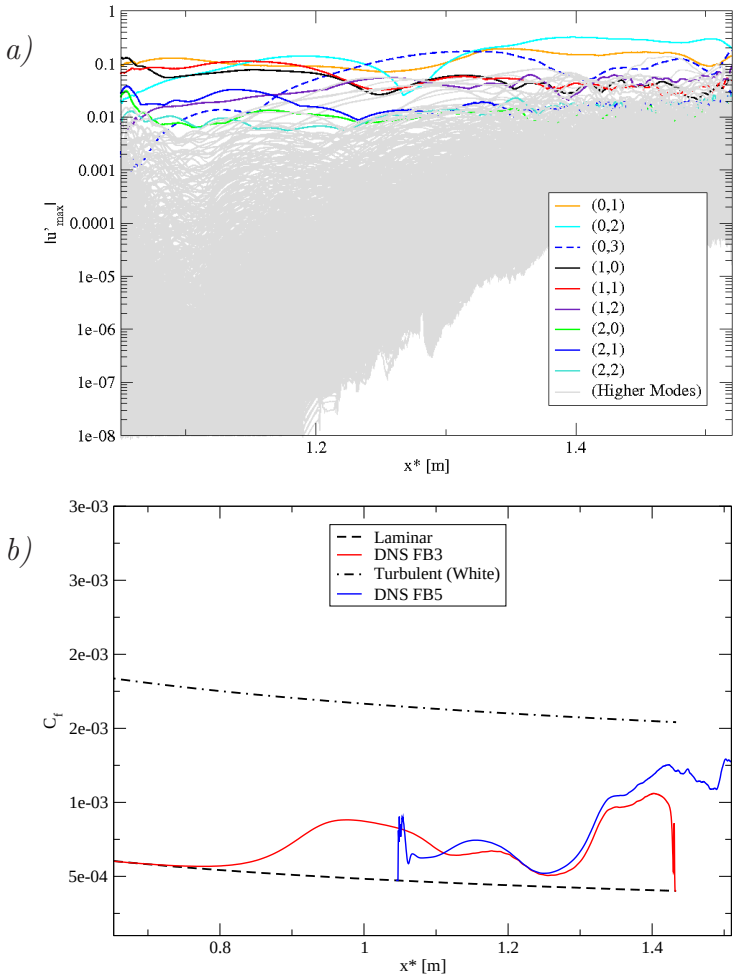

Figure 6.42: *a)* Streamwise development of u-velocity disturbance amplitudes for simulation *FB5*. Time dependent inflow forcing based on the results of simulation *FB3*. *b)* Average skin friction coefficient for simulation *FB5*. Sharp cone, $M = 7.95$, $T = 53.35K$.

Flow structures from simulation *FB6* are visualized in figure 6.44 by isosurfaces of Q=500 colored with streamwise vorticity and contours of azimuthal vorticity in the symmetry plane. Once again, the extremely long extent of the transitional region is evident. The development of Λ-vortices, hairpin-vortices and the eventual breakup of the coherent structures occurs extraordinarily slowly in comparison to incompressible flow. Figure 6.45 shows isosurfaces of Q=1500 (again colored with streamwise vorticity) and azimuthal vorticity in the symmetry plane near the end of the computational domain. From the azimuthal vorticity contours, it is clear that the flow remains quite coherent and there are large wave structures near the boundary layer edge. However, within the boundary layer the flow is becoming more random.

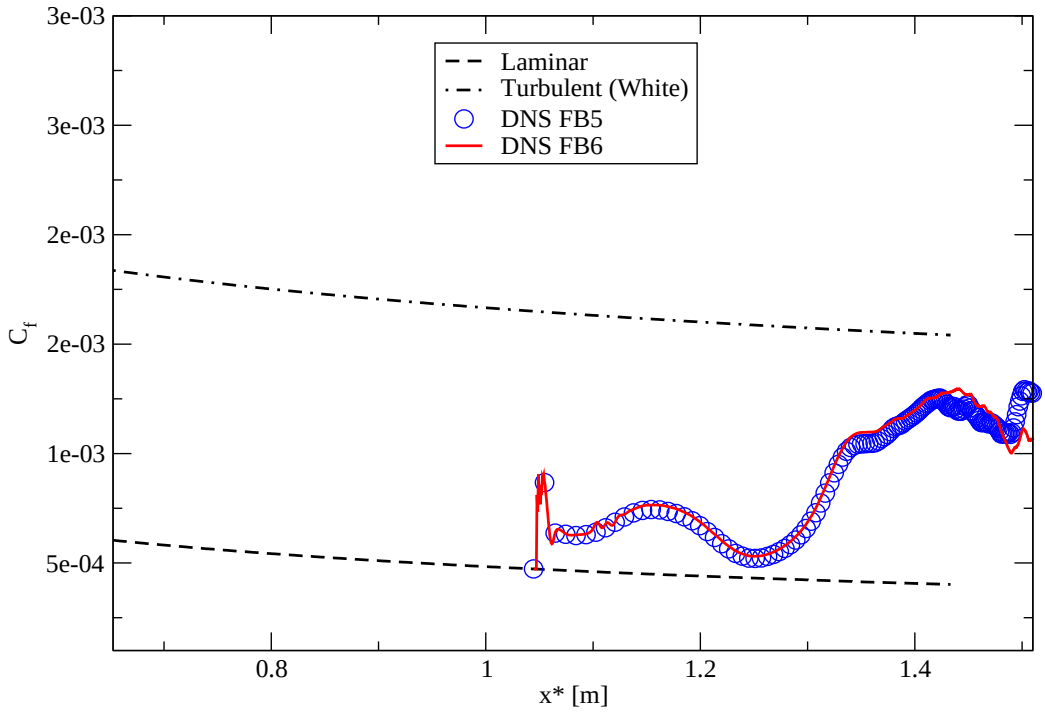

Figure 6.43: Time and azimuthal averaged skin friction coefficient. Open symbols are simulation *FB5* and solid line is simulation *FB6*. Sharp cone, $M = 7.95$, $T = 53.35K$.

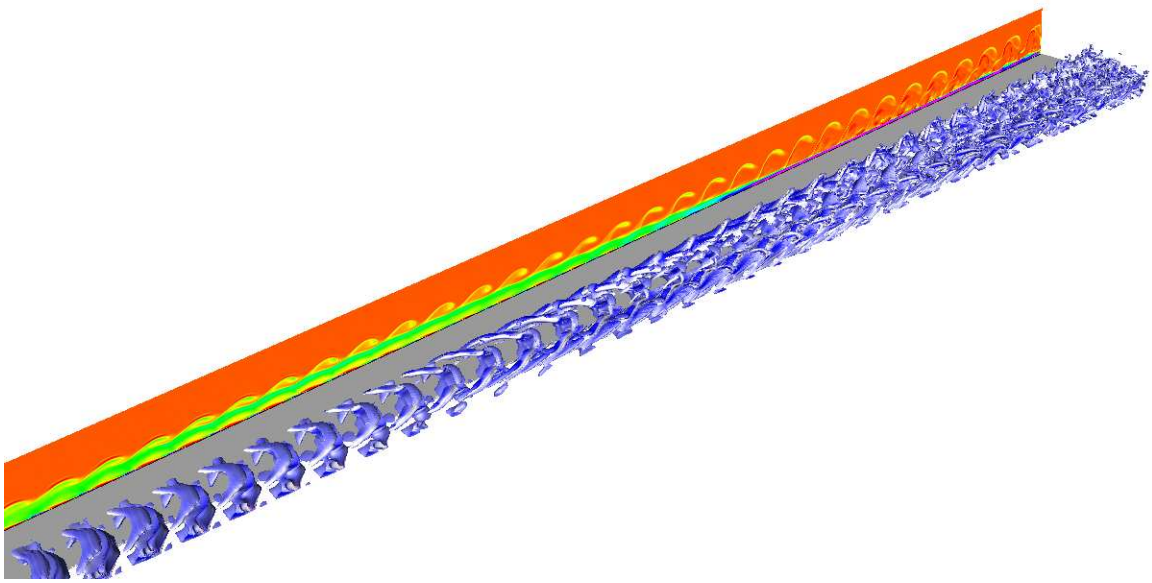

Figure 6.44: Isosurfaces of Q=500 colored with streamwise vorticity and contours of azimuthal vorticity in the symmetry plane. Results for simulation *FB6* with time dependent inflow forcing. Sharp cone, $M = 7.95$, $T = 53.35K$.

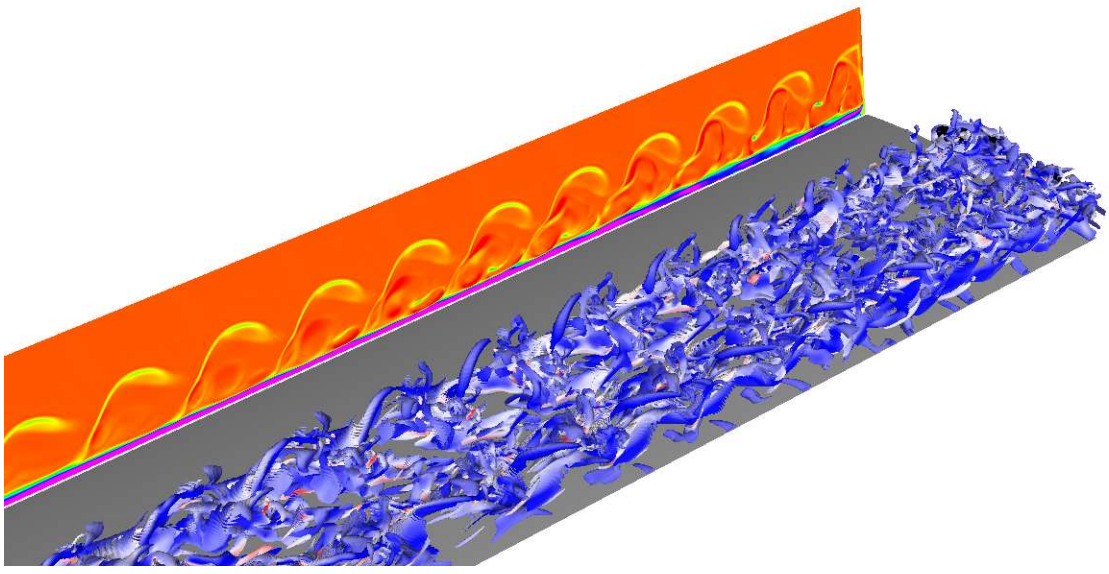

Figure 6.45: Isosurfaces of Q=1500 colored with streamwise vorticity and contours of azimuthal vorticity in the symmetry plane near the end of the computational domain. Results for simulation *FB6* with time dependent inflow forcing. Sharp cone, $M = 7.95$, $T = 53.35K$.

6.4.6 Comparison with Oblique Breakdown

Oblique breakdown is not a secondary instability mechanism in the classical sense. Rather than a primary disturbance causing nonlinear growth of a lower amplitude secondary disturbance, oblique breakdown is initiated only by a symmetric pair of oblique disturbance waves - modes (1,±1). A wave number diagram for this breakdown mechanism is presented in figure 6.46. The pair of oblique disturbances grow and eventually reach amplitudes large enough to cause nonlinear amplification of many higher modes. The signature modes generated in oblique breakdown are modes (0,2) and (1,3), as well as combinations of (even, even) and (odd, odd). As mentioned previously in section 1.2, the oblique breakdown mechanism was first discovered for supersonic flows by Thumm (1991) in DNS of flat plate boundary layer transition at M=1.6. Although for $M >\sim 4$ two-dimensional disturbances are most amplified linearly, slightly oblique waves experience similar linear growth and Husmeier (2008) demonstrated that oblique breakdown of shallow angle waves may also be relevant for hypersonic Mach numbers.

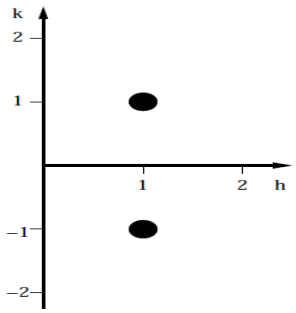

Figure 6.46: Wave number diagram for oblique breakdown which is initiated by a symmetric pair of oblique disturbance waves.

In order to compare with the previously discussed simulations of fundamental breakdown, a simulation of oblique breakdown was performed for the same flow conditions and computational domain as simulation *FB3*. The resolution for this simulation was $2000 \times 300 \times 55$ *modes*. The parameters were chosen for this simulation

based on a study conducted using temporal DNS for the same flow conditions (see chapter 7). The symmetric pair of oblique disturbances are forced with an amplitude $A_{1,1} = 2 * 10^{-2}$ and $k_c = 20$ at a frequency $\omega_r = 440.3$. The development of u-velocity disturbances and average skin friction coefficient are shown in figure 6.47. Mode (1,1) grows and begins to saturate at $x^* \approx 1.1m$. Near this streamwise location there is a small initial rise and then dip in the skin friction coefficient, similar to the initial rise and fall in the skin friction coefficient which accompanies the large amplitude mode (1,0) in that case. However, the rise is much smaller for the oblique breakdown due to the lower amplitude of mode (1,1) because it is not as strongly amplified as two-dimensional disturbances. After mode (1,1) saturates, modes (0,2), (0,4) and (1,3) surpass the amplitude of mode (1,1) and the flow begins to transition at $x^* \approx 1.2m$ with the accompanying rise in the skin friction. Flow structures from oblique breakdown are shown in figure 6.48 by isosurfaces of Q=400. The oblique disturbance waves form "rope like" streamwise structures before breaking up into two wedges of smaller scale motion.

In comparison to fundamental breakdown, the onset of transition and the rise in skin friction is much less dramatic and it seems for the investigated setup that fundamental breakdown is a stronger mechanism. However, it is extremely difficult to compare transition onset between these two mechanisms because they are of a completely different nature. The true onset of transition for fundamental breakdown could be considered to occur after the first rise in skin friction because this initial distortion of the mean flow is caused entirely by the axisymmetric primary disturbance wave. With this consideration, the true onset of transition occurs at roughly the same streamwise location ($x^* \approx 1.2m$) for both forcing mechanisms. At this point, the slope of the skin friction is much larger for the fundamental breakdown. However, it must be stressed that these results show behavior for the given forcing parameters and these two mechanisms are of a completely different nature. Therefore, it is difficult to compare them directly.

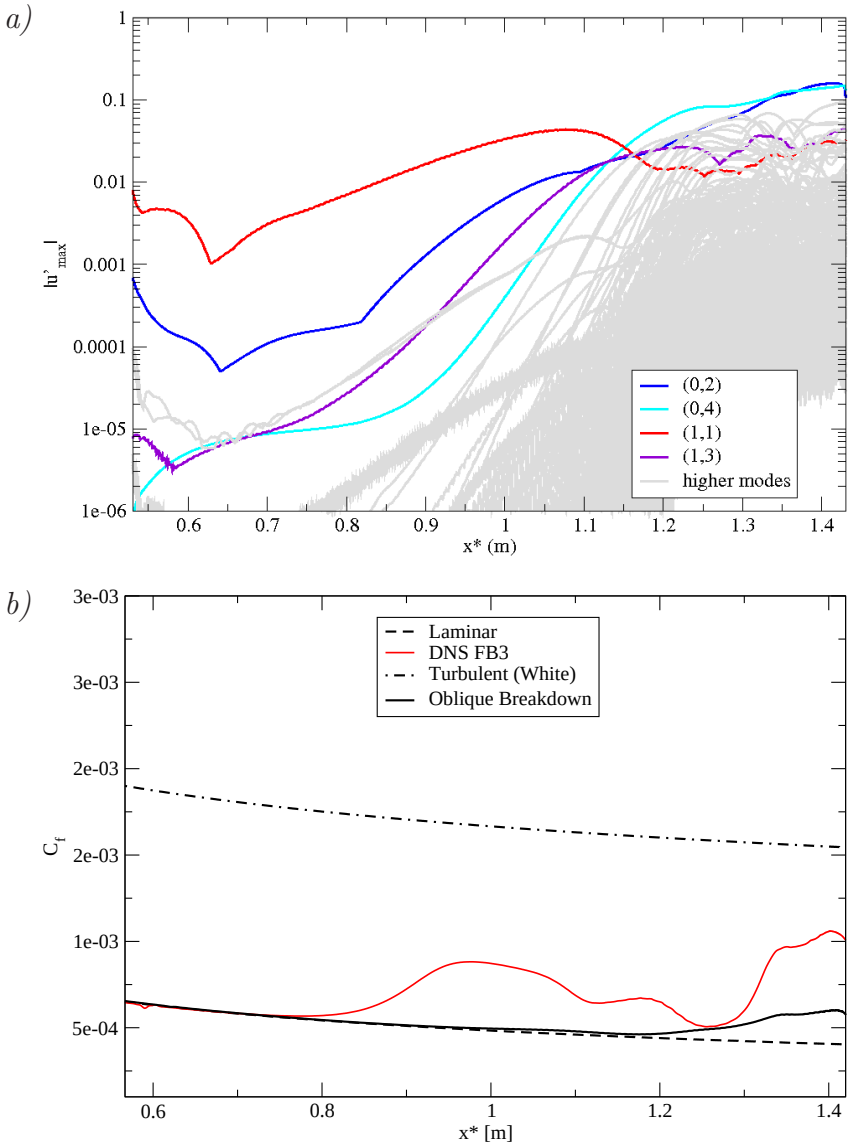

Figure 6.47: *a)* Streamwise development of u-velocity disturbance amplitudes for oblique breakdown. $k_c = 20$, $\omega_r = 440.3$, $A_{1,1} = 2 * 10^{-2}$. *b)* Average skin friction for oblique breakdown and fundamental breakdown (simulation *FB3*). Sharp cone, $M = 7.95$, $T = 53.35K$.

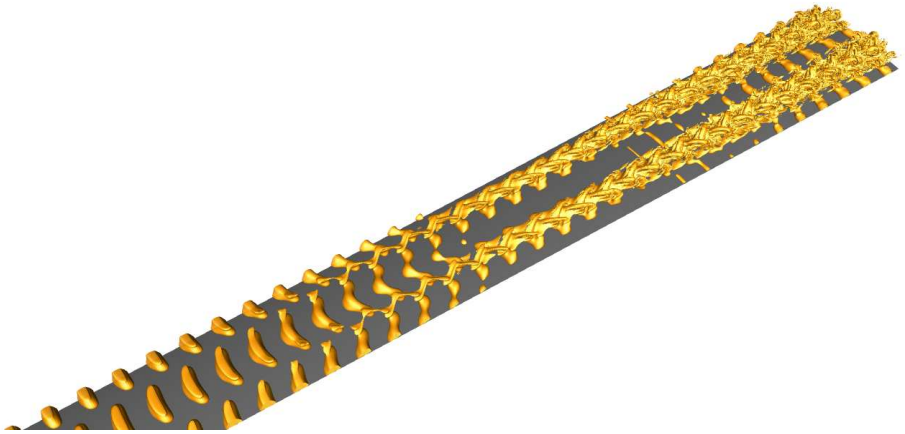

Figure 6.48: Isosurfaces of Q=400 for oblique breakdown. The oblique disturbance waves form rope like regions and eventually break up into two wedges of smaller scale structures. Sharp cone, $M = 7.95$, $T = 53.35K$.

6.4.7 Preliminary Summary of Controlled Transition Simulations

A series of highly resolved simulations of controlled transition were performed. These simulations utilized as many as 171 million grid points and have pushed the limits of today's most powerful supercomputers, requiring up to three weeks of continuous calculation on 1024 processors. Based on the results of wave packet simulations (see section 6.3), the main transition mechanism studied was fundamental (K-type) breakdown. In these simulations, a primary, axisymmetric disturbance wave (mode 1,0) was forced as well as oblique secondary disturbance waves (mode 1,$\pm$1). The frequency of these disturbances was chosen based on their linear behavior. In order to choose the optimal azimuthal mode number (k_c) for the oblique disturbances, a parameter study was performed and the mode with the strongest resonant growth was found to be $k_c = 46$. The simulations showed that the development of fundamental breakdown in the hypersonic boundary layer generally follows the same path as for incompressible flow. The large amplitude axisymmetric primary disturbance becomes modulated in the azimuthal direction due to resonant growth of oblique modes. This causes aligned Λ vortices accompanied hairpin vortices that form at the inclined tip

of the Λ structure. These coherent structures eventually breakup into smaller length scales. The key difference between the flow structures observed in the current simulations when compared to incompressible flow is the extremely long streamwise extent over which the transition process takes place. In contrast to incompressible flow, the nonlinear transition region appears to be as long or longer than the region of linear development. Average skin friction coeffcient curves for fundamental breakdown show an initial rise governed by the large amplitude of the primary disturbance followed by a dip caused by nonlinear saturation of the primary disturbance.. A second, steeper rise in skin friction occurs when all higher modes experience rapid nonlinear amplification. Unfortunately, due to the enormous computational effort required for these simulations, a fully turbulent state (based on theoretical skin friction estimates) was not reached for this breakdown scenario.

Finally, a simulation of oblique breakdown was performed for comparison with fundamental breakdown. Flow structures in oblique breakdown resemble those shown in previous studies (such as Mayer *et al.* (2009*b*)) at lower Mach numbers. For the investigated forcing scenarios, the onset of transition for oblique breakdown is less dramatic than for fundamental breakdown. Given the same computational domain and similar initial forcing amplitudes, the fundamental breakdown appears to progress farther into transition. However, it is extremely difficult to compare these mechanisms due to their entirely different natures. It should also be noted that although the initial forcing amplitude of mode (1,1) for oblique breakdown is comparable to the primary disturbance wave forced in the fundamental breakdown the ensuing disturbance development is different. Due to the receptivity process after the forcing from the disturbance slot, at the location where mode (1,1) begins to grow it is approximately one order of magnitude lower than mode (1,0) in the fundamental breakdown simulations. Thus, it is difficult to draw any concrete conclusions regarding the relative dominance of one transition mechanism over the other and it suffices to say that both are likely to be relevent for hypersonic boundary layers.

6.5 Summary of Mach 8 Spatial Simulations

The linear and nonlinear development of disturbances in a hypersonic boundary layer on a sharp cone were studied using spatial direct numerical simulations. Specific attention was paid to the nonlinear regime of transition. The main goals of this research were twofold:

1) Assess which nonlinear mechanism(s) may be relevent in a broad spectrum disturbance environment for the current flow conditions, and 2) perform controlled transition simulations of these mechanism(s).

As an initial step, axisymmetric pulse disturbances were introduced into the flow to generate a broad frequency spectrum of two-dimensional disturbances for comparison with LST data and to aid in the selection of disturbance frequencies for controlled transition simulations. These simulations revealed an unexpected, rapid nonlinear growth of low-frequency waves. Further examination showed that this growth is likely caused by resonance triads consisting of two relatively high frequency waves (within the band of most unstable second mode axisymmetric waves) and a third wave with a frequency equal to the difference in frequencies between the other two modes. Three dimensional simulations allowing only a single higher azimuthal mode showed that these low-frequencies resonances could heavily influence low-frequency oblique waves as well.

The next step in accomplishing the first research goal was to perform three-dimensional wave packet simulations featuring a broad spectrum of frequencies and wave numbers. Simulations of a wave packet forced with a moderately high amplitude ($A_{in} = 10^{-2}$) showed strong evidence of nonlinear interactions by the end of the computational domain. The most dominant nonlinear interaction within the wave packet appeared to be between axisymmetric and oblique waves of the same frequency. This pointed to the possible relevance of fundamental breakdown for the investigated flow. Notably, disturbance spectra from the wave packet simulations revealed no

evidence of subharmonic resonance which had been suggested as the dominant mechanism in Mach 6 experiments performed by Shiplyuk *et al.* (2003) and Bountin *et al.* (2008). Additionally, these simulations further confirmed the existence of the nonlinear growth of low-frequency modes which was observed in the two-dimensional and single higher mode simulations.

For goal number 2, a detailed study of fundamental resonance was performed using controlled disturbance inputs. A parameter study revealed strong resonant growth for several different azimuthal modes in the presence of an axisymmetric primary disturbance wave. The mode showing the largest growth rate after resonance ($k_c = 46$) was chosen for several highly resolved simulations of fundamental breakdown. Flow structures from these simulations revealed remarkable similarity to fundamental breakdown in incompressible flows and are dominated by the formation of aligned Λ vortices which begin stretching and breaking up into smaller scales. There is, however, one crucial difference between the presented simulations and fundamental breakdown in incompressible flows. For the hypersonic boundary layer, the streamwise extent over which the nonlinear regime of transition occurs is extraordinarily long. For these simulations the skin friction initially rises in response to the large amplitude primary disturbance wave and then features a dip before again rising sharply as nonlinear interactions cause many higher modes to rapidly reach large amplitudes. However, due to the enormous computational expense, the theoretical value for turbulent skin friction was approached, but not fully reached.

An additional continuous disturbance forcing simulation of the oblique breakdown mechanism was also performed for comparison with fundamental breakdown. The oblique breakdown mechanism also initiated transition for the investigated flow conditions and forcing parameters. However, the onset of transition was not as dramatic and the skin friction did not reach a level nearly as high as for the fundamental breakdown. It must be made clear that comparing these two mechanisms is quite difficult due to their completely different nature. Although the investigated oblique

breakdown did not progress as far into the transitional regime, it seems clear that both mechanisms are relevent for hypersonic boundary layers.

7. Transition in a Mach 8 Boundary Layer on a Sharp Cone: Temporal Direct Numerical Simulations

7.1 Computational Domain and Coordinate System

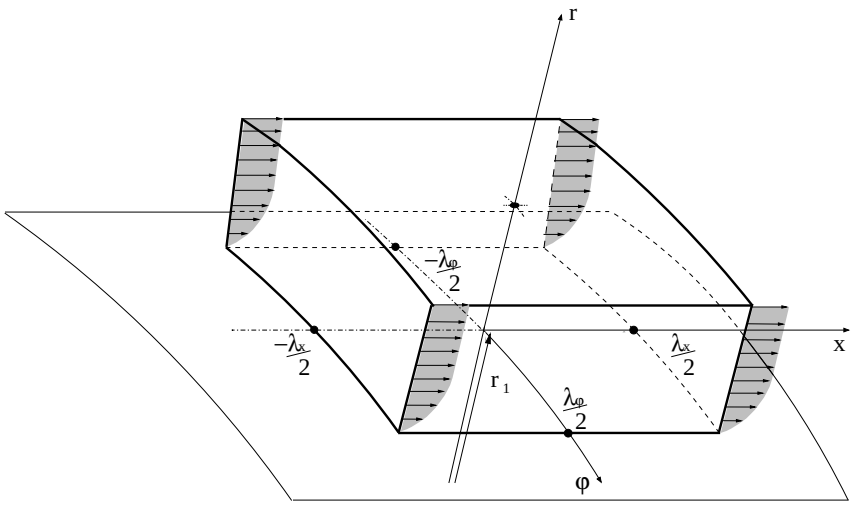

Figure 7.1: Computational domain used for Temporal Direct Numerical Simulations.

Figure 7.1 shows the computational domain used for Temporal Direct Numerical Simulations. The extent of the computational domain is determined by the disturbance wave lengths in streamwise and azimuthal direction, λ_x and λ_φ. Note that the symmetry in azimuthal direction allows for a diminution of the computational domain to half the azimuthal wave length in order to reduce the computational effort. In wall-normal direction, the computational domain extends from the wall to a height of about nine times the boundary layer thickness. The oblique shock, which is emanating from the cone tip, is not included in the computational domain. The influence of the domain height on the computed results is investigated in section 7.2.2. Due to the small extent of the computational domain in streamwise and azimuthal direction, a cylindrical coordinate system is applied. x indicates the streamwise direction parallel to the cone surface, r refers to the wall-normal direction orthogonal

to the cone surface and φ denotes the azimuthal direction.

7.2 Code Validation

The numerical method used for the investigation of the present hypersonic conical boundary layer flow is subjected to several tests in order to prove its correct functionality. Since a validation has to be performed with established scientific data, compressible linear stability theory (Mack, 1984) was chosen to evaluate the results of the temporal code. In particular, the validation is carried out by comparing the results of the temporal direct numerical simulations with results obtained from Mack's compressible linear stability solver for both, two- and three-dimensional disturbance waves. In the following, the temporal direct numerical simulations are performed considering the second viscosity coefficient $\lambda = 0.8$. This is necessary, because the second viscosity is implemented in Mack's linear stability solver. However, according to the majority of publications, the second viscosity coefficient is assumed to be zero in the remaining chapters of this thesis and only taken into account for validation purposes.

7.2.1 Comparison of Base Flow Profiles

Figure 7.2 shows three different sets of base flow profiles. Each set of base flow profiles consists of a streamwise velocity profile U, a temperature profile T and a density profile ρ plotted versus the the wall-normal coordinate r. Solid lines indicate the velocity, temperature and density distribution of the base flow computed with the second-order TVD (Total Variation Diminishing) finite volume code written by Gross & Fasel (2002). Symbols denote the base flow profile computed with the high-order accurate finite differences code and dashed lines label the similarity base flow profile. All profiles are taken at the same downstream position $R_x = 2024.17$. As can be seen from Figure 7.2, the similarity profiles and the profiles computed with the high-order

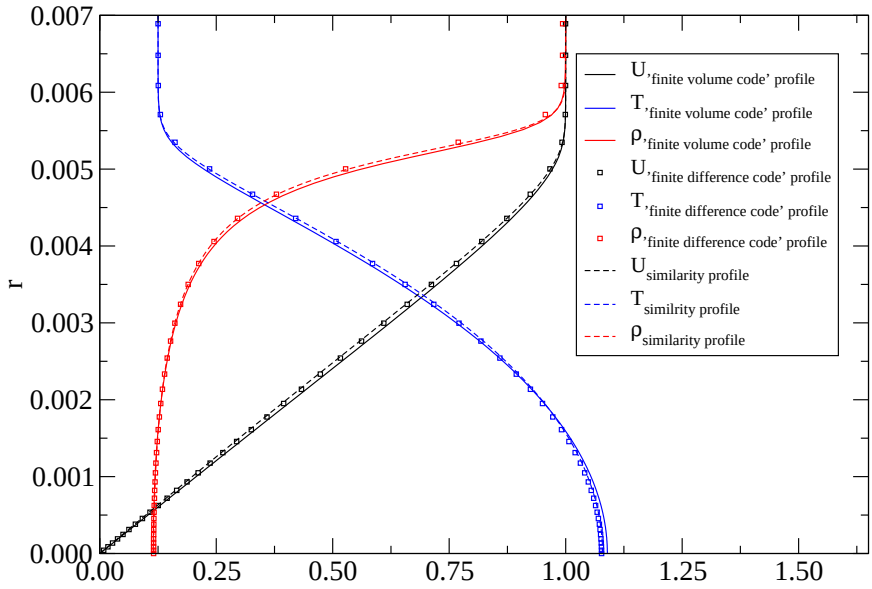

Figure 7.2: Comparison of base flow profiles at downstream location $R_x = 2024.17$. For visualization purposes T is scaled by a factor of 0.2. $M_e = 6.76$, $T_e^* = 71.75K$, $Re_e = 4,796,970$.

accurate finite differences code show an excellent agreement for all three quantities. The base flow profile computed with the finite volume code, however, slightly deviates from the latter two profiles. This base flow profile serves as an initial condition for the spatial high-order accurate finite differences code, which converges this initial base flow towards the similarity profile. The latter procedure results in an excellent match of the similarity base flow profile and the base flow profile obtained from the high-order accurate finite differences code. Thus, the base flow profile computed with the spatial high-order accurate finite differences code is used as an initial condition for all simulations in this thesis, except for the following validation, which is carried out with the similarity base flow profile.

7.2.2 Code Validation with LST for Two-Dimensional Disturbances

At first, the code is validated with results from linear stability theory for two-dimensional disturbances. In order to compare the results of the temporal direct

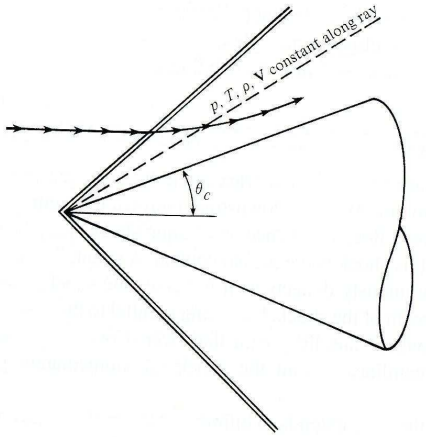

Figure 7.3: Hypersonic flow over a sharp cone. Taken from Anderson (2004).

	free-stream	boundary layer edge
Re	$3,333,333$	$4,796,970$
M	7.95	6.76
T	$53.35K$	$71.75K$

Table 7.1: Flow parameters used in Temporal Direct Numerical Simulations. $M_\infty = 7.95$, $T^*_\infty = 53.35K$, $Re_\infty = 3,333,333$.

numerical simulations with the results obtained from linear stability theory the boundary layer edge values have to be determined. Note that the conical flow field differs from the flow field of a flat plate or a cylinder. According to Anderson (2004), all flow properties of an inviscid flow field of a sharp cone between the cone surface and the oblique shock are constant along rays from the cone tip and the flow properties vary only from one ray to the next. This is illustrated in Figure 7.2.2. In contrast to that, flat plate and cylinder have a uniform flow field far away from the surface. Hence, in this thesis the boundary layer edge of the present conical flow is defined as the position, where the wall-normal gradient of the streamwise velocity $\frac{\delta U}{\delta r}$ has a local minimum (Laible *et al.*, 2008). The flow properties at this location are indicated with the subscript e and are summarized in Table 7.1. For comparison, Table 7.1 also contains the free stream values of the investigated flow.

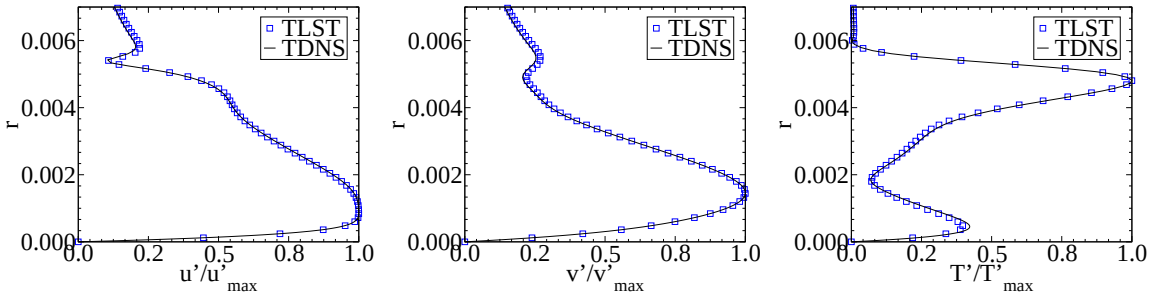

Figure 7.4: Comparison of wall-normal amplitude distributions for disturbance velocity in streamwise direction u' (left), disturbance velocity in wall-normal direction v' (center) and disturbance temperature T' (right) obtained from TDNS to Mangler-transformed amplitude distributions obtained from TLST. $A_{(1,0)} = 10^{-7}$, $k_c = 0$, $\alpha_r = 457.9$, $R_x = 2024.17$, $M_e = 6.76$, $T_e^* = 71.75K$, $Re_e = 4,796,970$.

Mack's linear stability solver is only applicable to a flat plate geometry. Therefore, the temporal direct numerical simulations have to be carried out with a very high local cone radius r_1 in order to ensure that azimuthal curvature effects do not play a role. For the present validation, the local cone radius r_1 is therefore multiplied by a factor 1000. In addition to that, the results of both methods are only compareable after applying the Mangler-transformation (Mangler, 1948), where the wall-normal similarity variables of flat plate and cone are related by $\eta_{plate} = \sqrt{3} \cdot \eta_{cone}$. Note that r is linked with η by $\eta = r \cdot \sqrt{Re_e/x}$, where x is the downstream position. Furthermore, the linear stability solver requires a similarity base flow profile as an initial condition. Hence, the same similarity base flow profile is used as an initial condition for the temporal code.

In this chapter, the disturbances are two dimensional, i. e. the azimuthal mode number is $k_c = 0$. The two-dimensional wave $(1, 0)$ is forced with the amplitude $A_{(1,0)} = 10^{-7}$. The low amplitude assures a linear disturbance development and therefore allows for a detailed comparison with linear stability theory.

Figure 7.4 shows the wall-normal amplitude distributions of the streamwise disturbance velocity u', the wall-normal disturbance velocity v' and the disturbance

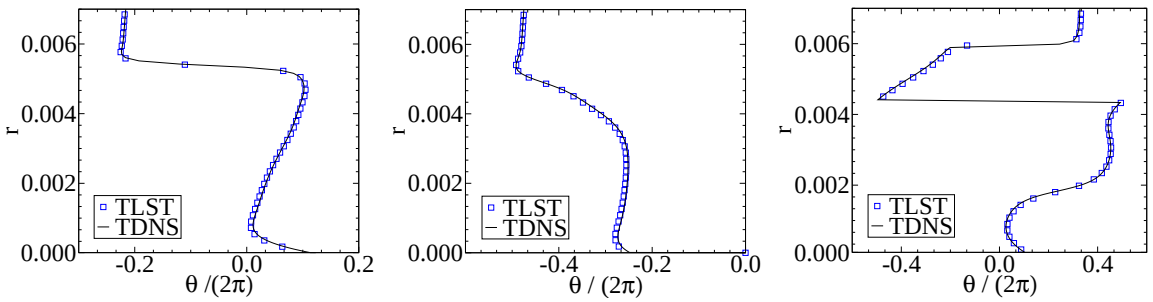

Figure 7.5: Comparison of wall-normal phase distributions for disturbance velocity in streamwise direction u' (left), disturbance velocity in wall-normal direction v' (center) and disturbance temperature T' (right) obtained from TDNS to Mangler-transformed phase distributions obtained from TLST. $A_{(1,0)} = 10^{-7}$, $k_c = 0$, $\alpha_r = 457.9$, $R_x = 2024.17$, $M_e = 6.76$, $T_e^* = 71.75K$, $Re_e = 4,796,970$.

temperature T', respectively, obtained from temporal DNS and temporal LST for a streamwise wave number $\alpha_r = 457.9$. The amplitude profiles of the quantities show a very good agreement. The double-peaked structure of the eigenfunctions is characteristic for high-speed flows.

The wall-normal phase distributions of the disturbance velocity in streamwise direction u', the disturbance velocity in wall-normal direction v' and the disturbance temperature T' obtained from both, temporal direct numerical simulations and linear stability theory are plotted in Figure 7.5. All three graphs show an excellent agreement. Furthermore, the frequency ω_r is plotted against the streamwise wave number α_r in Figure 7.6. It can be observed that the results of DNS and LST are in perfect agreement

As can be seen from Figure 7.7, where the temporal growth rate ω_i is given as a function of the streamwise wave number α_r, the agreement between temporal DNS and LST is also good for this quantity. Since the base flow is parallel, different criteria do not influence the growth rate. Therefore, the growth rates calculated with the density disturbance ρ', temperature disturbance T' or disturbance velocity

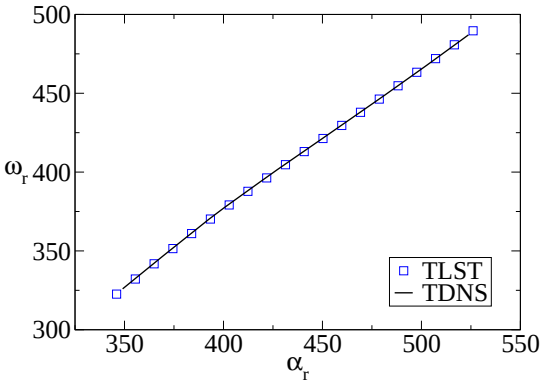

Figure 7.6: Comparison of frequency ω_r obtained from TDNS to frequency obtained form TLST. $A_{(1,0)} = 10^{-7}$, $k_c = 0$, $R_x = 2024.17$, $M_e = 6.76$, $T_e^* = 71.75K$, $Re_e = 4,796,970$.

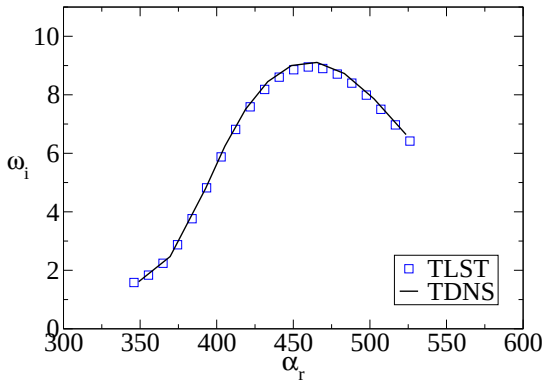

Figure 7.7: Comparison of temporal growth rate ω_i obtained from TDNS to temporal growth rate obtained form TLST. $A_{(1,0)} = 10^{-7}$, $k_c = 0$, $R_x = 2024.17$, $M_e = 6.76$, $T_e^* = 71.75K$, $Re_e = 4,796,970$.

v' according to

$$\omega_i = \frac{\partial}{\partial t}\left(ln\frac{A}{A_0}\right) \tag{7.1}$$

are the same as the growth rate calculated with the disturbance velocity in streamwise direction u', which is presented in Figure 7.7. According to Malik & Spall (1991), transverse curvature has a stabilizing influence on second mode disturbances. Hence, the growth rates presented in the following chapters are lower than those for the present simulations, where a thousand times larger local cone radius r_1 is enforced.

Moreover, the influence of the domain height is investigated. In Figure 7.8, the maximum temporal growth rate $\omega_{i,max}$ is plotted against the ratio of wall-normal coordinate r and boundary layer thickness $\delta_{99.9}$, where the maximum temporal growth rate $\omega_{i,max}$ is defined as the growth rate corresponding to the streamwise wave number $\alpha_r = 457.9$ and the boundary layer thickness $\delta_{99.9}$ is specified as the location where $U = 0.999 \cdot U_\infty$. It can be observed that the maximum temporal growth rate is constant and thus not influenced by the decrease of the domain height until a value of approximately twice the boundary layer thickness. In the present work, all simulations

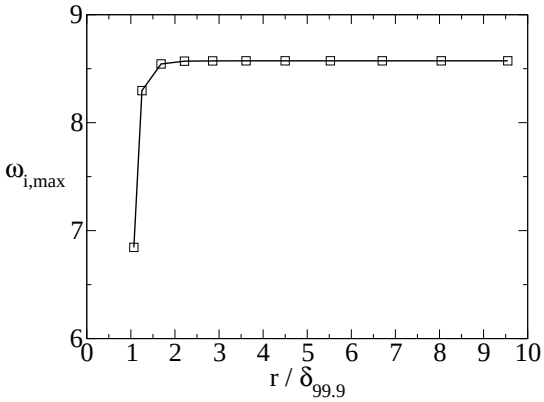

Figure 7.8: Influence of domain height on maximum temporal growth rate $\omega_{i,max}$. $A_{(1,0)} = 10^{-7}$, $k_c = 0$, $\alpha_r = 457.9$, $R_x = 2024.17$, $M_e = 6.76$, $T_e^* = 71.75K$, $Re_e = 4,796,970$.

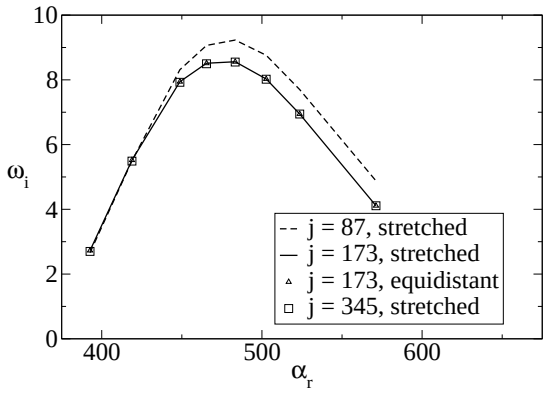

Figure 7.9: Influence of wall-normal grid resolution on temporal growth rate ω_i. $A_{(1,0)} = 10^{-7}$, $k_c = 0$, $R_x = 2024.17$, $M_e = 6.76$, $T_e^* = 71.75K$, $Re_e = 4,796,970$.

are carried out for a domain height of about nine times the boundary layer thickness in order to exclude the influence of an insufficient domain height.

Furthermore, the grid resolution in wall-normal direction is investigated. Figure 7.9 shows the temporal growth rate ω_i corresponding to four different grid resolutions. Reducing the numbers of grid points j from 345 to 173 does not influence the results of the temporal code. A further reduction to 87 grid points in wall-normal direction, however, causes an increase of the temporal growth rate. In addition to that, the influence of grid stretching is investigated. It can be seen from Figure 7.9 that an equidistant grid distribution in the boundary layer results in the same growth rates. Thus, the stretching in the previous cases has no negative influence. The four investigated grids are presented in Figure 7.10. In the following chapters the stretched grid with 345 points in wall-normal direction is used. Note that the boundary layer is resolved with 150 grid points.

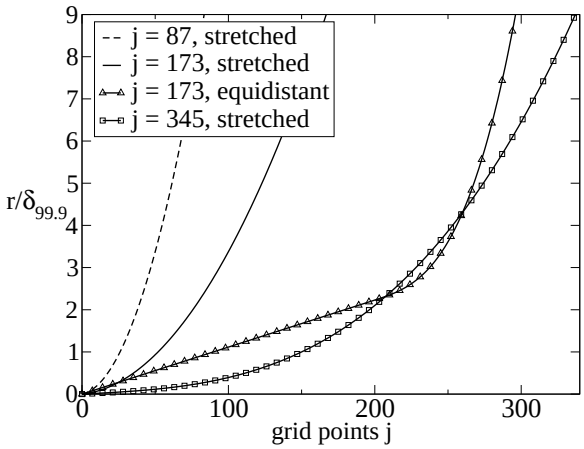

Figure 7.10: Comparison of different wall-normal grids used in Temporal Direct Numerical Simulations.

7.2.3 Code Validation with LST for Three-Dimensional Disturbances

Although the most unstable wave for the investigated flow regime is two-dimensional, the temporal code is also validated for a case of three-dimensional disturbances. The azimuthal mode number of the three-dimensional wave $(1,1)$ is $k_c = 20$ and the forcing amplitude is $A_{(1,1)} = 10^{-7}$. All other parameters remain as described above.

Figure 7.11 and Figure 7.12 show a comparison of the wall-normal amplitude and phase distributions, respectively, for the disturbance velocity in streamwise direction u', the disturbance velocity in wall-normal direction v' and the disturbance temperature T' obtained from temporal DNS to Mangler-transformed amplitude and phase distributions obtained from temporal LST for a streamwise wave number $\alpha_r = 523.6$. It can be seen that the agreement of all three quantities is very good.

In Figure 7.13 the frequency ω_r is given as a function of the streamwise wave number α_r. As for the two-dimensional case, the agreement between linear stability theory and temporal direct numerical simulation is excellent.

The temporal growth rate ω_i is plotted against the streamwise wave number α_r in Figure 7.14. Again, it can be observed that the overall agreement between DNS and LST is good. Note that according to the findings of Mack (1984) two-dimensional

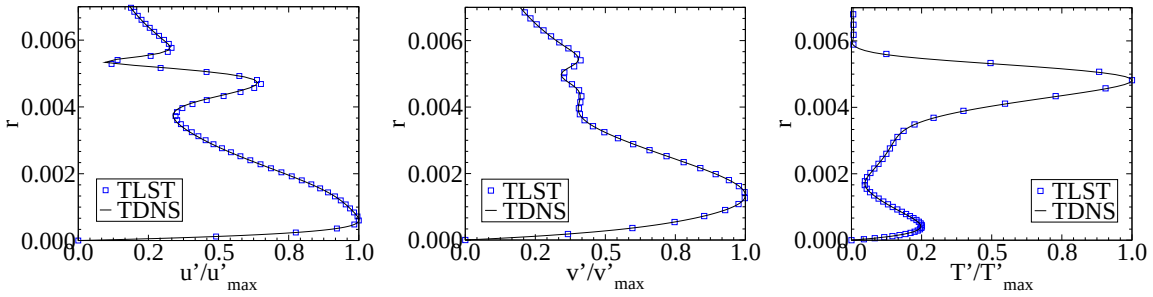

Figure 7.11: Comparison of wall-normal amplitude distributions for disturbance velocity in streamwise direction u' (left), disturbance velocity in wall-normal direction v' (center) and disturbance temperature T' (right) obtained from TDNS to Mangler-transformed amplitude distributions obtained from TLST. $A_{(1,1)} = 10^{-7}$, $k_c = 20$, $\alpha_r = 523.6$, $R_x = 2024.17$, $M_e = 6.76$, $T_e^* = 71.75K$, $Re_e = 4,796,970$.

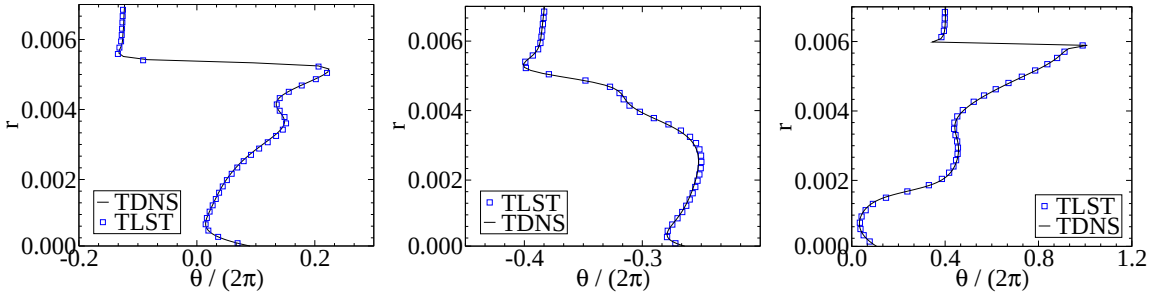

Figure 7.12: Comparison of wall-normal phase distributions for disturbance velocity in streamwise direction u' (left), disturbance velocity in wall-normal direction v' (center) and disturbance temperature T' (right) obtained from TDNS to Mangler-transformed phase distributions obtained from TLST. $A_{(1,1)} = 10^{-7}$, $k_c = 20$, $\alpha_r = 523.6$, $R_x = 2024.17$, $M_e = 6.76$, $T_e^* = 71.75K$, $Re_e = 4,796,970$.

waves are stronger amplified than three-dimensional disturbances. This behavior can be verified by comparing Figure 7.7 and Figure 7.14.

7.3 Oblique Breakdown

This section is dedicated to the investigation of oblique breakdown. Oblique breakdown is a viable path to transition, if the dominant disturbance waves are three-dimensional oblique waves. This is the case for supersonic boundary layers with

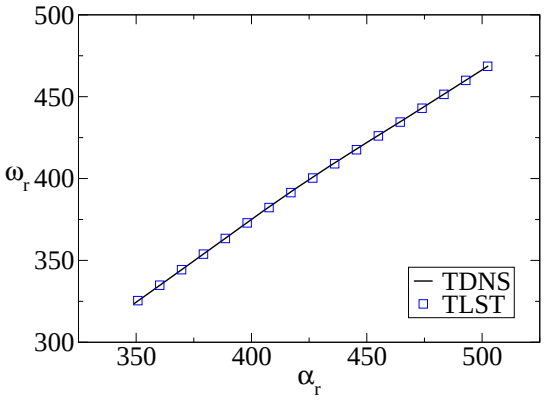

Figure 7.13: Comparison of frequency ω_r obtained from TDNS to frequency obtained form TLST. $A_{(1,1)} = 10^{-7}$, $k_c = 20$, $R_x = 2024.17$, $M_e = 6.76$, $T_e^* = 71.75K$, $Re_e = 4,796,970$.

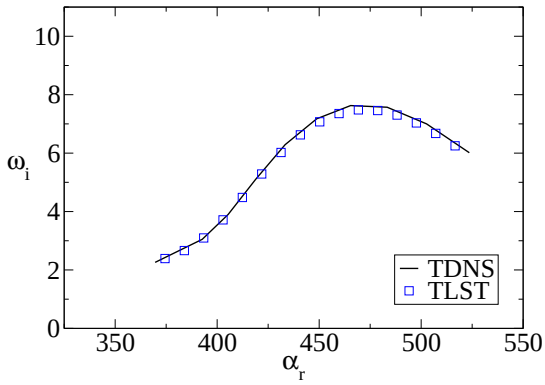

Figure 7.14: Comparison of temporal growth rate ω_i obtained from TDNS to temporal growth rate obtained form TLST. $A_{(1,1)} = 10^{-7}$, $k_c = 20$, $R_x = 2024.17$, $M_e = 6.76$, $T_e^* = 71.75K$, $Re_e = 4,796,970$.

$M \leq 4.5$. However, previous investigations revealed that oblique breakdown may also play an important role for hypersonic flows, like the present Mach 7.95 flow over a sharp circular cone. As a first step, the linear regime is investigated in section 7.3.1. Hereafter, a parameter study is carried out in section 7.3.2 in order to identify the most promising cases, characterized by the strongest amplification of signature modes of oblique breakdown, namely modes $(0, 2)$ and $(1, 3)$. Those cases are then investigated in more detail by means of higher resolved simulations. Finally, section 7.3.4 presents a brief summary of oblique breakdown simulations.

7.3.1 Investigation of the Linear Regime

An investigation of the linear regime is performed to identify the maximum temporal growth rate $\omega_{i,max}$ for waves with different azimuthal mode numbers k_c. It is well known that for hypersonic boundary layers the temporal growth rate ω_i decreases as the obliqueness of the disturbance waves is increased. This is confirmed by Figure 7.3.1, where the temporal growth rate ω_i for eleven different azimuthal mode

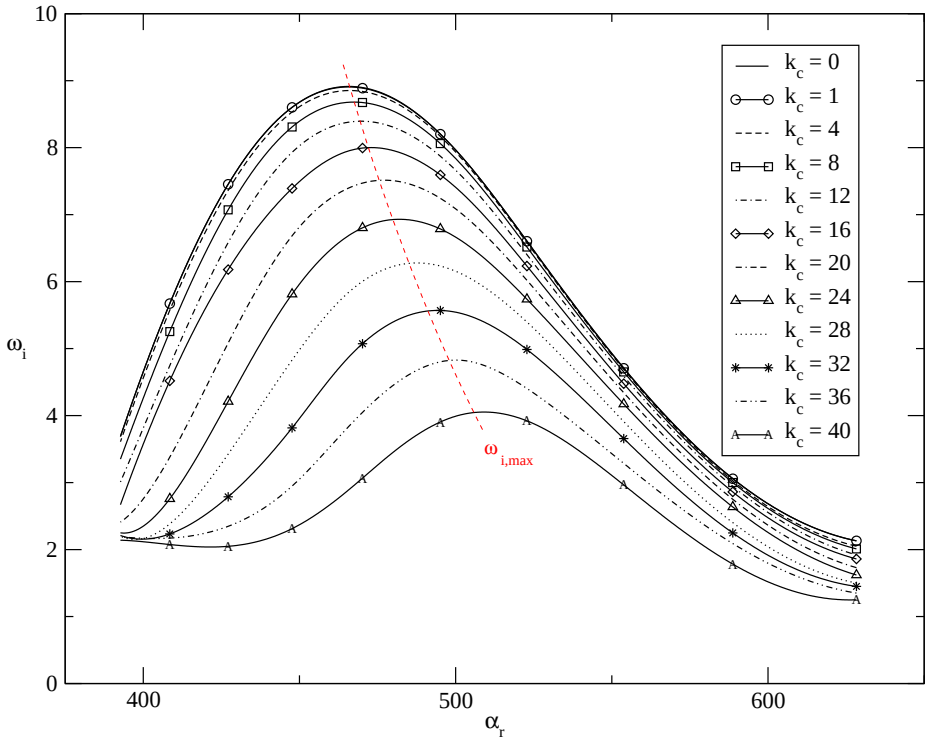

Figure 7.15: Temporal growth rates ω_i for $k_c = 0, 1, 4, 8, \ldots, 40$. $R_x = 2024.17$, $M_\infty = 7.95$, $T^*_\infty = 53.35K$, $Re_\infty = 3,333,333$.

numbers $k_c = 0, 1, 4, 8, \ldots, 40$ is plotted as a function of the streamwise wave number α_r. Figure 7.3.1 also shows that the streamwise wave number for which the temporal growth rate has a maximum is shifting towards higher values as the azimuthal mode number is increased. In order to determine the maximum value of the temporal growth rates $\omega_{i,max}$ more precisely, cubic splines are fitted through the data points obtained from temporal simulations. The maximum growth rates are indicated with the red dashed line.

7.3.2 Parameter Study

In the following, simulations for eleven different azimuthal mode numbers are performed in order to identify the cases, which show a fast onset of transition. The streamwise wave number α_r of each simulation is chosen such that it corresponds to

the streamwise wave number for which the temporal growth rate has a maximum as shown in Figure 7.3.1. The temporal development of the maximum disturbance velocity in streamwise direction $|u'|_{(h,k)}$ for the eleven azimuthal mode numbers k_c is shown in Figure 7.16. The simulations are performed with a resolution of nine Fourier modes in streamwise and four Fourier modes in azimuthal direction. In wall-normal direction 345 grid points are used, where the boundary layer is resolved with 150 points. Due to the low resolution the simulations for $k_c = 1, 4, 8, 12$ and 16 are terminated before the final time step is reached. For higher azimuthal mode numbers, however, resolution problems do not occur, since the growth rates of all modes are lower. Figure 7.16 reveals that the signature modes $(0, 2)$ and $(1, 3)$ exceed the amplitude of the forced disturbance mode $(1, 1)$ for the cases with an azimuthal mode number $k_c = 20, 24, 28$ and 32. This behavior indicates that oblique breakdown can be a viable path to transition for these particular azimuthal mode numbers. As the azimuthal mode number is increased to higher values ($k_c \geq 36$), the transition onset shifts to a later time instance. Thus, these azimuthal mode numbers aren't investigated further. In the following, the cases with an azimuthal mode number $k_c = 20$ and $k_c = 32$ are analyzed in more detail by increasing the resolution in streamwise and azimuthal direction. Due to the facts that, first, the simulation for the case with the azimuthal mode number $k_c = 1$ shows the strongest growth rate and, second, the result of the previous simulation did not reveal if the modes $(0, 2)$ and $(1, 3)$ exceed the amplitude of the oblique disturbance mode $(1, 1)$, this case is also investigated in more detail.

The resolution is increased to thirty three Fourier modes in streamwise and sixteen Fourier modes in azimuthal direction, which corresponds to total of $705,870$ grid points. Three simulations are performed with this resolution, namely the cases with an azimuthal mode number $k_c = 1$, $k_c = 20$ and $k_c = 32$. The previously presented simulations serve as an initial condition for these higher resolved simulations in order to reduce the computational effort. The red dashed lines in Figure 7.16 indicate the

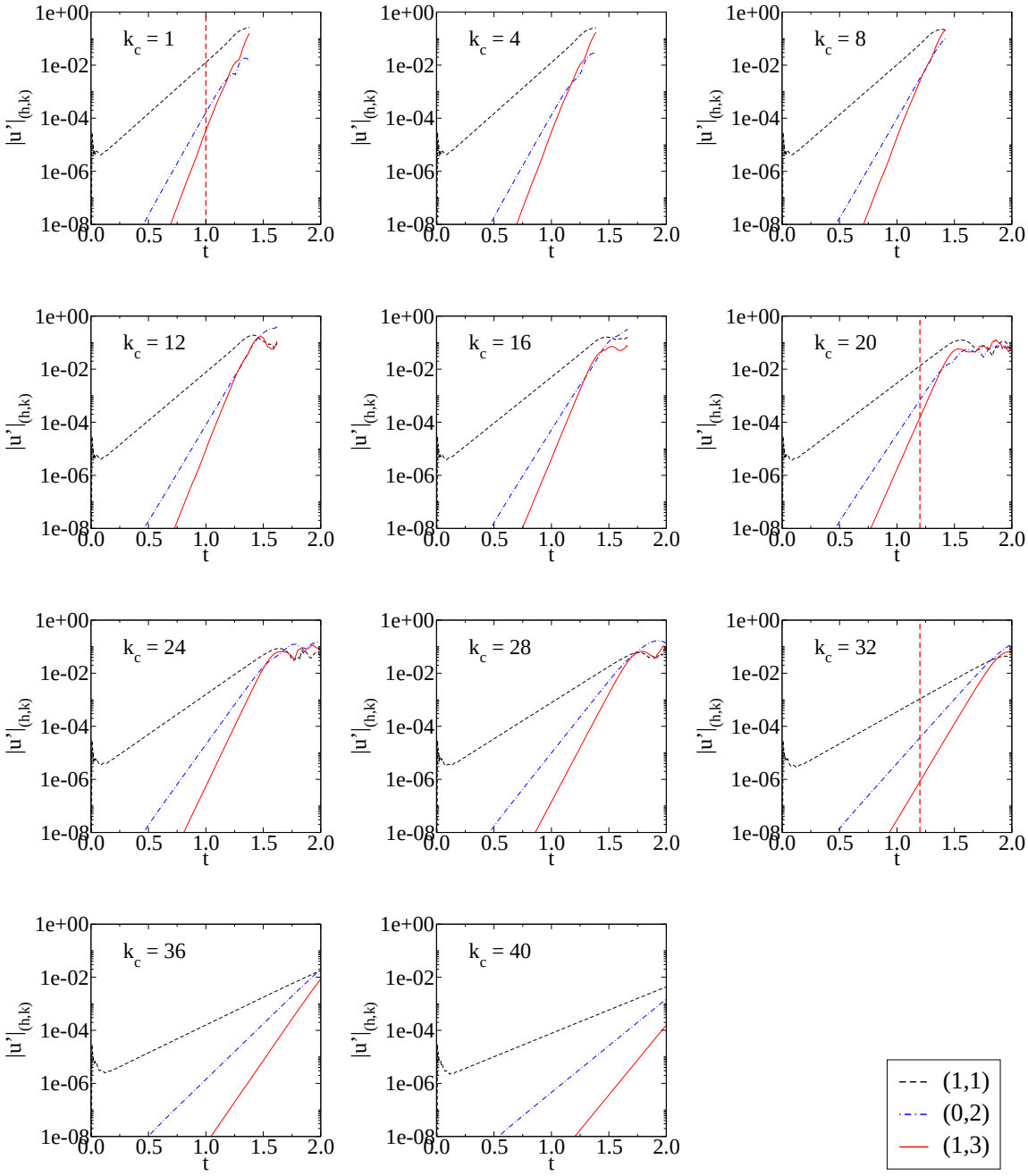

Figure 7.16: Temporal development of the maximum disturbance velocity in streamwise direction $|u'|_{(h,k)}$ for different azimuthal mode numbers k_c. $A_{(1,1)} = 10^{-4}$, $R_x = 2024.17$, $M_\infty = 7.95$, $T^*_\infty = 53.35K$, $Re_\infty = 3,333,333$.

time step at which the initial flow field for the continuation run is extracted. The simulations are continued from $t = 1.0$ in the $k_c = 1$ case and from $t = 1.2$ in the $k_c = 20$ and $k_c = 32$ cases. Figure 4.3 reveals that oblique breakdown is an unlikely path to transition for an almost two-dimensional disturbance wave with azimuthal mode number $k_c = 1$. It can be observed that the initially forced disturbance mode $(1, 1)$ saturates for $t > 1.3$ at an almost one order of magnitude higher amplitude level than mode $(1, 3)$. In addition, modes with even-odd and odd-even streamwise and azimuthal mode numbers combinations do not reach the amplitude level of the initially generated modes with even-even and odd-odd streamwise and azimuthal mode number combinations. In contrast, Figure 4.4 (left) demonstrates for the case with $k_c = 20$ that the dominant modes in the transition process, namely modes $(0, 2)$ and $(1, 3)$, exceed the amplitude of mode $(1, 1)$ for $t \approx 1.6$. The same behavior can be observed in Figure 4.4 (right) for the simulation with the azimuthal mode number $k_c = 32$. In this case, however, the transitional region is reached at a later time instance $t \approx 2.0$. Furthermore, both cases show that waves with odd-even and even-odd streamwise and azimuthal mode number combinations are rising and eventually reach the the same order of magnitude as mode $(1, 1)$. This precedes the turbulent flow regime. Note that all three figures confirm that the transition process is governed by waves with only odd-odd and even-even mode number combinations. In comparison to the simulations for $k_c = 1$ and $k_c = 32$, the case with an azimuthal mode number $k_c = 20$ shows the fastest onset of transition. However, it is important to note that this azimuthal mode number might not represent the optimal value, since the azimuthal mode numbers $k_c = 12$ or $k_c = 16$ also show a promising behavior according to Figure 7.16. Nevertheless, compared to $k_c = 12$ or $k_c = 16$ the azimuthal mode number $k_c = 20$ has the advantage of a smaller computational domain and thus reduces the computational effort significantly. Hence, another refinement of the resolution is performed for this case.

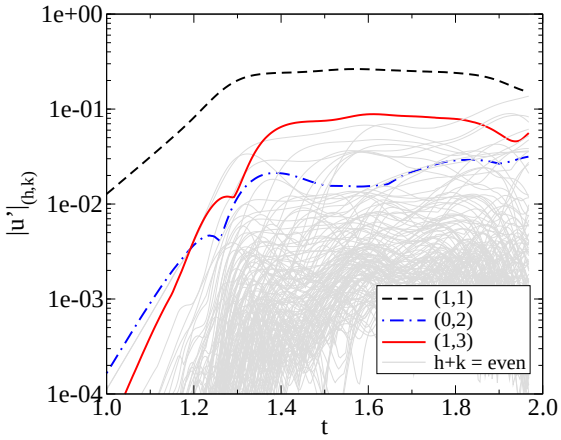

Figure 7.17: Temporal development of the maximum disturbance velocity in streamwise direction $|u'|_{(h,k)}$ for $k_c = 1$. $A_{(1,1)} = 10^{-4}$, $R_x = 2024.17$, $M_\infty = 7.95$, $T^*_\infty = 53.35K$, $Re_\infty = 3,333,333$.

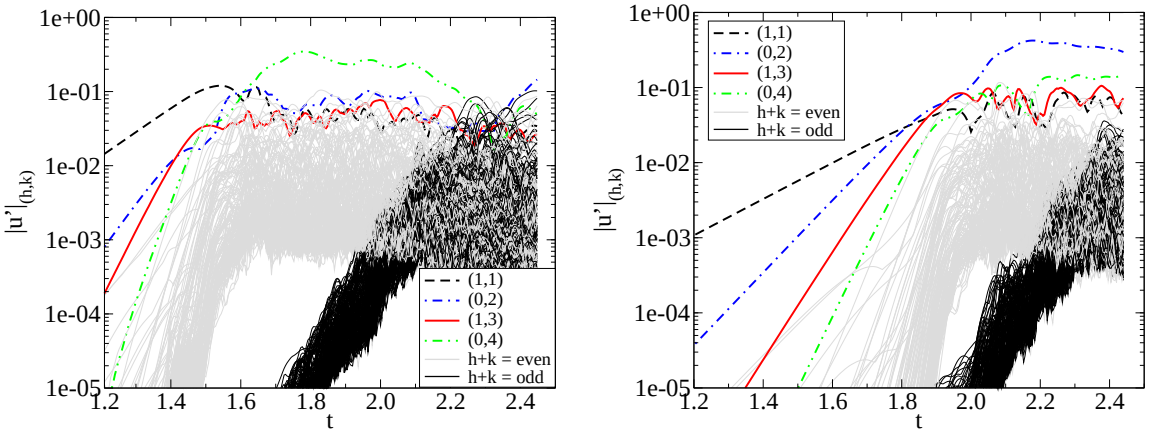

Figure 7.18: Temporal development of the maximum disturbance velocity in streamwise direction $|u'|_{(h,k)}$ for $k_c = 20$ (left) and $k_c = 32$ (right). $A_{(1,1)} = 10^{-4}$, $R_x = 2024.17$, $M_\infty = 7.95$, $T^*_\infty = 53.35K$, $Re_\infty = 3,333,333$.

7.3.3 Simulations with Increased Resolution

So far, the grid resolution was very low and therefore not appropriate for the investigation of the late stages of transition. Hence, a further refinement of the resolution is inevitable. The following simulation is performed for the azimuthal mode number $k_c = 20$. The computational domain is discretized with 63 Fourier modes in streamwise, 345 points in wall-normal and 64 Fourier modes in azimuthal direction, which corresponds to a total of $5,608,320$ grid points.

At first, averaged mean flow quantities are investigated. In particular, the skin friction coefficient $\overline{c}_f$, the Favre-averaged velocity profile $\tilde{u}$ and the streamwise and azimuthal averaged temperature profile $\overline{T}$ are presented in Figures 7.19, 7.20 and 7.21, respectively. The skin friction coefficient $\overline{c}_f$ is calculated according to

$$\overline{c}_f = \left. \frac{2\overline{\mu}\frac{\partial \overline{u}}{\partial r}}{Re} \right|_w, \tag{7.2}$$

where quantities with an overbar $\overline{\phi}$ indicate an average in streamwise and azimuthal direction

$$\bar{\phi} = \frac{1}{\lambda_\varphi \lambda_x} \int_0^{\lambda_\varphi} \int_0^{\lambda_x} \phi(x, \varphi) \mathrm{d}x \mathrm{d}\varphi. \tag{7.3}$$

Favre-averaged quantities $\tilde{\phi}$ are calculated by means of

$$\tilde{\phi} = \frac{\overline{\rho\phi}}{\overline{\rho}}. \tag{7.4}$$

Figure 7.19 shows the temporal evolution of the skin friction coefficient $\overline{c}_f$. At $t = 1.55$, a local maximum in the skin friction coefficient can be observed. Then, the skin friction coefficient sharply increases at $t \geq 1.6$, indicating the transition onset.

It reaches a maximum value of $\overline{c}_f = 0.0026$. For $t \geq 1.9$, the skin friction coefficient shows an enduring decrease. This behavior is related to the onset of the turbulent flow regime. For comparison, Figure 7.19 also contains the turbulent skin friction coefficient $\overline{c}_{f,turb}$, which is, according to White (1991), specified as

$$\overline{c}_{f,turb} = \frac{0.455}{S^2 ln^2 \left(\frac{0.06}{S} \frac{\mu_e^*}{\mu_w^*} \sqrt{\frac{T_e^*}{T_w^*}} Re_e \right)}, \tag{7.5}$$

where

$$S = \frac{\sqrt{\frac{T_{aw}^*}{T_e^*} - 1}}{sin^{-1}(A) + sin^{-1}(B)},$$

with

$$A = \frac{2a^2 - b}{\sqrt{4a^2 + b^2}}, \quad B = \frac{b}{\sqrt{4a^2 + b^2}}, \quad a = \sqrt{\frac{(\gamma - 1)}{2} \frac{T_e^*}{T_w^*} M_e^2} \quad \text{and} \quad b = \left(\frac{T_{aw}^*}{T_w^*} - 1 \right).$$

The adiabatic wall temperature is computed according to $T_{aw} = T_e + r\,(T_{0,e} - T_e)$, with $T_{0,e} = T_e\,(1 + (\kappa - 1)M_e^2/2)$. r indicates the recovery factor and is given as $r = Pr^{\frac{1}{3}} \approx 0.89$. The wall temperature and the boundary layer edge temperature are $T_w^* = 618.22K$ and $T_e^* = 71.75K$, respectively. According to Sutherland's law, the dynamic viscosities at the wall and at the boundary layer edge are given as $\mu_w^* = 3.1996 \cdot 10^{-4} Ns/m^2$ and $\mu_e^* = 4.9788 \cdot 10^{-5} Ns/m^2$, respectively. Equation (7.5) is only valid for a flat plate boundary layer. In order to apply the computed skin friction coefficient to a conical boundary layer, it must be multiplied by a factor G, where $1.1 < G < 1.15$ (White, 1991). The turbulent skin friction coefficient calculated from equation (7.5) and corrected with the factor $G = 1.15$ is $\overline{c}_{f,turb} = 0.002$. This value is lower than the maximum value of the skin friction coefficient computed from TDNS, but seems to be approached for times $t > 2.1$. Such an overshoot was also observed by Mayer *et al.* (2008) in their spatial simulation of oblique breakdown at Mach 3.

In addition, the temporal development of the Favre-averaged velocity profile $\tilde{u}$, plotted in Figure 7.20, is an appropriate quantity to characterize the transition process. It can be observed that the gradient $d\tilde{u}/dr$ at the wall increases with increasing time. This behavior is characteristic for the laminar-turbulent transition process. Note that the maximum wall gradient of the velocity profile is directly related to the maximum value of the skin friction coefficient. As the skin friction decreases, the gradient $d\tilde{u}/dr$ at the cone surface decreases accordingly and vice versa. Moreover, it can be seen from Figure 7.20 that the velocity profiles for $t \geq 1.35$ show two inflection points, which is another feature of the transitional flow regime. Furthermore, it can be observed that the boundary layer thickness subsequently increases to a value of approximately 2.5 times the laminar boundary layer thickness. Altough the velocity profile approaches the shape of a turbulent profile, a fully turbulent state is not yet reached. This can be concluded from the fact that the velocity profile at the last time instance $t = 2.11$ still contains inflection points.

Figure 7.21 presents the temporal evolution of the streamwise and azimuthal averaged temperature profile $\overline{T}$. Like the Favre-averaged velocity profiles, the temperature profiles become fuller as the flow becomes transitional. Furthermore, it can be seen that the boundary layer thickness increases with time. In addition, it can be verified that the flow hasn't reached a fully turbulent state, since a turbulent temperature profile shape is not completely developed.

An appropriate quantity to visualize the numerical results is the vorticity $\boldsymbol{\omega}$. The vorticity vector is calculated according to $\boldsymbol{\omega} = \bigtriangledown \times \boldsymbol{u}$. In scalar form the vorticity is given as

$$\begin{aligned} \omega_x &= r\frac{\partial w}{\partial r} - \frac{1}{r}\frac{\partial v}{\partial \varphi}, \\ \omega_r &= \frac{\partial u}{\partial \varphi} - \frac{\partial w}{\partial x}, \\ \omega_\varphi &= \frac{\partial v}{\partial x} - \frac{\partial u}{\partial r}. \end{aligned} \tag{7.6}$$

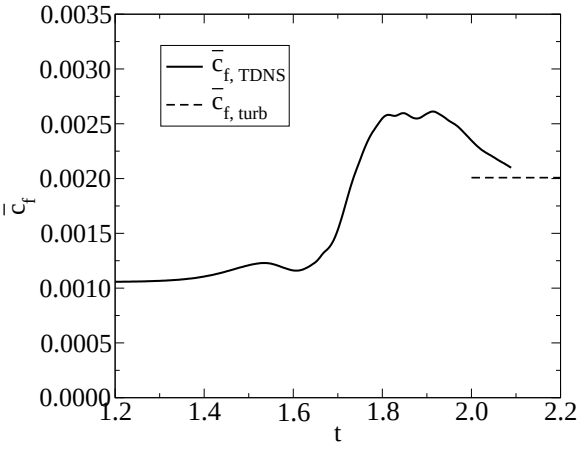

Figure 7.19: Temporal evolution of the skin friction coefficient $\bar{c}_{f,TDNS}$ obtained from TDNS compared to the skin friction coefficient $\bar{c}_{f,turb}$ obtained from equation (7.5). $A_{(1,1)} = 10^{-4}$, $R_x = 2024.17$, $M_\infty = 7.95$, $T^*_\infty = 53.35K$, $Re_\infty = 3,333,333$.

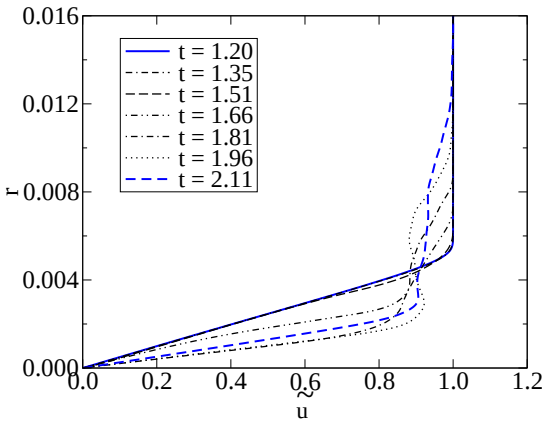

Figure 7.20: Temporal evolution of Favre-averaged velocity profile $\tilde{u}$. $A_{(1,1)} = 10^{-4}$, $R_x = 2024.17$, $M_\infty = 7.95$, $T^*_\infty = 53.35K$, $Re_\infty = 3,333,333$.

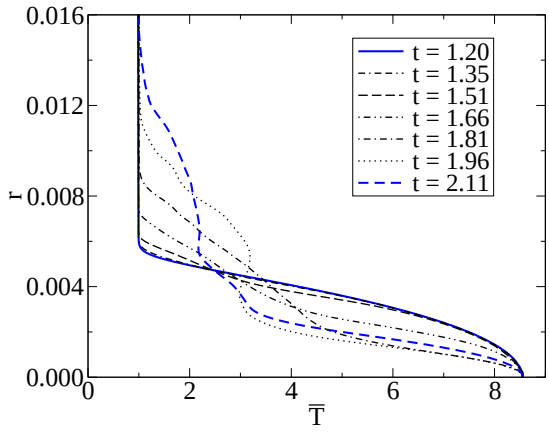

Figure 7.21: Temporal evolution of streamwise and azimuthal averaged temperature profile $\overline{T}$. $A_{(1,1)} = 10^{-4}$, $R_x = 2024.17$, $M_\infty = 7.95$, $T^*_\infty = 53.35K$, $Re_\infty = 3,333,333$.

The temporal evolution of the vorticity in azimuthal direction ω_φ in the (x-r)-plane at the streamwise centerline of the computational domain $\varphi = 0.078$ is shown in Figure 7.22. Note that negative vorticity values indicate a clockwise rotation. Throughout this thesis, a clockwise rotation is represented by dashed contour lines and blue isosurfaces, whereas a counterclockwise rotation is denoted by solid contour lines and red isosurfaces. Time instance $t = 1.35$ shows the steady laminar boundary layer. At $t = 1.51$, the boundary layer is distorted and shows the presence of rope-like structures in the outer portion of the boundary layer. These structures indicate the nonlinear regime. The formation of small clockwise and counterclockwise rotating vortices, originating from the rope-like structures, can be seen for $t = 1.66$. The break up into small scale structures at the tip of these structures can be observed for $t = 1.81$. Hereafter,a counterclockwise rotating vorticity layer in the center of the boundary layer has developed for $t = 1.96$. The boundary layer thickness increases with time due to fact that the near-wall boundary layer fluid undergoes a mixing with the fluid in the outer boundary layer region. Note that the flow pattern at $t = 2.11$ is not yet totally random. A fairly constant vorticity distribution in the near-wall region can be observed. For the different azimuthal position $\varphi = 0.0039$, the flow structures show less coherence, but the constant vorticity layer in the near-wall region is also present as shown in Figure 7.23. This is a further indication that turbulent flow is not yet fully established. The last time instance $t = 2.11$ is therefore associated with the late stages of transition, where the flow exhibits both, larger and smaller structures.

Figure 7.24 gives the temporal development of the streamwise vorticity ω_x in the (x-φ)-plane at $x = 0.0067$. Note that Figure 7.24 shows only one half azimuthal wave length due to symmetry enforced in azimuthal direction. It can be observed that the amount of streamwise vorticity subsequently increases with time. For $t = 1.51$ longitudinal structures start to develop, caused by the growing of the vortex mode $(0, 2)$. At $t = 1.66$, one such longitudinal structure can be clearly identified. It

eventually merges with its neighboring analog for $t = 1.81$. Finally, the development of small scale structures throughout the computational domain can be observed for $t = 1.96$ and $t = 2.11$. Compared to the azimuthal vorticity, the streamwise vorticity ω_x demonstrates a more random flow pattern. This is consistent with the findings of e.g. Eissler (1995), who reported that the spectrum is filled up first in azimuthal direction.

Furthermore, the flow structures are visualized by means of the Q-criterion. This criterion identifies coherent vortical structures and, according to Hunt *et al.* (1988), represents a relationship between the local strain and rotation rate. Q is positive, if the rotation rate $\Omega^2 = \Omega_{i,j}\Omega_{i,j}$ is greater than the strain rate $S^2 = S_{i,j}S_{i,j}$ and thus identifies a vortex core. It is defined as the second invariant of the velocity gradient vector $\bigtriangledown\mathbf{u}$. For a circular cylinder, the Q-criterion is specified as (Husmeier, 2008):

$$Q = -\frac{1}{2}\left(\frac{\partial v}{\partial x}\frac{\partial u}{\partial r} + \frac{\partial v}{\partial \varphi}\frac{\partial}{\partial r}\left(\frac{w}{r}\right) + \frac{\partial u}{\partial \varphi}\frac{\partial}{\partial x}\left(\frac{w}{r}\right)\right) \tag{7.7}$$

Isocontour plots of constant Q are given in Figure 7.25 and Figure 7.26. At $t = 1.35$, the characteristic structure of a linear oblique disturbance wave can be observed. The modulation of this structure at the outer portion of the boundary layer is shown for $t = 1.43$, which results in the development of hexagonal structures for $t = 1.51$. This effect is due to the development of the higher harmonics in the nonlinear regime. In particular, the superposition of the generated vortex mode $(0, 2)$ and the initially forced disturbance mode $(1, 1)$ leads to this particular pattern. At $t = 1.58$, the hexagonal structures break up and the development of two longitudinal structures can be seen, indicating the dominance of the streamwise vortex mode. The presence of these two longitudinal structures is more pronounced for $t = 1.66$. Simultaneously, a randomization of the flow within these structures takes place. Finally, Figure 7.26 b) and Figure 7.26 c) show that the longitudinal structures brake up into small scale

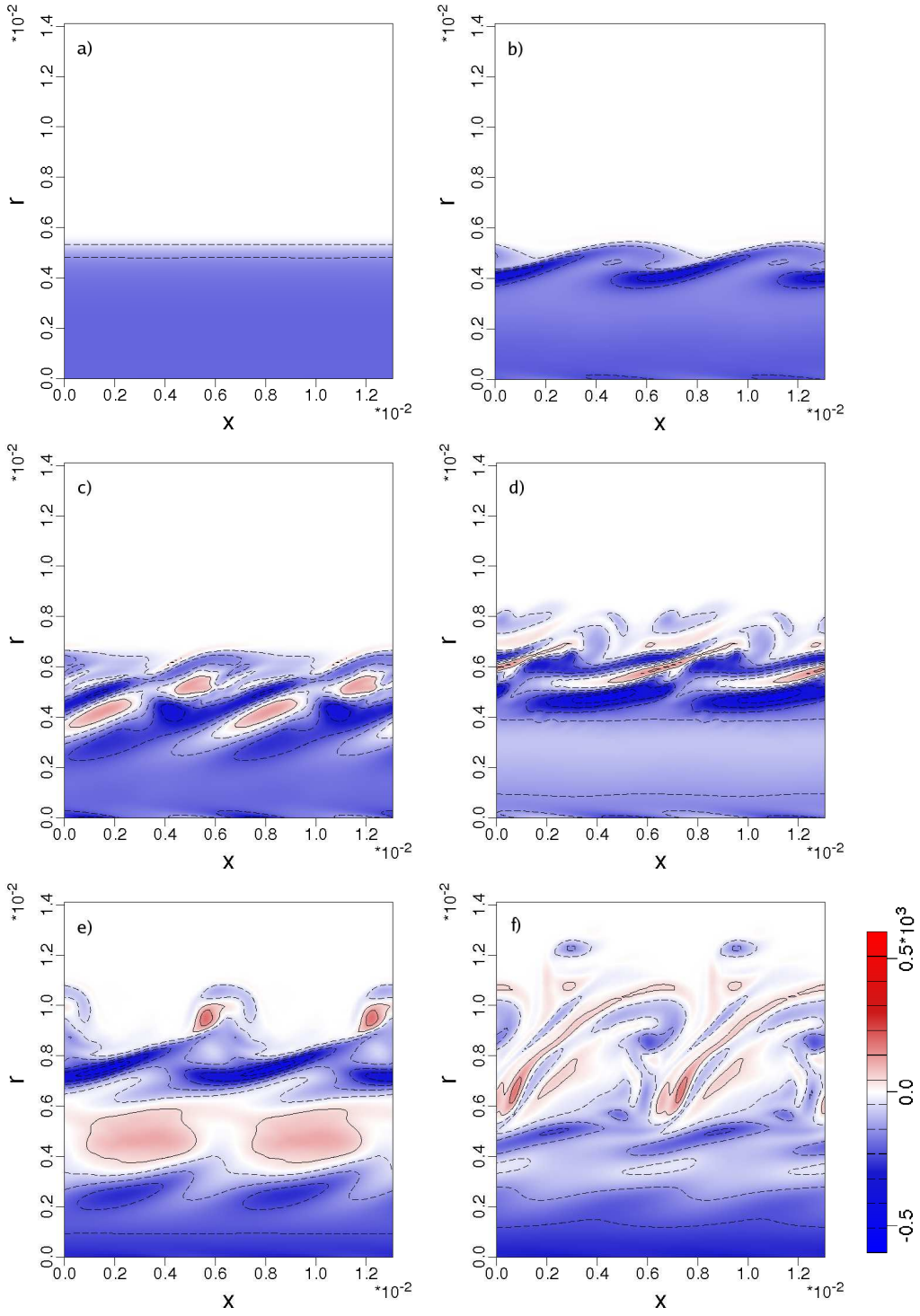

Figure 7.22: Isocontours of azimuthal vorticity ω_φ at $\varphi = 0.078$ for a) $t = 1.35$, b) $t = 1.51$, c) $t = 1.66$, d) $t = 1.81$, e) $t = 1.96$ and f) $t = 2.11$. $A_{(1,1)} = 10^{-4}$, $R_x = 2024.17$, $M_\infty = 7.95$, $T^*_\infty = 53.35K$, $Re_\infty = 3,333,333$.

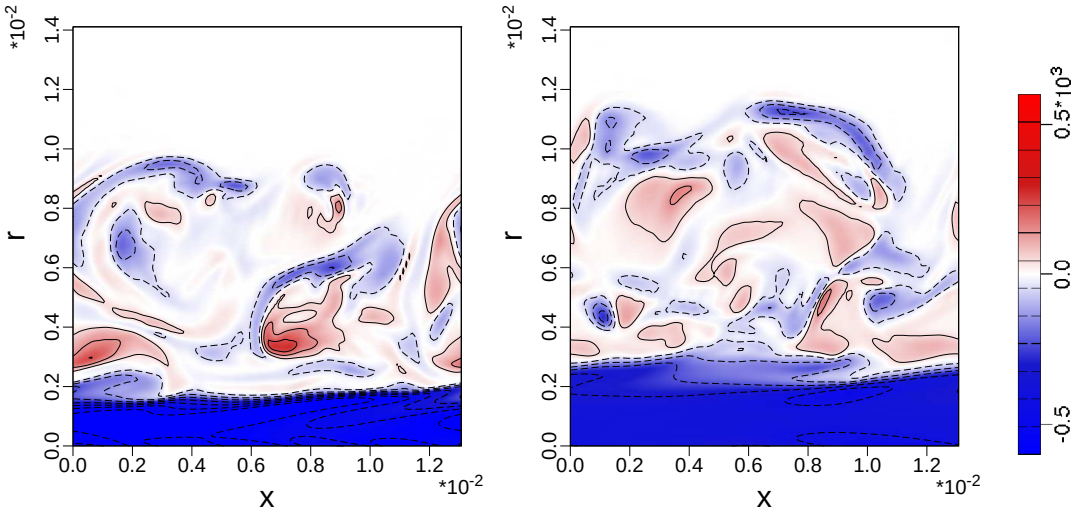

Figure 7.23: Temporal evolution of azimuthal vorticity ω_φ at $\varphi = 0.039$ for $t = 1.96$ (left) and $t = 2.11$ (right). $A_{(1,1)} = 10^{-4}$, $R_x = 2024.17$, $M_\infty = 7.95$, $T^*_\infty = 53.35K$, $Re_\infty = 3,333,333$.

structures, which spread across the whole computational domain. This represents the late stages of transition.

7.3.4 Preliminary Summary of Oblique Breakdown Simulations

Altough two-dimensional disturbance waves are stronger amplified than three-dimensional disturbance waves, oblique breakdown was found to be a viable path to transition for the investigated hypersonic flow over a sharp circular cone. A simulation of oblique breakdown all the way to the late stages of transition was carried out for the azimuthal mode number $k_c = 20$. The skin friction coefficient, the Favre-averaged velocity profile and the streamwise and azimuthal averaged temperature profile were analyzed and showed their characteristic transformation as the flow became transitional. Also, isocontours of vorticity in streamwise and azimuthal direction as well as isosurfaces of constant Q described the laminar-turblent transition process and revealed characteristic features of oblique breakdown. This includes the formation of hexagonal structures, followed by the development of longitudinal structures and

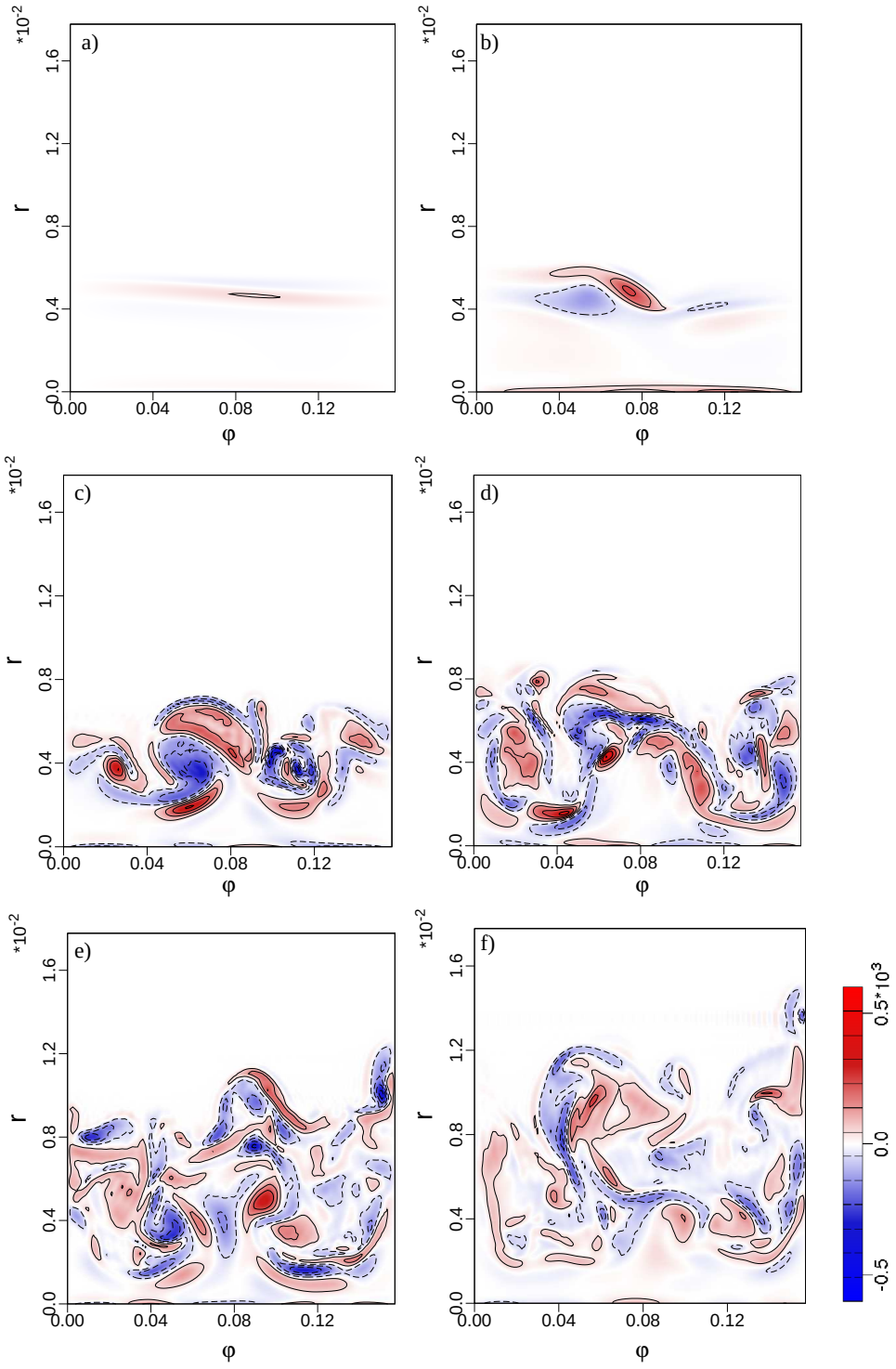

Figure 7.24: Temporal evolution of streamwise vorticity ω_x at $x = 0.0067$ for a) $t = 1.35$, b) $t = 1.51$, c) $t = 1.66$, d) $t = 1.81$, e) $t = 1.96$ and f) $t = 2.11$. Shown is half the azimuthal wavelength of the pair of secondary waves. $A_{(1,1)} = 10^{-4}$, $R_x = 2024.17$, $M_\infty = 7.95$, $T^*_\infty = 53.35K$, $Re_\infty = 3,333,333$.

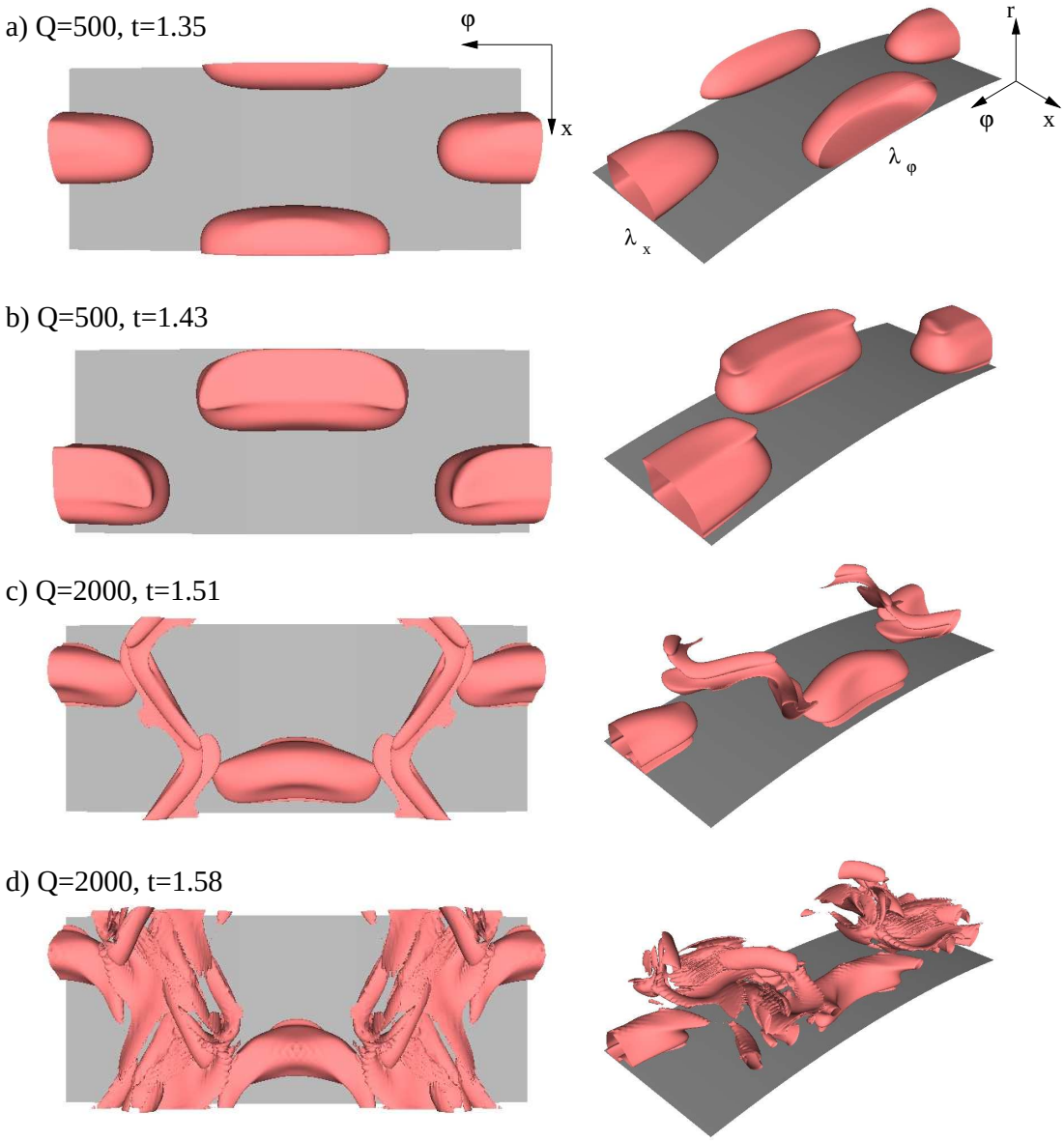

Figure 7.25: Temporal evolution of constant isosurfaces of Q for the early stages of transition at a) $t = 1.35$, b) $t = 1.43$, c) $t = 1.51$ and d) $t = 1.58$. $A_{(1,1)} = 10^{-4}$, $R_x = 2024.17$, $M_\infty = 7.95$, $T^*_\infty = 53.35K$, $Re_\infty = 3,333,333$.

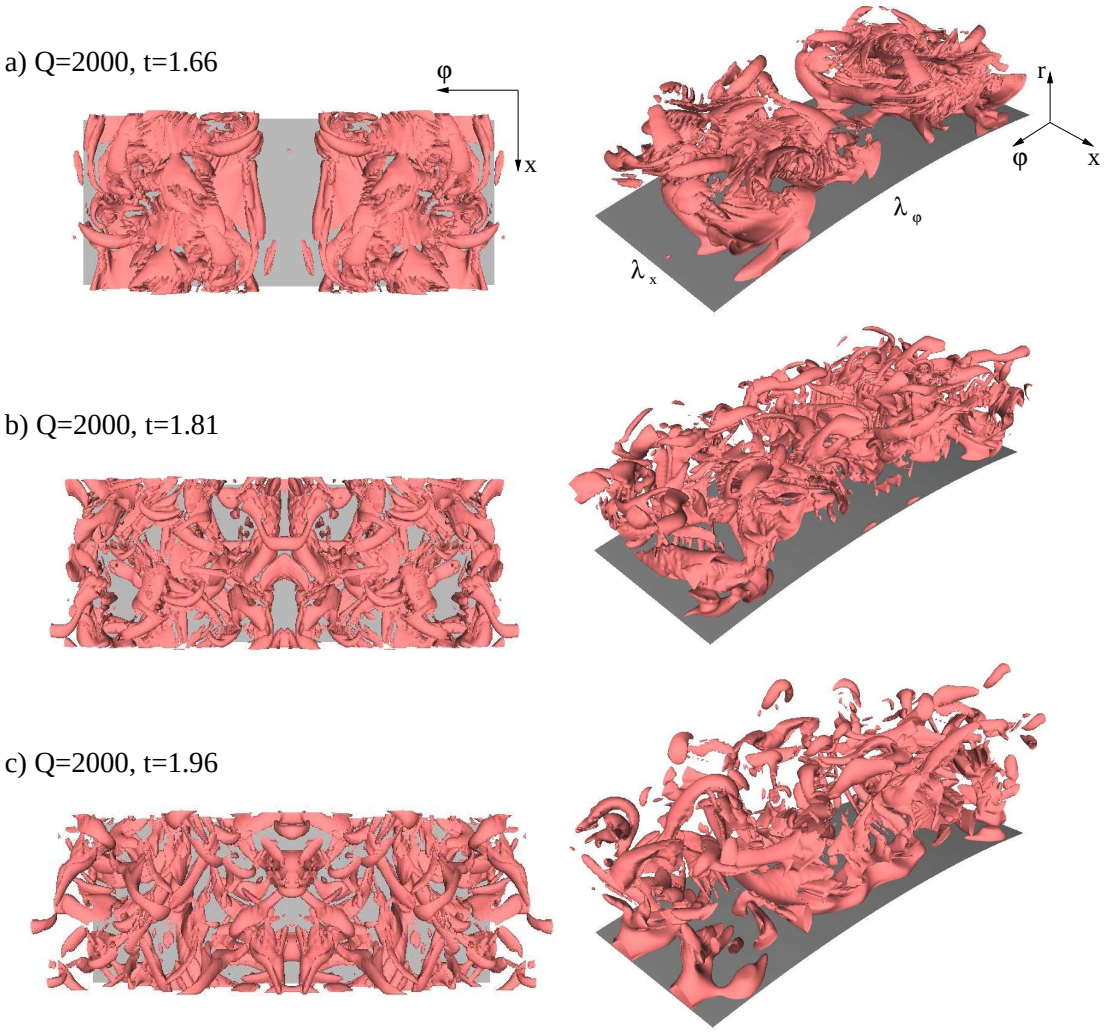

Figure 7.26: Temporal evolution of constant isosurfaces of Q for the late stages of transition at a) $t = 1.66$, b) $t = 1.81$ and c) $t = 1.96$. $A_{(1,1)} = 10^{-4}$, $R_x = 2024.17$, $M_\infty = 7.95$, $T^*_\infty = 53.35K$, $Re_\infty = 3,333,333$.

finally the break up into small scale structures.

7.4 Subharmonic Resonance

In the following, subharmonic nonlinear interactions between two-dimensional and three-dimensional disturbance waves are investigated. First, section 7.4.1 describes the linear behavior of the fast and slow boundary layer mode for the present setup. This is necessary for the understanding of the following chapters. Hereafter, the investigation of symmetric subharmonic resonance is presented in section 7.4.2.

7.4.1 Fast and Slow Mode Behavior

As already briefly mentioned in the introduction, it was found by Fedorov & Khokhlov (2002); Fedorov (2003) that Mack's so called first, second, etc. modes aren't distinct modes within the framework of the viscous analysis. In fact, there exist two boundary layer modes, namely mode F and mode S, where the latter has the characteristic properties of Mack's first and higher modes depending on the streamwise wave number α_r. Both boundary layer modes are involved in the transition process.

Fedorov (2003), Tumin (2007) and many other authors showed that the boundary layer modes undergo a synchronization with the acoustic spectrum for small streamwise wave numbers α_r. The name of mode S, also called slow mode, stems from the fact that it is synchronized for small α_r with the slow acoustic spectrum, having the phase speed $c_{ph,x} = 1 - 1/M$. Accordingly, mode F, also labeled as fast mode, is synchronized with the fast acoustic spectrum, having the phase speed $c_{ph,x} = 1 + 1/M$. The labeling 'mode F' and 'mode S' is commonly used for classification purposes, since the asymptotic behavior for small α_r is a characteristic behavior. With increasing streamwise wave number, two other synchronizations occur. There is one synchronization of mode F with the entropy and vorticity spectrum, having the phase speed $c_{ph,x} = 1$, as well as one synchronization of mode F with mode S. A synchro-

nization point is defined as the location of α_r where the phase speed $c_{ph,x} = \frac{\omega_r}{\alpha_r}$ of two or more waves is identical. Figure 7.27 shows the phase velocities $c_{ph,x}$ of the fast mode (mode F), slow mode (mode S) and the entropy and vorticity waves as function of the streamwise wave number α_r for the investigated setup ($k_c = 0$). The entropy and vorticity waves have the phase speed $c_{ph,x} = 1$, since they travel with the free-stream. Figure 7.27 and Figure 7.28 are both obtained from linear stability theory for the parameters presented in Table 7.1. It can be seen that the fast mode is synchronized with the entropy and vorticity waves for the streamwise wavenumber $\alpha_r = 359.5$. The synchronization of the fast and slow mode occurs for the streamwise wavenumber $\alpha_r = 427.6$. The two synchronizations lead to a significant increase in the temporal amplification of mode S. This effect can be observed in Figure 7.28, where the temporal growth rates ω_i of mode S and mode F are plotted as a function of the streamwise wavenumber α_r. Clearly, mode S is the dominant mode for the present setup. Note that Mack's first-mode region is represented for low streamwise wave numbers, whereas the second-mode region is represented for higher streamwise wave numbers after the synchronization. Note further that for certain flow conditions mode F can be amplified and mode S can be damped after the synchronization.

7.4.2 Parameter Study

According to Craik (1971), symmetric subharmonic resonance, involving one two-dimensional disturbance wave and a pair of oblique disturbance waves, occurs if the following constraints are fulfilled:

$$\alpha_{r,fund} = 2 \cdot \alpha_{r,sub} \tag{7.8}$$

$$\omega_{r,fund} = 2 \cdot \omega_{r,sub} \tag{7.9}$$

Figure 5.3 shows the temporal growth rate ω_i of two-dimensional disturbances as a

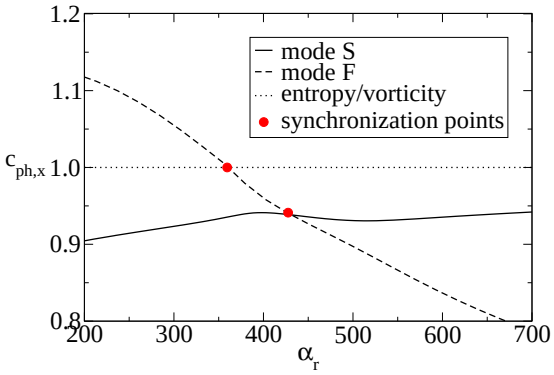

Figure 7.27: Phase velocities $c_{ph,x}$ of mode S, mode F and entropy/vorticity waves obtained from TLST. $R_x = 2024.17$, $M_e = 6.76$, $T_e^* = 71.75K$, $Re_e = 4,796,970$.

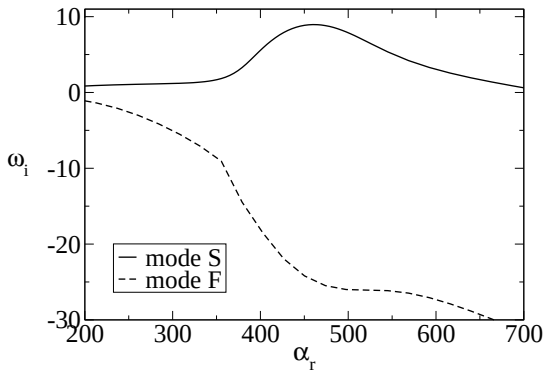

Figure 7.28: Temporal growth rates ω_i of fast and slow mode obtained from TLST. $R_x = 2024.17$, $M_e = 6.76$, $T_e^* = 71.75K$, $Re_e = 4,796,970$.

function of the the streamwise wavenumber α_r. The disturbance wave with the maximum temporal growth rate $\omega_{i,max}$ defines the streamwise wavenumber $\alpha_{r,fund} = 465.6$ of the primary, fundamental disturbance wave in the following study. This is indicated by the dotted, vertical line in Figure 5.3. Hence, the subharmonic streamwise wave number for a resonance according to Craik is given as $\alpha_{r,sub} = \frac{\alpha_{r,fund}}{2} = 232.8$, which is represented by the dashed, vertical line in Figure 5.3. The disturbance frequencies $\omega_{r,sub}$ and $\frac{\omega_{r,fund}}{2}$ are plotted against the azimuthal mode number k_c in Figure 7.30. The intersection point of both curves fulfills equation (7.9) and defines the subharmonic resonance point. Figure 7.30 (left) originates from temporal direct numerical simulations, whereas Figure 7.30 (right) is taken from linear stability theory. Note that DNS predicts a resonance point at $k_c = 70$, unlike LST that predicts $k_c = 68$. This discrepancy is due to the fact that, first, the second viscosity coefficient is set to zero for the temporal direct numerical simulations, second, curvature effects are not included in the LST computations and third, different base flow profiles are used. Moreover, it can be observed that according to Figure 7.30 (right) subharmonic resonance with oblique fast modes does not exist due to the absence of an intersection

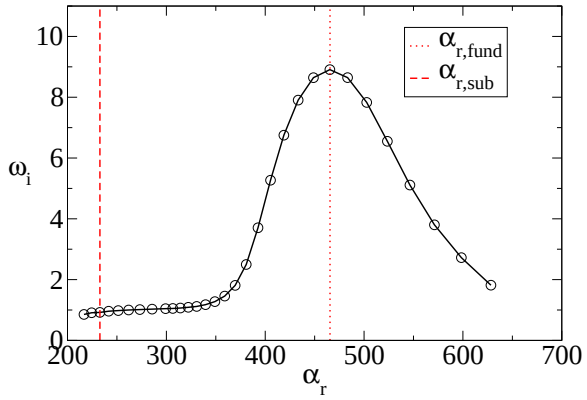

Figure 7.29: Temporal growth rate ω_i of two-dimensional disturbances. The dotted, vertical line indicates the streamwise wave number of the primary wave and the dashed, vertical line denotes the streamwise wave number of the secondary, subharmonic wave for subharmonic resonance investigated in this chapter. $R_x = 2024.17$, $M_\infty = 7.95$, $T^*_\infty = 53.35K$, $Re_\infty = 3,333,333$.

point of mode F with $\frac{\omega_{r,fund}}{2}$.

Note that according to Figure 7.30 the difference between the frequencies $\omega_{r,sub}$ and $\frac{\omega_{r,fund}}{2}$ is very small. Therefore, detuned subharmonic resonance may also occur for different azimuthal mode numbers. Hence, additional simulations with the azimuthal mode numbers of the secondary disturbance waves $k_c = 40$, $k_c = 50$, $k_c = 60$ and $k_c = 80$ are performed. For all cases, the fundamental mode, in the following denoted as mode $(2,0)$, is initially forced with the amplitude $A_{(2,0)} = 10^{-4}$ and the subharmonic modes, indicated by $(1,1)$, are forced with the amplitude $A_{(1,1)} = 10^{-6}$. The simulations are performed using nine Fourier modes in streamwise, 345 points in wall-normal and five Fourier modes in azimuthal direction. Figure 7.31 shows the temporal development of the maximum disturbance velocity in streamwise direction $|u'|_{(h,k)}$ for different azimuthal mode numbers of the secondary disturbance waves. Mode $(1,1)$ deviates from its eigenbehavior at about $t = 0.8$ for all cases. The departure of mode $(1,1)$ from its eigenbehavior proves that subharmonic resonance is present. However, the amplitude of mode $(1,1)$ levels off shortly after the resonance onset when mode $(2,0)$ saturates. All simulations show that the secondary three-

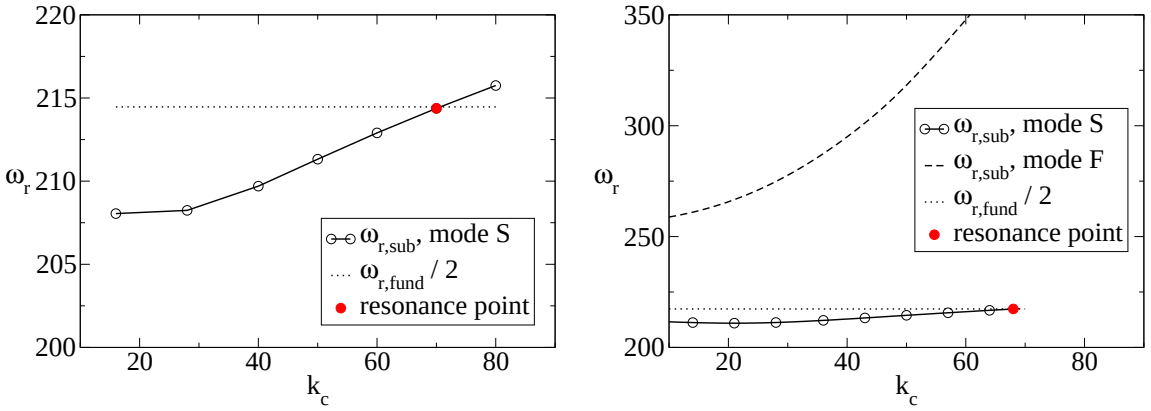

Figure 7.30: Frequencies ω_r of fundamental and subharmonic disturbances. Left: DNS, slow mode, $R_x = 2024.17$, $M_\infty = 7.95$, $T^*_\infty = 53.35K$, $Re_\infty = 3,333,333$. Right: LST, fast and slow mode, $R_x = 2024.17$, $M_e = 6.76$, $T^*_e = 71.75K$, $Re_e = 4,796,970$.

dimensional disturbances do not exhibit an enduring explosive growth, but saturate towards the end of the computation and never exceed the amplitude of the primary disturbance wave. It can therefore be concluded that subharmonic resonance plays a minor role for the present setup.

This conclusion, however, is contradictory to the results of Bountin *et al.* (2008), who reported subharmonic resonance in their $M = 5.95$ flat plate experiments. It might be speculated that in the experiments of Bountin *et al.* (2008) subharmonic resonance is caused by a higher amplitude of the secondary disturbance wave. Hence, a simulation is performed, where the initial amplitude of the secondary three-dimensional disturbance is increased to $A_{(1,1)} = 10^{-3}$. This amplitude value is higher than the initial amplitude of the primary disturbance and was chosen such that the amplitudes of the the primary and secondary disturbances are nearly the same after the receptivity region. Figure 7.32 presents the temporal development of the maximum disturbance velocity in streamwise direction $|u'|_{(h,k)}$ for the azimuthal mode numbers of the secondary disturbance waves $k_c = 70$ and $k_c = 50$. The graphs reveal that a higher initial amplitude of the secondary disturbance does not influence the behavior that was already presented in Figure 7.31. This is coherent with the

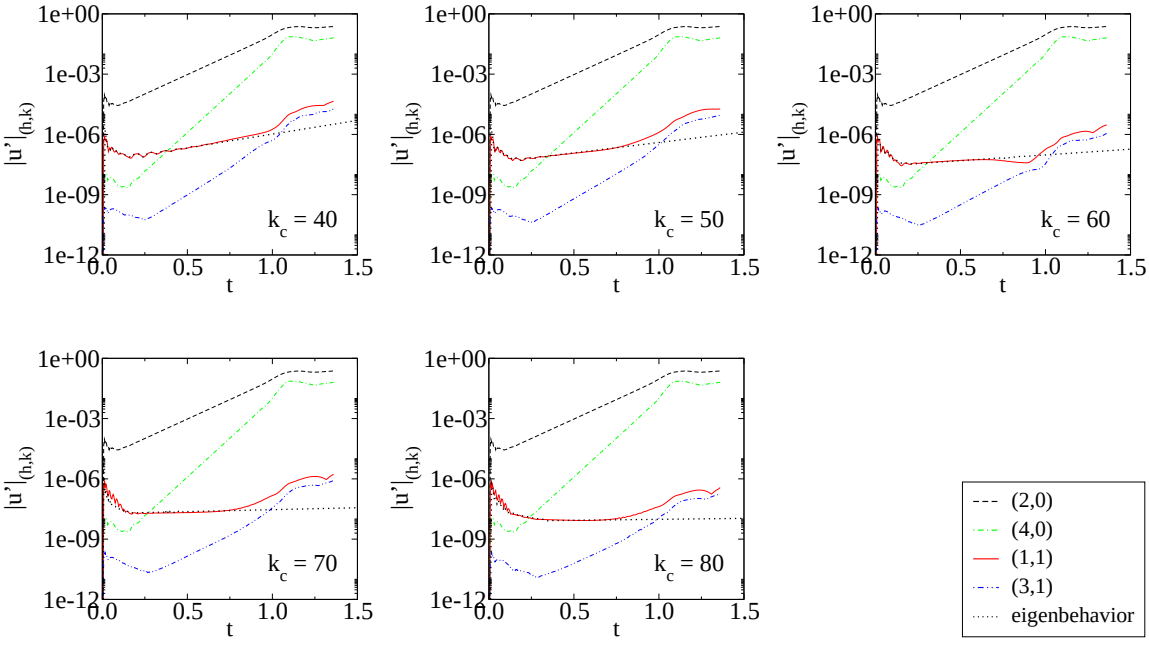

Figure 7.31: Temporal development of the maximum disturbance velocity in streamwise direction $|u'|_{(h,k)}$ for $k_c = 40, 50, 60, 70$ and 80. $A_{(2,0)} = 10^{-4}$, $A_{(1,1)} = 10^{-6}$, $R_x = 2024.17$, $M_\infty = 7.95$, $T^*_\infty = 53.35K$, $Re_\infty = 3,333,333$.

findings of Chang & Malik (1993), who also reported that an increase of the initial amplitude of the secondary disturbance does not cause an enduring explosive growth of mode $(1,1)$.

In conclusion, subharmonic resonance could be detected for the azimuthal mode number of the secondary, three-dimensional disturbance waves $k_c = 70$. Compared to oblique breakdown, subharmonic resonance is weak and plays a minor role for the given setup. The findings are consistent with those of Ng & Erlebacher (1992), Chang & Malik (1993), Eissler & Bestek (1996) and Husmeier (2008). Note that in contrast to Eissler & Bestek (1996) a departure of mode $(1,1)$ from its eigenbehavior does not occur immediately after the disturbance input, altough the resonance condition is always fulfilled. The deviation occurs when the amplitude level of the primary, two-dimensional disturbance wave has reached a value in the range from 0.2% to 1%. Altough the initial amplitude of the secondary disturbance was increased, the results

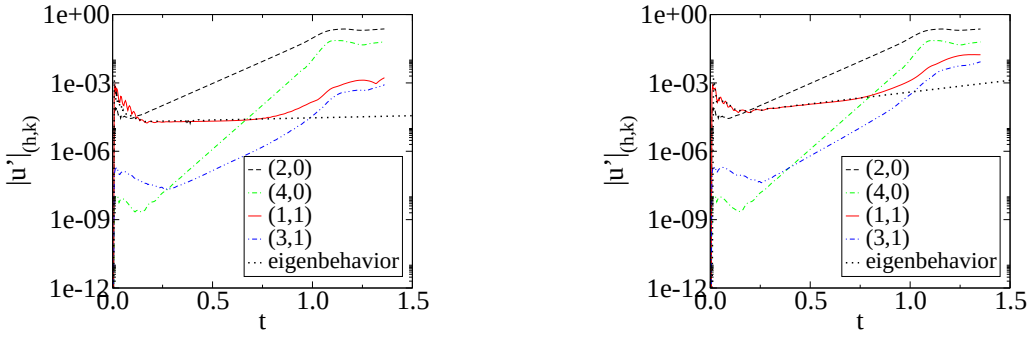

Figure 7.32: Temporal development of the maximum disturbance velocity in streamwise direction $|u'|_{(h,k)}$ for $k_c = 70$ (left) and $k_c = 50$ (right). $A_{(2,0)} = 10^{-4}$, $A_{(1,1)} = 10^{-3}$, $R_x = 2024.17$, $M_\infty = 7.95$, $T^*_\infty = 53.35K$, $Re_\infty = 3,333,333$.

show that subharmonic resonance appearently is not a viable path to transition for the investigated setup.

7.5 Fundamental Resonance

This section is dedicated to the investigation of fundamental resonance for a sharp circular cone at Mach 7.95. At first, an investigation of the linear flow regime is carried out in section 7.5.1. Then, a parameter study is performed in section 7.5.2 to identify cases that are promising to cause final breakdown to turbulence. In section 7.5.3, a highly resolved simulation of fundamental resonance is presented. Finally, section 7.5.4 gives a brief summary of the results.

7.5.1 Investigation of the Linear Regime

Fundamental resonance is characterized by nonlinear interactions between a primary, two-dimensional disturbance wave $(1, 0)$ and a pair of secondary, three-dimensional disturbance waves $(1, 1)$ with the same frequency and streamwise wave length. Note that according to Figure 5.3 the streamwise wave number of both, the two-dimensional, primary disturbance wave and the three-dimensional, secondary disturbance wave is given as $\alpha_r = 465.6$ for the present setup. As summarized by Herbert (1988), funda-

mental resonance is generally linked to secondary instabilities. Since Eissler & Bestek (1996) reported fundamental resonance governed by both, mode S and mode F different fundamental resonances, which involve different discrete eigenmodes, might be possible. In the following, results of lower-amplitude TDNS and TLST are used in order to locate possible resonance interactions between different discrete modes for the same frequency by applying Craik's resonance conditions. Note that this approach is not conventional, since, as mentioned above, fundamental resonance is commonly used in the context of secondary instability. The results of this study are illustrated in Figure 7.33, where the frequencies of waves with $\alpha_r = 465.6$ are plotted versus the azimuthal mode number. Note that the results in Figure 7.33 (left) are taken form temporal DNS, whereas Figure 7.33 (right) was calculated using Mack's temporal linear stability solver. As already presented in section 7.4, the differences between the graphs are due to the following facts: First, the second viscosity coefficient $\lambda = 0.8$ is not considered in the temporal direct numerical simulations. Second, curvature effects are present in the TDNS and third, different base flow profiles are used (section 7.2). Despite the different assumptions of TDNS and TLST, both figures show the same trends and thus can be compared qualitatively. As expected, a resonance point cannot be identified in Figure 7.33 (left). However, Figure 7.33 (right) reveals a possible resonance between a two-dimensional mode S and an oblique mode F with the same frequency for the azimuthal mode number $k_c = 26$. Hence, the questions arise, whether a fundamental resonance between a two-dimensional mode S and an oblique mode S is present, or whether a resonance between a two-dimensional mode S and an oblique mode F can be detected.

7.5.2 Parameter Study

Simulations are performed for several different azimuthal mode numbers of the secondary disturbance waves, $k_c = 20, 26, 30, 40 \ldots, 80$. These simulations are carried

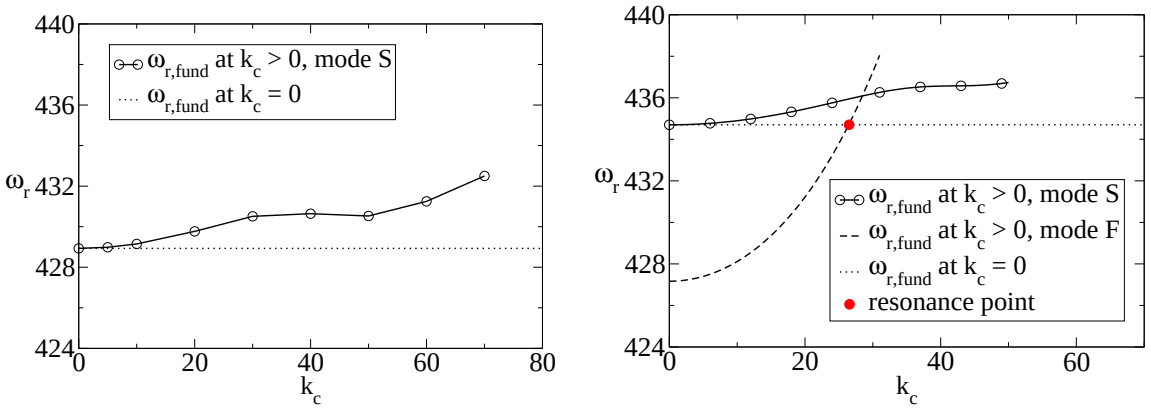

Figure 7.33: Fundamental frequency $\omega_{r,fund}$ for $k_c = 0$ and $k_c > 0$. Left: DNS, slow mode, $A_{(1,1)} = 10^{-7}$, $R_x = 2024.17$, $M_\infty = 7.95$, $T^*_\infty = 53.35K$, $Re_\infty = 3,333,333$. Right: LST, fast and slow mode, $A_{(1,1)} = 10^{-7}$, $R_x = 2024.17$, $M_e = 6.76$, $T^*_e = 71.75K$, $Re_e = 4,796,970$.

out with a sufficient resolution of nine Fourier modes in streamwise, 345 points in wall-normal and five Fourier modes in azimuthal direction. The disturbance waves $(1,0)$ and $(1,1)$ are forced with the amplitude $A_{(1,0)} = 10^{-4}$ and $A_{(1,1)} = 10^{-6}$, respectively. Figure 7.34 shows the temporal development of the maximum disturbance velocity in steamwise direction $|u'|_{(h,k)}$ for different azimuthal mode numbers of the secondary, oblique waves. All azimuthal mode numbers show that the secondary disturbance mode deviates from its linear eigenbehavior and exhibits resonant growth at around $t = 1.1$. This occurs when the primary, two-dimensional disturbance mode reaches an amplitude level of about one percent.

Figure 6.3 shows the temporal growth rate σ_i of the secondary, three-dimensional disturbance wave $(1,1)$ obtained from the maximum streamwise disturbance velocity as a function of the azimuthal mode number k_c for the particular time instances $t = 0.7$ and $t = 1.4$ of Figure 7.34 before and after the resonance onset, respectively. Before the resonance, the growth rate of mode $(1,1)$ shows its characteristic linear behavior: It decreases as the azimuthal mode number is increased and is even damped for $k_c > 60$. After the resonance, the secondary temporal growth rate σ_i has increased

for all azimuthal mode numbers k_c. The maximum of the secondary growth rate σ_i corresponds to the azimuthal mode number $k_c = 50$.

Furthermore, it can be observed from Figure 7.34 and Figure 6.3 that the results around $k_c = 26$ do not show a particularly pronounced growth of the secondary disturbance wave, which already indicates that the observed fundamental resonance is a secondary instability between the two slow modes. For further insight, the temporal development of the wall-normal amplitude distribution is investigated. Figure 7.36 shows the wall-normal amplitude distributions of the disturbance velocity in streamwise direction u' of the primary ($k_c = 0$) and secondary ($k_c = 50$) disturbance waves. It can be observed that the amplitude distribution of the secondary disturbance waves drastically changes its shape after the onset of fundamental resonance for $t \approx 1.1$. The maximum value, before the resonance located at $r \approx 0.00475$, shifts towards the wall. Apparently, the amplitude distribution of the secondary disturbance wave changes towards the amplitude distribution of the primary disturbance wave. This indicates that nonlinear effects (secondary instability) are responsible for the secondary disturbance growth. For comparison, Figure 7.37 presents the wall-normal amplitude distributions of the disturbance velocity in streamwise direction u' of the primary and secondary disturbance waves for the case with the azimuthal mode number $k_c = 26$. As for the $k_c = 50$ case, the shape of the eigenfunctions changes as the resonant growth sets in. Nevertheless, the effect is not as pronounced as for the case with the azimuthal mode number $k_c = 50$.

Figure 6.6 shows the temporal evolution of the wall pressure of the secondary disturbance wave $|p'|^{wall}_{(1,1)}$ for four different azimuthal mode numbers $k_c = 26$, $k_c = 50$, $k_c = 60$ and $k_c = 70$. Again, it can be observed that the strongest fundamental resonance occurs for the azimuthal mode number $k_c = 50$. In addition, the temporal development of the wall pressure for $k_c = 60$ and, in particular, $k_c = 70$ shows a modulation prior to the resonance onset. After resonance, the amplitude modulation disappears. A similar behavior was observed by Eissler & Bestek (1996) for a Mach 4.8

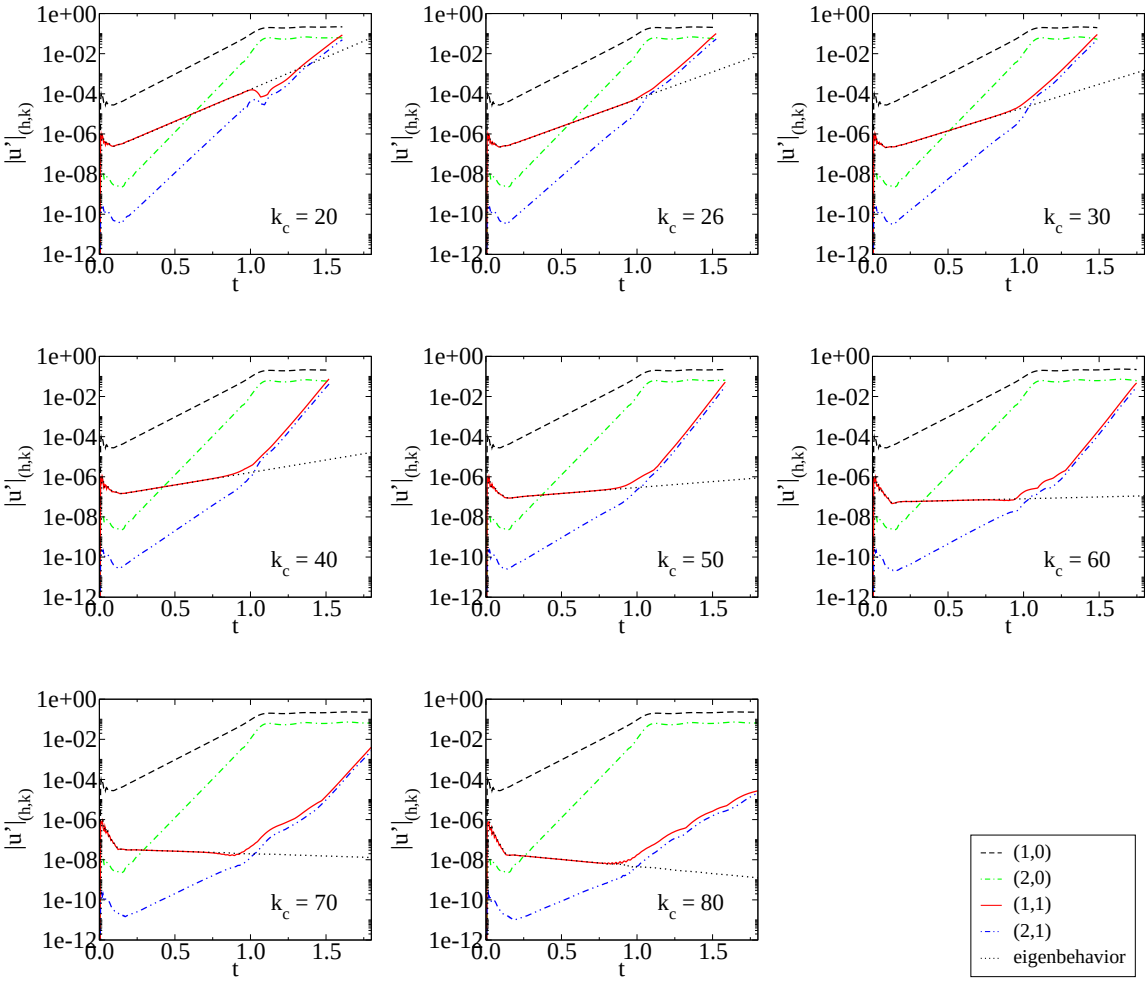

Figure 7.34: Temporal development of maximum disturbance velocity in streamwise direction $|u'|_{(h,k)}$ for nine different azimuthal mode numbers k_c. $A_{(1,0)} = 10^{-4}$, $A_{(1,1)} = 10^{-6}$, $R_x = 2024.17$, $M_\infty = 7.95$, $T^*_\infty = 53.35K$, $Re_\infty = 3,333,333$.

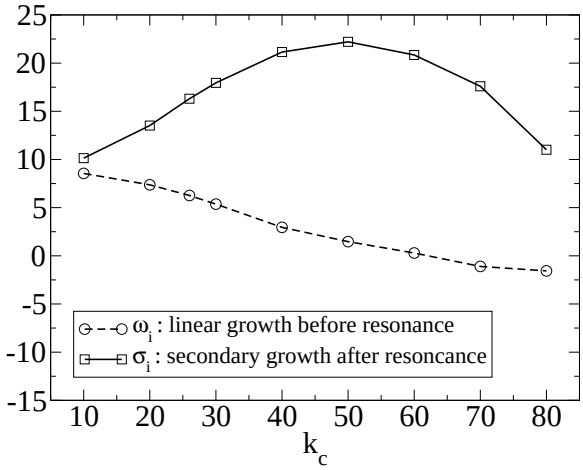

Figure 7.35: Temporal growth rate of secondary disturbance mode for $t = 0.7$ (before resonance) and $t = 1.4$ (after resonance). $A_{(1,0)} = 10^{-4}$, $A_{(1,1)} = 10^{-6}$, $R_x = 2024.17$, $M_\infty = 7.95$, $T^*_\infty = 53.35K$, $Re_\infty = 3,333,333$.

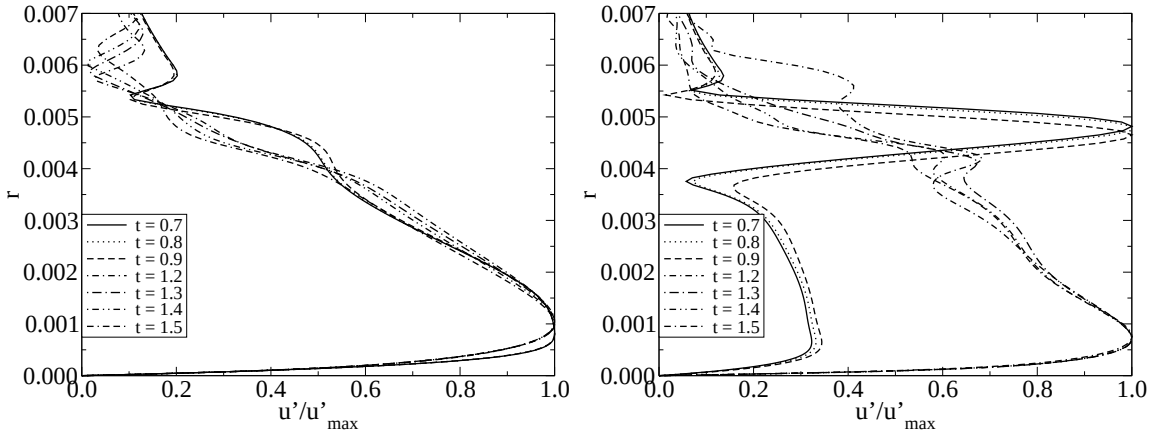

Figure 7.36: Comparison of wall-normal amplitude distributions for disturbance velocity in streamwise direction u' of primary (left) and secondary (right) disturbance mode for the azimuthal mode number $k_c = 50$. $A_{(1,0)} = 10^{-4}$, $A_{(1,1)} = 10^{-6}$, $R_x = 2024.17$, $M_\infty = 7.95$, $T^*_\infty = 53.35K$, $Re_\infty = 3,333,333$.

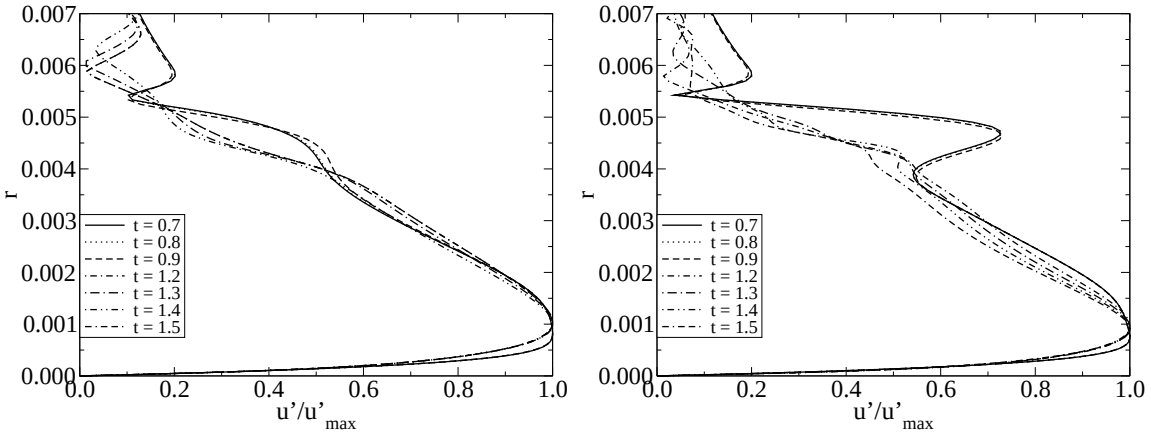

Figure 7.37: Comparison of wall-normal amplitude distributions for disturbance velocity in streamwise direction u' of primary (left) and secondary (right) disturbance mode for the azimuthal mode number $k_c = 26$. $A_{(1,0)} = 10^{-4}$, $A_{(1,1)} = 10^{-6}$, $R_x = 2024.17$, $M_\infty = 7.95$, $T^*_\infty = 53.35K$, $Re_\infty = 3,333,333$.

flow over a flat plate. They argued that such a modulation is due to the presence of two boundary layer modes (mode S and mode F). As the resonant growth sets in, only one boundary layer mode is dominant and the amplitude modulation vanishes. For the present setup however, the amplitude modulation only appears for very high azimuthal mode numbers, where the secondary disturbance wave is initially damped.

To close this chapter, it can be concluded that the identified fundamental resonance, which is particularly pronounced for the azimuthal mode number $k_c = 50$, might be caused by mode S only. Evidence for this conclusion is illustrated in Figure 7.28, which shows that the most dominant mode for the given setup is mode S, and in Figure 6.6, which demonstrates that no amplitude modulation and thus only one boundary layer mode is present for the most promising case with the azimuthal mode number $k_c = 50$. Furthermore, the wall-normal amplitude distributions before the resonance onset in Figure 6.4 and Figure 6.5 are typical for mode S in the linear regime.

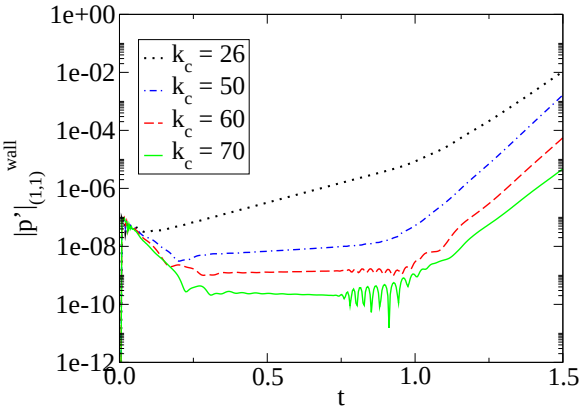

Figure 7.38: Temporal development of the wall pressure of the secondary disturbance wave $|p'|^{wall}_{(1,1)}$ for different azimuthal mode numbers k_c. $A_{(1,0)} = 10^{-4}$, $A_{(1,1)} = 10^{-6}$, $R_x = 2024.17$, $M_\infty = 7.95$, $T^*_\infty = 53.35K$, $Re_\infty = 3,333,333$.

7.5.3 Simulations with Increased Resolution

The simulation presented in this chapter is performed with 33 Fourier modes in streamwise, 345 points in wall-normal and 16 Fourier modes in azimuthal direction. In order to reduce the computational cost, mode $(1,0)$ and mode $(1,1)$ are initialized with $A_{(1,0)} = A_{(1,1)} = 10^{-4}$ and not like in the previous chapter with $A_{(1,0)} = 10^{-4}$ and $A_{(1,1)} = 10^{-6}$. Although both, the primary wave and the pair of secondary waves are forced with the same amplitude, this simulation can be considered to represent a classical fundamental breakdown, since at the resonance location the amplitude of mode $(1,1)$ is significantly lower than the amplitude of mode $(1,0)$. In this simulation, the pair of secondary, oblique waves has the azimuthal mode number $k_c = 50$ and the streamwise wave number $\alpha_r = 465.6$. As can be seen from Figure 6.7, the secondary, oblique disturbance waves $(1,1)$ depart from their eigenbehavior at $t \approx 0.9$ and exceed the amplitude level of the primary disturbance wave $(1,0)$ at $t \approx 1.5$, indicating a secondary instability. In addition, it can be observed that the vortex mode $(0,1)$ plays an important role, since it shows the highest amplitude in the transitional regime for $t > 1.4$. Note that this vortex mode is initially generated by interactions of e.g. the primary disturbance wave $(1,0)$ and the secondary disturbance waves $(1,1)$. Note

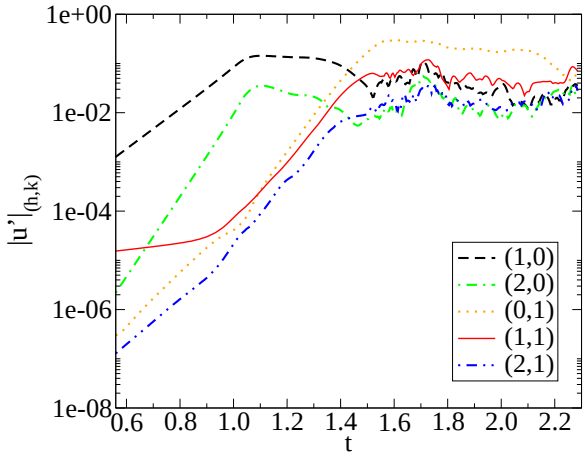

Figure 7.39: Temporal development of the maximum disturbance velocity in streamwise direction $|u'|_{(h,k)}$ for $k_c = 50$. $A_{(1,0)} = 10^{-4}$, $A_{(1,1)} = 10^{-4}$, $R_x = 2024.17$, $M_\infty = 7.95$, $T^*_\infty = 53.35K$, $Re_\infty = 3,333,333$.

further that in contrast to oblique breakdown the transition process of fundamental resonance is governed by modes with even-even and odd-odd as well as even-odd and odd-even streamwise and azimuthal mode number combinations.

A further refinement of the resolution to 63 Fourier modes in in streamwise, 345 points in wall-normal and 64 Fourier modes in azimuthal direction, corresponding to a total of $5,608,320$ grid points, allows for a thourough investigation of fundamental resonance. The following analysis is based on the investigation of the temporal evolution of the skin friction coefficient, the Favre-averaged velocity profile, the streamwise and azimuthal averaged temperature profile, the vorticity components in streamwise and azimuthal direction and the Q-criterion. The skin friction coefficient as well as the averaged quantities are computed according to equations (7.2), (7.3) and (7.4). The vorticity and the Q-criterion are obtained by equations (7.6) and (7.7), respectively.

At first, the temporal evolution of the Favre-averaged velocity profile $\tilde{u}$ is studied. It can be observed from Figure 7.40 that the profiles become fuller with increasing time due to the increased velocity gradient $d\tilde{u}/dr$ at the wall. Also, an increase in boundary layer thickness to a value of about 2.5 times the laminar boundary layer

thickness is noticeable. Moreover, the appearance of inflection points confirms the onset of transition. Note that a fully turbulent state isn't reached yet, since the profile at the last time instance $t = 1.98$ still contains inflection points.

The temporal development of the streamwise and azimuthal averaged temperature profile $\overline{T}$ is plotted in Figure 7.41. It can be observed that the profiles become fuller and the boundary layer becomes thicker as the flow reaches the transitional regime. Since the temperature profile at $t = 1.98$ still contains multiple inflection points, Figure 7.41 confirms that a fully turbulent flow regime isn't reached. As indicated by the insert in Figure 7.41, the temperature distributions for $t = 1.27$ and $t = 1.57$ show an increase in temperature close to the wall.

The temporal evolution of the skin friction coefficient $\overline{c}_f$ is shown in Figure 6.10. At $t \approx 1.0$, the initially laminar value of the skin friction increases to a value of $\overline{c}_f \approx 0.0018$, then remains approximately constant between $t \approx 1.1$ and $t \approx 1.6$, before it sharply increases for $t > 1.6$. This reflects the temporal evolution of the maximum disturbance velocity plotted in Figure 6.7. The growth of mode $(1, 0)$ up to $t \approx 1.05$ and its subsequent nonlinear saturation represents the first increase of the skin friction coefficient and its constant temporal development until $t \approx 1.6$, whereas the sharp increase of the skin friction coefficient at $t \approx 1.6$ coincides with the saturation of the secondary disturbance mode $(1, 1)$. The skin friction coefficient reaches a maximum value of $\overline{c}_f = 0.0045$ at $t = 1.87$ and then decreases for $t > 1.9$. Compared to the skin friction coefficient of oblique breakdown, it reaches values that are twice as high. Note that the skin friction coefficient obtained from TDNS for $t > 1.9$ doesn't agree with the turbulent skin friction coefficient $\overline{c}_{f,turb}$ obtained from equation (7.5). However, it is believed that the turbulent skin friction coefficient $\overline{c}_{f,turb}$ will be reached if the simulation is continued.

Figure 7.43 presents the temporal evolution of the azimuthal vorticity ω_φ in the (x-r)-plane at the the azimuthal location $\varphi = 0.0314$. From a steady laminar boundary layer at $t = 0.97$, wave-like structures develop for $t \geq 1.09$, which indicate the

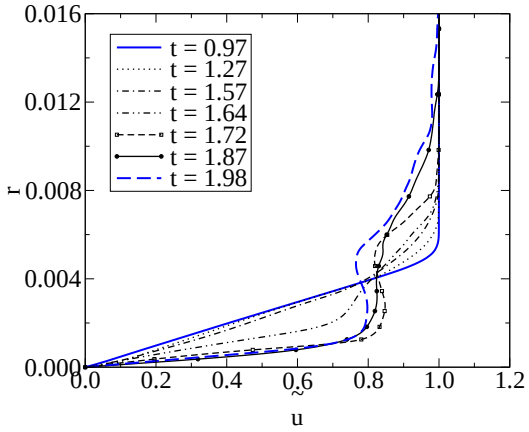

Figure 7.40: Temporal evolution of Favre-averaged velocity profile $\tilde{u}$. $A_{(1,0)} = 10^{-4}$, $A_{(1,1)} = 10^{-4}$, $R_x = 2024.17$, $M_\infty = 7.95$, $T^*_\infty = 53.35K$, $Re_\infty = 3,333,333$.

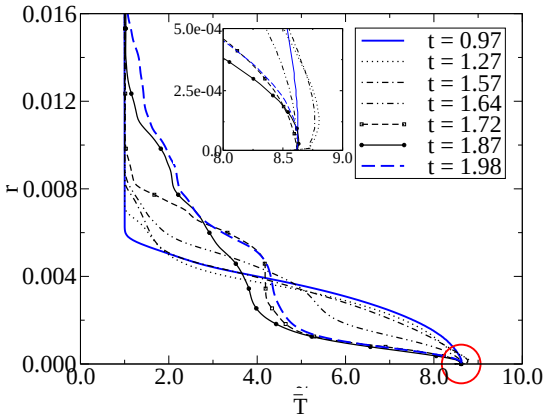

Figure 7.41: Temporal evolution of streamwise and azimuthal averaged temperature profile $\overline{T}$. $A_{(1,0)} = 10^{-4}$, $A_{(1,1)} = 10^{-4}$, $R_x = 2024.17$, $M = 7.95$, $T^*_\infty = 53.35K$, $Re_\infty = 3,333,333$.

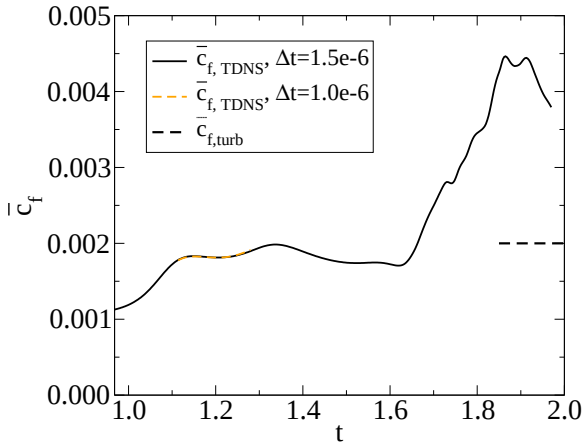

Figure 7.42: Temporal evolution of the skin friction coefficient $\overline{c}_{f,TDNS}$ obtained from TDNS compared to the skin friction coefficient $\overline{c}_{f,turb}$ obtained from equation (7.5). $A_{(1,0)} = 10^{-4}$, $A_{(1,1)} = 10^{-4}$, $R_x = 2024.17$, $M = 7.95$, $T^*_\infty = 53.35K$, $Re_\infty = 3,333,333$.

formation of Λ-vortices. These wave-like structures become more pronounced with increasing time. At $t = 1.74$, a layer of positive azimuthal vorticity has developed in the range from $r \approx 0.002$ to $r \approx 0.005$. Hereafter, the break up into smaller structures can be observed for $t = 1.86$ and $t = 1.98$. In addition, an increase in boundary layer thickness, which is typical for the transition process, is noticeable.

The temporal development of the streamwise vorticity ω_x in the (x-φ)-plane located at $x = 0.0067$ is shown in Figure 7.44. Note that only half the azimuthal wave length is shown due to the symmetry enforced in azimuthal direction. At $t = 1.35$, no streamwise vorticity is visible. Thus, the flowfield is still two-dimensional and laminar. At $t = 1.48$, however, the three-dimensional modulation of the flow structures is represented by the formation of vortical structures, indicated by an increased streamwise vorticity. This becomes more pronounced for $t = 1.74$. The increase of the boundary layer thickness and the break up into smaller structures can be observed for $t = 1.86$ and $t = 1.98$.

Figure 7.45 and Figure 7.46 show isosurfaces of constant Q at different times. The initially two-dimensional flow structure at $t = 1.35$ undergoes a modulation and becomes three-dimensional at $t = 1.48$. Hereafter, the formation of a Λ-vortex can be observed for $t = 1.61$ and $t = 1.74$. This is a well known feature of fundamental resonance (Klebanoff *et al.*, 1962). For visualization purposes, the vortex is indicated with dashed blue lines. Note that the tip of the Λ-vortex is lifted up, whereas the legs are closer to the wall. For $t = 1.86$, a hairpin vortex develops, which is indicated by the blue circle. The last time instance $t = 1.98$ shows that the flow breaks up into smaller structures. Once again, it can be observed that the flow still exhibits a noticeable coherence, indicating that turbulence is not yet reached.

Note that for this simulation higher streamwise and azimuthal modes of the v- and w-velocity components as well as the temperature show grid-mesh oscillations in the region close to the wall. These grid-mesh oscillations occur at first around $t = 1.15$ and are caused by a too large time step Δt. However, they are damped over time

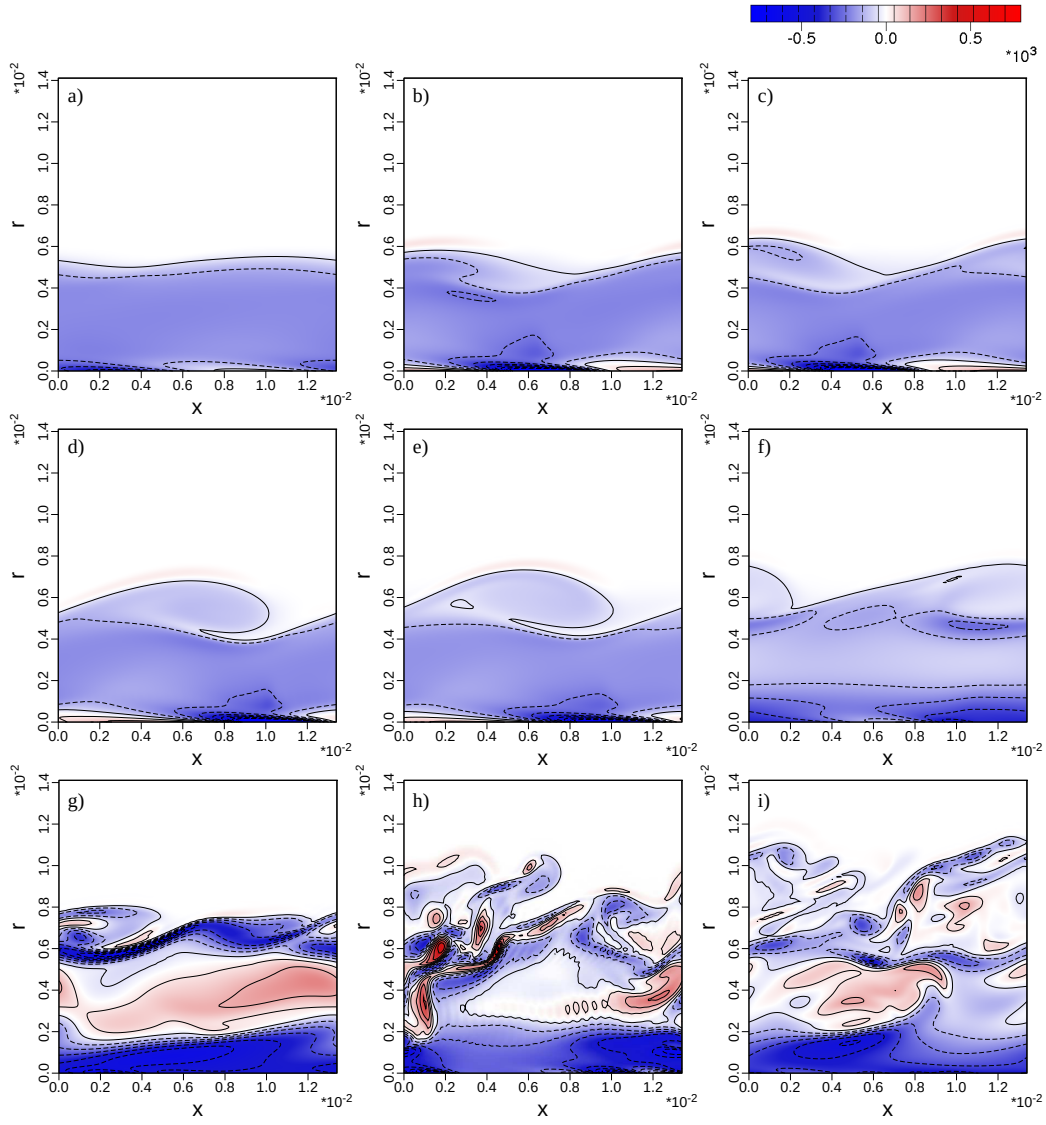

Figure 7.43: Temporal evolution of azimuthal vorticity ω_φ at $\varphi = 0.0314$ for a) $t = 0.97$, b) $t = 1.09$, c) $t = 1.23$, d) $t = 1.35$, e) $t = 1.48$, f) $t = 1.61$, g) $t = 1.74$, h) $t = 1.86$ and i) $t = 1.98$. $A_{(1,0)} = 10^{-4}$, $A_{(1,1)} = 10^{-4}$, $R_x = 2024.17$, $M_\infty = 7.95$, $T^*_\infty = 53.35K$, $Re_\infty = 3,333,333$.

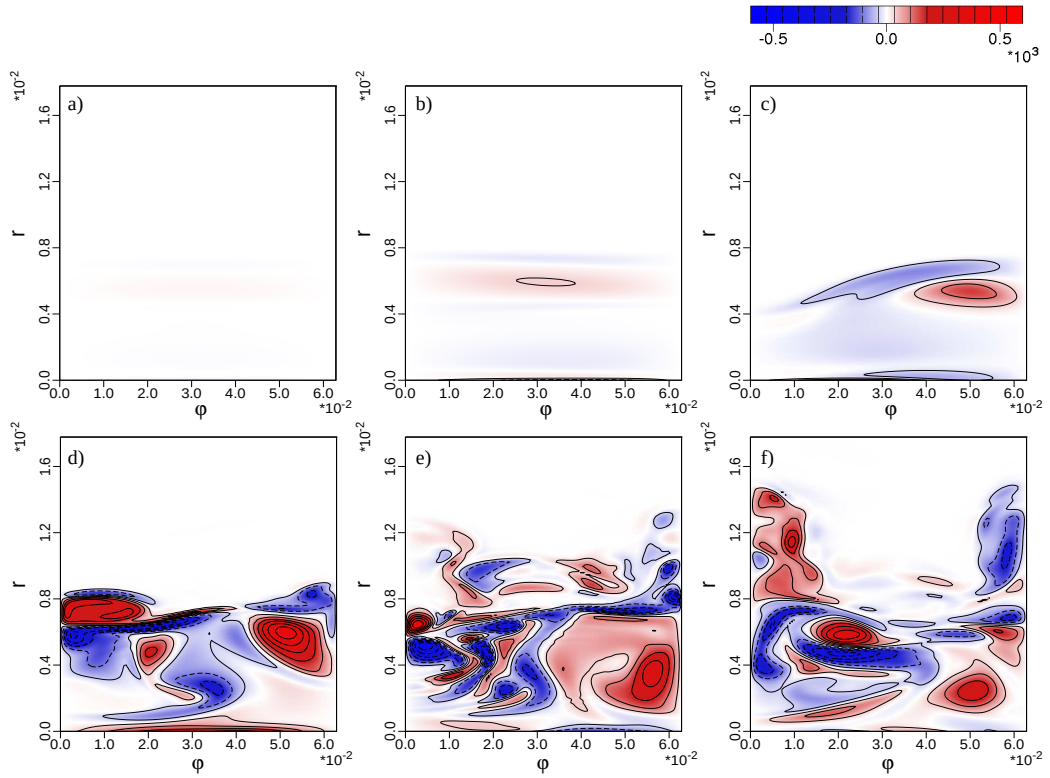

Figure 7.44: Temporal evolution of streamwise vorticity ω_x at $x = 0.0067$ for a) $t = 1.35$, b) $t = 1.48$, c) $t = 1.61$, d) $t = 1.74$, e) $t = 1.86$ and f) $t = 1.98$. Shown is half the azimuthal wavelength of the pair of secondary waves. $A_{(1,0)} = 10^{-4}$, $A_{(1,1)} = 10^{-4}$, $R_x = 2024.17$, $M_\infty = 7.95$, $T^*_\infty = 53.35K$, $Re_\infty = 3,333,333$.

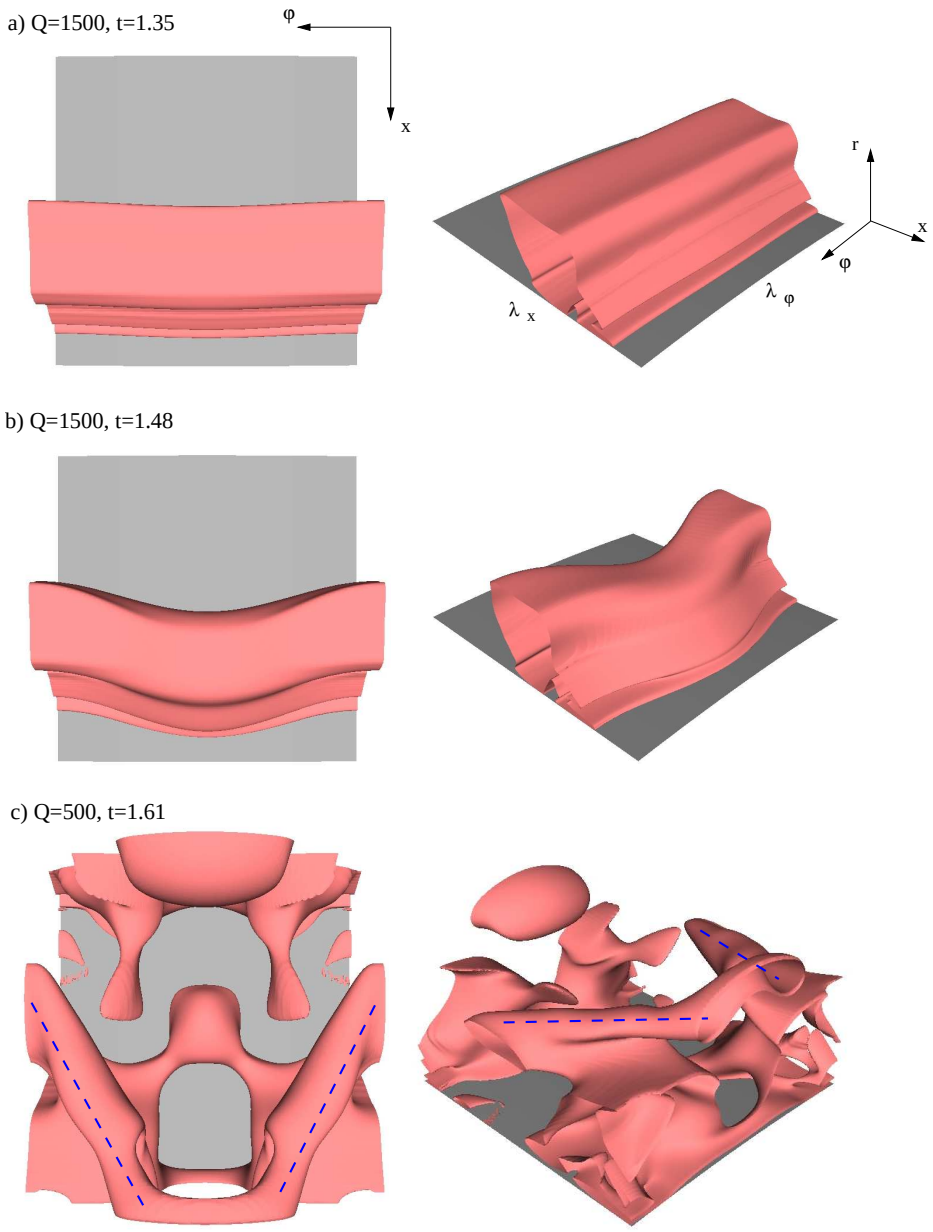

Figure 7.45: Temporal evolution of constant isosurfaces of Q for the early stages of transition at a) $t = 1.35$, b) $t = 1.48$ and c) $t = 1.61$. $A_{(1,0)} = 10^{-4}$, $A_{(1,1)} = 10^{-4}$, $R_x = 2024.17$, $M_\infty = 7.95$, $T^*_\infty = 53.35K$, $Re_\infty = 3,333,333$.

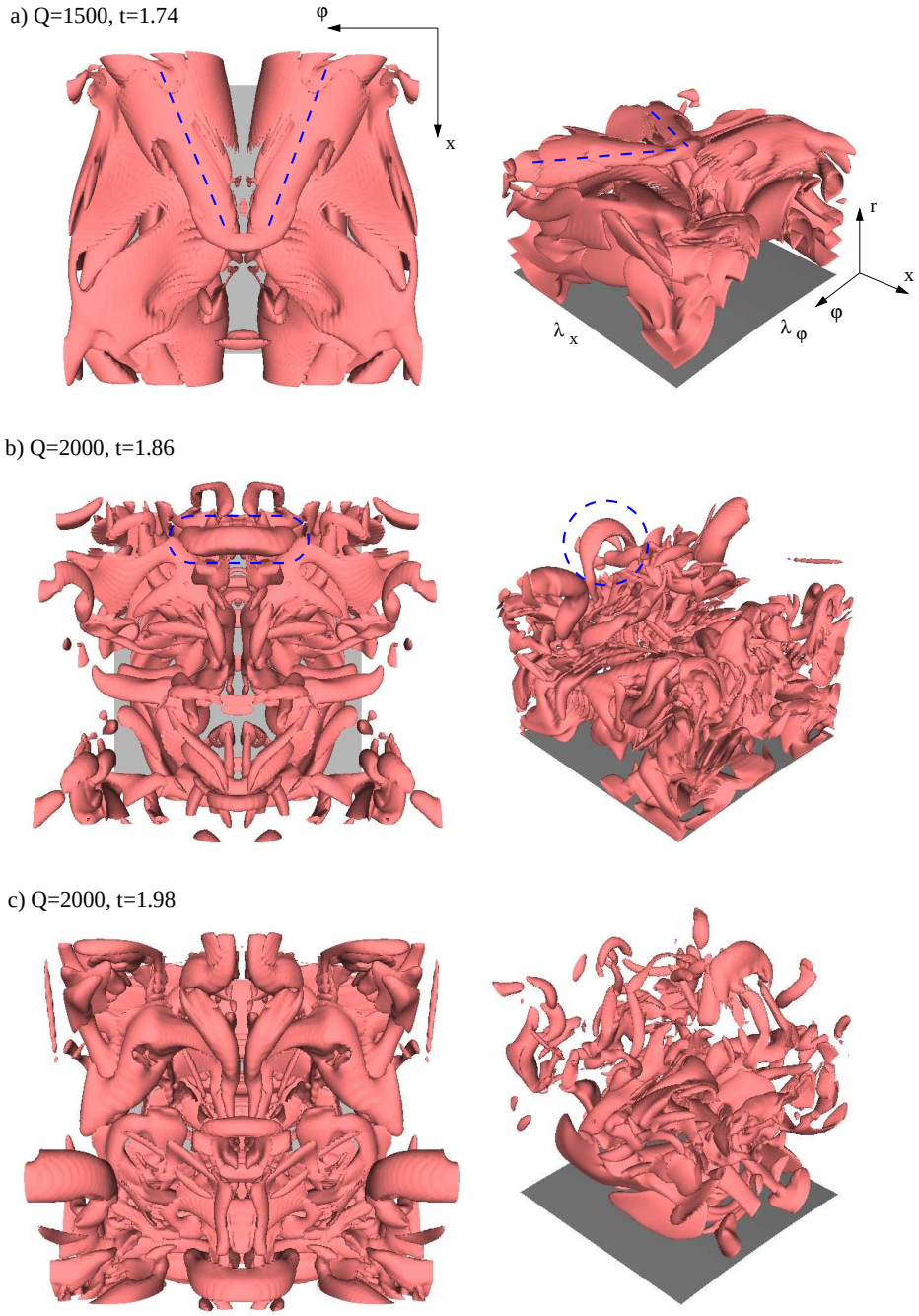

Figure 7.46: Temporal evolution of constant isosurfaces of Q for the late stages of transition at a) $t = 1.74$, b) $t = 1.86$ and c) $t = 1.98$. $A_{(1,0)} = 10^{-4}$, $A_{(1,1)} = 10^{-4}$, $R_x = 2024.17$, $M_\infty = 7.95$, $T^*_\infty = 53.35K$, $Re_\infty = 3,333,333$.

and eventually vanish, rather than terminating the simulation. In order to check if this has a negative influence on the results in this chapter, the simulation was rerun with a thirty three percent smaller time step for a time interval between $t = 1.1$ and $t = 1.3$. It was found that, first, the grid-mesh oscillations did not appear and, second, the results did not exhibit any notable difference compared to the simulation with the larger time step. This is e.g. illustrated in Figure 6.10, where the skin friction coefficient is plotted for both, the smaller and larger time steps. Note in particular that the above mentioned "bump" in the temperature distribution for $t = 1.27$ and $t = 1.57$ shown in Figure 7.41 is also present in the simulation with the smaller time step. It can be concluded that the simulation with the larger time step represents the correct physics and that the numerical instability has no negative influence on the results. All presented figures are therefore taken from the simulation with the larger time step.

7.5.4 Preliminary Summary of Fundamental Resonance Simulations

Numerical investigation of fundamental resonance for the given setup revealed that fundamental resonance between a two-dimensional and three-dimensional mode S is particularly pronounced for the azimuthal mode number of the secondary, oblique disturbance waves $k_c = 50$. In contrast, fundamental resonance between a two-dimensional mode S and a three-dimensional mode F could not be identified. A weak influence of mode F might be present in the amplitude modulation of the temporal evolution of the wall pressure for very high azimuthal mode numbers of the secondary, oblique disturbance waves ($k_c > 60$).

The identified fundamental resonance between the two slow modes was studied until the late stages of transition. The investigation of the mean flow quantities revealed characteristic features of the laminar-turbulent transition, such as an increase in boundary layer thickness, fuller mean flow profiles and a sharply increased skin fric-

tion coefficient. The flow structures, analyzed by means of vorticity and Q-criterion, showed the formation of Λ-vortices, hairpin vortices and the break up into smaller structures.

7.6 Comparison of Breakdown Scenarios

This chapter provides an attempt to compare the three previously investigated breakdown scenarios. In particular, the question arises, which of the scenarios is the most dominant transition process. Due to the different nature of the breakdown scenarios, the answer to this question is difficult. As presented in section 7.4, subharmonic resonance is apparently not important for the investigated sharp cone geometry and therefore won't be considered in the following comparison.

A simulation is performed where both, oblique breakdown and fundamental resonance are simultaneously forced in order to directly compare their influence on the transition onset. As known from previous chapters, each mechanism is dominant for a different azimuthal mode number k_c. Fundamental resonance is most pronounced for the azimuthal mode number of the secondary disturbance waves $k_c = 50$ and oblique breakdown was found to be strong for an azimuthal mode number $k_c = 20$. In addition, the streamwise wave numbers are slightly different for the two scenarios. The simulations of fundamental resonance were carried out with a streamwise wave number $\alpha_{r,fund} = 477.04$, whereas the simulations of oblique breakdown were performed for $\alpha_{r,obl} = 465.55$. Hence, the following approach is used to implement both mechanisms in one single computation:

The simulation is performed with an azimuthal extent of the computational domain corresponding to the azimuthal mode number $k_c = 10$ and an initial forcing of the modes $(1,0)$, $(1,2)$ and $(1,5)$ with the amplitudes $A_{(1,0)} = 10^{-4}$, $A_{(1,2)} = 10^{-4}$ and $A_{(1,5)} = 10^{-6}$, respectively. Mode $(1,2)$ corresponds to the oblique disturbance mode $(1,1)$ of the pure oblique breakdown simulations with an azimuthal mode num-

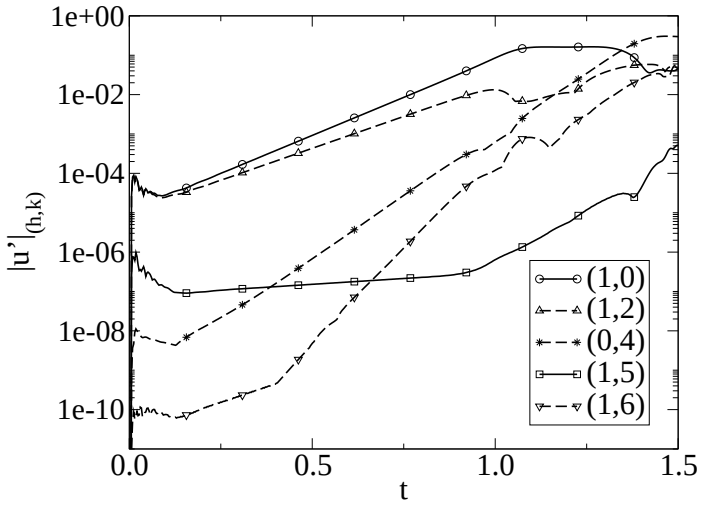

Figure 7.47: Comparison of oblique breakdown and fundamental resonance by means of the temporal development of the maximum disturbance velocity in streamwise direction $|u'|_{(h,k)}$. $A_{(1,2),obl} = 10^{-4}$, $A_{(1,0),fund} = 10^{-4}$, $A_{(1,5),fund} = 10^{-6}$. $R_x = 2024.17$, $M_\infty = 7.95$, $T^*_\infty = 53.35K$, $Re_\infty = 3,333,333$.

ber $k_c = 20$ and mode $(1,5)$ represents the secondary, oblique disturbance mode $(1,1)$ of the pure fundamental resonance simulations with an azimuthal mode number $k_c = 50$. The streamwise wave number α_r is chosen to be $\alpha_r = 470$. This value is a compromise, but as can be seen from Figure 7.3.1 still very close to the maximum amplification for both cases. The simulation is performed with seventeen Fourier modes in streamwise, 345 points in wall-normal and sixteen Fourier modes in azimuthal direction.

The result of the simulation is presented in Figure 7.6.1, which shows the temporal development of the maximum disturbance velocity in streamwise direction $|u'|_{(h,k)}$. The dashed lines indicate the modes that are related to oblique breakdown, in particular the initially forced mode $(1,2)$, the longitudinal vortex mode $(0,4)$ and mode $(1,6)$. These modes correspond to the modes $(1,1)$, $(0,2)$ and $(1,3)$ of the pure oblique breakdown simulations, respectively. The solid lines label modes that are related to fundamental resonance, namely the two-dimensional, primary disturbance mode $(1,0)$ and the secondary, three-dimensional disturbance mode $(1,5)$. As can be seen from

Figure 7.6.1, modes $(0, 4)$ and $(1, 6)$ exceed the amplitude level of the initially forced three-dimensional mode $(1, 2)$ at $t \approx 1.0$. The secondary disturbance mode $(1, 5)$ of fundamental resonance departs from its eigenbehavior at $t \approx 0.9$, but does not reach the amplitude level of the primary, fundamental disturbance mode $(1, 0)$. This behavior demonstrates that oblique breakdown seems to govern the transition process for the present setup, whereas fundamental resonance apparently plays a weaker role. However, oblique breakdown shows for $t > 0.9$ a slightly different behavior from the results presented in section 7.3 due to wave interactions with the additionally forced modes. Furthermore, one has to keep in mind that the onset of transition based on fundamental resonance depends on the amplitude of the secondary disturbance. A higher initial amplitude of the secondary disturbance mode would lead to an advanced transition onset. This demonstrates that an ultimate conclusion cannot not be drawn from the presented results.

Both, oblique breakdown and fundamental resonance are strong mechanisms for the investigated Mach 7.95 flow over a sharp circular cone, but a combined simulation of these scenarios does not reveal any conclusive trends. The interpretation of the results is difficult and based on speculations. Hence, continuative investigations are necessary, including an investigation of the developing flow structures. This, however, requires higher resolved simulations, which won't be conducted in the framework of this thesis.

7.7 Summary of Mach 8 Temporal Simulations

Laminar–turbulent transition in a hypersonic boundary layer on a sharp circular cone was investigated using temporal direct numerical simulations. The numerical simulations were performed for a hypersonic flow under cold wind tunnel conditions at $M_\infty = 7.95$, $T^*_\infty = 53.35K$ and $Re_\infty = 3,333,333$. First, the temporal code was validated by means of linear stability theory. Then, three different transition mecha-

nisms were investigated by introducing low-amplitude disturbances into the laminar boundary layer in order to study their temporal development. In particular, oblique breakdown, subharmonic resonance and fundamental resonance were analyzed. It was shown that oblique breakdown and fundamental resonance are viable paths to transition, whereas subharmonic resonance plays a minor role for the investigated setup.

The validation was performed by comparing the results obtained from temporal direct numerical simulations with the results computed from compressible linear stability theory. An excellent agreement between both methods was achieved. The validation was successful for both, two- and three-dimensional disturbances. Moreover, the influence of the domain height and the wall-normal grid resolution on the TDNS results were investigated.

Oblique breakdown is governed by a pair of oblique disturbance waves with equal, but opposite wave angles. It was shown that the transition is based on interactions of modes with odd-odd and even-even mode number combinations ($h + k =$ even). Eventually, a transitional flow regime is reached, characterized by the growth of odd-odd and even-even mode number combinations and, associated with that, a significant increase in the skin friction coefficient. The process of laminar-turbulent transition was also described by the temporal evolution of the Favre-averaged velocity profiles and the streamwise and azimuthal averaged temperature profiles. When the flow became transitional, the profiles became fuller and showed an increase in boundary layer thickness as well as the development of inflection points. Furthermore, the temporal evolution of the flow structures, visualized by means of the streamwise and azimuthal vorticity and the Q-criterion, showed the characteristic properties of oblique breakdown. The formation of hexagonal structures, followed by the development of longitudinal structures and eventually the break up into small scale structures was observed. Altough two-dimensional disturbances are stronger amplified than three-dimensional waves for the present flow at Mach 7.95, oblique breakdown was

demonstrated to be a viable path to transition for the investigated azimuthal mode number $k_c = 20$. Hence, it can be concluded that oblique breakdown is an important mechanism also for hypersonic flow regimes.

Interactions between a two-dimensional, primary wave and a pair of three-dimensional secondary waves with half the frequency and twice the streamwise wave length of the primary wave govern symmetric subharmonic resonance. For the given setup, the subharmonic resonance conditions are fulfilled for secondary disturbance waves with the azimuthal mode number $k_c = 70$. However, it was shown that subharmonic resonance is weak when compared to other mechanisms. It can therefore be concluded that subharmonic resonance is an unlikely breakdown mechanism for the investigated hypersonic boundary layer on a sharp circular cone.

Fundamental resonance is governed by interactions between a two-dimensional, primary disturbance wave and a pair of three-dimensional, secondary disturbance waves with the same frequency and streamwise wave length as the two-dimensional wave. It was shown that only one boundary layer mode, namely mode S, is dominant for the investigated setup. Fundamental resonance between a two-dimensional mode S and a three-dimensional mode F could not be detected. A weak influence of mode F might be present for very high values of the azimuthal mode number of the secondary disturbance waves ($k_c > 60$), indicated by an amplitude modulation in the temporal evolution of the wall pressure. In contrast, fundamental resonance between the two slow modes exhibits strong resonant growth, in particular for secondary, oblique waves with the azimuthal mode number $k_c = 50$. It was therefore investigated until the late stages of transition. As for oblique breakdown, the Favre-averaged velocity profiles and the streamwise and azimuthal averaged temperature profiles became fuller and showed an increase in boundary layer thickness as well as the development of inflection points. All three features are characteristic for the laminar-turbulent transition process. In addition, the investigation of the flow structures by means of the streamwise and azimuthal vorticity and the Q-criterion demonstrated the three-dimensional

modulation of the initially two-dimensional flow field, leading to the formation of Λ-vortices. This was followed by the development of hairpin vortices and the break up into smaller structures.

A single low resolved simulation was performed to compare the investigated breakdown scenarios and to get an idea which of the mechanisms is the most dominant transition process. For the particular setup, oblique breakdown seemed to be the favored mechanism. However, final conclusions could not be made due to the low resolution and the different nature of the breakdown scenarios, i.e. for example the fact that oblique breakdown is governed by a pair of oblique, primary waves, whereas fundamental resonance is governed by a two-dimensional, primary wave *and* a pair of oblique, secondary disturbance waves at lower amplitude. In order to compare these mechanisms in more detail, higher resolved simulations are inevitable.

It is important to note that the temporal approach contains numerous assumptions, which decrease the computational cost, but also influence the results. Despite these assumptions, the temporal approach provides reasonable results about the local flow behavior and is an excellent tool for parameter studies. The presented temporal direct numerical simulations of a hypersonic boundary layer at $M = 7.95$ on a sharp circular cone are therefore very helpful for the setup of more expensive spatial simulations.

8. Conclusions

8.1 Supersonic Flat–Plate Boundary Layer at Mach 3

The nonlinear transition regime of a supersonic flat–plate boundary layer was investigated using linear stability theory (LST) and direct numerical simulations (DNS). To date, the most dominant nonlinear mechanism that eventually transitions a laminar, supersonic boundary layer to turbulence is still unknown. The knowledge of the relevant nonlinear mechanisms is however mandatory for the accurate determination of the transition onset. Previous investigations (Fasel *et al.*, 1993; Kosinov *et al.*, 1994) of the nonlinear transition regime discovered two main nonlinear mechanisms, the so-called "oblique breakdown" mechanism and "asymmetric subharmonic resonance". Several questions related to both mechanisms are still unresolved and hence, are the main focus of this research.

We identified oblique breakdown in the experiments by Kosinov and his co-workers who investigated asymmetric subharmonic resonance in a Mach 2 flat-plate boundary layer (Mayer *et al.*, 2007; Mayer & Fasel, 2008). By disturbing only the fundamental frequency from the experiments, it was possible to show that the nonlinear wave interactions for the fundamental frequency exhibited features of a new breakdown mechanism that could be linked to oblique breakdown. A DNS of a broadband disturbance environment (Mayer *et al.*, 2009*a*) further suggests that oblique breakdown might be the most dominant nonlinear mechanism. However, a nonlinear mechanism is only relevant for the transition process if this mechanism can indeed completely transition a laminar boundary layer to turbulence. To answer this question the entire transition path from the linear regime to the final breakdown to turbulence was simulated for a Mach 3 boundary layer using DNS. Oblique breakdown was initiated by harmonically forcing two oblique instability waves with equal but opposite wave angle. The numerical simulations clearly demonstrated that oblique breakdown

is capable of transitioning a laminar boundary layer to fully developed turbulence. Typical mean-flow properties of a turbulent, supersonic boundary layer were reached close to the end of the computational domain. In the transitional regime, the skin friction increased significantly in streamwise direction until a peak was reached. The following decay of the skin-friction coefficient approached correlations and comparable data for turbulent boundary layers in the literature. Downstream of the peak in skin friction, the flow lost its periodicity in time with respect to the initial forcing frequency. A logarithmic region in the van Driest transformed mean streamwise velocity profile was formed and the power spectra of velocity components exhibited well-known theoretical scaling laws.

As a summary of this research it can be concluded that independent of the transition scenario (natural transition or controlled transition) oblique breakdown may be the most relevant nonlinear transition mechanism for supersonic boundary layers. Hence, for flat-plate or circular cone geometries at zero angle of attack, the transition onset can be determined by considering the nonlinear wave interactions of an oblique breakdown mechanism. As illustrated in chapter 5, the transition onset is located at the streamwise position where the skin friction coefficient deviates from its laminar distribution. This event occurs when the streamwise amplitude levels of the steady vortex modes $[0, \pm 2]$ surpasses the streamwise amplitude distribution of the initially forced wave modes $[1, \pm 1]$. This fact may serve as a simple criterion for the determination of the streamwise location of the transition onset.

8.2 Hypersonic Sharp Cone Boundary Layer at Mach 8

The linear and nonlinear development of disturbances in a hypersonic boundary layer on a sharp cone were studied using spatial direct numerical simulations. Particular attention was paid to the nonlinear regime of transition. For this research, the flow conditions from the experiments by Stetson *et al.* (1983*b*) were used.

Axisymmetric pulse disturbances were introduced into the flow to generate a broad frequency spectrum of two-dimensional disturbances for comparison with LST data and to aid in the selection of disturbance frequencies for controlled transition simulations. These simulations revealed an unexpected, rapid nonlinear growth of low-frequency waves. Further examination showed that this growth is likely caused by resonance triads consisting of two relatively high frequency waves (within the band of most unstable second mode axisymmetric waves) and a third wave with a frequency equal to the difference in frequencies between the other two modes. Three–dimensional simulations allowing only a single higher azimuthal mode showed that these low-frequencies resonances could heavily influence low-frequency oblique waves as well.

Simulations of three-dimensional wave packets forced with a moderately high amplitude ($A_{in} = 10^{-2}$) showed strong evidence of nonlinear interactions by the end of the computational domain. The most dominant nonlinear interaction within the wave packet appeared to be between axisymmetric and oblique waves of the same frequency. This pointed to the possible relevance of fundamental breakdown for the investigated flow. A detailed study of fundamental resonance was performed using controlled disturbance inputs. A parameter study revealed strong resonant growth for several different azimuthal modes in the presence of an axisymmetric primary disturbance wave. The mode showing the largest growth rate after resonance ($k_c = 46$) was chosen for several highly resolved simulations of fundamental breakdown. Flow structures from these simulations revealed remarkable similarity to fundamental breakdown in incompressible flows and are dominated by the formation of aligned Λ vortices which begin stretching and breaking up into smaller scales. However, for the hypersonic boundary layer, the streamwise extent over which the nonlinear regime of transition occurs is extraordinarily long. For these simulations the skin friction initially rises in response to the large amplitude primary disturbance wave and then features a dip before again rising sharply as nonlinear interactions cause many higher modes to

rapidly reach large amplitudes.

An additional simulation of the oblique breakdown mechanism was also performed for comparison with fundamental breakdown. The oblique breakdown mechanism also initiated transition for the investigated flow conditions and forcing parameters. However, the onset of transition was not as dramatic and the skin friction did not reach a level nearly as high as for the fundamental breakdown. It must be made clear that comparing these two mechanisms is quite difficult due to their completely different nature. Although the investigated oblique breakdown did not progress as far into the transitional regime, it seems clear that both mechanisms are relevent for hypersonic boundary layers.

Additionally, Temporal direct numerical simulations were performed to compliment the spatial simulations. First, the temporal code was validated by comparing results with linear stability theory. Then, three different transition mechanisms were investigated by introducing low-amplitude disturbances into the laminar boundary layer in order to study their temporal development. In particular, oblique breakdown, subharmonic resonance and fundamental resonance were analyzed. It was shown that oblique breakdown and fundamental resonance are viable paths to transition, whereas subharmonic resonance seems to be a weaker mechanism for the investigated flow.

It was shown that in the case of oblique breakdown, transition is based on interactions of modes with odd-odd and even-even mode number combinations ($h + k =$ even). Eventually, a transitional flow regime is reached, characterized by the growth of odd-odd and even-even mode number combinations and, associated with that, a significant increase in the skin friction coefficient. The process of laminar-turbulent transition was also studied by the temporal evolution of the Favre-averaged velocity profiles and the streamwise and azimuthal averaged temperature profiles. When the flow became transitional, the profiles became fuller and showed an increase in boundary layer thickness as well as the development of inflection points. Furthermore, the temporal evolution of the flow structures, visualized by means of the streamwise

and azimuthal vorticity and the Q-criterion, showed the characteristic properties of oblique breakdown. The formation of hexagonal structures, followed by the development of longitudinal structures and eventually the break up into small scale structures was observed. Altough two-dimensional disturbances are stronger amplified than three-dimensional waves, oblique breakdown was demonstrated to be a viable path to transition for the investigated azimuthal mode number $k_c = 20$. Hence, it can be concluded that oblique breakdown is also a relevant mechanism for hypersonic boundary layers.

Fundamental resonance is governed by interactions between a two-dimensional, primary disturbance wave and a pair of three-dimensional, secondary disturbance waves with the same frequency and streamwise wave length as the two-dimensional wave. It was shown that only one boundary layer mode, namely mode S, is dominant for the investigated setup. Fundamental resonance between a two-dimensional mode S and a three-dimensional mode F could not be detected. A weak influence of mode F might be present for very high values of the azimuthal mode number of the secondary disturbance waves ($k_c > 60$), indicated by an amplitude modulation in the temporal evolution of the wall pressure. In contrast, fundamental resonance between the two slow modes exhibits strong resonant growth, in particular for secondary, oblique waves with the azimuthal mode number $k_c = 50$. It was therefore investigated until the late stages of transition. As for oblique breakdown, the Favre-averaged velocity profiles and the streamwise and azimuthal averaged temperature profiles became fuller and showed an increase in boundary layer thickness as well as the development of inflection points. All three features are characteristic for the laminar-turbulent transition process. In addition, the investigation of the flow structures by means of the streamwise and azimuthal vorticity and the Q-criterion demonstrated the three-dimensional modulation of the initially two-dimensional flow field, leading to the formation of Λ-vortices. This was followed by the development of hairpin vortices and the break up into smaller structures.

It is important to note that the temporal approach contains numerous assumptions, which decrease the computational cost, but also influence the results. Despite these assumptions, the temporal approach provides reasonable results about the local flow behavior and is an excellent tool for parameter studies. The presented temporal direct numerical simulations of a hypersonic boundary layer at Mach 8 on a sharp circular cone are therefore very helpful for the setup of the computationally more expensive spatial simulations in future research.

Appendix A: Publications generated with funding from this grant

Publications generated with funding from this AFOSR grant are:

1. Mayer, C.S.J., Wernz, S. and Fasel, H.F., 2007, "Investigation of Oblique Breakdown in a Supersonic Boundary Layer at Mach 2 Using DNS," AIAA-2007-0949.
2. Husmeier, F., and Fasel, H. F., 2007, "Numerical Investigations of Hypersonic Boundary Layer Transition for Circular Cones," AIAA-2007-3843.
3. Mayer, C.S.J. and Fasel, H.F., 2008, "Investigation of Asymmetric Subharmonic Resonance in a Supersonic Boundary Layer at Mach 2 Using DNS," AIAA-2008-0591.
4. Mayer, C.S.J., von Terzi, D.A. and Fasel, H.F., 2008, "DNS of complete transition to turbulence via oblique breakdown at Mach 3," AIAA-2008-4398.
5. Mayer, C.S.J., von Terzi, D.A. and Fasel, H.F., 2009, "DNS of complete transition to turbulence via oblique breakdown at Mach 3: Part II," AIAA-2009-3558.
6. Sivasubramanian, J., Mayer, C.S.J., Laible, A.C., and Fasel, H.F., 2009, "Numerical Investigation of Wavepackets in a Hypersonic Cone Boundary Layer at Mach 6," AIAA-2009-3560.
7. Sivasubramanian, J., and Fasel, H.F., 2009, "Investigation of Transition Initiated by a Wave Packet in a Hypersonic Cone Boundary Layer," 62nd Annual Meeting of the APS Division of Fluid Dynamics, Minneapolis, MN, Nov. 22-24.
8. Von Terzi, D.A., Mayer, C.S.J., and Fasel, H.F., 2009, "The Late Nonlinear Stage of Oblique Breakdown to Turbulence in a Supersonic Boundary Layer," 7th IUTAM Symposium on Laminar-Turbulent Transition, Stockholm, Sweden.
9. Zengl, M., Von Terzi, D.A., and Fasel, H.F., 2009, "Numerical Investigation of Subharmonic-Resonance Triads in a Mach 3 Boundary Layer," 7th IUTAM Symposium on Laminar-Turbulent Transition, Stockholm, Sweden.

10. Sivasubramanian, J., and Fasel, H.F., 2010, "Numerical Investigation of Boundary-Layer Transition Initiated by a Wave Packet for a Cone at Mach 6," AIAA-2010-0900.

11. Koevary, C., Laible, A., Mayer, C., and Fasel, H.F., 2010, "Numerical Simulations of Controlled Transition for a Sharp Circular Cone at Mach 8," AIAA-2010-4598.

12. Gross, A., and Fasel, H.F., 2010, "Modification of Ninth-Order Weighted Essentially Nonoscillatory Scheme for Mixed Subsonic/Supersonic Flow," AIAA Journal, Vol. 48, No. 11, pp. 2698-2702.

13. Gross, A., and Fasel, H.F., 2010, "Numerical Investigation of Supersonic Flow for Axisymmetric cones," Mathematics and Computers in Simulation, Vol. 81, No. 1, pp. 133-142.

14. Mayer, C.S.J., Wernz, S. and Fasel, H.F., 2011, "Numerical investigation of the nonlinear transition regime in a Mach 2 boundary layer," J. Fluid Mech., 668, 113-149.

15. Mayer, C.S.J., von Terzi, D.A. and Fasel, H.F., 2011, "Direct Numerical Simulation of Complete Transition to Turbulence Via Oblique Breakdown at Mach 3," J. Fluid Mech. (in press).

References

Adams, N. A. & Kleiser, L. 1993 Numerical simulation of transition in a compressible flat plate boundary layer. In *Transitional and Turbulent Compressible Flows* (ed. L. D. Kral & T. A. Zang), *FED* 151, pp. 101–110. ASME.

Anderson, J. D. 2004 *Modern Compressible Flow*, 3rd edn. McGraw-Hill.

Balakumar, P. 2003 Transition in a supersonic boundary-layer due to roughness and acoustic disturbances. AIAA-2003-3589.

Balakumar, P. & Malik, M. R. 1992 Discrete modes and continuous spectra in supersonic boundary layers. *J. Fluid Mech.* **239**, 631–656.

Bayliss, A., Maestrello, L., Parikh, P. & Turkel, E. 1985 Wave phenomena in a high reynolds number compressible boundary layer. In *Stability for Time Dependent and Spatially Varying Flows* (ed. D. L. Dwoyer & M. Y. Hussaini), pp. 188–205. Springer.

Berlin, S., Wiegel, M. & Henningson, D. S. 1999 Numerical and experimental investigations of oblique boundary layer transition. *J. Fluid Mech.* **393**, 23–57.

Berry, S. A., Auslender, A. H., Dilley, A. D. & Calleja, J. F. 2001 Hypersonic boundary–layer trip development for hyper–x. *Journal of Spacecraft and Rockets* **38** (6), 853–864.

Berry, S. A. & Horvarth, T. J. 2007 Discrete roughness transition for hypersonic flight vehicles. AIAA-2007-0307.

Bertolotti, F. P. 1991 Compressible boundary layer stability analyzed with the PSE equations. AIAA-1991-1637.

Bertolotti, F. P., Herbert, T. & Spalart, P. R. 1992 Linear and nonlinear stability of the Blasius boundary layer. *J. Fluid Mech.* **242**, 441–471.

Bestek, H. & Eissler, W. 1996 Direct numerical simulation of transition in Mach 4.8 boundary layers at flight conditions. In *Engineering Turbulence Modelling and Experiments* (ed. Rodi & Bergeles), , vol. 3. Elsevier Science.

Borg, M. P., Schneider, S. P. & Juliano, T. J. 2008 Effect of freestream noise on roughness-induced transition for the x–51a forebody. AIAA-2008-0592.

Bountin, D., Shiplyuk, A. & Maslov, A. 2008 Evolution of nonlinear processes in a hypersonic boundary layer on a sharp cone. *J. Fluid Mech.* **611**, 427–442.

Canuto, C., Hussaini, M., Quateroni, A. & Zang, T. 1988 *Spectral Methods in Fluid Dynamics*. Springer.

Casper, K. M., Beresh, S. J., Henfling, J. F., Spiller, R. W., Pruet, B. & Schneider, S. P. 2009 Hypersonic wind-tunnel measurements of boundary-layer pressure fluctuations .

Cavalieri, D. A. 1995 On the experimental design for instability analysis on a cone at Mach 3.5 and 6.0 using a corona discharge perturbation method. Master's thesis, Illinois Institute of Technology.

Chang, C. L. & Malik, M. R. 1993 Linear and nonlinear PSE for compressible boundary layers. *Tech. Rep.* CR-191537. NASA.

Chang, C. L. & Malik, M. R. 1994 Oblique-mode breakdown and secondary instability in superonic boundary layers. *J. Fluid Mech.* **273**, 323–360.

Chang, C. L., Malik, M. R., Erlebacher, G. & Hussaini, M. Y. 1991 Compressible stability of growing boundary layers using Parabolized Stability Equations .

Chen, F. J., Malik, M. R. & Beckwith, I. E. 1989 Boundary-layer transition on a cone and flat plate at Mach 3.5. *AIAA J.* **27**, 687–693.

Cheng, F., Zhong, X., Gogineni, S. & Kimmel, R. L. 2003 Magnetic effects on second-mode instability of a weakly ionized Mach 4.5 boundary layer. *Phys. Fluids A* **15** (7), 2020–2040.

Coles, D. 1954 Measurements of turbulent friction on a smooth flat plate in supersonic flow. *J. Aero. Sci.* **21**, 433–448.

Corke, T. C., Cavalieri, D. A. & Matlis, E. 2002 Boundary-layer instability on sharp cone at Mach 3.5 with controlled input. *AIAA J.* **40** (5), 1015–1018.

Craik, A. D. D. 1971 Non-linear resonant instability in boundary layers. *J. Fluid Mech.* **50**, 393–413.

Dinavahi, S. P. G. & Pruett, C. D. 1993 Analysis of direct numerical simulation data of a Mach 4.5 transitional boundary-layer flow. In *Transitional and Turbulent Compressible Flows* (ed. L. D. Kral & T. A. Zang), *FED* 151, pp. 147–153. ASME.

Eissler, W. 1995 Numerische Untersuchungen zum laminar-turbulenten Strömungsumschlag in Überschallgrenzschichten. PhD thesis, Universität Stuttgart.

Eissler, W. & Bestek, H. 1996 Spatial numerical simulations of linear and weakly nonlinear wave instabilities in supersonic boundary layers. *Theoret. Comput. Fluid Dyn.* **8**, 219–235.

El-Hady, N. M. 1991 Spatial three-dimensional secondary instability of compressible boundary-layer flows. *AIAA J.* **29**, 688–696.

El-Hady, N. M. 1992 Secondary instability of high-speed flows and the influence of wall cooling and suction. *Phys. Fluids A* **4**, 727–743.

Erlebacher, G. & Hussaini, M. Y. 1990 Numerical experiments in supersonic boundary-layer stability. *Phys. Fluids A* **2**, 94–104.

Fadlun, E. A., Verzicco, R., Orlandi, P. & Mohd-Yusof, J. 2000 Combined immersed-boundary finite-difference methods for three-dimensional complex flow simulations. *J. Comp. Phys.* **161**, 35–60.

Fasel, H. 1976 Investigation of the stability of boundary layers by a finite-difference model of the Navier-Stokes equations. *J. Fluid Mech.* **78**, 355.

Fasel, H., Thumm, A. & Bestek, H. 1993 Direct numerical simulation of transition in supersonic boundary layer: Oblique breakdown. In *Transitional and Turbulent Compressible Flows* (ed. L. D. Kral & T. A. Zang), *FED* 151, pp. 77–92. ASME.

Fasel, H. F. & Konzelmann, U. 1990 Non-parallel stability of a flat-plate boundary layer using the complete Navier-Stokes equations. *J. Fluid Mech.* **221**, 311–347.

Fasel, H. F. & Saric, W. S., ed. 1999 *Proceedings of the IUTAM Symposium on Laminar–Turbulent Transition, Sedona, Arizona, USA*. Springer.

Fedorov, A. V. 2003 Receptivity of a high-speed boundary layer to acoustic disturbances. *J. Fluid Mech.* **491**, 101–129.

Fedorov, A. V. & Khokhlov, A. P. 2002 Receptivity of hypersonic boundary layer to wall disturbances. *Theoret. Comput. Fluid Dyn.* **15**, 231–254.

Fernholz, H. H. & Finley, P. J. 1980 A critical commentary on mean flow data for two-dimensional compressible turbulent boundary layers. AGARD Report 254. Advisory Group for Aerospace Research and Development.

Ferziger, J. H. 1998 *Numerical Methods for Engineering Application*, 2nd edn. Wiley-Interscience.

Fezer, A. & Kloker, M. 2004 Grenzschichtumschlag bei Überschallströmung. Sonderforschungsbericht 259. DFG.

Gaydos, P. & Tumin, A. 2004 Multimode decomposition in compressible boundary layers. *AIAA J.* **42**, 1115–1121.

Goldstein, D., Handler, R. & Sirovich, L. 1993 Modeling a no-slip flow boundary with an external force field. *J. Comp. Phys.* **105**, 354–366.

Govindarajan, R., ed. 2004 *Proceedings of the IUTAM Symposium on Laminar–Turbulent Transition, Bangalore, India*. Springer.

Graziosi, P. & Brown, G. L. 2002 Experiments on stability and transition at Mach 3. *J. Fluid Mech.* **472**, 83–124.

Gross, A. & Fasel, H. F. 2002 High-order WENO schemes based on the Roe approximate Riemann solver. AIAA-2002-2735.

Gross, A. & Fasel, H. F. 2008 High-order accurate numerical method for complex flows. *AIAA J.* **46**, 204–214.

Guarini, S. E., Moser, R. D., Shariff, K. & Wray, A. 2000 Direct numerical simulation of a supersonic turbulent boundary layer at Mach 2.5. *J. Fluid Mech.* **414**, 1–33.

Harris, P. J. 1997 Numerical investigation of transitional compressible plane wakes. PhD thesis, The University of Arizona.

Hein, S., Bertolotti, F. P., Simen, M., Hanifi, A. & Henningson, D. 1996 Linear nonlocal instability analysis – the linear nolot code –. Internal Document IB 223-94 A56. DLR, Göttingen, Germany.

Heisenberg, W. 1948 Zur statistischen Theorie der Turbulenz. *Zeitschrift für Physik* **124**, 628–657.

Henningson, S. & Schmid, P. J. 2001 *Stability and Transition in Shear Flows*, 1st edn. Springer.

Herbert, T. 1988 Secondary instability of boundary layers. *Ann. Rev. Fluid Mech.* **20**, 487–526.

Herbert, T. 1994 Parabolized stability equations. AGARD Report 793. Advisory Group for Aerospace Research and Development.

Hingst, U. G. 1990 Laminar/turbulent flow transition effects on high speed missile domes. AGARD Report CP 493. Advisory Group for Aerospace Research and Development.

Horvath, T. 2002 Boundary layer transition on slender cones in conventional and low disturbance mach 6 wind tunnels. AIAA-2002-2743.

Hunt, J. C. R., Wray, A. A. & Moin, P. 1988 Eddies, streams, and convergence zones in turbulent flows. In *Proceedings of the 1988 Summer Conference*. Stanford University.

Husmeier, F. 2008 Numerical investigations of transition in hypersonic flows over circular cones. PhD thesis, The University of Arizona.

Husmeier, F. & Fasel, H. F. 2007 Numerical investigations of hypersonic boundary layer transition for circular cones. AIAA-2007-3843.

Husmeier, F., Mayer, C. S. J. & Fasel, H. F. 2005 Investigation of transition of supersonic boundary layers at Mach 3 using DNS. AIAA-2005-0095.

Jiang, L., Choudhari, M., Chang, C.-L. & Liu, C. 2006 Numerical simulations of laminar-turbulent transition in supersonic boundary layer. AIAA-2006-3224.

Johnson, H. B., Candler, G. V. & Hudson, M. L. 1997 Numerical study of hypersonic boundary layer transition on a blunt body. AIAA-1997-0554.

Kachanov, Y. S. 1994 Physical mechanisms of laminar boundary-layer transition. *Ann. Rev. Fluid Mech.* **26**, 411–482.

Kendall, J. M. 1975 Wind tunnel experiments relating to supersonic and hypersonic boundary-layer transition. *AIAA J.* **13**, 290–299.

Kimmel, R. L., Poggie, J. & Schwoerke, S. N. 1999 Laminar-turbulent transition in a mach 8 elliptic cone flow. *AIAA J.* **37**, 1080–1087.

Klebanoff, P. S., Tidstrom, K. D. & Sargent, L. M. 1962 The three-dimensional nature of boundary layer instability. *J. Fluid Mech.* **12**, 1–34.

Kleiser, L. & Zang, T. A. 1991 Numerical simulation of transition in wall-bounded shear flows. *Ann. Rev. Fluid Mech.* **23**, 495–537.

Kloker, M. 1993 Direkte Numerische Simulation des laminar-turbulenten Strömungsumschlages in einer stark verzögerten Grenzschicht. PhD thesis, Universität Stuttgart.

Korejwo, H. A. & Holden, M. S. 1992 Ground test facilities for aerothermal and aero-optical evaluation of hypersonic interceptors. AIAA-1992-10744.

Kosinov, A. D., Maslov, A. A. & Shevelkov, S. G. 1990 Experiments on the stability of supersonic laminar boundary layers. *J. Fluid Mech.* **219**, 621–633.

Kosinov, A. D., Semionov, N. V., Shevelkov, S. G. & Zinin, O. I. 1994 Experiments on the nonlinear instability of supersonic boundary layers. In *Nonlinear Instability of Nonparallel Flows* (ed. D. T. Valentine, S. P. Lin & W. R. C. Philips), pp. 196–205. Springer.

Kosinov, A. D. & Tumin, A. 1996 Resonance interaction of wave trains in supersonic boundary layer. In *Nonlinear Instability and Transition in Three-Dimensional Boundary Layers* (ed. P. W. Duck & P. Hall), pp. 379–388. Kluwer Academic Publishers.

Laddon, D. W. & Schneider, S. P. 1998 Measurements of controlled wave packets at mach 4 on a cone at angle of attack. AIAA-1998-0436.

Laible, A. C., Mayer, C. S. J. & Fasel, H. F. 2008 Numerical investigation of supersonic transition for a circular cone at Mach 3.5. AIAA-2008-4397.

Laible, A. C., Mayer, C. S. J. & Fasel, H. F. 2009 Numerical investigation of transition for a cone at mach 3.5: Oblique breakdown. AIAA-2009-3557.

Laufer, J. & Vrebalovich, T. 1960 Stability and transition of a supersonic laminar boundary layer on an insulated flat plate. *J. Fluid Mech.* **9**, 257–299.

van Leer, B. 1982 Flux-vector splitting for the Euler equations. In *International Conference on Numerical Methods in Fluid Dynamics*, , vol. 170, pp. 507–512. Springer-Verlag.

Lees, L. & Lin, C. C. 1946 Investigation of the stability of the laminar boundary layer in a compressible fluid. NACA Technical Report 1115.

Lei, J. & Zhong, X. 2009 Linear stability study of hypersonic boundary layer transition on blunt circular cones. AIAA-2009-939.

Lei, J. & Zhong, X. 2010 Linear stability analysis of nose bluntness effects on hypersonic boundary layer transition. AIAA-2010-898.

Linnick, M. N. & Fasel, H. F. 2005 A high-order immersed interface method for simulating unsteady in compressible flows on irregular domains. *J. Comp. Phys.* **204**, 157–192.

Ma, Y. & Zhong, X. 2003 Receptivity of a supersonic boundary layer over a flat plate. part 1. wave structures and interactions. *J. Fluid Mech.* **488**, 37–78.

Mack, L. M. 1965 Computation of the stability of the laminar boundary layer. In *Methods of Comp. Physics* (ed. B. Alder, S. Fernbach & M. Rotenberg), , vol. 4, pp. 247–299. Academic Press.

Mack, L. M. 1969 Boundary-layer stability theory. Internal Document 900-277. Jet Propulsion Laboratory, Pasadena, California.

Mack, L. M. 1975 Linear stability theory and the problem of supersonic boundary-layer transition. *AIAA J.* **13**, 278–289.

Mack, L. M. 1984 Boundary-layer linear stability theory. AGARD Report 709. Advisory Group for Aerospace Research and Development.

Mack, L. M. 1987 Stability of axisymmetric boundary layers on sharp cones at hypersonic mach numbers. AIAA-1987-1413.

Mack, L. M. 2000 Early history of compressible linear stability theory. In *Laminar-Turbulent Transition* (ed. H. F. Fasel & W. S. Saric), pp. 9–34. Springer.

Maeder, T., Adams, N. A. & Kleiser, L. 2001 Direct simulations of turbulent supersonic boundary layers by an extended temporal approach. *J. Fluid Mech.* **429**, 187–216.

Maekawa, H., Watanabe, D., Ozaki, K. & Takami, H. 2007 Direct numerical simulation of a spatially evolving supersonic transitional/turbulent boundary layer. In *Proc. of 5th Int. Symp. on Turbulence and Shear Flow Phenomena TSFP-5*, , vol. 1, pp. 301–306. Elsevier.

Malik, M. R. 1989 Prediction and control of transition in supersonic and hypersonic boundary layers. *AIAA J.* **27**, 1487–1493.

Malik, M. R. 1990 Numerical methods for hypersonic boundary layer stability. *J. Comp. Phys.* **86**, 376–413.

Malik, M. R. & Spall, R. E. 1991 On the stability of compressible flow past axisymmetric bodies. *J. Fluid Mech.* **228**, 443–463.

Mangler, W. 1948 Zusammenhang zwischen ebenen und rotationssymmetrischen Grenzschichten in kompressiblen Flüssigkeiten. *Z. Angew. Math. Mech.* **28** (4), 97–103.

Martin, M. P. 2007 Direct numerical simulation of hypersonic turbulent boundary layers. Part 1. Initialization and comparison with experiments. *J. Fluid Mech.* **570**, 347–364.

Masad, J. A. & Nayfeh, A. H. 1990 Subharmonic instability of compressible boundary layers. *Phys. Fluids A* **2**, 1380–1392.

Mayer, C. S. J. 2004 Stability investigation of a flat plate boundary layer with an adverse pressure gradient at Mach 3. Master's thesis, The University of Arizona.

Mayer, C. S. J. & Fasel, H. F. 2008 Investigation of asymmetric subharmonic resonance in a supersonic boundary layer at Mach 2 using DNS. AIAA-2008-0591.

Mayer, C. S. J., Laible, A. C. & Fasel, H. F. 2009*a* Numerical investigation of transition initiated by a wave packet on a cone at Mach 3.5. AIAA-2009-3809.

Mayer, C. S. J., von Terzi, D. A. & Fasel, H. F. 2008 DNS of complete transition to turbulence via oblique breakdown at Mach 3. AIAA-2008-4398.

Mayer, C. S. J., von Terzi, D. A. & Fasel, H. F. 2009*b* DNS of complete transition to turbulence via oblique breakdown at Mach 3: Part. ii. AIAA-2009-3558.

Mayer, C. S. J., Wernz, S. & Fasel, H. F. 2007 Investigation of oblique breakdown in a supersonic boundary layer at Mach 2 using DNS. AIAA-2007-0949.

Medeiros, M. A. F. & Gaster, M. 1999 The production of subharmonic waves in the nonlinear evolution of wavepackets in boundary layers. *J. Fluid Mech.* **399**, 301–318.

Meitz, H. & Fasel, H. F. 2000 A compact-difference scheme for the Navier-Stokes equations in vorticity-velocity formulation. *J. Comp. Phys.* **157**, 371–403.

Ng, L. & Erlebacher, G. 1992 Secondary instabilities in compressible boundary layers. *Phys. Fluids A* **4**, 710–726.

Normand, X. & Lesieur, M. 1992 Direct and large-eddy simulations in the compressible boundary layer. *Theoret. Comput. Fluid Dyn.* **3**, 231–252.

Parikh, P. G. & Nagel, A. L. 1990 Application of laminar flow control to supersonic transport configurations. Technical Report CR-181917. NASA.

Peskin, C. S. & McQueen, D. M. 1989 A three-dimensional computational method for blood flow in the heart. 1. immersed elastic fibers in a viscous incompressible fluid. *J. Comp. Phys.* **81**, 372–405.

Pirozzoli, S., Grasso, F. & Gatski, T. B. 2004 Direct numerical simulation and analysis of a spatially evolving supersonic turbulent boundary layer at M=2.25. *Phys. Fluids* **16**, 530–545.

Poggie, J., Kimmel, R. L. & Schwoerke, S. N. 2000 Traveling instability waves in a mach 8 flow over an elliptical cone. *AIAA J.* **38**, 251–258.

Poinsot, T. & Lele, S. 1992 Boundary conditions for direct simulations of compressible viscous flows. *J. Comp. Phys.* **101**, 104–129.

Pruett, C. D. & Chang, C. L. 1993 A comparison of PSE and DNS for high-speed boundary-layer flows. In *Transitional and Turbulent Compressible Flows* (ed. L. D. Kral & T. A. Zang), *FED* 151, pp. 57–67. ASME.

Pruett, C. D. & Chang, C.-L. 1995 Spatial direct numerical simulation of high-speed boundary-layer flows. part II: Transition on a cone in Mach 8 flow. *Theoret. Comput. Fluid Dyn.* **7**, 397–424.

Pruett, C. D. & Zang, T. A. 1992 Direct numerical simulation of laminar breakdown in high-speed, axisymmetric boundary layers. *Theoret. Comput. Fluid Dyn.* **3**, 345–367.

Pruett, C. D., Zang, T. A., Chang, C.-L. & Carpenter, M. H. 1995 Spatial direct numerical simulation of high-speed boundary-layer flows. part I: Algorithmic considerations and validation. *Theoret. Comput. Fluid Dyn.* **7**, 49–76.

Reda, D. C. 2002 Review and synthesis of roughness-dominated transition correlations for reentry applications. *Journal of Spacecraft and Rockets* **39** (2).

Reed, H. L. 1993 Direct numerical simulation of transition: The spatial approach. AGARD Report 793. AGARD-FDP-VKI Special Course.

Reshotko, E. & Tumin, A. 2004 Role of transient growth in roughness-induced transition. *AIAA J.* **42**, 766–770.

Roy, C. J. & Blottner, F. G. 2006 Review and assessment of turbulence models for hypersonic flows. *Prog. Aerospace Sci.* **42**, 469–530.

Schlatter, P. & Henningson, D. S., ed. 2009 *Proceedings of the IUTAM Symposium on Laminar–Turbulent Transition, Stockholm, Sweden*. Springer.

Schmisseur, J. D., Schneider, S. P. & Collicot, S. H. 2002 Supersonic boundary-layer response to optically generated freestream disturbances. *Experiments in Fluids* **33**, 225–232.

Schneider, S. P. 2001*a* Effects of high-speed tunnel noise on laminar-turbulent transition. *Journal of Spacecraft and Rockets* **38** (8), 323–333.

Schneider, S. P. 2001*b* Hypersonic laminar instability on round cones near zero angle of attack. AIAA-2001-0206.

Schneider, S. P. 2007 Effects of roughness on hypersonic boundary-layer transition. AIAA-2007-0305.

Schneider, S. P. 2008 Development of hypersonic quiet tunnels. *Journal of Spacecraft and Rockets* **45** (4), 641–664.

Schneider, S. P., Collicott, S. H., Schmisseur, J. D., Ladoon, D., Randall, L. A., Munro, S. E. & Salyer, T. R. 1996 Laminar-turbulent transition research in the Purdue Mach 4 quiet-flow Ludwieg tube. AIAA-1996-2191.

Scott, W. 1996 USAF, NASA programs to push hypersonic boundaries. *Aviation Week and Space Technology* pp. 22–23.

Seddougui, S. O. & Bassom, A. P. 1997 Instability of hypersonic flow over a cone. *J. Fluid Mech.* **345**, 383–411.

Shiplyuk, A. N., Bountin, D. A., Maslov, A. A. & Chokani, N. 2003 Nonlinear mechanisms of the initial stage of laminar-turbulent tansition at hypersonic velocities. *J. Appl. Mech. Tech. Phys.* **44** (5), 1–12.

Spalart, P. R. 1988 Direct simulation of a turbulent boundary layer. *J. Fluid Mech.* **187**, 61–98.

Stetson, K. F. 1988 On nonlinear aspects of hypersonic boundary-layer stability. *AIAA J.* **26**, 883–885.

Stetson, K. F. 1990 Hypersonic transition testing in wind tunnels. In *Instability and Transition* (ed. M. Y. Hussaini & R. G. Voigts), , vol. I, pp. 91–100. Springer.

Stetson, K. F. & Kimmel, R. L. 1992*a* Example of second-mode instability dominance at a Mach number of 5.2. *AIAA J.* **30**, 2974–2976.

Stetson, K. F. & Kimmel, R. L. 1992*b* On hypersonic boundary-layer stability. AIAA-1992-0737.

Stetson, K. F. & Kimmel, R. L. 1993 On the breakdown of a hypersonic laminar boundary layer. AIAA-1993-0896.

Stetson, K. F. & Rushton, G. H. 1967 A shock tunnel investigation of the effects of nose bluntness, angle of attack and boundary layer cooling on boundary layer transition at a mach number of 5.5. *AIAA J.* **5**, 899–906.

Stetson, K. F., Thompson, E. R., Donaldson, J. C. & Siler, L. G. 1983*a* Laminar boundary layer stability experiments on a cone at Mach 8. part I: Sharp cone. AIAA-1983-1761.

Stetson, K. F., Thompson, E. R., Donaldson, J. C. & Siler, L. G. 1983*b* Laminar boundary layer stability experiments on a cone at Mach 8. part II: Blunt cone. AIAA-1984-0006.

Tannehill, J. C., Anderson, D. A. & Pletcher, R. H. 1997 *Computational Fluid Mechanics and Heat Transfer*, 2nd edn. Taylor & Francis.

von Terzi, D. A. 2004 Numerical investigation of transitional and turbulent backward-facing step flows. PhD thesis, The University of Arizona.

von Terzi, D. A., Linnick, M. N., Seidel, J. & Fasel, H. F. 2001 Immersed boundary techniques for high-order finite-difference methods. AIAA-2001-2918.

Thumm, A. 1991 Numerische Untersuchungen zum laminar-turbulenten Strömungsumschlag in transsonischen Grenzschichtströmungen. PhD thesis, Universität Stuttgart.

Thumm, A., Wolz, W. & Fasel, H. 1989 Numerical simulation of Tollmien-Schlichting waves in compressible transsonic boundary layers on plates. *Z. Angew. Math. Mech.* **69**, 598–600.

Tumin, A. 2007 Three-dimensional spatial normal modes in compressible boundary layers. *J. Fluid Mech.* **586**, 295–322.

Tumin, A. 2008 Private communication.

Tumin, A., Wang, X. & Zhong, X. 2007 Direct numerical simulation and the theory of receptivity in a hypersonic boundary layer. *Phys. Fluids* **19** (1), 014101.

Tumin, A., Wang, X. & Zhong, X. 2010 Numerical simulation and theoretical analysis on hypersonic boundary–layer receptivity to wall blowing–suction. AIAA-2010-0534.

Wendt, V. 1993 Experimentelle Untersuchung der Instabilität von ebenen und konischen laminaren Hyperschallgrenzschichten. DLR-FB 93-56. DLR, Göttingen, Germany.

White, F. M. 1991 *Viscous Fluid Flow*. McGraw-Hill.

Zang, T. A., Chang, C.-L. & Ng, L. L. 1992 The transition prediction toolkit: LST, SIT, PSE, DNS, and LES, 5th Symposium on Numerical and Physical Aspects of Aerodynamic Flows.

Zhong, X. 1998 High-order finite-difference schemes for numerical simulation of hypersonic boundary-layer transition. *J. Comp. Phys.* **144**, 662–709.

Zhong, X. 2001 Leading-edge receptivity to free-stream disturbance waves for hypersonic flow over a parabola. *J. Fluid Mech.* **441**, 315–367.

Zhong, X. 2005 Effect of nose bluntness on hypersonic boundary layer receptivity over a blunt cone. AIAA-2005-5022.

Zhong, X. 2007 Numerical simulation of surface roughness effects on receptivity of hypersonic flow over blunt cones. AIAA-2007-0944.

Zhong, X. & Tatineni, M. 2003 High-order non-uniform grid schemes for numerical simulation of hypersonic boundary-layer stability and transition. *J. Comp. Phys.* **190**, 419–458.